UNIVERSITAT
POLITÈCNICA de
VALÈNCIA

INSTITUT DE DISSENY IFABRICACIÓ (IDF)

**SYNTHESIS AND CHARACTERIZATION OF SOME
NANO-SELENIDES AND THEIR APPLICATION IN
SOLAR CELLS**

BY

SUZAN KAMAL ABDEL HAMIED SABER

DOCTORAL THESIS

May 2018

Supervised by: **Prof.Dr.Bernabé Marí Soucase**

This page intentionally left blank

Table of Contents

Chapter 1.   Introduction

Part I: Basic Photovoltaic Physics

Chapter 2. The semiconductor materials. Literature Review

Chapter 3. Experimental Techniques Methodology and Characterization

Chapter 7. Conclusion

List of abbreviations and symbols

Symbols	abbreviations
A	Absorbance
AM 1.5	Air Mass 1.5 Irradiation Spectrum
BB	Black Body
^{o}C	Degree Celsius
CB	Conduction band
CdS	Cadmium sulfide
CIS	Copper indium diselenide
CIGS	Copper indium gallium diselenide
$CIGS_2$	Copper indium gallium disulfide
CIGSS	Copper indium gallium selenide sulfide
Cu	Copper
d	lattice spacing in crystal
EDS	Energy Dispersive Spectroscopy
Eg/EG	Energy band gap
EQE	External Quantum efficiency
eV	electron volt
FCC	Face centered cubic
FF	Fill Factor in efficiency calculations
Ga	Gallium
h	hour
hkl	Miller indices in lattice
IB	intermediate band
IBSC	Intermediate band solar cell
IGB	In gap band
I_m	Maximum current of a cell
In	indium
i: ZnO	intrinsic zinc oxide
J_{sc}	Short circuit current

7

KeV	Kilo electron Volt
ml	Milliliter
Mo	molybdenum
Mpp	Maximum power point
N-type	Negative type material
nm	Nanometer (10^{-9} meter)
ODC	Ordered Defect Compound
Pm	pico meter
p_m	Output power of the solar cell
P_{sun}	incoming power of the sun
P-type	positive type material
R_s	Series resistance
R_p	Shunt resistance
S	Sulfur
Se	Selenium
SEM	Scanning Electron Microscopy
T	Temperature
μm	micro meter (10^{-6} meter)
Uv – Vis	Ultraviolet – Visible
V	Voltage
VB	Valence Band
Vm	Maximum Voltage of Cell
Voc	Open circuit voltage
W	Watt
XRD	X-ray diffraction
ZnS	zinc sulfide

List of Figures

9

11

List of tables

DEDICATION

To the soul of my mother, God bless her.

To my beloved, appreciated, respectful husband: MOSTAFA ESMAIEL SEDDKY MOSTAFA.

To my piece of heart, my lovely son: MALEK MOSTAFA ESMAIEL SEDDKY.

To my father, sisters and brothers.

Abstract

Increasing global energy consumption together with environmental concerns has led to much interest in alternative, cleaner sources of energy such as solar photovoltaic. Researchers in the solar cell community have been looking for ways to reduce costs while maintaining or increasing already high efficiencies. A fundamental understanding of the materials under consideration is essential to rapid development of new technologies. TheI-III-VI$_2$ thin films offer promising systems for achieving high efficiency solar cells at lower costs. In fact, by tailoring the chemistry of the compounds it is possible to change the bandgap of the material in order to collect sunlight more efficiently. First of all, this thesis focuses on absorber layer material preparation and characterization, especially nanocrystalline thin films and consideration of both structural and electrical characteristics of such main cell absorber layer.The thesis examines how different preparation techniques and material usage could affect the properties of the synthesized thin films (absorber layer).

In this study CuInSe$_2$ and CuInS$_2$ thin films were deposited onto ITO glass substrate using the electrodeposition technique in aqueous solution. The electrodeposited films were characterized by X-ray diffraction (XRD), scanning electron microscopy (SEM) and energy dispersive X-ray analysis (EDS). The annealing effects on the electrodeposited precursors were investigated. The chalcopyrite structure of CuInSe$_2$/CuInS$_2$ showed an enhancement of crystallinity after subsequent selenization/sulfurization treatment in Se/S atmosphere, respectively. XRD and SEM studies revealed a dramatic improvement of the crystalline quality of CIS films after annealing treatments. The optical properties of annealed CuInSe$_2$-Se and CuInSe$_2$-S thin films have been studied in order to determine the effect of annealing process in different selenium and sulfur atmosphere. The optical transmittance spectra were measured in the wavelength range 400 - 1000 nm of the visible region.The optical band gap were found to be 1.48 and 1.35 eV, for CuInSe$_2$-Se and CuInSe$_2$-S which is agreement with the reported values of the optical band gap of CuInSe$_2$ and CuInS$_2$ [22], As we notice the difference in annealing temperatures and time also affects the resultant band gap energy in addition to the Se/S percentages in both samples. Mott-Schottky measurements were used to assess the conductivity type of the films and their carrier concentration. The prepared samples underwent an etching process to remove the binary accumulated Cu$_{2-x}$(Se,S) phases shown in FESEM pictures. This etching process has shown a

noticeable decrease in both, the flat band potencial, V_{fb} (V), and the number of acceptors, N_A (cm^{-3}) in selenized $CuInSe_2$ and sulfurized $CuInS_2$ samples.

In the second step we modified copper indium $CuIn_xCr_yGa_{1-x-y}Se_2$ where x=0.4, y= (0.0, 0.1, 0.2, 0.3) superstrate layer by spin coating process. $CuIn_xCr_yGa_{1-x-y}Se_2$ where x=0.4, y= (0.0, 0.1, 0.2, 0.3) nanoparticles have been synthesized firstly using a wet chemical hydrothermal method. This method is based on a non-vacuum thermal process without any additional selenization process. Introducing different metal sources in an autoclave with ethylenediamine as solvent, CIGS nanoparticles were obtained at different temperatures range 190-230°C. The X-ray diffraction (XRD) results confirmed the formation of a tetragonal $CuIn_xCr_yGa_{1-x-y}Se_2$ chalcopyrite structure. The morphology and crystal size of the prepared nanoparticles were determined by field emission scanning electron microscopy (FE-SEM), energy dispersive X-ray analysis (EDS) and high-resolution transmission electron microscopy (HR-TEM).The conductivity of the synthesized nanoparticle samples was measured in a range of temperature between 20 and 200°C by impedance spectroscopy in the frequency interval of $10^{-1} < f < 10^7$ Hz applying a 0.1 V signal amplitude.

Finally, we turned again to the study of the annealing temperature effect on Kesterite materials but this time in those of very low-cost materials and environmentally friendly Cu_2ZnSnS_4. We studied the growth of quaternary Cu_2ZnSnS_4 (CZTS) kesterite thin films by a single step electrochemical deposition followed by annealing at low temperature. The influence of different annealing atmospheres at constant annealing times (t = 45 min) and fixed preparation controlling parameters; i.e., starting materials (precursor metal salts) solution concentration, time of deposition and electrodeposition potential. Structural, compositional, morphological, and optical properties, as well as photoelectrochemical properties were studied. The films, sulfurized during 2 hours, showed a prominent kesterite phase with a nearly stoichiometric composition. Samples were characterized by X-ray diffraction (XRD), scanning electron microscopy (SEM), EDS and UV-VIS-NIR spectrometry. X-ray diffraction and confirmed the formation of pure kesterite CZTS films. SEM shows that films are compact with dense morphology and homogeneous distribution. EDS analyzed the elemental constituents of the quaternary Cu_2ZnSnS_4 with an apparent Cu deficiency and S rich for the sulfurized samples. From optical study, the energy gap was indexed for the sulfurized samples, Eg=1.52 eV. Under illumination sulfurized CZTS films

exhibits negative photocurrent and positive photovoltage values confirming the p-type character of the films.

Motivation and objectives

Both superstrate and substrate device structures are currently being pursued for copper indium gallium selenide (CuIn(Ga)Se$_2$, CIGS) device fabrication. The film growth, interdiffusion and hence the device properties are dependent on the device structure. Those CIGS solar cells, based on the superstrate structure (CIS, CIGS or CZTS), are inferior to the substrate structure, because of the interdiffusion of CdS during high temperature CIGS film growth. A best device efficiency of 10.2% and 19.2% was reported for the superstrate structure.

Chalcopyrite based solar modules uniquely combine advantages of thin film technology with the efficiency and stability of conventional crystalline silicon cells. It is therefore believed that chalcopyrite-based modules can take up a large part of the photovoltaic (PV) market growth once true mass production is started.

The most important chalcopyrite compounds for photovoltaic applications are CuInSe$_2$, CuInS$_2$, kesterite CZTS and CuGaSe$_2$ with bandgaps of 1.0, 1.5, 1.6 and 1.7 eV, respectively. Together with related materials they offer high optical absorption and a wide range of lattice constants and bandgaps. The compounds can be alloyed to obtain intermediate bandgaps. Starting with single crystals, chalcopyrite based solar cells have been under investigation since 1974. The first chalcopyrite cells had a CuInSe$_2$ absorber and therefore the technology is most advanced for lower gap materials with a composition close to CuInSe$_2$. Today the efficiency of lab scale thin film devices is close to 20%, efficiency comparable to the best multicrystalline silicon cells. Many scaling up and manufacturing issues have been resolved.

Chalcopyrites clearly offer the highest efficiency potential among all thin film technologies. The record efficiency for a small, lab scale cell is close to 20%, using just a single layer antireflective coating and a standard metal grid but none of the complex concepts that have been used to produce record silicon cells. Submodule efficiencies are at almost 17%, and square foot and larger modules range from 14 to 12% efficiency.

The low-cost potential is roughly comparable to that of other thin film technologies and is rooted in the use of inexpensive substrates, effective use of raw materials, high throughput, and large

area deposition at low temperatures as well as monolithic interconnection. Apart from the substrate, the total thickness of a chalcopyrite cell, including all films, is in the range of 2 to 4 µm, which implies that the raw material usage is only a tiny fraction of the material input for a silicon cell. Mass production will not be limited by the availability of raw materials.

The energy payback time (EPBT) is obviously an important parameter when considering how far photovoltaics can contribute to the future energy supply. The much lower thermal budget of thin film preparation (lower process temperatures as well as short process times) leads to a significant benefit.

As we will show in this study, there is considerable flexibility concerning the choice of components of a chalcopyrite cell or module as well as concerning the preparation methods for these components. It is therefore the main objective of this study is to design different absorber material (substrate) products with an optimum efficiency/cost trade-off for various applications, with power demands ranging from mW to MW and with illumination intensity ranging from indoor, low level to high level under concentration.

Those chosen chalcopyrite materials in this study is CIS, CIGS and CZTS were studied previously in different manners and we aimed to reproduce them in a modified manner. Studying a critical factor in the synthesis process of these materials, (annealing temperature relation with annealing time), in a successful attempt to reach an effecting parameter of the massive production of this type of solar cells. Then applying different preparation technique (spin coating process) in another attempt to prepare the CIGS thin films by a very low-cost preparation technique by synthesis of CIGS as nanocrystalline powders by hydrothermal process then converting them into thin films in such a case we save the annealing process time and power. In addition, incorporation of Chromium metal as dopant with different percentages in order to get new chalcopyrite material with suitable high efficiency values of the developed cell.

The outline of this thesis is as follows:

- ♣ Chapter 1 is an introductory part to the thesis and it is divided into two parts:
  PartI: study the Basic Photovoltaic Physics and
  PartII: includes the state of the art of thin film solar cells.
- ♣ Chapter 2 introduces the literature reviews on photovoltaic solar energy materials.

- Chapter 3 including all the experimental techniques used i.e; electrodeposition, spin coating process and hydrothermal auto-clave method and characterizations tools used.

- Chapters 4 present the effect of annealing temperature and time relation on the electrodeposited p-type $CuInSe_2$ and $CuInS_2$, mott-schottcky measurements were also presented.

- Chapter 5 focus on Cr doped CIGS thin films prepared by spin coating process from nano-crystalline CIGS:Cr powders hydrothermally synthesized.

- Chapter 6 CZTS single step electrodeposited kesterite thin films and studying the effect of annealing temperature on the properties of the synthesized films.

- Chapter 7 summarizes the work presented here and the overall, additionally possible future guidelines in applying the research capabilities and building from the significant results described in this dissertation.

Resumen (Castellano)

El aumento del consumo de energía global junto con las preocupaciones ambientales ha generado mucho interés por las fuentes de energía alternativas y limpias, como la energía solar fotovoltaica. Los investigadores en la comunidad fotovoltaica han estado buscando formas de reducir costos mientras mantienen o aumentan las eficiencias. Una mejor comprensión de los materiales implicados es esencial para el rápido desarrollo de nuevas tecnologías. Las películas delgadas I-III-VI$_2$ ofrecen sistemas prometedores para lograr células solares de alta eficiencia a un costo menor. De hecho, al adaptar la composición de los compuestos, es posible cambiar la banda prohibida del material para captar la luz solar de manera más eficiente.

Esta tesis se centra en la preparación y caracterización del material de la capa absorbente, especialmente las películas delgadas nanocristalinas y la consideración de las características estructurales y eléctricas de dicha capa principal absorbente de células. La tesis examina cómo las diferentes técnicas de preparación y uso del material podrían afectar las propiedades del películas delgadas sintetizadas.

Películas delgadas CuInSe$_2$ y CuInS$_2$ se depositaron sobre sustratos de vidrio ITO usando la técnica de electrodeposición en solución acuosa. Las películas electrodepositadas se caracterizaron por difracción de rayos X (XRD), microscopía electrónica de barrido (SEM) y análisis de rayos X de energía dispersiva (EDS). Se investigaron los efectos de recocido sobre los precursores electrodepositados. La estructura de calcopirita de CuInSe$_2$/CuInS$_2$ mostró una mejora de la cristalinidad después del tratamiento posterior de selenización/sulfurización en atmósfera Se/S, respectivamente. Los estudios de XRD y SEM revelaron una mejora de la calidad cristalina de las películas de CIS después de los tratamientos térmicos. Las propiedades ópticas de las películas delgadas recocidas CuInSe$_2$-Se y CuInSe$_2$-S se han estudiado para determinar el efecto del proceso de recocido en diferentes ambientes de selenio y azufre.

Además, modificamos el CuIn$_x$Cr$_y$Ga$_{1-x-y}$Se$_2$ de cobre indio, donde x = 0.4, y = (0.0, 0.1, 0.2, 0.3) la capa de superestrato por el proceso de recubrimiento por centrifugado. CuIn$_x$Cr$_y$Ga$_{1-x-y}$Se$_2$ donde x = 0.4, y = (0.0, 0.1, 0.2, 0.3) nanopartículas han sido sintetizadas en primer lugar usando un método hidrotermal químico húmedo que se basa en un proceso térmico sin vacío sin ningún proceso de selenización adicional. Introduciendo diferentes fuentes de metal en un autoclave con etilenamina como solvente, se obtuvieron nanopartículas de CIGS a diferentes temperaturas en

un rango de 190-230 °C. Los resultados de la difracción de rayos X (XRD) confirmaron la formación de una estructura de calcopirita $CuIn_xCr_yGa_{1-x-y}Se_2$ tetragonal.

Finalmente, se estudióel efecto de la temperatura de recocido en los materiales tipo Kesterita (como el Cu_2ZnSnS_4)que son materiales de muy bajo costo y que no dañan el medio ambiente. Estudiamos el crecimiento de las películas delgadas cuaternarias Cu_2ZnSnS_4 (CZTS) de kesterita mediante un depósito electroquímico de un solo paso seguido de un recocido a baja temperatura. La influencia de diferentes atmósferas de recocido a tiempos de recocido constantes (t = 45 min) y parámetros de control de preparación fijos; es decir, concentración de la solución de materiales de partida (sales de metales precursores), tiempo de deposición y potencial de electrodeposición. Se estudiaron las propiedades estructurales, de composición, morfológicas y ópticas, así como las propiedades fotoelectroquímicas.

Resum (Valencià)

L'augment del consum d'energia global juntament amb les preocupacions ambientals ha generat molt d'interès per les fonts d'energia alternatives i netes, com ara l'energia solar fotovoltaica. Els investigadors de la comunitat fotovoltaica han estat buscant formes de reduir costos mentre mantenen o augmenten les eficiències. Una millor comprensió dels materials implicats és essencial per al ràpid desenvolupament de noves tecnologies. Les pel·lícules primes I-III-VI$_2$ ofereixen sistemes prometedors per aconseguir cèl·lules solars d'alta eficiència a un cost menor. De fet, en adaptar la composició dels compostos, és possible canviar la banda prohibida del material per captar la llum solar de manera més eficient.

Aquesta tesi se centra en la preparació i caracterització del material de la capa absorbent, especialment les pel·lícules primes nanocristal·lines i la consideració de les característiques estructurals i elèctriques d'aquesta capa principal absorbent de cèl·lules. La tesi examina com les diferents tècniques de preparació i ús del material podrien afectar les propietats del pel·lícules primes sintetitzades.

Pel·lícules primes CuInSe$_2$ i CuInS$_2$ es van dipositar sobre substrats de vidre ITO usant la tècnica d'electrodeposició en solució aquosa. Les pel·lícules electrodepositades es van caracteritzar per difracció de raigs X (XRD), microscòpia electrònica de rastreig (SEM) i anàlisi de raigs X d'energia dispersiva (EDS). Es van investigar els efectes de recuit sobre els precursors electrodepositats. L'estructura de calcopirita de CuInSe$_2$/CuInS$_2$ va mostrar una millora de la cristal·linitat després del tractament posterior de selenització/sulfurització en atmosfera de Se o S, respectivament. Els estudis de XRD i SEM van revelar una millora de la qualitat cristal·lina de les pel·lícules de CIS després dels tractaments tèrmics. Les propietats òptiques de les pel·lícules primes recuites CuInSe$_2$-Es i CuInSe$_2$-S s'han estudiat per determinar l'efecte del procés de recuit en diferents ambients de seleni i sofre.

A més, modifiquem el CuIn$_x$Cr$_y$Ga$_{1-x-y}$Se$_2$ de coure indi, on x = 0.4, i = (0.0, 0.1, 0.2, 0.3) la capa d'superstrat pel procés de recobriment per centrifugat. CuIn$_x$Cr$_y$Ga$_{1-x-y}$Se$_2$ on x = 0.4, i = (0.0, 0.1, 0.2, 0.3) nanopartícules han estat sintetitzades en primer lloc fent servir un mètode hidrotermal químic humit que es basa en un procés tèrmic sense buit sense cap procés de selenización addicional. Introduint diferents fonts de metall en un autoclau amb etilenamina com solvent, es van obtenir nanopartícules de CIGS a diferents temperatures en un rang de 190-230 °C. Els

resultats de la difracció de raigs X (XRD) van confirmar la formació d'una estructura de calcopirita $CuIn_xCr_yGa_{1-x-y}Se_2$ tetragonal.

Finalment, es va estudiar l'efecte de la temperatura de recuit en els materials tipus kesterita (com el Cu_2ZnSnS_4) que són materials de molt baix cost i que no danyen el medi ambient. Vam estudiar el creixement de les pel·lícules primes quaternàries Cu_2ZnSnS_4 (CZTS) de kesterita mitjançant un dipòsit electroquímic d'un sol pas seguit d'un recuit a baixa temperatura. La influència de diferents atmosferes de recuit a temps de recuit constants (t = 45 min) i paràmetres de control de preparació fixos; és a dir, concentració de la solució de materials de partida (sals de metalls precursors), temps de deposició i potencial d'electrodeposició. Es van estudiar les propietats estructurals, de composició, morfològiques i òptiques, així com les propietats fotoelectroquímiques.

Chapter1. Introduction:

Part I: Basic Photovoltaic Physics

1. 1.1.Energy

Energy is the capability of a system to do work. There are various types of energy that can be changed from one form to another.

Energy divided and exists in two main forms:

    i.   Potential energy or stored energy.

    ii.   Kinetic energy or moving energy.

Every form has several types of energy such as: heat, light, electrical, and others. Energy is never created (nor destroyed or lost), but it can be transformed from one type to others. Electricity is produced from a power plants when the energy stored in coal or the energy from rushing water from waterfalls transforms into energy. Energy is measured in electron volts (eV) or joules (J), where 1 eV = 1.6×10^{-19} J. For example, a photon of yellow light has about 2 eV of energy [1].

1.1.2. Power

Power is the rate at which work is done or the rate at which energy is transformed from one place to another or transformed from one type to another. For example, if 2 J of energy were used in one second, the power rating would be 2 J/s. Power is often measured in watts (W), where 1 W = 1 J/s. We usually discuss the power of electricity rather than the energy because electrical energy usually flows over time. Electrical power is calculated by

Power [watts] = Current [amps] x Voltage [volts].

Typical light lamps require 60 W of power to operate. For comparison, consider that about 100 mW/cm^2 of power would be incident on a solar cell in sunlight. If the solar cell is 1 cm^2 and 30% efficient, then 30 mW of electrical power would be produced. If this cell were used with a 1000-sun concentrator, collecting light from 1000 cm^2 of area, then 30 W of electrical power would be produced [1-5].

1.1.3. Efficiency

System efficiency is defined as the rational percentage of the drawn out amount of useful energy from the system to the total fed up energy into the system and is usually expressed as following:

$$\text{Efficiency of system} \ = \ \frac{\text{drawn out amount of useful energy from the system}}{\text{total fed up energy into system}}$$

As power is similar to energy, except for the addition of the time factor, the efficiency of a photovoltaic cell can also be calculated by dividing the electrical power that the cell generates by the total power of the light energy incident on the cell:

$$\text{Efficiency of solar system} \ = \ \frac{\text{resulted useful power out of system}}{\text{total power fed into system}}$$

This resulted in a creation of electron flow which in turn results in an electrical voltage. This voltage is very small, but by connecting a large number of cells, they can reach the desired voltage.

Characteristic curves of a solar panel:

 (1) I-V curve.

 (2) P-V curve.

These two curves represent the ratio between the current or power generated off and the voltage across the panel. These two curves are shown in Figure 1.1.To determine the quality of a solar panel in energy terms, there is a term called form factor (fill factor), this factor relates the maximum power that is able to provide the panel with the maximum power that could really offer. The value of this factor is usually between 0.7 / 0.8, with 1 being the best possible value [7].
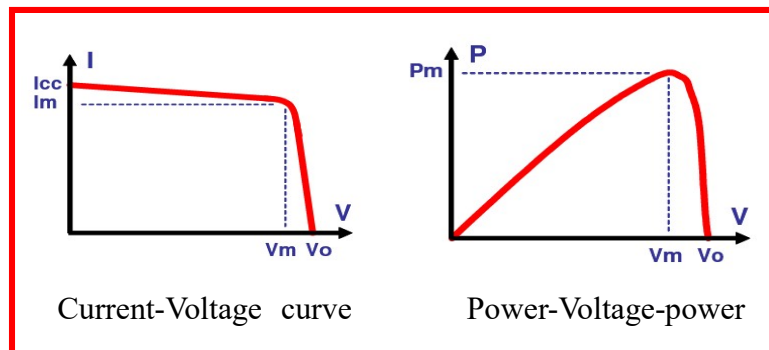
Figure **1. 1.** Current-voltage and Power-voltage curves for a solar cell.

1.1.4. Electricity

Electricity is defined as a flux of charged particles. Current is the rate of flow of these charged particles—or moving electrons. Voltage is the "pressure" causing the flow, and the resistance of a material describes the degree to which this flow is inhibited [2,3].

1.1.4.1. Electric Fields

An electric field is a region of influence of an electrostatic force on charges that could be placed within the field. For example, in its simplest form, a positive charge would attract a negative charge placed nearby [2,3].

1.1.4.2. Current

Electrical current can be defined as a measure of the flow of positive charge. The charge is measured in coulombs and time in seconds, the rate at which charges flow is measured in coulombs/second, just like flowing water. The term amps is used to indicate the number of coulombs per second, where 1 A = 1 C/s. Multijunction solar cells can generate about 10 A/cm^{2}of current when used with solar concentrators at 1000x concentration [3,5].

1.1.4.3. Voltage

Voltage acts like the pump that causes the current flow through the pipe. Voltage describes the amount of energy contained by each charge (or group of charges). Because a joule is the standard unit of energy and coulomb the standard unit of charge, the units for voltage are joules per coulomb, which is more typically referred to as a volt (1 V=1 J/C). GaInP/GaAs/Ge multijunction solar cells, typically generate about 2.5 volts [3,6].

1.1.4.4. Resistance

Resistance can be considered as the length and diameter of a "pipe" through which current flows. Resistance restricts the flow of current. The higher the resistance—either because the pipe diameter is small or the pipe length is long—the less current will be able to flow. The lower the resistance, the more current will flow—or the less voltage is required to cause the same current flow. The narrower or longer the conducting material, the more resistance it will have. In most cases, a lower resistance is desired, so designers try to keep "diameters" wide and distances short. Resistance is typically measured in ohms as follow:

$$\text{Resistance [ohms]} = \frac{\text{Voltage [volts]}}{\text{Current [amps]}}$$

This relationship implies that if a material has a high resistance, even a high voltage will create only small currents. Such materials are referred to as insulators. For this if the resistance is small, current can be large even with small voltages. Such materials with low resistance are referred to as conductors [3,7].

1.1.5. Circuits

Are the paths or routes where the electrical current movements start and finishes in the same place where power can be delivered. It seems to be continuous and the charges flow can easily move. In electrical devices the electricity in the form of voltage and current collection is transformed inside the electrical circuits by such a way to power for lighting and other working functions of electricity [3,7].

1.1.5.1. Series Circuits

Elements in a circuit are said to be in series with each other if the same collection of charges moving in a current flow through them one after another is a must (Figure 1.2(a)).

1.1.5.2. Parallel Circuits

Elements in a circuit are said to be in parallel with each other if a split in the current path orders the charges flow to be through one or the other, but not both elements (Figure 1.2 (b)).
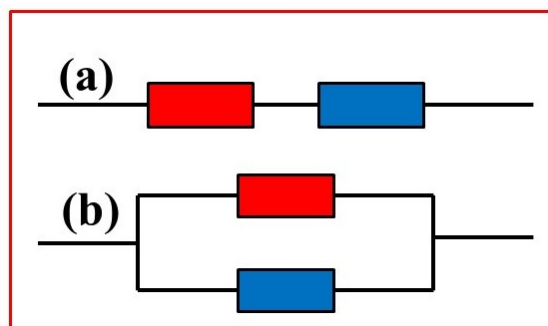
Figure **1. 2.** a) Two elements connected in series, b) parallel connection

1.1.5.3. Short Circuits

Short circuits are alternative paths where the charges can move through them. This is called a short circuit (Figure 1.3), these short circuits prevent the devices from receiving those energized

charges. If the path has no resistance, there is no voltage change, and thus, no work is done even though current is flowing. Most of those alternative charges paths usually have a resistance with a considered quantity that leads to dangerous levels of power. In the design of photovoltaic cells, the current generated by the cell when it is short-circuited, I_{sc}, is an important characteristic quantity describing the behavior and effectiveness of the cell [9].

1.1.5.4. Open Circuits

Open circuits, like short circuits, similarly prevent the normal flow of charges through a device. In an open circuit, however, the flow of charges is stopped entirely. For example, inspecting a burned-out light lamp may reveal a broken filament (the wire that normally shining brightly as current passes through it). This broken filament breaks the flow path of charges. The voltage across an open circuit can be very high, but with no current flow, no power is used [10].

In the design of photovoltaic cells, an open-circuit situation may be intentionally created to measure the behavior of the photocell. This open-circuit voltage is denoted as V_{oc}.
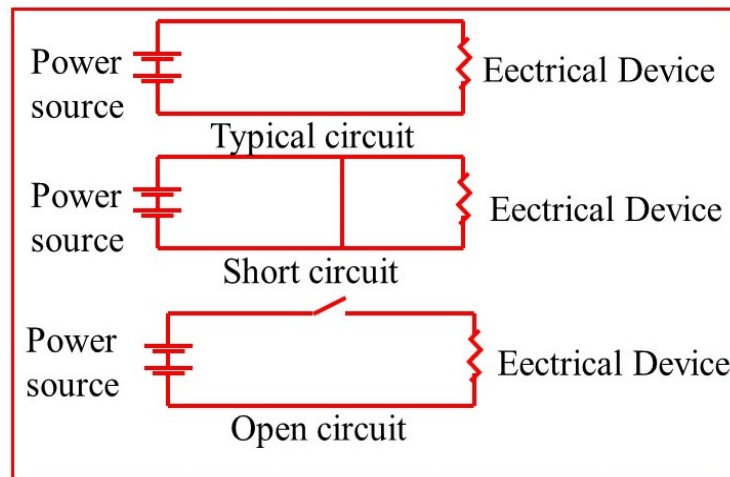
Figure **1. 3**. Short and Open circuits.

1.1.6. Diffusion

Diffusion is the movement of particles from a region of higher concentration to a region of lower concentration. A concentration gradient is a difference in the concentrations of particle type. When concentration gradients occur in isolation, there is chemical potential energy—the potential for movement exists. The concentration gradients of the particles will not exist for long

time as their potential energy changes into kinetic energy with the movement and diffusion of the particles [11].

1.1.7. Atomic Theory

Quantum theory supposes that electrons can occupy only discrete energy levels. The theory was with good explanation for the crystal structures of the semiconductor materials, where the photons of light can be absorbed in materials in a way that generates electrical current by transformation from one energy level to another.

1.1.7.1. Bohr Model of the Atom

The classical Bohr model of the atom is helpful in providing a convenient description of the atom. This model arranges the electrons in planetary-like orbits around the center of the atom, which is consisted of protons and neutrons. The external orbiting electrons are referred as valence electrons. These electrons are perhaps the basic essential component of the atom as it describes how these atoms interact chemically and physically with other atoms in their environment [12]. Bohr model for atom structure are indicated in (Figure 1.4).
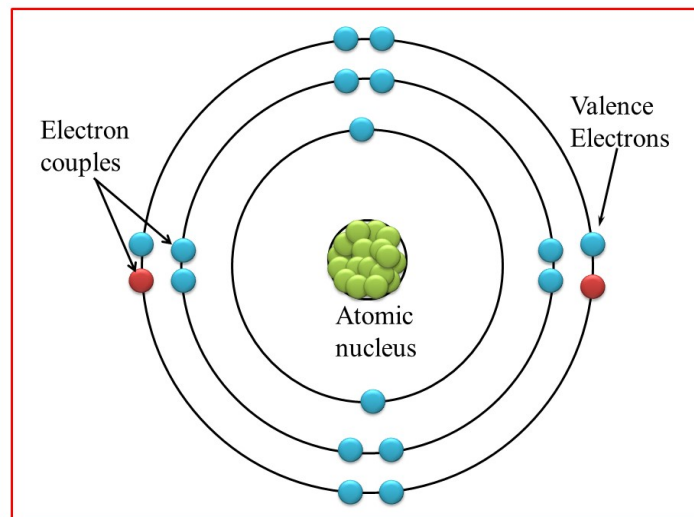
Figure **1.4.**Bohr atom.

1.1.7.2. Band Theory of Solids

The electrical properties of a material depend on both the valence band and the conduction band. The valence band includes the energy levels where most of the electrons (at the absolute zero temperature, for all electrons) can be found. Electrons found in the higher-energy conduction

band are considered free electrons. Free electrons are shared among all the atoms of the solid and are not associated with any other atom. Therefore, they are very mobile. Any applied electric field can create an electrical current with these electrons. Both insulator and semiconductor materials, the valence and conduction bands are separated by a region called the bandgap [13].
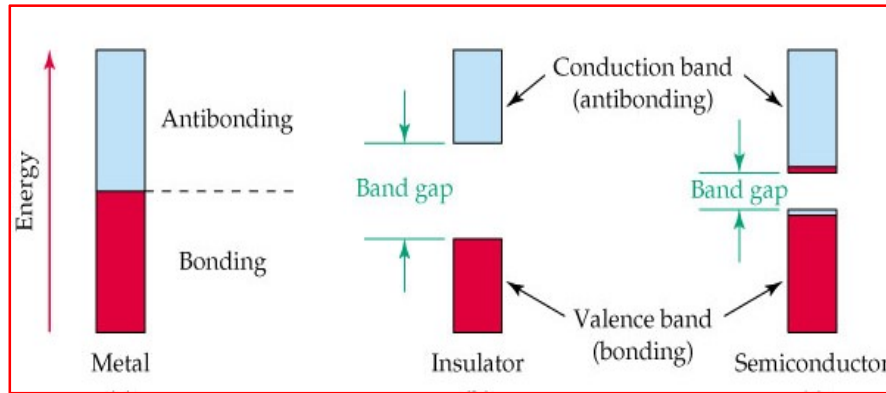
Figure **1. 5**. Band gap description for metal, insulator and semiconductor

The band gap is a region of forbidden energy levels, as defined by the quantum aspects of modern atomic theory. The difference between the lowest energy level of the conduction band and the highest energy level of the valence band is called the band gap energy (Eg). At temperatures above absolute zero, electrons may possess enough thermal energy (at least Eg) to be excited across the forbidden energy gap into the conduction band. This occurrence is less likely if the band gap energy is large, as in insulators. In conductors, the conduction band and the valence bands overlap, and conduction of electrons occurs, even at absolute zero [14]. This situation explains why insulators are poor conductors of electrical current, whereas conductors are not. Semiconductors have band gap energies somewhere in between (Figure 1.5 and Figure 1.6).
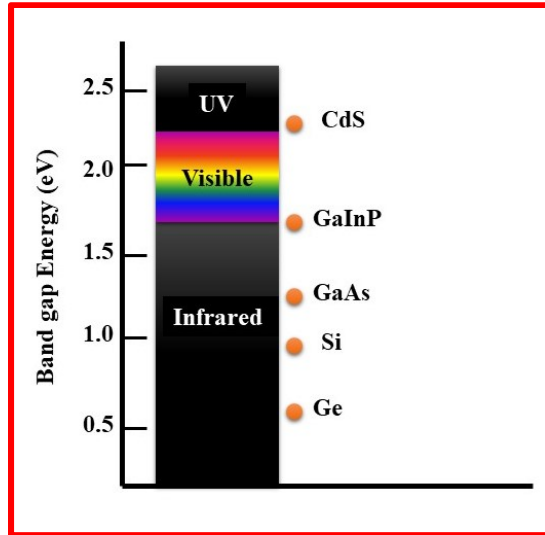
Figure **1.6.** Band gaps of some common semiconductors.

1.1.8. Semiconductors: p-n Junctions

Pure semiconductor materials have four covalent bond structures with other atoms, such as silicon. However, to design an electronic device means intentionally to add impurities in the semiconductor materials so that there will be fewer or more valence electrons. This practice of "doping" a material produces a variety in the new designed materials which are very useful in a broad number of different applications. Pure crystal structures of such substances use every electron in forming their covalent bonds. However, when doped with Group V elements such as phosphorus, an extra electron is available that is automatically promoted to the conduction band as the rest of the phosphorus atom takes on the four-bond behavior of a Group IV element. This material is described as n-doped (additional free electrons are generated by adding impurities to the basic crystal structure). An inverse situation occurs when doping with a Group III element such as boron. Instead of creating extra free electrons, "holes" are created where electrons normally occur to complete the four-covalent-bond structure. These p-doped regions (n is for negative electrons and p is for positive holes) take electrons from the valence band, leaving a hole where an electron could have been (in an opposite fashion compared to n-doped regions) [15]. Free holes and electrons are mobile charge carriers. Both types of mobile carriers are present in n-doped material, but in this case, electrons are referred to as the majority carriers and holes are referred to as minority carriers. Inversely, in p-doped material, holes are the majority carriers and electrons are the minority carriers. When two different types of semiconductor

material are brought together—one being p-doped and the other n-doped—interesting electrical behavior develops near this pn junction [16].

1.1.9. Light

The sun sends the energy to the earth in form of radiation energy. This radiated energy is transferred to the earth carried by tiny particles having no mass called photons. Photons behave like waves and, as such, have a characteristic wavelength, frequency, and energy. It is the energy of these photons that is used in photovoltaic cells to excite electrons so that an electrical current can be produced [17].

1.1.9.1. Waves

Figure 1.7. illustrates that the wavelength of a wave is the distance between two successive peaks, or maxima, of a wave.
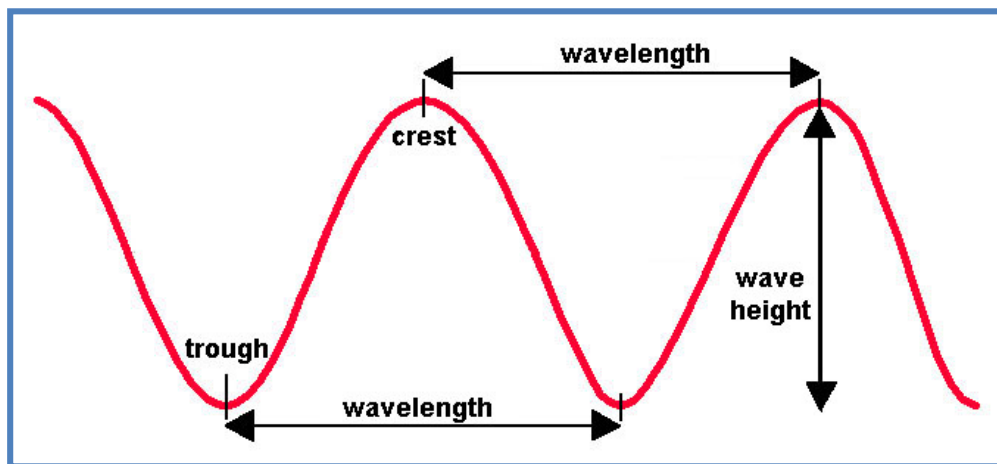
Figure**1.7.** Wavelength of wave.

The frequency of a wave is a measure of how many peaks are observed in one second from a stationary point along a wave's path. The product of the wavelength and frequency gives the wave's velocity: $v = \lambda . f$, where v = velocity in meters per second, λ = wavelength in meters, and f = frequency in hertz.

All irradiative, or light, energy travels at the same velocity, commonly known as the speed of light, which is about 300,000,000 m/s (3×10^8 m/s, or about 186,000 mi/s). Because the velocity of light is a constant and also a product of frequency and wavelength, specific frequencies of light are associated with specific wavelengths, and vice versa. For example, blue light has a

frequency of about 667×10^{12} Hz. To calculate blue light's associated wavelength, the above equation is rearranged for wavelength, λ., to get λ= v / f.

Then, substituting the values, we find:

λ blue = (300,000,000 m/s) / (667 x 10^{12} Hz) = 450 x 10^{-9} m = 450 nm.

The same is true for all colors of the spectrum—each color has a corresponding wavelength and, therefore, a corresponding frequency. The red end of the visible light spectrum has lower frequencies and longer wavelengths, and the blue end of the spectrum has higher frequencies and shorter wavelengths. Even shorter and longer wavelengths (higher and lower frequencies, respectively) are possible for photons. In fact, the region with frequencies just less than that of red is called infrared (infra means under) and those with higher than the highest frequency of the visible violet color (ultra means higher). The entire range of possible photon wavelengths and frequencies is referred to as the electromagnetic spectrum [18].

1.1.9.2. Electromagnetic Spectrum

All energy carried by photons is referred to as electromagnetic (EM) energy and cross all possible values for wavelength and frequencies. Ranges of this spectrum—from shortest wavelength to longest—are referred to as gamma rays, X-rays, ultraviolet, visible light, infrared, microwaves, and radio waves. The energy carried by a photon is calculated by multiplying the frequency of the photon by a universal constant, h, called Planck's constant:

$E = h.\nu$

Where E is the energy in joules or electron volts, h is Planck's constant (6.63×10^{-34}J-s, or 4.1357×10^{-15} eV-s), and ν is the frequency of the photon in Hz. In photovoltaics and semiconductors, this energy is often measured in electron volts eV). An electron volt is the energy required to increase the electric potential, or energy, of the charge on one electron by one volt. Energy, like wavelength and frequency, is unique for a specific part of the electromagnetic spectrum [19].

1.1.10. The Solar Spectrum

Stars, including our own sun, emit energies covering a range of wavelengths of the EM spectrum. However, different types of stars produce differing amounts of energy in each region of the spectrum. Our sun emits more photons in the visible light and surrounding regions than in

any other part of the EM spectrum. This phenomenon may be why our eyes have evolved to see that part of the EM spectrum and not microwaves, gamma rays, or any of the other wavelengths that are emitted at lower intensities by our sun [20].
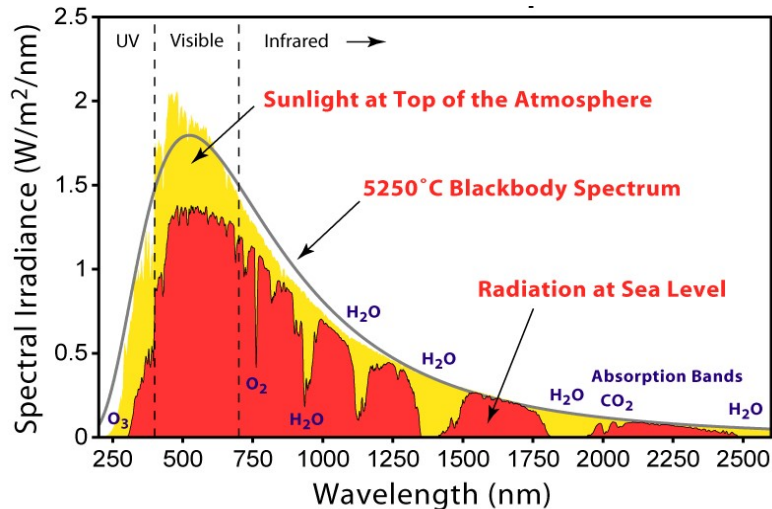
Figure **1.8.** Solar radiation spectrum.

Figure 1.8. includes a spectrum of the sun's light that reaches Earth's upper atmosphere. We can notice that the peak region is from 400 to 700 nanometers (nm), which is the visible range of the spectrum. Also note that there are a large number of photons through most of the infrared region of the spectrum (700 to 10,000 nm). At the higher-energy, shorter-wavelength end of the spectrum, the number of photons drops off dramatically. The sun's spectrum contains very little light with wavelengths shorter than about 300 nm (i.e., photon energy greater than about 4 eV). The Earth's atmosphere protects us from the higher-energy forms of light, such as ultraviolet rays. In fact, the existence of life on Earth would be far less likely if these more damaging forms of energy were more abundant. The terrestrial spectrum in (Figure1.8.) describes the light that actually reaches the Earth's surface after passing through the atmosphere. Notice that there are various wavelengths in which the number of photons is greatly reduced as compared to the space solar spectrum. This difference is due to photons being absorbed by atmospheric gases, the best-known being ozone (O_3), which absorbs higher-energy (lower-wavelength) ultraviolet light below 400 nm. Photons with wavelengths near 900, 1100, and 1400 nm are absorbed by water vapor in the atmosphere [21].

1.1.11. Photon Absorption

Photovoltaic cells are designed to capture the photons of the solar spectrum. Energies in the visible range are especially important to consider, but energy is available in the near-infrared, as well. Solar cell designs that more efficiently absorb these photons must consider the specific energies of these wavelengths. Photons with energies equal to or greater than the band gap are absorbed as their energy promotes electrons into the conduction band. If photons have energy exceeding the semiconductor's band gap, the excess is usually sputtered as heat and is thus wasted. Alternatively, photons whose energies are less than the band gap are not absorbed at all but are transmitted through the material and their energy is not used. If the photon's energy is equal to the band gap, the energy transfer, in terms of its photovoltaic usefulness, is as close to 100% efficient as is thermodynamically possible [22].

1.1.11.1. Photocurrent

The amount of current produced by a photovoltaic cell is directly related to the number of photons absorbed. The lower the band gap, the more photons are absorbed and the greater the number of electrons promoted into the conduction band, and thus, available for current production. The absorption of photons, of course, will only occur if their energies exceed the band gap. But such absorption does not occur precisely at the surface of materials, but rather, may penetrate deeply before being absorbed. Silicon and germanium, for example, have a much lower absorption coefficient than does gallium arsenide. For this reason, thicker layers of silicon and germanium are required to absorb equivalent numbers of sufficiently energetic photons. Generated current, then, also depends on the absorptivity of a material and its thickness. Two important performance parameters for a PV cell are its short-circuit current (I_{sc}), and maximum-power current (I_{mp}). As its name implies, the I_{sc} is the current produced by the cell when a zero-resistance short is placed across its terminals. The I_{sc} is easily measured in a laboratory setting. The I_{mp} is the current produced under maximum power conditions and is more representative than I_{sc} of operational performance [23].

1.1.11.2. Photovoltage

The output voltage of a PV cell is directly related to the energy of the electrons promoted or excited into the conduction band. The higher the band gap, the greater the energy of the electrons in the conduction band must be. The voltage created by a semiconductor can easily be

determined firstly, by dividing the band gap value (in electron volts) by the charge of an electron (the "e" in eV). For reasons, the voltage generated is typically around 0.4 V lower than the results of such a calculation, so 0.4 V must be subtracted from the previous result. For example, GaAs has a band gap of 1.4 eV, so it would create an output voltage of 1.0 V (1.4 eV/e = 1.4 V; 1.4 V – 0.4 V = 1.0 V).

Two important voltage performance parameters are open-circuit voltage (V_{oc}) and maximum-power voltage (V_{mp}). The V_{oc} is a measurement of the output voltage of a solar cell with no current flowing from it, which is a value easily measured in a laboratory setting. But V_{mp} is more indicative than V_{oc} of actual performance [24].

1.1.11.3. Fill Factor and Maximum Power

Figure 1.9. shows the current-voltage (I-V) curve indicating the behavior of a sample PV cell over all a full range of currents and voltages. By definition, V_{oc} and I_{sc} are the x and y intercepts, respectively, of such a plot. And it is a characteristic of photovoltaic cells; they represent upper limits for voltage and current, respectively. As already noted, V_{mp} and I_{mp} are more appropriate measures of actual performance. The performance parameter, fill factor, is commonly used to collectively describe the degree to which V_{mp} matches V_{oc} and I_{mp} matches I_{sc}. Fill factor is given by the following:

Fill factor = (I_{mp} x V_{mp}) / (I_{sc} x V_{oc}), and because the maximum power, P_{max} = (I_{mp} x V_{mp}),

Fill factor = P_{max} / (I_{sc} x V_{oc}). Fill factors for our high-efficiency cells are typically in the range of 80% to 90%, where 100% would be ideal. These curves may vary depending on the type and amount of radiation and temperature of the panel [25].
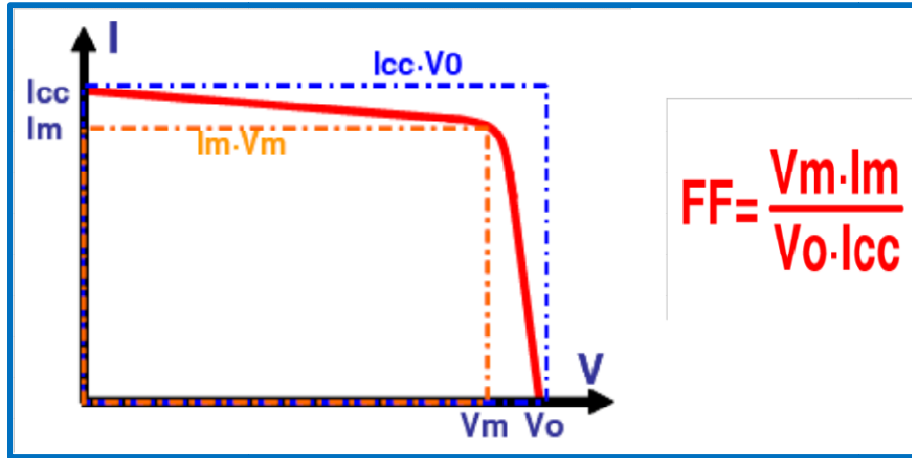
Figure 1. 9. I-V curve and FF equation.

1.1.12. Single-Junction Solar Cell Design

The maximum power is obtained within high current and voltage optimization of necessary comparison. In order to get maximum optimized current, it is advisable to capture lots of photons from the spectrum of solar radiation energy as much as possible. Small band gap materials are preferred in selection for band gap construction. Those photons with lower radiation energies will be available for electrons excitation from valence band into conduction band. On the other hand the photons of higher energies who own much higher energy will lose these energies in form of heat and will not be transformed into electrical energies.

Solar cells engineering designers tends to choose those of intermediate band gaps (near the middle of the energy spectrum for solar radiation) to make a balance between selected materials, photocurrent and output current of the device [26].

1.1.13. Multijunction Solar Cell Design

Multijunction cells use a combination of semiconductor materials to get more efficiently capture of a larger photon energies range. They do so without sacrificing photovoltage or creating A "sun" as a unit of concentration. For example, 500 suns would be 500 times the intensity of the sun at all wavelengths. "One-sun" implies no concentration is taking place [27].

1.1.14. Bandgap Selection

Figure1.10. shows the spectrum of sunlight split and distribution over a variety of semiconductor materials by using a prism.
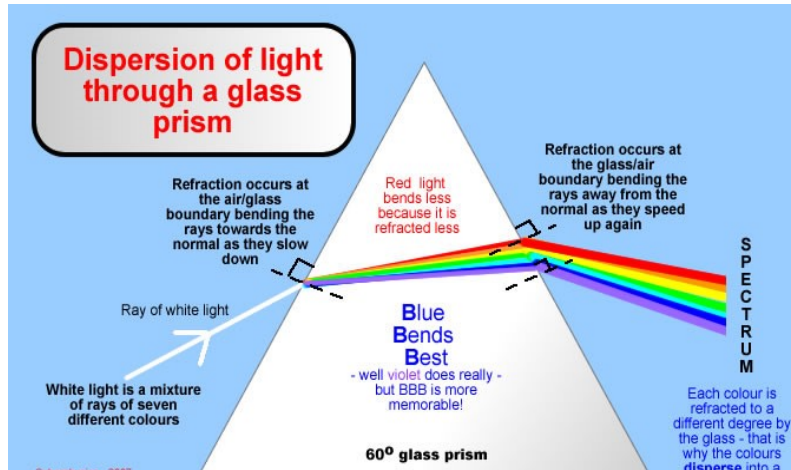
Figure1.10. Dispersion of sunlight and distribution over variety of semiconductor materials through a prism.

Different semiconductor materials could be used that would be in good matching at each portion of the spectrum. Such an arrangement for the selection of solar cells materials is reasonable, acceptable theoretically and mechanically, but designing is an abrupt led to be problematic.

In that case the more adequate solution is to arrange a multiple layer display. Those multiple layers of semiconductor materials will be arranged from top (higher band gap materials) to bottom (lower band materials). Those on top with larger band gap energies will absorb photons with higher energies photons, then transmitting lower energy photons to following layers in arrange. This strategy is the characteristic feature of multijunction solar cells [28].

1.1.15. Lattice Matching

The maximum current conductivity and high optical transparency between the top and bottom cells in monolithic multijunction devices can be produced if all layers have similar crystal lattice, and structures. Mismatch in the crystal lattice constants creates defects or dislocations in the lattice where recombination centers can occur. Recombination results in the loss of photogenerated minority carriers (e.g., electrons drop from the conduction band back into the valence band) and significantly degrades the photovoltaic quality of the device. Such effects will decrease the open-circuit voltage, short-circuit current density (J_{sc}), and fill factor, which represents the relationship, or balance, between current and voltage for effective power output [29].

1.1.16. Cell Optimization

In order to maximize the efficiency of multijunction devices, bandgap and lattice matching are very important desirable characteristic for such designs. Monolithic design needs all to be grown in one piece, series-connected, two-terminal multijunction device where each of the sub cells should have matched currents. For that, they should absorb photons at the same overall rate, thus producing the same current [30].

1.1.16.1. Current Matching

The output current of the multijunction solar cell depend on the nature of its series connection, where it is always limited by the smallest produced currents of any individual junction. For this reason, it is desirable to design each junction to produce the same amount of photocurrent [31].

1.1.16.2. Power Production

Maximizing total power—the product of total current and total voltage—is the photovoltaic designer's ultimate goal. Multijunction designs, as compared to single-junction designs, have reduced currents. Multijunction designs are advantageous in that they inherently reduce current while increasing voltage [32].

1.1.16.3. Concentration Systems

Concentrators are a vital component of terrestrial multijunction solar cell systems. By dramatically increasing the total power produced by a given solar cell 100- to 1200-fold, the increased cost of that cell is more readily justified. In addition, high solar concentrations actually work to improve the performance of multijunction solar cells [33].

Part II: State of the Art of Thin Film Solar Cells

1.2. CIGS Thin Film Solar Cells

$Cu(InGa)Se_2$-based solar cells have often been touted as being among the most promising of solar cell technologies for cost-effective power generation. This is partly due to the advantages of thin films for low-cost, high-rate semiconductor deposition over large are as using layers only a few microns thick and for fabrication of monolithically inter connected modules. Perhaps more importantly, very high efficiencies have been demonstrated with $Cu(InGa)Se_2$ at both the cell and the module levels. Currently, the highest solar cell efficiency is 18.8% with 0.5 cm^2 total

44

area fabricated by the National Renewable Energy Laboratory (NREL) [34]. Furthermore, several companies have demonstrated large are a modules with efficiencies >12% including a confirmed 13.4% efficiency on a 3459 cm^2 module by Showa Shell [35]. Finally, Cu(InGa)Se$_2$ solar cells and modules have shown excellent long-term stability [36] in outdoor testing. In addition to its potential advantages for large-area terrestrial applications, Cu(InGa)Se$_2$ solar cells have shown high radiation resistance, compared to crystalline silicon solar cells [37,38] and can be made very light weight with flexible substrates, so they are also promising for space applications.

Recently CuInGaSe$_2$ (CIGS) thin film solar cell with an active area of 0.5 cm^2 made by ZSW company exhibits the highest efficiency of 20.3% (Table 1.1) [39]. A several companies such as First Solar, Nanosolar, Globalsolar, Miasole′, Solopower, Honda, Sharp, A vancis etc., have been immensely involving to developing and producing CIGS based thin film solar cell mani-modules to target production of several GW/Yr range around the world. For example, the Solyndra company initiated a new approach to develop 1.8 m long cylindrical tube CIGS modules, as fluorescent tubes and panel width of 1 m to reach 110 MW [40]. The Cu$_x$S/CdS thin film solar cells may be origin for the development of CIGS thin film solar cells in step by step process in which Cu$_x$S is unstable compound with time [41].

Table 1.1. Highest reported efficiencies of solar cells with prominent materials

S.No	Solar Cells	η (%)	Ref.
1	CIGS	20.3	[16]
2	CdTe	15.8	[17]
3	CZTS	10	[18]
4	GaAs multijunction	41.1	[19]
5	Si	24.5	[20]
6	Polymer	7	[21]
7	DSSC	11	[22]

In order to improve stability of compound, In is added to it to make strong covalent bonding that turns into CuInS$_2$. The theoretical models reveal that 1.55 eV band gap absorber materials are optimal to capture maximum solar spectrum. In this juncture, CuInS$_2$ is suitable material but its

performance is inferior to CuInSe$_2$. The band gap of CuInSe$_2$ is 1.1 eV therefore band gap needs to be increased by adding either Ga or Al in it. Thus, the CIGS thin film solar cells now occupy main stream of market as next generation of photovoltaics.

1.3 Multiple Junction GaAs Based Thin Film Solar Cells

The leading laboratories such as Fraunhofer Institute for Solar Energy Systems, National Renewable Energy Laboratory, Spectrolab, Emcore, etc., have been developing III–V group based monolithic Ga$_{0.35}$In$_{0.65}$P/Ga$_{0.83}$In$_{0.17}$As/Ge multijunction thin film solar cells [42].

The III-V semiconductor family possesses a number of attractive properties for fabricating solar cells. The bandgaps of the binary III-V semiconductors are conveniently scattered around the solar spectrum with further bandgap tuning possible through alloys of group III and V elements. Most III-V semiconductors share the zinc blende crystal structure, lending the family to hetero structure solar cells and multijunction configurations [43]. The majority of III-V materials have direct bandgaps, leading simultaneously to large absorption coefficients for photons with energies in excess of the bandgap and short radiative lifetimes (ns); the absorption coefficients for a series of III-V semiconductors are shown in Figure 1.11. In comparison to silicon solar cells, the active region of III-V solar cells is thin, no more than a couple of micrometers and epitaxial crystal growth techniques exist that are capable of depositing extremely high-quality layers of III-V semiconductor, leading to almost ideal semiconductor junctions. Many high-performance III-V solar cells have been demonstrated to date, namely the highest efficiency single-junction solar cell (GaAs), multijunction solar cell (InGaP/GaAs) and concentrator solar cell [44].

Despite their high performance and potentially low use of semiconductor material, the reare disadvantages to III-V-based solar cells. The materials are relatively expensive and some rare elements, such as indium are used and the metal-organic precursors commonly used during cell fabrication are highly toxic and often pyrophoric. Finally, the lack of a chemically inert and electrically passivating oxide, equivalent to SiO$_2$, complicates the cell design and places the solar cell at risk of corrosion. Nevertheless, the superior efficiency and radiation tolerance of III-V multijunction solar cells initially led to their use in space and satellite applications and subsequently in terrestrial concentrator systems. The III-V semiconductor family spans the ultraviolet, visible and infrared wavelengths offering the possibility to efficiently absorb the

broad solar spectrum and also finding application for thermo photovoltaics, the conversion of lower temperature radiation to electricity [45,46]. A map of semiconductor bandgap and lattice parameter for most relevant binary and ternary zinc blende III-V materials [47], as well as for silicon and germanium [48]. A key attribute of the III-V material system is the ability to grow hetero structures composed of different semiconductor alloys, enabling binary, ternary, quaternary and even quinternary alloys to be combined. Traditionally a high-efficiency III-V solar cell would be grown lattice matched to a convenient substrate, often GaAs, Ge or InP placing some restriction on the bandgap combinations that could be attained. However, recent progress in controlling defect introduction during lattice relaxation has enabled highly efficient lattice mismatched solar cells to be grown, where the lattice parameter varies within the cell [49]. The direct bandgap of III-V solar cells and high material quality means than some devices operate close to the radiative limit. In this limit, the dominant solar cell loss is unavoidable radiative recombination.

1.4. GaAs Solar Cells

GaAs solar cells hold the record for the highest efficiency single-junction solar cells fabricated to date. Table 6.1 lists some notable cells with different efficiencies showing a remarkable recent result of 27.6% under 1-sun AM1.5G.

A typical p/n GaAs solar cell is shown in Figure 6.4 showing both the layer structure and the associated band diagram. Typically, the junction is formed 0.5 μm from the front window layer and a back surface field (BSF) is formed by the $Al_{0.3}GaAs$ layer to ensure the diffusion gradient for minority holes is directed towards the junction [50].

InGaP has also been used very successfully as a window layer material on account of extremely low InGaP/GaAs interface recombination velocity [51], resulting in a marginally higher power-conversion efficiency in an n/p configuration [52].

1.5. InP Solar Cells

InP solar cells are highly desirable as space solar cells on account of their exceptional tolerance to radiation [53]. Typical device designs closely follow that of GaAs except that there is no suitable window material to passivate the front surface. Instead, shallow homo junction designs with appropriate metal contacts have reached efficiencies of 19% AM0 [54,55].

1.6. InGaAsP and GaN

Under solar concentration the limiting efficiency rises and the optimal bandgap energy shifts to lower energy. The reason for this difference has very little to do with the solar spectrum, but arises from the increased voltage of the solar cell under concentrated sunlight. Since the optimal bandgap energy for power-conversion is a balance between photogeneration and recombination, increasing the solar concentration shifts the balance to favor higher levels of recombination and hence a lower optimal band-gap energy [56,57].The electricity costs 3$/watt for multijunction solar cells, whereas it is 8$/watt for Si solar cells but much more complexity is involved for designing and fabrication of former. The multijunction thin film solar cells are promising candidates for terrestrial and extraterrestrial applications owing to the highest conversion efficiency of 41.1% over the cell area of 0.5 cm^2 under 400–500 suns in the concentrated systems, whereas the same cells show efficiency of less than 30% under 1 sun (1.5 AM) [58]. Similarly, the Spectrolab developed metamorphic $Ga_{0.44}In_{0.56}P/Ga_{0.92}In_{0.08}As/Ge$ multijunction thin film solar cells, which show efficiency of 40.7% under 240 suns, whereas lattice matched $Ga_{0.44}In_{0.56}P/Ga_{0.92}In_{0.08}As/Ge$ multijunction cells exhibit more or less same efficiency of 40.1% [42]. As we know the absorber with band gap of 1.55 eV in the single junction solar cell is optimal to absorb high intensities photons from the solar spectrum. However, the multijunction solar cells utilize all the wavelength photons of solar spectrum by graded band gap absorber cells that enhance efficiency of cells.
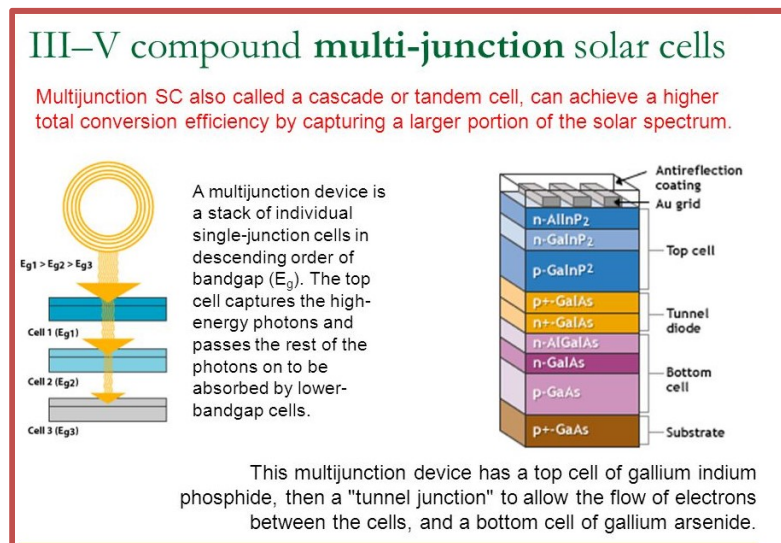
Figure **1. 11.** Multijunction thin film solar cells in which part of the spectrum observed by each sub cell noted in color and the participation mechanism of different band gap absorbers.

Over all aspects of lattice mismatch and band gap grading, III–V compounds are best suit for multijunction solar cells comparing with other materials. The fundamental principle behind the Physics of multijunction solar cells is that the absorbers of top InGaP, second AlGa(In)As, third Ga(In)As and bottom Ge sub cells in the multijunction solar cells. The absorber of top cell absorbs ultraviolet and partial visible region photons with energy greater than or equal to Eg1. The near infrared region photons with less than Eg1 energy hit second cell by passing through top cell where the photons greater than or equal to Eg2 are absorbed by second cell AlGa(In)As absorber. The same phenomena is applicable to third cell Ga(In)As absorber. The bottom Ge cell absorbs rest of low energy or infrared region photons. The voltage of multijunction cell is combination of voltage of each cell, whereas the lowest current of the sub cell dictates current of device since the cells are connected in series. The efficiency of cell can be increased by properly equaling current of each cell in the multijunction. In order to improve cell current, the thickness of top cell is increased hence absorption by top absorber increases thus current increases in the cell. The current is high in Ge sub cell since most of the spectrum covers by Ge[60,61].

1.7. Plastic Solar Cells

Plastic or polymer solar cells are based light weight thin film solar cells. A number of major companies such as Konarka, Solarmer, Fiber Inc, Plextronics, etc., have sincerely devoted their effort to increase efficiency of the cells. The efficiency of polymer based solar cells steadily reaches from 3 to 10% as a milestone [62,63]. The Konarka company first introduced its polymer based thin film solar cell prototype modules to the market even though the efficiency of module is low around 3% that would be also profitable because of low cost production. The low efficiency flexible prototype modules have been using in calculators, laptop computers, cell phones, iPods, carrying bags, umbrellas, etc. So far, the highest reported efficiency on polymer thin film solar cells is 6.8% [64].
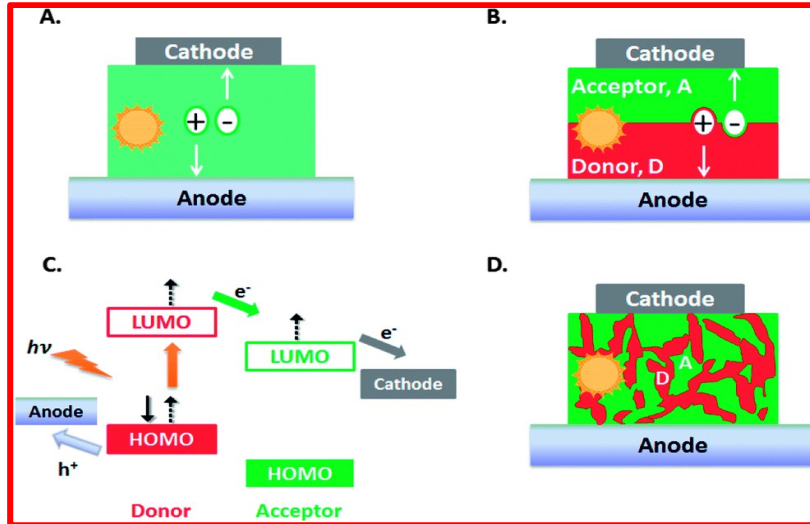
Figure 1. 12. (A) Single layered organic solar cell, (B) Planar heterojunction, (C) Exciton dissociation (donor – acceptor), and (D) bulk heterojunction.

There are different kinds of heterojunction plastic solar cells (Figure 1.12);

(i) one is planar heterojunction that the electron donor (copper phthalocyanine) and the electron acceptor (perylene tetracarboxylic derivative) are sand witched between reflecting metal (Al, Ag, or Au) and poly(3,4-ethylenedioxyl-enethiophene):polystyrene sulfonic acid (PEDOT:PSS) coated TCO (ITO or FTO) [65,66]

(ii) bulk heterojunction consists of a typical structure of glass/ITO/40 nm PEDOT:PSS/P3HT(1 wt.%)-PCBM(0.8 wt.%)TiO$_x$/100 nm Al thin film, which exhibits efficiency of 5% in which poly(3,4-ethylenedioxyl-enethiophene):polystyrene sulfonic acid (PEDOT:PSS) is used as a conducting layer for hole transport and poly (3-hexylthiophene), that is, P3HT with band gap of 1.6–2.0 eV acts as electron donor, whereas phenyl C61-butyric acid methyl ester (PCBM) contributes acceptor. The TiO$_x$ with band gap of 3.7 eV grown by sol–gel technique is virtually used as an optical spacer [67]. The interface between n and p is randomly distributed all over the place in the bulk heterojunction, since both donor and acceptor contributors are mixed unlike conventional heterojunction solar cells. The schematic diagram of bulk heterojunction solar cell is shown in Figure(1.12)[68]. The generated electron–hole pair (exciton) has diffusion length of 10 nm or less. Hence, it has to find donor–acceptor interface within diffusion length of 10 nm otherwise it undergoes recombination without getting separation. In this case, the morphology of active layer plays a dominant role for separation of electron–hole pair to drive electrons and

holes to their respective electrodes by avoiding suppression of excitons. In such a way the domain size of active layer should be kept double size of exciton diffusion length.

(iii) The order heterojunction solar cells are made with nanostructured TiO_2 templates/P3HT polymer that the polymer is inserted into TiO_2, as shown in Figure 1.4C. The radius of straight and continuous pores should be slightly less than diffusion length of exciton of polymer. The ordered heterojunction solar cells exhibit efficiency of 5%. Recently Heliatek company claims efficiency of 7.7% for tandem organic photovoltaic cell over the area of 1.1 cm^2 [69].

The dye sensitized solar cells (DSC) first developed by Gratzel in 1991 is also known as Gratzel cells. The typical configuration of laboratory DSC consists of TCO (SnO_2:F) coated glass substrate/TiO_2/Ruthenium polypyridyl complex (N3 ($RuL_2(NCS)_2$, L=2,20,-bipyridyl-4,40-($COOH)_2$)) dye/electrolyte/Pt/TCO glass, which shows efficiency of 10.8%. In the cell Pt is counter electrode (Figure 13). The interface is between organic donor and inorganic nonporous TiO_2 acceptor. When the light hits cell, the ruthenium dye absorbs it and electron injection takes place into TiO_2 conduction band.
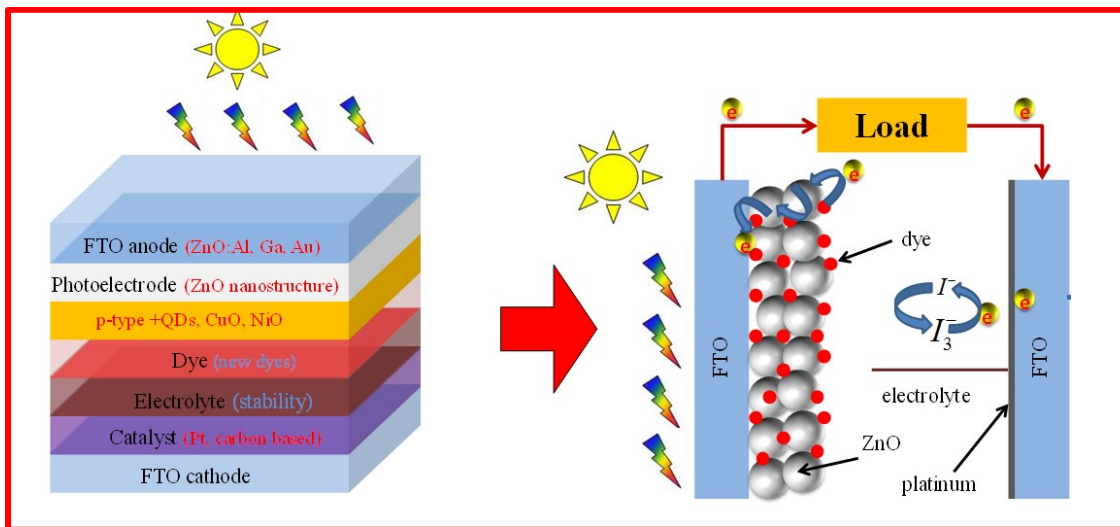
Figure 1. 13. Dye sensitized solar cell.

1.8. Photovoltaic Conversion

Solar cell or photovoltaic cell is nothing but p–n junction when the photons with energy greater than or equal to the band gap of p-absorber this has led to solar cells, the electrons excite from valence band to conduction band in the absorber. Thus electron-hole pairs are created. The electrons cross barrier from p- to n- region and holes from n- to p- region in order to release their

energy before taking place recombination. In other words, the electron–hole pairs, which are within one diffusion length from the built-in electric field of the junction are separated giving rise to photovoltage and photocurrent. The interface is usually homojunction or heterojunction or Schottky barrier [70].

1.8.1. Heterojunction

It is an interface formed between two semiconductors of different energy gaps, a small band gap semiconductor known as "absorber," in which optical absorption takes place and a large band gap semiconductor, known as "window," that is highly transparent to solar radiation. In the heterojunction, the front surface recombination loss is eliminated. However, interface recombination cannot be ignored. Two different kinds of configurations are possible: front-wall configuration in which photons first incident on the absorber layer, whereas they first incident on window layer in the back-wall configuration.

The output current of circuit can be related to:

$$J = J_{PH} - J_D - J_{SH} \qquad (1:1)$$

from the equivalent circuit of solar cell (Figure 1.14A), where J_{PH} is photogenerated current, J_D is diode current, and J_{SH} is shunt current [71]

$$(J_{SH} = Vj/R_{SH}) \qquad (1:2)$$

The expression for output voltage can also be written as

$$V = J_{RS} - Vj \qquad (1:3)$$

where R_S is series resistance and Vj is voltage across diode and resistor R_{SH}. A solar cell behaves like a p–n junction in dark and the current–voltage relationship of the junction in dark is represented by the standard Shockley diode equation

$$J_D = J_0\{exp[qVj = Ak_BT] - 1\} \qquad (1:4)$$

where J_0 is reverse saturation current, A is diode quality factor, q is electron charge, k_B is Boltzmann constant, T is absolute temperature. By substituting Equation (1.2), Equation (1.3), and Equation (1.4) in Equation (1.1), the final derivation for output current results in combination of diode forward current and light generated current for solar cell under light illumination [72].

$$J = J_0 \left[\exp \frac{q}{Ak_BT} (V - JR_S) - 1 \right] + \left(\frac{V - R_SJ}{R_{SH}} \right) - J_{PH} \tag{1:5}$$
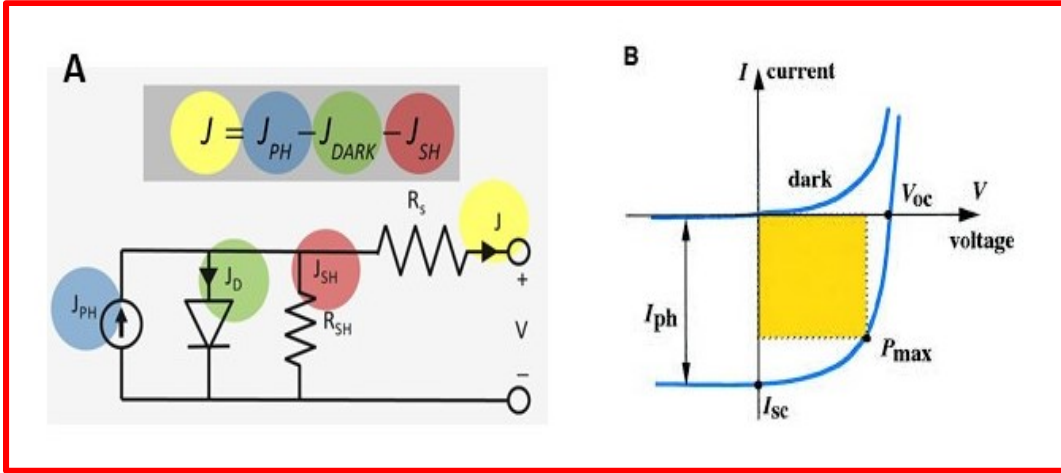
Figure **1. 14**. (A) Equivalent circuit of solar cell, and (B) J–V characteristics of solar cell under dark and light illumination**.**

1.8.1.1. Open-Circuit Voltage

When J=0, the corresponding voltage known as open-circuit voltage is denoted by V_{oc}. It is seen that the reverse saturation current increases, the open-circuit voltage decreases in the solar cell. The experiments on several CIS, CIGS, and CGS cells reveal that the V_{oc} increases linearly with increasing Eg up to certain point then it becomes nonlinear, as shown in Figure 14. In linear portion the expression follows as [73]:

V_{oc}= Eg/q -0.5 (1:6)

The Voc equals to the length between quasi Fermi levels of window and absorber in the inorganic semiconductor solar cells. In the case of plastic solar cells, the V_{oc} is determined by the distance between the highest occupied molecular orbital (HOMO) level of the electron donors and the lowest unoccupied molecular orbital (LUMO) level of the electron acceptors, for which the equation is derived as [74].

$$V_{oc} = \frac{1}{q} \left(\left| E_{HOMO}^{Donor} \right| - \left| E_{LUMO}^{Acceptor} \right| \right) - 0.3 \text{ V} (1:7)$$

1.8.1.2. Short-circuit Current

When V=0, the corresponding current is known as short-circuit current and is denoted by J_{sc}. It depends upon the incident photon flux, absorption coefficient and collection efficiency.

1.8.1.3. Fill Factor (FF)

FF, defined as the ratio of maximum power delivered by the cell to the product of J_{sc} and V_{oc}, is given by:

$$FF = \frac{J_m \ V_m}{J_{sc} V_{oc}} (1:8)$$

where J_m and V_m are the current and voltage corresponding to the maximum power point respectively (Figure 1.6B). The FF is one of the parameters to measure stability of solar cell. Poor FF is always observed for low efficiency cells. The high series resistance and low shunt resistance result in low FF in the solar cells. The highest reported FF is 88% for multijunction solar cells.

1.8.1.4. Efficiency

The conversion efficiency (η) of the solar cell is given by:

$\eta = J_m V_m / P_{in}$ (1:9)

where P_{in} is the total input power to the cell.

1.8.2. Homojunction

It is an interface formed between the p- and n-regions of a single semiconductor. The best-known examples are Si and GaAs solar cells. In general, homojunction exhibits high efficiency, particularly in direct band gap materials with high absorption coefficient but there are appreciable losses due to front surface recombination [75].

1.8.3. Schottky Barrier

It is a metal–semiconductor junction in which a blocking contact is formed. The performance is usually limited by large thermionic emission currents that reduce the open-circuit voltage. A thin insulating layer, usually, oxide is employed in metal–insulator–semiconductor (MIS) and

semiconductor–insulator–semiconductor (SIS) configurations to reduce forward currents and improve the open circuit voltage [76].

1.9. Criteria for the Choice of Heterojunction Pair in the Thin Film Solar Cells

1.9.1. Band Gap of Absorber

The band gap is the first order parameter in deciding the semiconductor pair for the heterojunction. Based on theoretical considerations, Loferski [81] proposed a plot of theoretical conversion efficiency versus band gap of the semiconductor. It is seen that a semiconductor with a band gap of about 1.55 eV is ideal for absorber to achieve maximum conversion efficiency. In addition, it should be a direct band gap material with high optical absorption coefficient. It should preferably be a p-type material because of longer electron diffusion length[78].

1.9.2. Band Gap of Window Material

A wide band gap n-type semiconductor with a low series resistance is very essential to function solar cells well [79].

1.9.3. Electron Affinities

Electron affinity of the absorber and window materials should be compatible so that no potential spike occurs at the junction for the minority photoexcited carriers [80].

1.9.4. Lattice and Thermal Mismatch

The lattice and thermal mismatch between the absorber and window material should be as small as possible to reduce interface state density and recombination losses through such states [81].

1.9.5. Electrical Contacts

It should be possible to form low resistance electrical contacts to both n- and p-type materials. So far, the suitable metal electrical contact is not probably found for p-CdTe absorber [82].

1.9.6. Cell Stability and Life Time

The cell must have stable performance and long operating life at least more than a decade. The cell must pass damp heating or the rmocycling test in order to compile market standards to introduce into public [83].

1.9.7. Deposition Methods

Convenient deposition methods for thin film formation process with highly controlled production are completely necessary. The cost-effective techniques such as ink-based printings, screen printings, doctor blade, spray, spin-coating, etc., are encouraging techniques while costly vacuum techniques such as thermal, sputtering, MOCVD, MBE, etc., are part of the process for cutting edge technologies whereby cost is negligible [84,85].

1.9.8. Materials

Materials used in solar cells fabrication must have some characteristically safety precautions at least to be nontoxic with no environmental degradation. For example, Sn, Fe, Al, Si, etc., based compound semiconductors are adjusted for thin film solar cells. If toxic compounds are used, intensive high care conditions must be taken in consideration, for example, the case of H_2Se, H_2S annealing atmosphere gases, Hydrazine, etc.[86].

1.9.9. Window Materials

The wide band gap semiconductor materials usually n-type or doped with suitable n dopants to obtain the required low resistivity are used as window materials [87]. The CdS is the most widely studied window material with absorbers like Cu_2S, CdTe, InP, $CuInS_2$, $CuInSe_2$ $CuIn_{1-x}Ga_xSe_2$, etc., others include CdZnS, In_2O_3:Sn, ZnO, SnO_2:F, etc. In the case of CdS, CdZnS, and ZnO suitable dopants such as In or Al are used to obtain high conductivity with reasonably high transmission. Higher V_{oc} and J_{sc} are reported with CdZnS as a window instead of CdS in the heterojunction solar cells [88].

1.9.10. Absorber Materials

The performance of heterojunction thin film solar cell is basically dependent on the choice of the optimum absorber material. The material should be a direct band gap semiconductor with a high absorption coefficient [89]. A plot of absorption coefficient of different semiconductors as a function of photon energy (hυ) yields in the band gap value. There are a number of possible materials with band gap neighborhood of 1.5 eV. However, other factors such as technology and stability are also important. The solar cells based on absorber materials like Si, a-Si, GaAs, CdTe, InP, $CuInSe_2$, CIGS, Zn_3P_2, CZTS, WSe_2, etc., have received much attention [90]. The search for innovative materials has led to investigations on efficiencies in excess of 10%. The

studies on ternary, quaternary, and pentenary semiconductor materials with considering the band gap and lattice constants in matching the window materials are important. The family of ternary chalcopyrite's offers many attempts for obtaining absorber materials because of their favorable optical and electrical properties [91]. The materials are of current technological interest since they also find application in other solid-state devices like visible and infrared light emitting diodes, infrared detectors, parametric oscillators, up converters and far infrared generators. Among those ternary chalcopyrite semiconductors, copper based I–III–VI$_2$ semiconductors have attracted many investigators. The basic scale of thin film solar cells is that low lattice in coincidence between the absorber and window layers which reduces interfacial states [92].

1.10. Copper Based I–III–VI$_2$ Semiconductors

The compound semiconductors, particularly CuInX$_2$ (X= S, Se) or Cu(In$_{1-x}$Ga$_x$) Se$_2$ have several desirable features as absorbers in the thin film solar cells [93].

(i) They are direct band gap semiconductors with a high absorption coefficient.

(ii) They can be deposited either in n- or p-type. However, the CuGaSe$_2$ always have p-type conductivity. A wide variation in the conductivity can be controlled by changing the atomic ratios of cations or by doping with different dopants [94].

(iii) The electron affinities of these semiconductors appear compatible with CdS, CdZnS, indium tin oxide (ITO) such that deleterious conduction band spikes are unlikely upon heterojunction formation.

(iv)The notice lattice match is good with CdS and CdZnS which help in minimizing the interfacial state density.

(v) The materials can be deposited in thin film form employing suitable techniques for large scale production.

(vi)The materials should be more stable than Cu$_x$S. In the ternaries, trivalent indium seems to bind copper tightly in the chalcopyrite lattice suppressing the undesirable copper migration into CdS, which is observed in the Cu$_x$S/CdS solar cells[95].

1.11. Nanocrystalline materials:

Nanocrystalline materials have been the subject of widespread research over the past couple of decades with significant advancement in their understanding especially in the last few years [96]. As the name suggests, they are single or multi-phase polycrystals with nano scale ($1*10^9$–$250*10^9$ m) grain size. At the upper limit of this regime, the term "ultrafine grain size" is often used (grain sizes of 250–1000 nm). Nanocrystalline materials are structurally characterized by a large volume fraction of grain boundaries, which may significantly alter their physical, mechanical, and chemical properties in comparison with conventional coarse-grained polycrystalline materials [97], which have grain sizes usually in the range 10–300 nm. As the grain size is decreased, an increasing fraction of atoms can be ascribed to the grain boundaries.

Nanocrystalline materials may exhibit increased strength/hardness, improved toughness, reduced elastic modulus and ductility, enhanced diffusivity, higher specific heat, enhanced thermal expansion coefficient (CTE), and superior soft magnetic properties in comparison with conventional polycrystalline materials [98]. This has been the incentive for widespread research in this area, and lately, with the availability of advanced tools for processing and characterization, there has been an escalation of work in this field. Nanostructured materials provide us not only with an excellent opportunity to study the nature of solid interfaces and to extend our understanding of the structure–property relationship in solid materials down to the nanometer regime, but also present an attractive potential for technological applications with their novel properties [99].

References

[1]R. Feynman, R. Leighton, and M. Sands, The Feynman Lectures on Physics, Vol. 1 (Addison-Wesley, Menlo Park, California, 1963) Chap. 4.

[2] T. F. Stocker, D. Qin, G.-K. Plattner, M. M. B. Tignor, S. K. Allen, J. Boschung, A. Nauels, Y. Xia, V. Bex, and P. M. Midgley, eds., Climate Change 2013 - The Physical Science Basis: Working Group I Contribution to the Fifth Assessment Report of the Intergovernmental Panel on Climate Change (Cambridge University Press, Cambridge, United Kingdom, 2014).

[3]L. Freris and D. Infield, Renewable Energy in Power Systems (John Wiley & Sons Inc, Chichester, United Kingdom, 2008).

[4]M. Beerepoot and A. Marmion, Policies for renewable heat (OECD/IEA, Paris, France, 2012).

[5]G. Masson, M. Latour, M. Rekinger, I.-T. Theologitis, and M. Papoutsi, "Global Market Outlook for Photovoltaics 2013-2017," European Photovoltaic Industry Association, Brussels, Belgium (2013).

[6]G. Masson, S. Orlandi, and M. Rekinger, "Global Market Outlook for Photovoltaics 2014-2018," European Photovoltaic Industry Association, Brussels, Belgium (2014).

[7]D. Neamen, Semiconductor Device Physics: Basic Principles, 4th ed. (McGraw-Hill, New York, NY, USA, 2012).

[8]E. Becquerel, Compt. Rend. 9 (1839) 561.

[9]L.O. Grondhal, Rev. Mod. Phys. 5 (1933) 141.

[10]https://en.wikipedia.org/wiki/Series_and_parallel_circuits.

[11] Thin Films and Nanostructures Waveguide Spectroscopy of Thin Films,2005, Volume 33 I, Seial Editors VLADIMIR AGRANOVICH, Author: Alexander Vasil'evich Khomchenko.

[12] Thin Film Solar Cells Fabrication, Characterization and Applications Edited by Jef Poortmans and Vladimir Arkhipov IMEC, Author: Jef Poortmans | Vladimir Arkhipov.

[13] Thin-Film Crystalline Silicon Solar Cells Physics and Technology, Edited by: Rolf Brendel, Author: Rolf Brendel | Adolf Goetzberger.

[14] Advanced Characterization Techniques for Thin Film Solar Cells, Edited by Daniel Abou-Ras, Thomas Kirchartz, and Uwe Rau, Author: Uwe Rau | Daniel Abou-Ras | Thomas Kirchartz.

[15] Metal Based Thin Films for Electronics, Klaus Wetzig, Claus M. Schneider (Eds.), Author: Klaus Wetzig | Claus M. Schneider

[16] Topics in Applied Physics Volume 98 Topics in Applied Physics is part of the SpringerLink service, Author: Masanori Okuyama | Yoshihiro Ishibashi

[17] Adhesion aspects of thin films, volume 2, Editor: K.L. Mittal ///vs P/// UTRECHTBOSTON 2005 VSP, Author: K.L. Mittal

[18] Ferroelectric Thin-film Waveguides in integrated optics and optoelectronics,Authors: A M Prokhorov | Yu S Kuz'minov | O A Khachaturyan

[19] Practical Design and Production of Optical Thin Films Second Edition, Revised and Expanded Ronald R. Willey Willey Opt, Author: Ronald R. Willey

[20]J. Zhao, A. Wang, P. Altermatt, M.A. Green, Appl. Phys. Lett. 66 (1995) 3636.

[21]H.Y. Chen, J. Hou, S. Zhang, Y. Liang, G. Yang, Y. Yang, et al., Nature 3 (2009) 649.

[22] S. Ito, T.N. Murakami, P. Comte, P. Liska, C. Gratzel, M.K. Nazeeruddin, et al., Thin Solid Films 516 (2008) 4613.

[23] T. Cheyney, Photovoltaics International, second ed., (2008), www.pv-tech.org, (p.76).

[24] R.R. King, D.C. Law, K.M. Edmondson, C.M. Fetzer, G.S. Kinsey, H. Yoon, et al., Adv. OptoElectron. (2007), (ID 29523).

[25] N.H. Karam, R.R. King, M. Haddad, J.H. Ermer, H. Yoon, H.L. Cotal, et al., Solar Energy Mater. Solar Cells 66 (2001) 453.

[26] M. Yamaguchi, T. Takamoto, K. Araki, Solar Energy Mater. Solar Cells 90 (2006) 3068.

[27] S.H. Lee, K.L. Chen, S. Gallo, III-V Multijunction Solar Cells, Iowa State University, 2008. (Private communication).

[28] M.R. Reyes, K. Kim, D.L. Carroll, Appl. Phys. Lett. 87 (2005) 083506.

[29] R. Janssen, 'Introduction to polymer solar cells (3y280), 2010.' (Private communication)

[30] A.C. Mayer, S.R. Scully, B.E. Hardin, M.W. Rowell, M.D. McGehee, Mater. Today 10 (2007) 28.

[31] C.W. Tang, Appl. Phys. Lett. 48 (1986) 183.

[32] J.Y. Kim, S.H. Kim, H.-H. Lee, K. Lee, W. Ma, X. Gong, et al., Adv. Mater. 18 (2006) 572.

[33] W. Cai, X. Gong, Y. Cao, Solar Energy Mater. Solar Cells 94 (2010) 114.

[34] Wikipedia, Solar Cell.

[35] K. Kim, J. Liu, M.A.G. Namboothiry, D.L. Carroll, Appl. Phys. Lett. 90 (2007) 163511.

[36] The Worldbank, (2014), wdi.worldbank.org.

[37] S. Dai, J. Weng, Y. Sui, C. Shi, Y. Huang, S. Chen, et al., Solar Energy Mater. Solar Cells 84 (2004) 125.

[38] M. Gratzel, Nature 414 (2001) 338.

[39] T.D. Nielsen, C. Cruickshank, S. Foged, J. Thorsen, F.C. Krebs, Solar Energy Mater. Solar. Cells 94 (2010) 1553.

[40] S.R. Kodigala, Ph.D. Thesis, Sri Venkateswara University, Tirupati, 1992.

[41] J. Malmstrom, J. Wemmerberg, M. Bodegard and L. Stolt 17th European PV conference 2001, 1265; H.W. Schock, U. Rau, T. Dullaber, G. Hamma, M. Balboul, T.M-. Friedelmeier, A. Jasemeck, I. Kotschau, H. Kerber and H. Wiesner, in proc. 16th Europ. Photovoltaic. Sol. Em. Conf. 2000, 301–308.

[42] R.H. Bube, Heterojunctions for thin film solar cells, in: Solar Materials Science, Academic Press, New York, NY, 1980.

[43] H.Y. Chen, J. Hou, S. Zhang, Y. Liang, G. Yang, Y. Yang, et al., Nature 3 (2009) 649.

[44]S. Ito, T.N. Murakami, P. Comte, P. Liska, C. Gratzel, M.K. Nazeeruddin, et al., Thin Solid Films 516 (2008) 4613.

[45]T. Cheyney, Photovoltaics International, second ed., (2008), www.pv-tech.org, (p.76).

[46]N.H. Karam, R.R. King, M. Haddad, J.H. Ermer, H. Yoon, H.L. Cotal, et al., Solar Energy Mater. Solar Cells 66 (2001) 453.

[47]M. Yamaguchi, T. Takamoto, K. Araki, Solar Energy Mater. Solar Cells 90 (2006) 3068.

[48]S.H. Lee, K.L. Chen, S. Gallo, III-V Multijunction Solar Cells, Iowa State University, 2008. (Private communication).

[49]M.R. Reyes, K. Kim, D.L. Carroll, Appl. Phys. Lett. 87 (2005) 083506.

[50] R. Janssen, 'Introduction to polymer solar cells (3y280), 2010.' (Private communication)

[51]A.C. Mayer, S.R. Scully, B.E. Hardin, M.W. Rowell, M.D. McGehee, Mater. Today 10 (2007) 28.

[52]C.W. Tang, Appl. Phys. Lett. 48 (1986) 183.

[53]J.Y. Kim, S.H. Kim, H.-H. Lee, K. Lee, W. Ma, X. Gong, et al., Adv. Mater. 18 (2006) 572.

[54]W. Cai, X. Gong, Y. Cao, Solar Energy Mater. Solar Cells 94 (2010) 114.

[55]Wikipedia, Solar Cell.

[56]K. Kim, J. Liu, M.A.G. Namboothiry, D.L. Carroll, Appl. Phys. Lett. 90 (2007) 163511.

[57]Karl Leo. www.heliatek.com, (accessed June 2010).

[58]S. Dai, J. Weng, Y. Sui, C. Shi, Y. Huang, S. Chen, et al., Solar Energy Mater. Solar Cells 84 (2004) 125.

[59]T.D. Nielsen, C. Cruickshank, S. Foged, J. Thorsen, F.C. Krebs, Solar Energy Mater. Solar. Cells 94 (2010) 1553.

[60]S.R. Kodigala, Ph.D. Thesis, Sri Venkateswara University, Tirupati, 1992.

[61] J. Malmstrom, J. Wemmerberg, M. Bodegard and L. Stolt 17th European PV conference 2001, 1265; H.W. Schock, U. Rau, T. Dullaber, G. Hamma, M. Balboul, T.M-. Friedelmeier, A. Jasemeck, I. Kotschau, H. Kerber and H. Wiesner, in proc.16th Europ. Photovoltaic. Sol. Em. Conf. 2000, 301–308.

[62]R.H. Bube, Heterojunctions for thin film solar cells, in: Solar Materials Science, Academic

[64]H.F. Wolf, Semiconductors, Wiley Interscience, New York, NY, 1971.

[65] M. Savelli, J. Bougnot, B.O. in: Seraphin (Ed.), Solar Energy-Solid State Physics Aspects, Topics in Applied Physics, Vol. 31, Springer-Verlag, Berlin, 1979.

[66]D.L. Feucht, J. Vac. Sci. Technol. 14 (1977) 57.

[67]C.J. Nuese, J. Educ. Mod. Mat. Sci. Eng. 2 (1980) 113.

[68]R. Singh, K. Rajkanan, D.E. Brodie, J.H. Morgan, IEEE Trans. Electron Devices ED-27,(1980) 656.

[69]E. Bucher, Appl. Phys. 17 (1978) 1.

[70]O. Lupan, T. Pauporte, L. Chow, B. Viana, F. Pelle, L.K. Ono, et al., Appl. Surf. Sci.256 (2010) 1895.

[71]G. Haake, Solar Energy Mater. Solar. Cells 14 (1986) 233.

[72]T. Pisarkiewicz, K. Zakrzewska, E. Leja, Thin Solid Films 153 (1987) 479.

[73]R.H. Bube, A.L. Fahrenbruch, Fundamentals of Solar Cells, Academic Press, New York, 1983.

[74]J.L. Shay, J.H. Wernick, Ternary Chalcopyrite Semiconductors: Growth, Electronic Properties and Applications, Pergamon Press, New York, 1975.

[75]S.K. Chang, H.L. Park, H.K. Kim, J.S. Hwang, C.H. Chung, W.T. Kim, Phys Stat. Solidi (B) 158 (1990) K115.

[76]L. Roa, C. Rincon, J. Gonzalez, M. Quintero, J. Phys. Chem. Solids 51 (1990) 551.

[77]M. Robbins, V.G. Lambrecht Jr., Master. Res. Bull. 8 (1973) 703.

[78]H. Neff, P. Lange, M.L. Fearheiley, K.J. Backmann, Appl. Phys. Lett. 47 (1985) 1089.

[79]I.V. Bodnar, B.V. Korzun, A.I. Lukomski, Phys. Stat. Solidi (B) 105 (1981) K143.

[80]B.R. Pamplin, R.S. Feigelson, Thin Solid Films 60 (1979) 141.

[81]G.H. Chapman, J. Shewchun, B.K. Garside, J.J. Loferski, R. Beaulieu,

Solar Energy Mater. 1 (1979) 451.

[82]J. Shewchun, J.J. Loferski, R. Beaulieu, G.H, Chapman and B.K. Garside,

J. Appl. Phys. 50 (1979) 6978.

[83]T. Loher, W. Jaegermann, C. Pettenkofer, J. Appl. Phys. 77 (1995) 731.

[84]M. Gloeckler, MS Thesis, Colorado State University, Fort Collins, CO 80523, 2003.

[85]G. Liu, T. Schulmeyer, J. Brotz, A. Klein, W. Jaegermann, Thin Solid Films 431 (2003) 477.

[86]L.L. Kazmerski, F.R. White, M.S. Ayyagari, Y.J. Juang, R.P. Patterson, J. Vac. Sci.Technol. 14 (1977) 65.

[87]K.J. Bachmane, E. Buchler, J.L. Shay, S. Wagner, Appl. Phys. Lett. 29 (1976) 121.

[88]L.L. Kazmerski, P.J. Ireland, F.R. White, R.B. Cooper, in: Proc. 13th IEEE Photovoltaics Specialists Conference, 1978, p. 620.

[89]L.L. Kazmerski, P. Shelden, in: Proc. 13th IEEE Photovoltaics Specialists Conference, 1978, 541.

[90]L.L. Kazmerski, in: G.D. Holah (Ed.), Ternary Compounds 1977, Vol. 35, 1977, p. 217 (London; Inst. Phys.).

[91]M. Robbins, V.G. Lambrecht Jr., Mater. Res. Bull. 8 (1973) 703.

[92]I.V. Bodnar, B.V. Korzun, A.I. Lukomski, Phys. Stat. Solidi (B) 105 (1981) K143.

[93]S.J. Fonash, Solar Cell device Physics, Academic Press, New York, 1981.

[94] H.L. Hwang, C.Y. Sun, C.Y. Leu, C.C. Cheng, C.C. Tu, Rev. Phys. Appl. 13 (1978) 745.

[95] H. Hahn, G. Frank, W. Klinger, A.D. Meyer, G. Strorger, Z. Anorg. Aug. Chem. 271 (1953) 153.

[96] Contreras M et al., Prog. Photovolt. 7, 311–316 (1999).

[97] Tanaka et al., Proc. 17th Euro. Conf. Photovoltaic Solar Energy Conversion, 989–994 (2001).

[98] S.A. Monolache, L. Andronic, A. Duta, E. Enesca, J. Optoelectron. Adv. Mater. 9 (2007) 1269.

[99] A. Nagaoka, K. Yoshino, H. Taniguchi, T. Taniyama, H. Miyake, Jpn. J. Appl. Phys.50 (2011) 128001.

Chapter 2. The semiconductor materials. Literature Review

2.1. THE SUN

The sun is an average star. It has been burning for more than 4-billion years, and it will burn at least that long into the future before erupting into a giant red star, engulfing the earth in the process. Some stars are enormous sources of X-rays; others mostly generate radio signals. The sun, while producing these and other energies, releases 95% of its output energy as light, some of which cannot be seen by the human eye. The peak of its radiation is in the green portion of the visible spectrum. Most plants and the human eye function best in green light since they have adapted to the nature of the sunlight reaching them.

The sun is responsible for nearly all of the energy available on earth. The exceptions are attributable to moon tides, radioactive material, and the earth's residual internal heat. Everything else is a converted form of the sun's energy: Hydropower is made possible by evaporation-transpiration due to solar radiant heat; the winds are caused by the sun's uneven heating of the earth's atmosphere; fossil fuels are remnants of organic life previously nourished by the sun; and photovoltaic electricity is produced directly from sunlight by converting the energy in sunlight into free charged particles within certain kinds of materials [1].

2.2. Photovoltaic Power Systems:

Photovoltaic (PV) power systems are one of today's fastest growing renewable energy technologies. Solar cells, which are the foundation of PV systems, convert the energy in sunlight directly into electricity. Consequently, the "fuel" is free. The term "photo" comes from the Greek "phos," which means "light." "Volt" is named for Alessandro Volta (1745-1827), a pioneer in the field of electricity. Electricity is produced when sunlight strikes the semiconductor material in a photovoltaic (solar) cell, creating an electric current [2].

Photovoltaic energy systems can be as small as a few solar cells or as big as a large array of PV modules, which are made up of interconnected groups of solar cells. Most modules are about the size of a coffee table top, though they can be manufactured in many different sizes and shapes.

The simplest and smallest PV systems are those that provide power for small consumer items like solar calculators and wrist watches. Larger PV systems were originally developed for use in

space. They now power nearly every satellite circling the Earth, because they operate reliably for long periods of time and require little maintenance [3].

There are different energy forms, i.e; electrical, chemical, or mechanical energy, and they can be used to distinguishtheir forms of change,i.e; movement, heating, or chemical change. Human beings need energy to move their bodies, to cook, to heat and light houses, or to drive vehicles. An active young man needs about 2500 kcal (2.9 kWh) per day to fulfil his daily energy requirements. This means the energy of about 1060 kWh per year. The present global energy consumption is around 19 000 kWh per inhabitant per year. It means that on average a man consumes about 19 times more energy than is needed for his survival and satisfactory health [4,5].

The mankind has witnessed an enormous increase in energy consumption during last 100 years. While in 1890 the energy use per inhabitant per year was around 5800 kWh it reached 20200 kWh in 1970. Since 1970 the energy use has dropped to the present level of 19000 kWh per inhabitant per year. The increase in energy use in the 20th century can be related to an evolution process that has started about five centuries ago. The underlying motivation of this process was formulated during the Enlightenment period in the 18[th]century as the philosophy of human progress. The aim of the process was an examination of the surrounding world and its adaptation to the needs of people whose life would become more secure and comfortable. This process was accompanied by growing industrialization and mass production, which were demanding more and more energy [6,7]. At the end of the 19th century coal was the main source of energy. In this period electricity was introduced in the industrialized countries as a new and elegant form of energy. This form of energy was quickly applied on a large scale. The widespread growth of electricity use led to construction of hydroelectric plants and hydropower became an important source of energy in the first half of the 20th century [8,9].

In the period after the World War II much effort was put into the reconstruction of the society. The emphasis was directed on the growth and efficiency of the mass production. New technologies and new materials, such as plastic, were applied in the production. The energy demand was tremendously growing in this period. Oil and gas started to play an important role as energy sources in the second half of the 20th century. Coal, oil, and gas form today dominant sources of energy. These three energy sources, also known as fossil fuels, are called the

traditional energy sources. In this period nuclear energy was introduced as a new source of energy. Increasing and more efficient mass production resulted in the low price of many household products. The consumption of the products grew enormously and therefore it is not surprising that we characterize today society as a consumption society [10,11,12].

Nevertheless, it has become evident at the end of the 20th century that the philosophy of human progress that has manifested itself in a huge production and consumption of goods has a negative side too. It has been recognized that a massive consumption of fossil fuels in order to full fil the present energy demands has a negative impact on the environment. The deterioration of environment is a clear warning that the present realization of human progress has its limitations [13]. The emerging international environmental consciousness was formulated in a concept of a sustainable human progress. The sustainable human progress is defined as: "… to ensure that it (sustainable development) meets the needs of the present without compromising the ability of future generations to meet their own needs". A new challenge has emerged at the end of the 20[th]century that represents a search for and a utilization of new and sustainable energy sources. The urge of this challenge is underlined by limited resources of the fossil fuels on the Earth and increasing demand for energy production. This is the reason why the attention is turning to the renewable energy sources. Energy is an essence of any human activity. When we are interested in how the human civilization has been producing and using energy, we can describe it in terms of an energy system [14,15]. The main characteristics of the energy system are: the population, the total consumption of energy, and the sources and forms of energy that people use. The energy system at the beginning of the 21[st]century is characterized by six billion people that live on the Earth and the total energy consumption of approximately 1.3×10^{10} kW[16].

2.3. Photovoltaics advantages:

- Have no moving parts (in the classical mechanical sense) to wear out.
- Contain no fluids or gases (except in hybrid systems) that can leak out, as do some solar-thermal systems.
- Consume no fuel to operate
- Have a rapid response, achieving full output instantly
- Can operate at moderate temperatures

- Produce no pollution while producing electricity (although waste products from their manufacture and toxic gases in the event of catastrophic failure and disposal may be a concern).

- Require little maintenance if properly manufactured and installed

- Can be made from silicon, the second most abundant element in the earth's crust [17].

- Modular permitting for a wide range of solar-electric applications such as:

  - Small scale for remote applications and residential use

  - Intermediate scale for business and neighborhood supplementary power

  - Large scale for centralized energy farms of square kilometers size

- Have a relatively high conversion efficiency giving the highest overall conversion efficiency from sunlight to electricity yet measured

- Have wide power-handling capabilities, from microwatts to megawatts

- Have a high power-to-weight ratio making them suitable for roof application

- However, there are ambivalent views about solar, or photovoltaic, cells' ability to supply a significant amount of energy relative to global needs.

• Those pro, contend: Solar energy is abundant, inexhaustible, clean, and cheap.

• Those can, claim: Solar energy is tenuous, undependable, and expensive beyond practicality.

There is some truth to both of these views. The sun's energy, for all practical purposes, is certainly inexhaustible. However, even though sunlight striking the earth is abundant, it comes in rather a dilute form [18,19].

2.4. Photovoltaic effect and principle of solar cell operation

One important way to convert solar radiation into electricity occurs by the photovoltaic effect which was first observed by Becquerel [20]. It is quite generally defined as the emergence of an electric voltage between two electrodes attached to a solid or liquid system upon shining light onto this system. Practically all photovoltaic devices incorporate a pn-junction in a semiconductor across which the photovoltage is developed. These devices are also known as solar cells. A cross-section through a typical solar cell is shown in Fig. 2.1. The semiconductor material has to be able to absorb a large part of the solar spectrum. Dependent on the absorption

properties of the material the light is absorbed in a region more or less close to the surface. When light quanta are absorbed, electron hole pairs are generated and if their recombination is prevented they can reach the junction where they are separated by an electric field. Even for weakly absorbing semiconductors like silicon most carriers are generated near the surface. This leads to the typical solar cell structure of
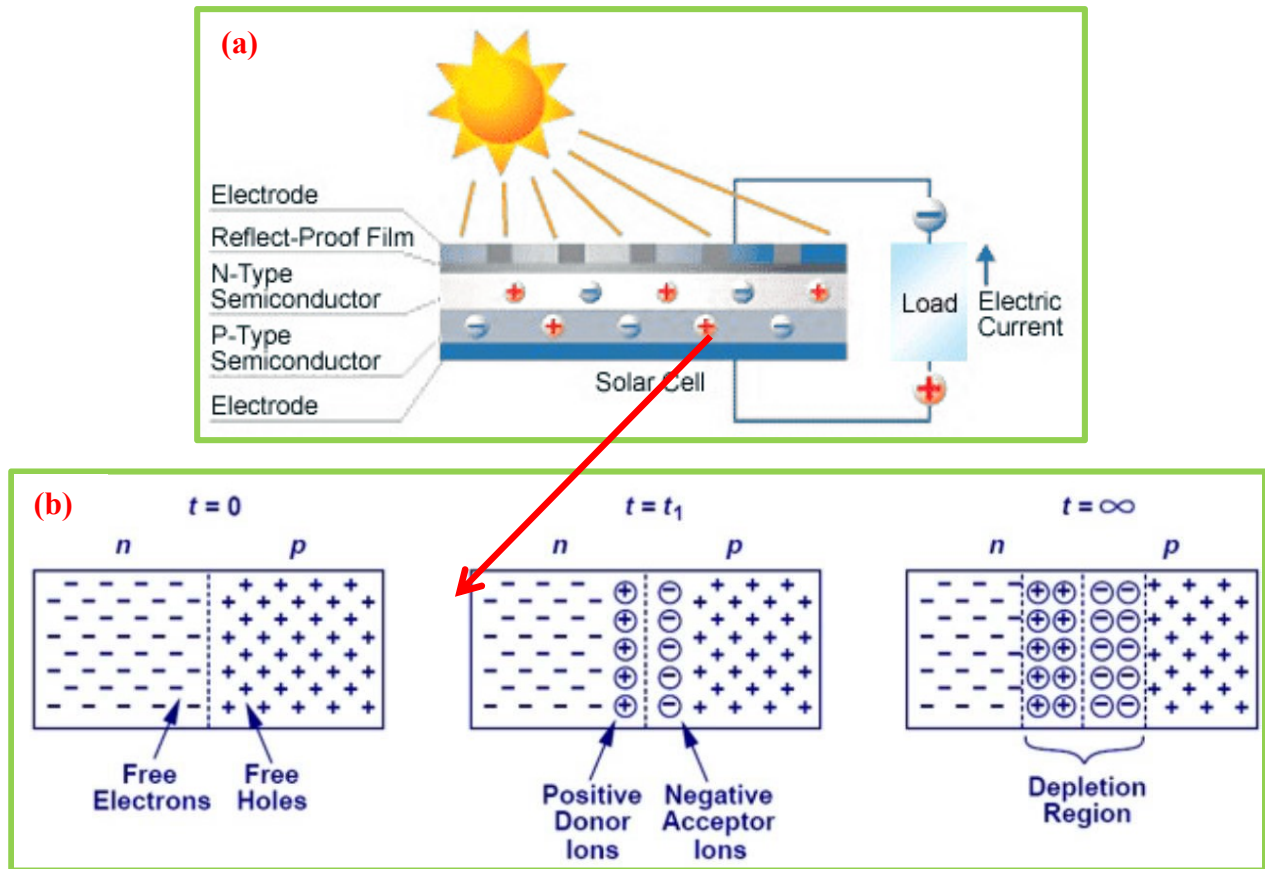
Figure2.1.(a) A cross-section through a typical solar cell and (b) the p-njunction explanation diagram.

which separates the emitter and base layer is very close to the surface in order to have a high collection probability for free carriers. The thin emitter layer above the junction has a relatively high resistance which requires a well-designed contact grid also shown in the figure. The operating principles have been described in many publications [21] and will not be addressed further here. For practical use solar cells are packaged into modules containing either a number of crystalline Si cells connected in series or a layer of thin-film material which is also internally series connected. The module serves two purposes, it protects the solar cells from the ambient and it delivers a higher voltage than a single cell which develops only a voltage of less than 1 V.

1.2. PV world market, market shares of different materials, future prospects Today's photovoltaic market is about 277 MW (in 2000) corresponding to a value of over US$ 1 billion. This is a remarkable market but still far away from constituting a noticeable contribution to the world energy consumption. Market growth in the last decade was between 15 and 25% as is shown in Figure 2.2. This market growth would be very satisfying for any conventional product but in the case of PV it is entirely insufficient if we consider the goals. The main motivation for developing solar energy is the desire to get away from depletable fossil fuels with their adverse effect on the environment. At the present growth rate, it will take us far into the second half of this century gets a relevant contribution by PV to world energy demand. As will be pointed out below, support programs in several countries are already accelerating market growth. Besides the terrestrial market there is also the space market which has entirely different boundary conditions and also different materials requirements. In order to keep the volume of this paper at a reasonable size, space solar cell materials will not be included [22,23].

Figure 2.2. Development of the world market shares in photovoltaics over the last decade in megawatts per year.

2.5. Photovoltaic technologies

The first practical use of solar cells was the generation of electricity on the orbiting satellite Vanguard 1 in 1958. These first solar cells were made from single crystal silicon wafers and had efficiency of 6 %. The space application was for some time the only application of solar cells. The energy crisis in the seventies of the 20th century accelerated a search of new energy sources for terrestrial applications. This search resulted in a growing interest for PV solar energy. The major obstacle of using solar cells for terrestrial electricity generation has been a much higher

price of the solar electricity when compared to the price of electricity generated from the traditional sources. Therefore, there has been much effort in the field of solar cells to reduce the price of solar electricity to a level that is comparable to the conventional electricity. The single crystal silicon wafer-based solar cells that had been used in space became also the first solar cells to be used for terrestrial generation of electricity. In order to decrease the material costs of crystalline silicon solar cells, research has been directed to develop low cost thin-film solar cells, which represent second generation solar cells for terrestrial application.
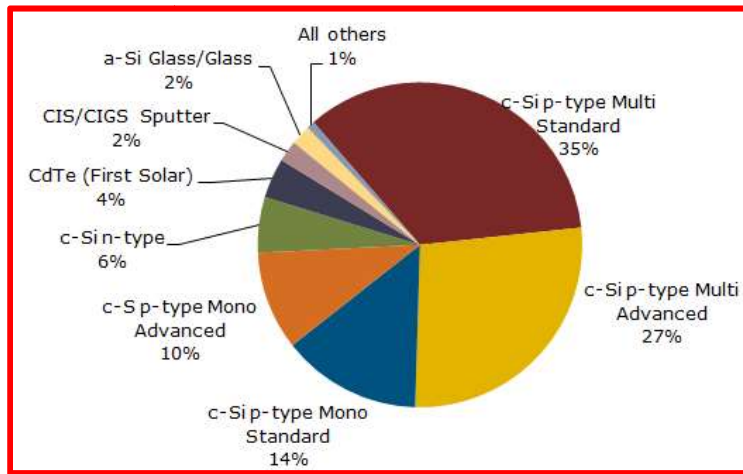
Figure 2.3. Market shares of different photovoltaic materials.

There are several semiconductor materials that are potential candidates for thin-film solar cells, namely copper indium gallium diselenide (CuInGaSe$_2$=CIGS), cadmium telluride (CdTe), hydrogenated amorphous silicon (a-Si:H), thin-film polycrystalline silicon (f-Si). The titanium oxide nanocrystals covered with organic molecules represent so called dye-sensitized nano-structred solar cells. It is expected that the efficiency of commercial second generation solar modules is likely to reach 15%. Conversion efficiency has to be increased substantially in order to progress further. Calculations based on thermodynamics demonstrate that the limit on the conversion efficiency of sunlight to electricity is 93% as opposed to the upper limit of 33% for a single junction solar cell, such as a silicon wafer and most present thin-film solar cells. This suggests that the performance of solar cells could be improved 2-3 times when different concepts were used to produce a third generation of high efficiency, thin-film solar cells (Figure 2.3) [24].

2.6. A brief history of the I-III-VI$_2$ family

The history of CuInSe$_2$ begins with the research carried out in the Bell Telephone laboratories in the early 70'seven though its synthesis and characterization have already been studied by Hahn in 1953 [25]. Along with new ternary chalcopyrite materials, it was also characterized by other groups [26]. The Bell Labs had grown crystals of a wide selection of these materials reporting their structural and electro-optics properties [27,28]. In that period, a solar cell with an efficiency of 12% based on CdS evaporated onto a p-type CuInSe$_2$ single crystal was realized [29]. In 1977, depositing by flash-evaporation a CdS thin film onto a single crystal of p-type CuGaSe$_2$, a solar cell that exhibited an energy conversion efficiency of up to 7 % was realized [30].

CuInSe$_2$ is a semiconducting compound of the I-III-VI$_2$ family with a direct band gap of 1.05 eV. Its chalcopyrite structure makes a good match to wurtzite CdS with only 1.2% lattice mismatch. This explains the good efficiency for the first time obtained with CuInSe$_2$ single crystal and put in evidence that CuInSe$_2$/CdS was the sixth system, along with junctions based on Si, GaAs, CdTe, InP, and Cu$_x$S that showed energy conversion efficiency up to 10%. Besides, CuInSe$_2$ is a direct band gap semiconductor, which minimizes the requirements for minority carrier diffusion length, and exhibits the highest absorption coefficient ($3x10^5$ cm^{-1}) in the visible region of the solar spectrum. These considerations make CuInSe$_2$ the best-suited material for the fabrication of an all polycrystalline thin film solar cell.

There has been relatively little effort devoted to devices realized on a CuInSe$_2$ single crystal apart from this first work, because of the difficulty in growing high-quality crystals. But, the aforementioned properties of CuInSe$_2$ channeled all the attention to thin-film solar cells because of their intrinsic advantages. The first thin-film CuInSe$_2$/CdS solar cell was fabricated by Kazmerski et al. in 1976 [31] by using films deposited by evaporation of CuInSe$_2$ powder in excess of Se vapor. This solar cell showed an efficiency of about 4-5%.

Boeing laboratories, 1981, the first high-efficiency all thin film solar cell based on the system n-ZnCdS/p-CuInSe$_2$ was realized with a conversion efficiency of about 9.4% and in 1985 they reached the efficiency of 11.4% [32].

Since the early 80's, ARCO Solar and Boeing have tackled the difficult issues involved with industrial production such as through put and yield. These efforts have led to many advances in the technology of CuInSe$_2$ solar cells.

The two groups have characterized their R&D approaches in different ways. The diversity of the two approaches consists basically in the $CuInSe_2$ (CISe) deposition methods, while the architecture of the device remains essentially the same.

The Boeing method includes the co-evaporation from separate sources of the single elements for CISe deposition. These films were deposited on alkali-free glass or ceramic covered by a thin layer of Mo, which acts as a positive electrode. The devices were finally completed by evaporating, on top of the CISe film, two layers of CdS (or ZnCdS), the first one was an intrinsic layer and the second one heavily doped with indium in order to ensure a best photocurrent collection. The two methods, introduced by Boeing and ARCO Solar, still remain the most common techniques for producing high efficiency cells and modules. Boeing was focused on co-evaporation of individual elements from separate crucibles while ARCO Solar was more confident in a two-stage process in which a low-temperature deposition of Cu and In was followed by a heat treatment at high temperature in H_2Se ambient.

With the "Boeing" basic structure, in 1996 a fantastic result was reached for all the thin film solar cell: a conversion efficiency of 17.7%. This improvement was obtained by using $CuGa_XIn_{1-X}Se_2$ as absorber layer. Effects of partial substitution of Ga for In appeared to be optimized for X=0.25. The band gap of the quaternary compound varies from 1.04 eV for X=0 to 1.7 eV for X=1; this means that the substitution of Ga for In causes an increase in open-circuit voltage, but a decrease in short-circuit current and fill factor and only for X=0.25 does the system reach the right equilibrium. Adjusting the Ga concentration profile into the absorber layer, in order to enhance the collection of the photo-generated carriers, it was possible to fabricate thin film solar cells based on the $CdS/CuGaInSe_2$ system with an efficiency of 18.8% in 1999, of 19.2% in 2003 and of 20.3% in 2011 [34]. This last result is the highest value for energy conversion efficiency in an all thin film photovoltaic device.

Let's summarize the key enhancements to the method that gave the more efficient cells (coevaporation-Boeing).

1. Soda lime glass replaced ceramic or borosilicate glass substrates. This change was made for the lower costs of soda lime glass and its good thermal expansion match with $CuInSe_2$. An increase in processes tolerance and device functioning were the result. It was soon clear that the

better results obtained came primarily from the beneficial inter diffusion of sodium from the glass [35].

2. The high thickness of the In-doped CdS or ZnCdS film was replaced by a thin un-doped CdS layer followed by a conducting Al-doped ZnO (ZAO) film. This was effective in increasing the photocurrent having enlarged the spectral response in the blue region wavelengths.

3. The absorber energy gap was increased from 1.02 eV for $CuInSe_2$ to 1.1–1.2 eV for $Cu(In,Ga)Se_2$ by the partial substitution of In with Ga, leading to an important increase in efficiency.

4. Innovative absorber deposition processes were developed to obtain energy gap gradients improving the photovoltage and current collection [36].

The key operation of photovoltaic cells is its "sandwich" distribution of materials endowed with different shape, so that some of them have excess electrons and others, on the contrary, have deficit. Photons of sunlight carry on the energy that tear off the remaining electrons from a layer and makes them move toward the "gaps" of the other (Figure 2.4. CIGS solar cell array and diagram).

The first copper chalcopyrite PV devices were introduced in 1976 in the form of copper-indium-di-selenide ($CuInSe_2$ or CIS) by Kazmerski and co-workers (Kazmerski et al., 1976) [37]. CIS has a band gap of 1 eV, however, by substituting either Ga for In or S for Se the band gap can be continuously engineered from around 1 eV to as high as around 2.5 eV (Wolden et al., 2011) [66]. Consequently, the abbreviations CIS, CIGS, CIGS or CIGSSe are generally used to describe this material, depending on how many elements are involved.

With up to five elements and numerous binary and ternary phases, the CIGSSe system presents much greater complexity than the other commercial PV technologies.
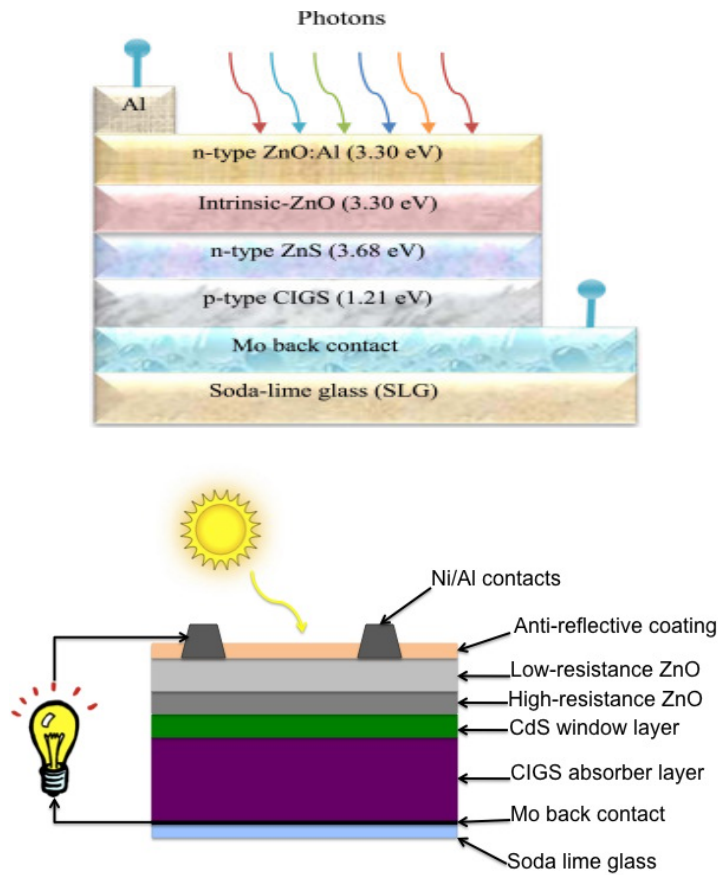
Figure 2.4. Solar Cell array and diagram for CIGS.

Extensive theoretical work helped to understand the electronic structure and role of defects (Siebentritt et al.,2010), and today it is well-known that sodium (Na) plays a critical role in the morphology and electronic properties of CIGS (Hedström et al., 1993) [153,68]. Originally Na diffused into the CIGS layer from the soda lime glass substrates, but nowadays more controlled and systematic approaches that employ sputtered layers of Na-containing material have been developed to gain control over Na introduction (Granath et al., 2000; Ruckh et al., 1994) [69,70]. Concerning the window layers, CdS is still the first choice, but both In and Zn sulfides are being investigated to substitute CdS in the long term (Panthani et al., 2008) [71]. Nevertheless, there are strong interactions between buffer and absorber layer, and in general simultaneous optimization of these layers is required to improve efficiency. Regarding flexible CIGS solar cells, further development of transparent ultra-barriers is required to improve the long-term stability.

CIGS is the only commercial TF technology that has continually reported efficiency improvements of its record cells during the last decade, surpassing the 20-percent threshold and

making it the clear efficiency leader among TF technologies (Green et al., 2012; Wolden et al., 2011) Today, several companies are producing commercial CIGS modules in the range of 10–50 MW/year with Japanese manufacturer Solar Frontier on the forefront selling 14.5% efficient modules from GW-scale production (Sugimoto et al., 2011) [66,72,73]. Substrates include soda lime glass, metal foils, or high temperature polyimide that aroused substantial interest for BIPV and portable power applications.

The basic structure of CIGS devices fabricated by current manufacturing schemes begins with the deposition of a Mo back contact followed by the p-type CIGS absorber (1–3 lm), a thin buffer layer (50–100 nm), and a doped ZnO serving as the transparent front contact.

Nevertheless, a variety of companies are working on the large-area commercialization of this technology by applying various manufacturing schemes, especially regarding the CIGS absorber (Tiwari et al., 2010) [74]. At present, the maturity of commercial module technologies is in the rangeof 60–80%. Much of this difference attributed to the quality of the absorber layer (Stolt et al., 1993; Gabor et al., 1994), and its corresponding manufacturing approach, with the most important routes being (i) coevaporation, (ii) metal selenisation/sulphurisation, and (iii) solution-based processing. In-line production using co-evaporation is pursued by companies such as Q-Cells, Manz AG, and Global Solar. Challenges involve the cosine flux distribution of the evaporation sources, the diffuse conditions of high vacuum, and sources have to be mounted in a top-down configuration for large glass substrates heated to $600^{\circ}C$ [68,75]. Another challenge with co-evaporation is that the relatively unreactive Se must always be supplied in great excess, leading to practical concerns related to condensation and materials management (Wolden et al., 2011) [66]. Selenisation and/or sulphurisation of pre-deposited metal films in a defined stoichiometry is the second common method to fabricate CIGS absorber layers on module-size substrates. The metal films can be deposited by various methods but are in most cases sputter-deposited onto the substrate and then converted to CIGS through annealing in a gaseous atmosphere. Solar Frontier, Honda Soltec, and Avancis are the most prominent commercial representatives of this approach. As compared to co-evaporation the chalcogen utilization can be improved by more than an order of magnitude, whereas the sources are either elemental vapors or hydride gases such as H_2Se or H_2S. The latter have the advantage of being more reactive and easy to control, though they present safety concerns due to their toxicity (Wolden et al., 2011) [66].
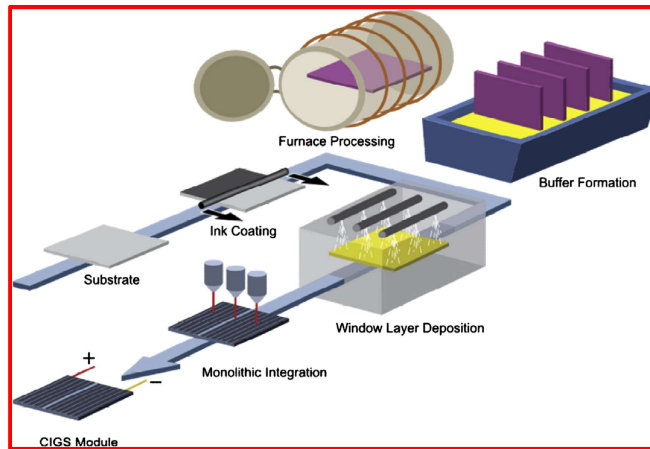
Figure2.5. Main stages of typical solution based thin film deposition/processing schemes (as in the case of CIGS manufacturing. Source: van Hest and Ginley (2009).

The best module efficiency obtained with this process up to date is as high as 15.7% (Green et al., 2012), whereas Manz AG very recently announced a total average panel efficiency of 14.6%, which according to the company sets a world record for thin-film solar panels [72]. Due to the high price pressure on the module market, a variety of companies is currently trying to abandon vacuum processes in their process scheme. This would help to reduce capital requirements, improve the utilization of applied materials, lower the energy requirements during fabrication, and improve the compatibility with roll to roll (R2R) processing Hibberd et al., 2010 [76]. In principle, such schemes are based on two-step processes, where a glass or foil substrate coated – by solution-based processes, electrodeposition, or particulate deposition – and followed by a high temperature annealing/sintering step. Record cell efficiencies of more than 15% have been obtained by a number of such techniques (Bhattacharya et al., 2000; Todorov et al., 2012) [77,79]. The integration of multiple evaporation or sputtering sources provides versatility that allows controlling the film composition and the corresponding phase profile, but also requires a large capital investment (Habas et al., 2010) [83]. Furthermore, a considerable amount of energy is required to deposit material from the target sources, and the relatively slow throughput and low materials utilization are not beneficial for large-scale production (Habas et al.,2010; Wang, 2011; Hibberd et al., 2010) [76,83,88,89]. Therefore, nonvacuum based deposition methods have been developed to tackle these issues. The straightforward comparative advantages of such methods include atmospheric pressure processing significantly lowering capital equipment costs, suitability for large-area and flexible substrates, higher throughput, and the combination of more efficient materials usage and lower temperature processing (Figure 5.) (van Hest and Ginley,

2009) [90]. Ideally, such approaches are based on R2R substrate handling instead of wafer batches, with the materials deposited from gases or solutions without the need of vacuum. The incredible array of such methods applicable to PV device fabrication ranges from coating processes such as electrochemical and chemical bath deposition, spin- or spray coating, to direct-write techniques like inkjet printing (Habas et al., 2010) [83]. Fig. 2.6 depicts the most representative basic process schematics for electrodeposition, spray coating, die coating, and inkjet printing (Krebs, 2009; Steirer et al., 2009; Hoth et al., 2007)[91-93].
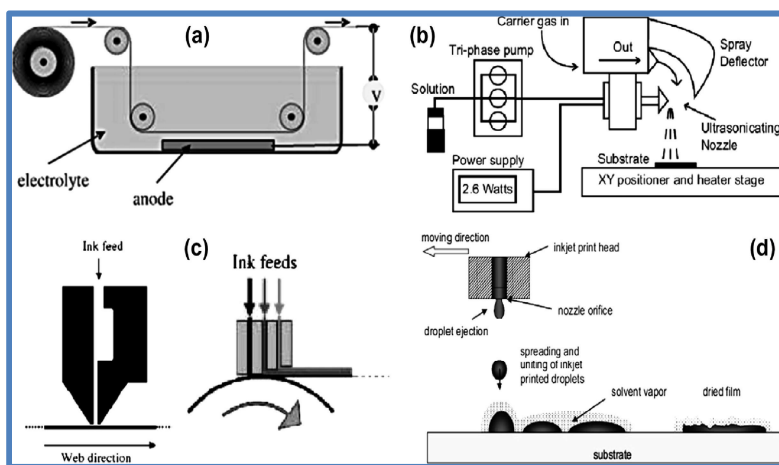
Figure 2.6. Process schematics for (a) roll-to-toll electrodeposition, which may also be representative for chemical bath deposition (without anode and appliedvoltage potential), (b) spray coating, (c) die coating heads for single and multiple layers, and (d) inkjet printing. Adapted from: Krebs (2009) and Steirerand et al. (2009), http://www.isetinc.com/technology-overview/, December, 2012.

2.7. A brief history of CZTS based solar cells

2.7.1. Introduction into CZTS based solar cells

Up to date TF solar cells based on the ternary chalcopyrite structure $CuInSe_2$ (CIS) have emerged as one of the most successful ones, progressing from first proof-of-concepts (Wagner et al., 1974) to high-efficiency record devices of over 20% for laboratory scaled CIGS devices and over 15% for modules (Green et al., 2012) that are presently manufactured in the hundreds of MW to GW range (Wolden et al., 2011) [66,72,94]. As these production volumes increase, concerns have been risen regarding the price and the availability of In, and whether it may limit the amount of chalcopyrite PV that can be manufactured at low cost. To tackle the aforementioned issues, Copper-zinc-tinsulphide/selenide ($Cu_2ZnSnS_4(Se_4)$, CZTS or CZTS(e)) entered the spotlight of researchers all over the world. CZTS is the I_2–II–IV–VI_4 quaternary

compound semiconductor that is obtained by replacing one half of the indium atoms in CuInSe$_2$ with zinc (group II) and the other half with tin (group IV). Depending on the ordering of the metals along the long c-axis of the structure, the kesterite or the stannite structure is obtained (Mitzi et al., 2011; Schorr,2011) [88,96]. All components of CZTS are abundant in the earth's crust (Cu: 50–70 ppm, Zn: 75–80 ppm, Sn: 2.2 ppm, S:260 ppm) and they possess extremely low toxicity (Siebentritt and Schorr, 2012; Emsley, 1998; Katagiri et al., 2009) [97-100].

The compound exhibits intrinsic point defects that lead to p-type semiconductor behavior (Delbos, 2012), and has a direct band gap and an absorption coefficient of more than 104 cm^{-1} suitable for TF PV applications (Ito and Nakazawa, 1988; Chan et al., 2010) [101-103]. With a predicted and experimentally verified band gap ranging from 1.0 eV for Cu$_2$ZnSnSe$_4$ (Friedlmeier et al., 1997; Todorov et al., 2010; Altosaar et al., 2008) to 1.5 eV for Cu$_2$ZnSnS$_4$ (Friedlmeier et al., 1997; Chen et al., 2009; Moynihan et al., 2011; Mellikov et al., 2011; Tanaka et al., 2005; Moriya et al., 2006; Scragg et al., 2008; Kamoun et al., 2007), the material system is well suited to enable high-efficient single junction solar cells (Shockley and Queisser, 1961), and in addition the band gap is tunable due to the variation of the S/Se ratio (Timmo et al., 2012). It was shown recently that the crystal structure allows some slight shifts from the stoichiometric composition (Choubrac et al., 2012) [80,81,104-106,109, 111,112,114-116,120-122,206].

The device structure of CZTS solar cells is similar to CIGS and can be obtained by replacing the CIGS absorber layer by CZTS in Fig. 2.7c. Ito and Nakazawa reported the photovoltaic effect of CZTS for the first time in 1988, while achieving an open-circuit voltage of 165 mV (Ito and Nakazawa, 1988) [102]. During the past decade the technical transformation of CZTS into an absorber layer in solar cell devices has mainly been established by Katagiri and coworkers by employing various vacuum-based physical vapor deposition methods and subsequent sulphurisation (Katagiri et al., 1997; Katagiri et al., 2001; Katagiri, 2005; Jimbo et al., 2007) [123-125,128]. More recently, studies on the sulphurisation of metal layers (Kurihara et al., 2009), co-evaporation (Repins et al., 2012), and non-vacuum techniques (Deligianni et al., 2012; Ahmed et al., 2012; Guo et al., 2010) attracted significant attention (Delbos, 2012). More and more work was done on non-vacuum solution-based processing approaches (Mitzi, 2009; Steinhagen et al., 2009; Kumar et al., 2009; Fella et al., 2011) [67,86,87,101,129,131-133,135,136,138]. This evolution may have been additionally triggered by the very successful IBM-approach applying spin-coating of a particle-containing solution diluted in hydrazine to

fabricate $Cu_2ZnSn(S,Se)_4$ based PV devices with over 11.1% conversion efficiency (Todorov et al., 2010; Barkhouse et al., 2012; Bag et al., 2012; Todorov et al., 2012), impressively demonstrating the potential of these deposition technologies as well as of the material system [79-81,139,140].
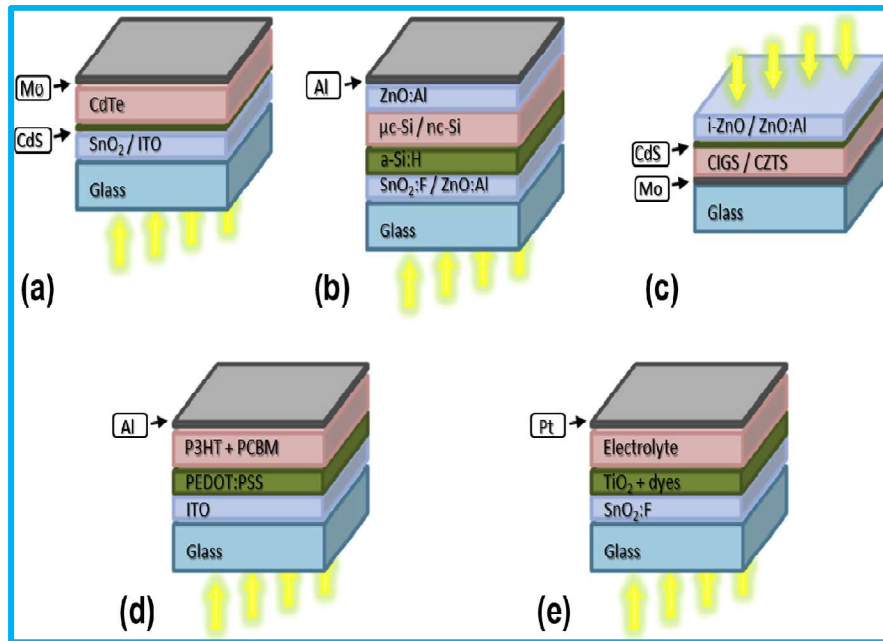
Figure 2.7. Basic device structures of the main TF solar cell approaches: (a) CdTe, (b) a-Si/l-Si, (c) CIGS/CZTS, (d) OPV, and (e) DSSC. Please not that different variations of these structures in terms of material, morphology, and layer sequence exist, respectively.

The most important manufacturing routes are (i) solution-based precursor fabrication followed by a short annealing, (ii) annealing of nano-crystalline precursors, (iii) low-temperature co-evaporation followed by a short annealing, (iv) sputter deposition followed by long annealing in H_2S, and (v) fast co-evaporation (Redinger et al., 2011; Riha et al., 2009) [141,144]. One interesting fact regarding the processing of CZTS is that a non-vacuum based processing scheme is still leading to highest efficiencies, even though very recently Repins and co-workers published a 9.15% efficient CZTS based solar cell fabricated by vacuum-based 4-source co-evaporation, stating that the ease of composition and phase control is responsible for the success of the solution based processes (Katagiri et al., 1997) [123]. The evolution of the power conversion of the main published CZTS based solar cell fabrication schemes is summarized in (Figure 2.8).
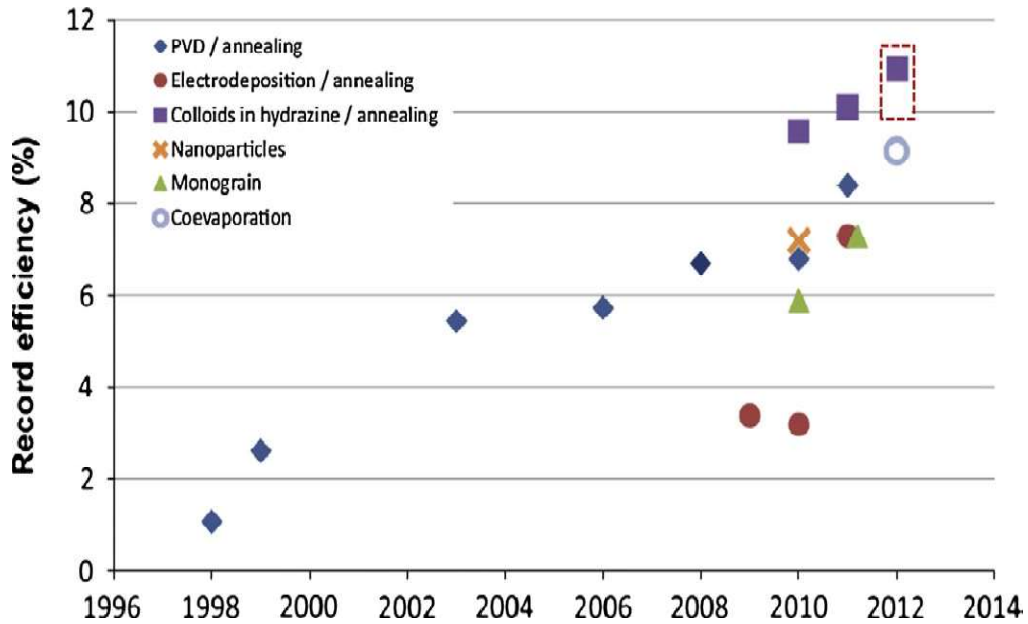
Figure 2.8. Evolution of record efficiencies for CZTS-based thin film solar cells fabricated by various process schemes. The red marking shows the updated value as published in Steinhagen et al. (2009), Delbos (2012).

The knowledge gathered by CIGS scientists on back contact, buffer and window layers, etc. in the past few years was very helpful be to achieve a quite fast learning curve regarding device fabrication and related conversion efficiency of CZTS based solar cells. Nevertheless, to keep up this pace and push the record values to higher numbers, processes as used in the case of CIGS solar cells may need to be tuned, as it is suggested by theory (Repins et al., 2011) and by detailed experimental investigation of crystal structure, phase transformations during growth, related defects, etc. (Siebentritt and Schorr, 2012) [97,130]. For example, as it has been shown recently by Scragg and co-workers that the Mo back contact and CZTS(e) suffer from a detrimental reaction causing the formation of $MoS_{(2)}$ and secondary phases at the CZTS/Mo interface during thermal processing (Scragg et al., 2012)[119].

2.7.2. Crystal structure, defects, and composition

Until recently, it was not clear whether the crystal structure of $Cu_2ZnSn(S,Se)_4$ is a kesterite (Hall et al., 1978) or a stannite one (Bernardini et al., 2000), whereas these two structures just differ in the ordering of Cu and Zn (Fig. 9)[185,146]. Finally, in a comprehensive neutron diffraction study of various $Cu_2ZnSn(S,Se)_4$ compounds, it was shown that Cu_2ZnSnS_4 and $Cu_2ZnSnSe_4$ occur in the kesterite structure, and not in the stannite structure, even though both show a certain disorder in between the Cu and Zn sites (Siebentritt and Schorr, 2012; Schorr,

2011) [96,97]. This disorder may be explained by a co-existence of kesterite and stannite, even though density functional theory calculations predict kesterite as the most stable phase for the sulphide and the selenide (Raulot et al., 2005; Paier et al., 2009; Persson, 2010) [147-149]. However, the energy difference of the stannite structure is only slightly larger, and since the band gaps predicted for the stannites are smaller than those of the kesterite, a co-existence of both structures could lead to the relatively low open-circuit voltages observed in kesterite solar cells as compared to the band gap (Mitzi et al., 2011) [88]. Another important structural parameter in chalcopyrites and kesterites is the tetragonal distortion, which is the deviation of c/2a from 1 (here, c is the long axis, and a is the short axis), since this deviation leads to a crystal full field and a non-degenerate valence band maximum (Shay and Wernick, 1975) [150]. Values have been determined experimentally as well as calculated whereas all calculations find a small tetragonal distortion of $0.998 = c/2a = 1.006$ (Siebentritt and Schorr, 2012) [97]. However, so far there is no agreement between the different methods regarding the trends between sulphide and selenide and between kesterite and stannite (Siebentritt and Schorr, 2012) [97].
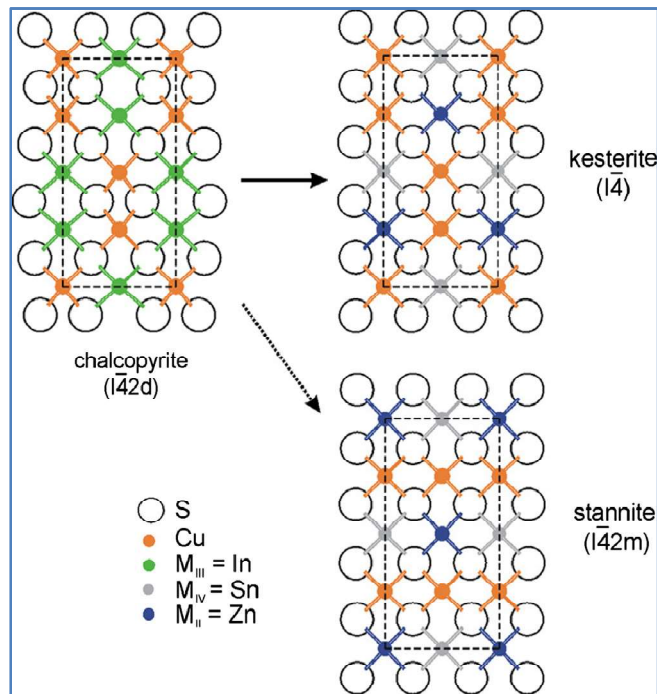
Figure 2.9. Schematic illustration of chalcopyrite structure, as well as kesterite and stannite structures. The unit cell boundaries are denoted with dashed lines. Source: Mitzi et al. (2011).

As in the case of CIGS materials, the doping and thus the bend bending in CZTS based solar cells is believed to be obtained by defects (Delbos, 2012; Siebentritt and Schorr, 2012) [97,101].

Published theoretical studies on defects in kesterites are all based on density functional theory (Nagoya et al., 2010; Biswas et al., 2010; Chen et al., 2010) [107,151,152]. Even though defect level predictions have to be taken with care (Siebentritt et al., 2010), regarding defect formation energies, which depend on composition and on the Fermi level, some clear trends are observed: The defect with the lowest formation energy is the acceptor Cu_{Zn} defect. Further low energy formation acceptors are Cu_{Sn} as well as V_{Cu} (Chen et al., 2010; Chen et al., 2010) [107,108,153]. Donor defect levels such as VS or Zn_{Cu} in general show higher formation energies, which in combination with the low, often even negative formation energy of Cu_{Zn} explains that Cu_2ZnSnS_4 and $Cu_2ZnSnSe_4$ so far have always found being p-type.
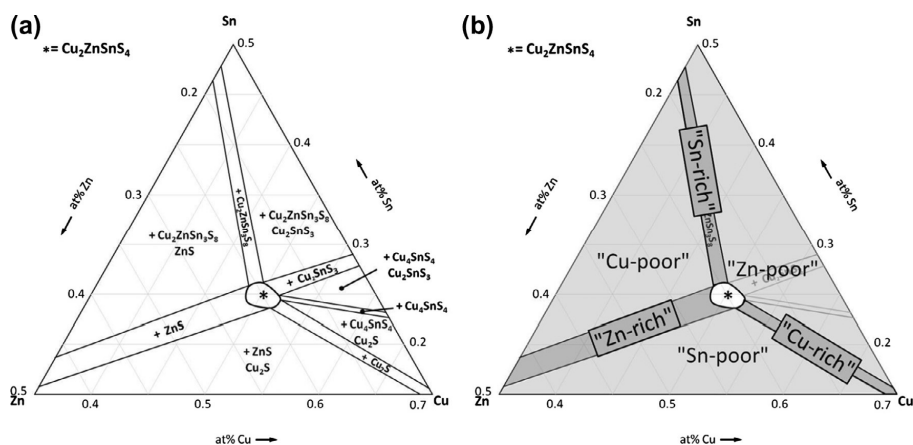
Figure 2.10. (a) Ternary CZTS phase diagram including the expected secondary phases at 400°C, (b) ternary CZTS phase diagram including regions as defined in Chen et al. (2010) giving hints which secondary phases should be expected to form at that composition.

Experimental phase diagrams have been published for $Cu_2ZnSnSe_4$ (Fig. 2.10a) Olekseyuk et al., 2004; Scragg, 2010, as well as for $Cu_2ZnSnSe_4$ (Dudchak and Piskach, 2003) [117,118,154,155]. Both phase diagrams predict a small region of single phase kesterite, allowing 1–2% (absolute) deviation in the composition at temperatures around 550 °C, which is significantly less than in the case of chalcopyrites allowing Cu deficiency of 4% (absolute) Go¨decke et al., 2000 [156]. The highest efficiencies have been obtained in the Zn-rich and Cu-poor region of the metal compositions (Fig. 2.10b) Delbos, 2012; Katagiri et al., 2009[101,126]. Due to the complexity of the $Cu_2ZnSnSe_4$ material and the number of elements, a large number of secondary phases exist. The most likely one is ZnS(e), which has been experimentally verified (Redinger et al., 2011; Redinger et al., 2011) [141,142]. Even though ZnS(e) – due to its wide band gap and usually relatively low conductivity – is not expected to reduce the open-circuit voltage or decrease the

shunt resistance of the solar cell, it may however be responsible for the high series resistance observed (Mitzi et al., 2011) [88]. In this context, lower band gap phases such as SnS(e), $Cu_2S(e)$, Cu–Sn–S(e) may be more unfavorable due to their lower band gap and/or their high conductivity (Siebentritt and Schorr, 2012) [97]. In Fig. 2.10b the expected secondary phases as related to the compositional regions as given by (Scragg, 2010) [117,118]. The unit cell boundaries are denoted with dashed lines. Source: Mitzi et al. (2011) [88].

2.7.3. Sulphurisation/selenisation and recrystallization

CZTS absorber layers fabrication by non-vacuum or solution-based processes is usually split into a two-step process scheme, where the needed elements are first incorporated during an ambient/low temperature process followed by an annealing step. Further elements (like chalcogens as in the case for CZTS) can be incorporated during this second annealing step to tailor the stoichiometry and crystal structure of the final film. Figure 2.11.depicts the process schemes for various two-step processes as from vacuum as well as non-vacuum deposition methods (Razykovet al., 2011) [157]. This is contrary to vacuum-based methods such as co-evaporation, reactive sputtering or pulsed laser deposition, which are able to perform the film fabrication within a one-step process, where all the elements are incorporated simultaneously. Such processes yield better results for CIGS based solar cells, but until now this was not the case for CZTS, even though very recently a 9.15% efficient CZTS based solar cell fabricated by vacuum-based 4-source co-evaporation has been published (Repins et al., 2012) [129]. In this context, it cannot be concluded that one of the processes (one- or two-step) is inherently better. Rather it appears that temperature and atmosphere control during the one-step deposition or annealing step are essential, and that this finally leads to improved control of composition and crystal structure (Delbos, 2012; Repins et al., 2012) [101,129]. Nevertheless, due to the complexity of the $Cu_2ZnSnS(e)_4$ materials and the number of elements, the advantage of the solution-based processes to precisely control composition and phases within the precursor substances may be a big one and may be responsible for the success of these methods so far. Regarding the formation of the quaternary CZTS structure temperatures between 500 and 600 ^{o}C are needed (Washio et al., 2011) [158]. Before the formation of the quaternary form, successive reactions form binaries and ternaries, whereas at room temperature, only binaries such as CuZn, Cu_3Sn or Cu_5Zn_8 are formed (Volobujeva et al., 2009; Schurr et al., 2009). At temperature between 550 and 580 ^{o}C ZnS(e) reacts with $Cu_2SnS(e)_3$ to form $Cu_2SnZnS(e)_4$Washio et al.,

2011; Volobujeva et al., 2009; Schurr et al., 2009; Ganchev et al., 2011[110,158,160,161]. In order to control the reactions during the annealing step it is important to control temperature ramps and times since too steep temperature ramps or too short annealing times can inhibit the formation of large grains (Ge et al., 2012; Maeda et al.,2011) [162,163].
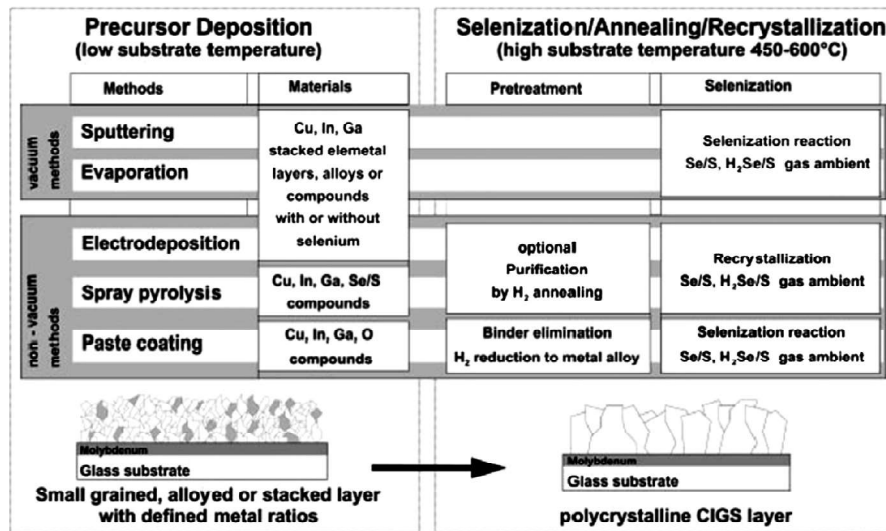
Figure 2.11. Various process sequences for the sulphurisation/selenisation of precursor materials for CIGS(e) cells. The most common sequences for CZTS(e) materials can be assumed equal. Source: Granneman et al. (2010).

The final layer has to be Zn-rich in order to lead to high-efficient devices (Figs. 2.10 and 2.11). By using Zn-rich growth conditions ZnS(e) formation is promoted; as a consequence, ZnS(e) reaction with Cu_2SnS_3 is increased (Nagoya et al., 2010; Chen et al., 2010) [107,151]. In addition, the formation of Cu_2X has to be prevented as much as possible, since the presence of $Cu_2S(e)$ leads to increased layer resistance, reduced efficiency, and to voids and defects during cyanide etching after deposition (Delbos, 2012; Muska et al., 2011) [101,164]. A $Cu_2S(e)$-rich layer is also promoted by the decomposition of CZTS at high temperatures, according to the chemical equilibrium between $Cu_2ZnSnS(e)_4$ and solid $Cu_2S(e)$ and the gaseous binaries ZnS(e), SnS(e), and S(e) which are then lost (Redinger et al., 2011; Redinger et al., 2011) [141,142]. In addition, SnS sublimes at 350 and Zn at 430 ^{o}C (Redinger and Siebentritt, 2010; Teeter et al., 2010), whereas SnSe evaporates at 370 and Sn at 460°C (Weber et al., 2010; Yoo et al., 2012) [143,165,166]. In addition, the selenization of CZTS or pre-annealed precursor layers may be dependent on the structure of the stacked films. A high grade of selenization without the appearance of secondary phases may be achieved if using precursor stacks of Mo/Zn/SnS/Cu or Mo/SnS/CuS/ZnS without the formation of CZTS (Salome et al., 2012) [167].

As can be concluded from the above paragraph, it is essential to prevent CZTS decomposition as well as binary losses during annealing. This can be achieved by (i) controlling the atmosphere during the thermal treatment, or by (ii) annealing time and heating/cooling rates. Regarding point one, SnS(e) losses can be reduced/prevented by introducing gaseous SnS(e) Redinger et al., 2011, increasing partial pressure of chalcogen (Fella et al., 2011), or performing the chalcogenation in a small closed container (Biccari et al., 2011) [138,141,142,168]. Regarding the second point, a two-stage annealing sequence appears preferential, where CZTS formation is done during a short (a few minutes) step, followed by a longer (up to a few hours) step for the grain growth. In the case of stacked metals and regarding the reaction mechanisms, Cu must not be deposited first, and Cu and Sn should be in close contact. Superior combinations for the formation of large CZTS grains are therefore Zn(S,Se)/Cu/Sn or Zn(S,Se)/Sn/Cu (Yoo and Kim, 2011; Delbos, 2012; Araki et al., 2008) [101,169,170].

2.7.4. Electrodeposition of CZTS based solar cells

In the last decade, Electrodeposition (ED) was thoroughly investigated and applied for the deposition of CIGS TF solar cells (Bhattacharya, 2009; Hodes, 1995; Schlesinger and Paunovic, 2000; Lincot et al., 2004) [172-175]. Several groups, including EDF-CNRS and the related spin-off NEXCIS, CIS Solar Technologies, and CIS CuT have been using such approaches and obtained cells with efficiencies greater than 10% (Lincot et al., 2004; Razykov et al., 2011), whereas NREL achieved efficiencies as high as 15.4% with a hybrid approach additionally using vacuum deposition (Bhattacharya et al., 1999) [175-177].

First publications of the use of ED to fabricate CZTS thin films were made in 2008 (Scragg et al., 2008; Scragg et al., 2008) and 2009 (Scragg et al., 2009; Hideaki et al., 2009; Ennaoui et al., 2009) [115-117,178,179]. Three process schemes are employed for the ED of CZTS: (i) direct compound deposition (Pawar et al., 2010a; Pawar et al., 2010b; Chan et al., 2010; Cui et al., 2011; Septina et al., 2013; Gea et al., 2012; Jeon et al., 2011a; Jeon et al., 2011b), (ii) co-deposition of a mixed/alloy Cu-Sn-Zn precursor (Chan et al., 2010; Schurr et al., 2009; Ganchev et al., 2011; Hideaki et al., 2009; Ennaoui et al., 2009; Ganchev et al., 2010; Li et al., 2011; Li et al., 2012; Schurr et al., 2009; Ennaoui et al., 2009; Jusˇkeˇnas et al., 2012), and (iii) stacked deposition of sequential layers (SEL) of Cu, Sn and Zn (Scragg et al., 2008; Ahmed et al., 2012;

Scragg et al., 2008; Kurihara et al., 2009; Scragg et al., 2010; Araki et al., 2009; Sarswat et al., 2012; Scragg et al., 2008; Zhang et al., 2009) [67, 103,110,111,115-118,132,161,171,180-190].

The first approach is experimentally challenging and only recently more reports on the fabrication of kesterite compounds from direct single-step electrodeposition were published, even though in some cases the films have been additionally sulfurized / selenized. Although, so far no working devices have been presented due to insufficient film quality, the progress is promising, and further optimizations of the electrolyte and electrodeposition conditions as well as the sulfurization parameters may lead to improvements regarding photovoltaic applications.

The general idea of co-deposition is to produce an already homogeneously mixed precursor, which may lead to a more uniform CZTS film in the following annealing step. However, there are some difficulties with the use of a mixed electrolyte. The main problem is that the optimum conditions for the electrochemical deposition of one metal may be different for another one, due to – for example – the difference in their standard reduction potentials. In the case of three different metals, these conditions have to be adjusted in order to meet the requirements of all three as good as possible. Hence, targeting co-deposition is nontrivial, and adjusting the composition in a rational manner is very difficult (Scragg, 2010) [117]. So far, the most efficient solar cell device including a CZTS absorber from electrodeposited Cu–Zn–Sn precursors yielded 3.4% (Ennaoui et al.,2009) [179].The most significant benefit of using the SEL approach is the ability to easily vary the composition and deposition parameters for every layer. For example, the thickness of each layer can be adapted, or the electrolyte pH and additive composition can be optimized in order to achieve high deposition rates, high efficiency and good morphology. Although the single layers are stacked and therefore separated in the precursor film, they can be intermixed by appropriate heat treatments. Since obtaining high quality kesterite absorbers needs annealing for the sulfurization / selenisation anyway, a pre-treatment to achieve this mixing is quite straightforward. This is even more of an issue when using electrodeposition to produce a layered precursor, since the standard reduction potentials of Cu, Sn and Zn are very different; for example, the potential required to electrodeposit Cu would lead to an oxidation and subsequent peeling of a Zn deposit (Scragg, 2010) [117]. For example, it has been shown that a Mo/Zn/Sn/Cu stack was most favorable for CZTS formation and gave better adhesion to the substrate (Araki et al., 2008) [170]. This stacking order is not easy to achieve by electrodeposition, and the deposition sequence preferred by the electrochemical approach would

be Mo/Cu/Sn/Zn (Scragg, 2010) [117]. So far, Cu_2ZnSnS_4 films prepared by sulfurization of an electrodeposited precursors stack lead to the highest efficiency of all electrochemical methods, namely 7.3% (Ahmed et al., 2012) [132].

The main growth criteria, especially for large area high throughput deposition, are uniformity on the (i) microscopic (e.g. the morphology of the electrodeposited material) and the (ii) macroscopic scale (e.g. the thickness/density of coverage of the substrate area), as well as the control of bulk electrolyte flow (e.g. convection inside the solution). The growth mechanisms of electrodeposited films can be very complex, and may be influenced by the deposition potential, or by the interactions between the solute and the substrate. To improve morphology, surfactants are added to the solutions to control the properties of the electrode-solution interface. Regarding convection, natural currents are responsible for maintaining a constant current during potentiostatic electrodeposition. In order to avoid thickness variations, convection must be deliberately provided in a uniform way (Scragg, 2010) [117].

2.7.5. Spin/spray/blade coating of CZTS based solar cells

Direct liquid deposition approaches, including solution, particle and mixed solution-particle precursors, are particularly attractive for large-scale manufacturing due to their compatibility with ultrahigh-throughput deposition techniques Todorov and Mitzi, 2010 [80]. This approach was pioneered by Kapur and co-workers at ISET (Kapur et al., 1987; Kapur et al., 2003), and more recently championed by Nanosolar (Wolden et al., 2011) [66,192,193]. Currently, Nanosolar's first commercially operational production line produces panels certified 11.4 to 11.6% efficiency and holds the world record for printed solar cells at 15.3% total-area efficiency for lab cells (http://www.nanosolar.com, December, 2012). Regarding CZTS, first approaches employed spray pyrolysis from metal chlorides and thiourea as metal and sulfur sources, respectively (Nakayama and Ito, 1996) [194]. This process was further optimized to yield nominally single phase CZTS in the as-deposited state without further annealing or sulfurization treatment, leading to almost stoichiometric CZTS films (Kumar et al., 2010) [137]. Nevertheless, an appropriate sulfurization/selenisation process is necessary to obtain high quality CZTS(e) films by using spray-based deposition (Yoo and Kim, 2011; Madarasz et al., 2001; Rajeshmon et al., 2011; Guo et al., 2009) [143,169,195,196]. Since then, various synthesis routes for CZTS, CZTSe, and CZTS(e) solutions were presented (Fella et al., 2011; Fischereder et al., 2010; Edler

et al., 2012; Ilari et al., 2012), with efficiencies of up to 6% using open atmosphere type CVD (Washio et al., 2012) [138,159,197-199]. A sol–gel-like approach for spin-coating CZTS films was reported in 2007 also resulting in an almost stoichiometric composition (Tanaka and Moritake, 2007) [113]. With a similar approach, the same group published the first report on a CTZS device incorporating absorber, buffer layer and TCO layers all deposited from solution processing: The device with a structure of glass/Mo/CZTS/CdS/AZO/Al yielded 1.01% conversion efficiency which was later improved to 1.61% (Moritake et al., 2009) [200]. Recently, a sol–gel method applying metals and sulfur in ethanol including a post-deposition annealing in N_2+H_2S (5%) atmosphere at 530 ^{o}C for 30 min yielded 5.1% efficient devices (Woo et al., 2012) [201].
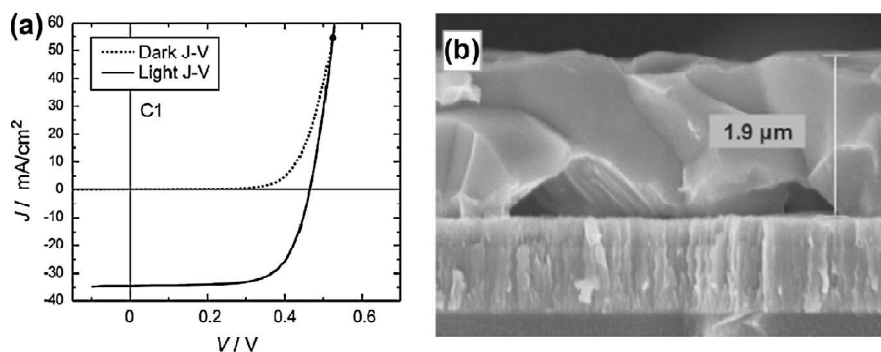
Figure 2.12. (a) J–V characteristics for 11.1% efficient record solar cell based on a soda lime glass/Mo/CZTSSe/CdS/ZnO/ITO structure and (b) SEM images of the cross section of a CZTSSe film on Mo-coated glass. Source: Barkhouse et al. (2012).

As in CIGS, also particle-based precursors have been examined (Todorov et al., 2009)[80]. Precursors, comprising reasonably uniform particles in the range of 200 nm have been obtained, but the needed organic binders hindered crystal growth. First devices with CZTS nanoparticles without or with post-deposition annealing in Se atmosphere at 500°C reached 0.23% or 0.74% efficiency, respectively (Steinhagen et al., 2009; Guo et al., 2009) [134,135]. Various synthesis routes for CZTS, CZTSe, and CZTS(e) solutions with nanoparticles and grains were presented (Rath et al., 2012; Shavel et al., 2010; Wei et al., 2010; Zhou et al., 2010) [202-205]. Mono-grain (MG) solar cells were developed, based on growth of high-quality CZTSSe crystals in KI melts, whereas every MG is coated by CdS, embedded in a single layer of organic resin, and individually contacted (Mellikov et al., 2011; Krustok et al., 2010; Mellikov et al., 2009; Timmo et al., 2010; Mellikov and et al., 2011) [121-206-208]. So far, the record performance of MG solar cells with a S/Se gradient was published to be 7.4% (Kauk et al., 2011), whereas the

technology is commercialized Austrian/Estonian company Crystalsol (http://www.crystalsol.at, December, 2012) [209].So far the most prominent technology is being developed at the IBM T.J. Watson Research Center, based on mixed inks of a combination of dissolved and solid components:(Emsley, 1998) To process CZTSSe, metal chalcogenides as well as elemental sulfur and selenium are dissolved in hydrazine solutions (Mitzi, 2009; Mitzi, 2009; Milliron et al., 2006; Mitzi et al., 2004; Mitzi et al., 2008) [84-88,209-211]. However, since ZnS(e) does not readily dissolve in hydrazine under ambient conditions, hybrid solution-particle inks were prepared by dissolving Cu_2S and SnS(e) in hydrazine and adding elemental zinc powder to the solution (Todorov et al., 2010) [80,81]. Via spin-coating of multiple layers of the solutions and a heat-treatment at temperature in excess of 500 ^{o}C, CZTSSe devices based on a soda limeglass/Mo/CZTSSe/CdS/ZnO/ITO structure have been prepared, leading to a up-to-date record power conversion efficiency for CZTSSe-based solar cells of 11.1% (Fig. 13) Todorov et al., 2012[79,82]. Regarding a manufacturable technology, the transfer of this approach from pure hydrazine solutions to more industry-friendly aqueous-based (diluted hydrazine) solvents, with device efficiencies reaching 8.1%, appears very important (Mitzi, 2010; Todorov et al., 2011) [81]. Very recently, a couple of publications on CZTS film formation based on the successive ionic layer adsorption and reaction (SILAR) method which have been presented by Su et al., 2012; Gao et al., 2012; Mali et al., 2012; Shinde et al., 2012; Lokhande et al., 2011 [45,212,215]. This method appears to be an especially simple and inexpensive method for the synthesis of large-area thin film photovoltaics. Nevertheless, so far presented device efficiencies are in the area of 1.85% (Mali et al., 2012) [214].

References:

1. Ehrenreich, Henry; Martin, John H. 1979 (Sept.)."Solar Photovoltaic Energy." Physics Today. Vol. 32 (No.9); pp. 25-32.
2. C.W. Tang, Appl. Phys. Lett. 48 (1986) 183.
3. M. Yamaguchi, "Super-High Efficiency III-V Tandem and Multijunction Cells", in Clean Electricity from Photovoltaics, M.D. Archer, R. Hill, eds., Imperial College Press, London, 2001; Vol. 1, Chapter 8, pp. 347–375.
4. W. Palz "Power for the World: The Emergence of Electricity from the Sun," Pan Stanford Publishing, 2010, DOI 10.4032/9789814303385.
5. P. Wurfel, "Physics of Solar Cells" 2nd edn, Wiley, Wiley VCH, Weinheim, 2007.
6. International Energy Agency, "World Energy Outlook 2011." 2011.
7. Greenpeace and the European Photovoltaic Industry Association, "Solar Generation VI," 2011.

8. European Climate Foundation, "Roadmap 2050, a practical guide to a prosperous, low-carbon Europe," 2010.

9. International Energy Agency, "Technology Roadmap, Solar photovoltaic energy," IEA, 2009.

10. A. Zaman and S. Lockman, "Solar industry growth: you ain't seen nothing yet. The grid parity decade," Piper Jaffray Investment Research, 2011.

11. D. Abou-Ras, G. Kostorz, D. Bremaud, M. K¨alin, F. V. Kurdesau, A. N. Tiwari, and M. D¨obeli, "Formation and characterisation of $MoSe_2$ for $Cu(In,Ga)Se_2$ based solar cells," Thin Solid Films, 480–481, no. 0, pp. 433–438, Jun. 2005.

12. R. J. Matson, O. Jamjoum, A. D. Buonaquisti, P. E. Russell, L. L. Kazmerski, P. Sheldon, and R. K. Ahrenkiel, "Metal contacts to $CuInSe_2$," Solar Cells, 11, no. 3, pp. 301–305, 1984.

13. T. Nakada, Y. Hirabayashi, T. Tokado, D. Ohmori, and T. Mise, "Novel device structure for $Cu(In,Ga)Se_2$ thin film solar cells using transparent conducting oxide back and front contacts," Solar Energy, 77, no. 6, pp. 739–747, 2004.

14. P. J. Rostan, J. Mattheis, G. Bilger, U. Rau, and J. H. Werner, "Formation of transparent and ohmic $ZnO:Al/MoSe_2$ contacts for bifacial $Cu(In,Ga)Se_2$ solar cells and tandem structures," Thin Solid Films, 480–481, pp. 67–70, Jun. 2005.

15. T. Nakada, "Microstructural and diffusion properties of CIGS thin film solar cells fabricated using transparent conducting oxide back contacts," Thin Solid Films, 480–481, no. 0, pp. 419–425, 2005.

16. J. Malmstrom, "On generation and recombination in $Cu(In,Ga)Se_2$ thin film solar cells," Uppsala University, Uppsala, Sweden, 2005.

17. G. Voorwinden, R. Kniese, and M. Powalla, "In-line $Cu(In,Ga)Se_2$ co-evaporation processes with graded band gaps on large substrates," Thin Solid Films, 431–432, no. 0, pp. 538–542, 2003.

18. E. Wallin, T. Jarmar, U. Malm, M. Edoff, and L. Stolt, "Influence of the average Se-to metal overpressure during co-evaporation of $Cu(In_xGa_{1-x})Se_2$," Thin Solid Films, 519, no. 21, pp. 7237–7240, 2011.

19. A. M. Gabor, J. R. Tuttle, M. H. Bode, A. Franz, A. L. Tennant, M. A. Contreras, R. Noufi, D. G. Jensen, and A. M. Hermann, "Band-gap engineering in Cu (In,Ga) Se_2 thin films grown from (In, Ga) $_2Se_3$ precursors," Solar Energy Materials and Solar Cells, 41, pp. 247–260, 1996.

20. A.E. Becquerel, Comt. Rend. Acad. Sci. 9 (1839) 561.

21. A. Goetzberger, J. Knobloch, B. Voss, Crystalline Silicon Solar Cells, Wiley, New York, 1998.

22. M.A. Green, Silicon Solar Cells: Advanced Principles and Practice, Bridge Printery, Sidney, 1995.

23. S. M. Schleussner, T. T¨orndahl, M. Linnarsson, U. Zimmermann, T. W¨atjen, and M. Edoff, "Development of gallium gradients in three-stage $Cu(In,Ga)Se_2$ co-evaporation processes," Progress in Photovoltaics: Research and Applications, 20, no. 3, pp. 284–293, 2012.

24. A. Brummer, V. Honkim¨aki, P. Berwian, V. Probst, J. Palm, and R. Hock, "Formation of $CuInSe_2$ by the annealing of stacked elemental layers—analysis by in situ high-energy powder diffraction," Thin Solid Films, 437, no. 1–2, pp. 297–307, Aug. 2003.

25. F. Hergert, S. Jost, R. Hock, and M. Purwins, "A crystallographic description of experimentally identified formation reactions of Cu(In,Ga)Se$_2$," Journal of Solid State Chemistry, 179, no. 8,pp. 2394–2415, Aug. 2006.

26. J. Lindahl, J. T. Ẅatjen, A. Hultqvist, T. Ericson, M. Edoff, and T. T̈orndahl, "The effect of Zn$_{1-x}$Sn$_x$O$_y$ buffer layer thickness in 18.0% efficient Cd-free Cu(In,Ga)Se$_2$ solar cells," Progress in Photovoltaics: Research and Applications, p. n/a–n/a, Jul. 2012.

27. D. Hariskos, S. Spiering, and M. Powalla, "Buffer layers in Cu(In,Ga)Se$_2$ solar cells and modules," Thin Solid Films, 480–481, pp. 99–109, 2005.

28. S. Siebentritt, "Alternative buffers for chalcopyrite solar cells," Solar Energy, 77, no. 6,pp. 767–775, Dec, 2004.

29. U. Rau and M. Schmidt, "Electronic properties of ZnO/CdS/Cu(In,Ga)Se$_2$ solar cells aspects of heterojunction formation," Thin Solid Films, 387, no.1–2, pp. 141–146, 2001.

30. P. O. Grabitz, U. Rau, and J. H. Werner, "Electronic in homogeneities and the role of the intrinsic ZnO layer in Cu(In,Ga)Se$_2$ thin film solar cells," in Proceedings of the 20th European Photovoltaic Solar Energy Conference, 2005, pp. 1771–1774.

31. N. Naghavi, G. Renou, V. Bockelee, F. Donsanti, P. Genevee, M. Jubault, J. F. Guillemoles, and D. Lincot, "Chemical deposition methods for Cd-free buffer layers in CI(G)S solar cells: Role of window layers," Thin Solid Films, 519, no. 21, pp. 7600–7605, 2011.

32. W.Walukiewicz, "Mechanism of Fermi-level stabilization in semiconductors," Physical Review B, 37, no. 9, pp. 4760–4763, 1988.

33. S. B. Zhang, S. H. Wei, and A. Zunger, "A phenomenological model for systematization and prediction of doping limits in II-VI and I-III-VI$_2$ compounds," Journal of Applied Physics, 83, p. 3192, 1998.

34. S. B. Zhang, S. H. Wei, A. Zunger, and H. Katayama-Yoshida, "Defect physics of the CuInSe$_2$ chalcopyrite semiconductor," Physical Review B, 57, no. 16, pp. 9642–9656, 1998.

35. K. Yoshino, H. Yokoyama, K. Maeda, T. Ikari, J. Cryst. Growth 211 (2000) 476.

36. Thin Films and Nanostructures Waveguide Spectroscopy of Thin Films,2005, Volume 33 I, Serial Editors Vladimir Agranovich, Author: Alexander Vasil'evich Khomchenko.

37. K.H. Kim, M.S. Kim, B.T. Ahn, J.H. Yun, K.H. Yoon, In: 4th World Conference on Photovoltaic Energy Conversion, 2006, p. 575. 37. Kazmerski L, White F, Morgan G, *Appl. Phys. Lett.* 29, 268, 269 (1976).

38. Mickelsen R, Chen W, *Proc. 15th IEEE Photovoltaic Specialist Conf.*, 800–804 (1981).

39. Mickelsen R, Chen W, *Proc. 16th IEEE Photovoltaic Specialist Conf.*, 781–785 (1982).

40. Chen W *et al.*, *Proc. 19th IEEE Photovoltaic Specialist Conf.*, 1445–1447 (1987).

41. Potter R, *Sol. Cells* 16, 521–527 (1986).

42. Hedstr¨om J *et al.*, *Proc. 23rd IEEE Photovoltaic Specialist Conf.*, 364–371 (1993).

43. Gabor A *et al.*, *Sol. Energy Mater. Sol. Cells* 4, 247–260 (1996).

44. Tarrant D, Ermer J, *Proc. 23rd IEEE Photovoltaic Specialist Conf.*, 372–375 (1993).

45. Lokhande, C., Shinde, N., Kim, J., Moon, J., 2011. Invertis J. Renew.Energy 1, 142.

46. Contreras M et al., Prog. Photovolt. 7, 311–316 (1999).

47. Wieting R, AIP Conf. Proc. 462, 3–8 (1999).

48. Burgess R et al., Proc. 20th IEEE Photovoltaic Specialist Conf., 909–912 (1988).

49. Jasenek A et al., Thin Solid Films 387, 228–230 (2001).

50. Hahn H et al., Z. Anorg. Allg. Chem. 271, 153–170 (1953).

51. Shay J, Wernick J, Ternary Chalcopyrite Semiconductors: Growth, Electronic Properties, and Application, Pergamon Press, Oxford (1974).

52. Tell B, Shay J, Kasper H, Phys. Rev. B4, 4455–4459 (1971).

53. Tell B, Shay J, Kasper H, J. Appl. Phys. 43, 2469, 2470 (1972).

54. Wagner S, Shay J, Migliorato P, Kasper H, Appl. Phys. Lett. 25, 434, 435 (1974).

55. Shay J, Wagner S, Kasper H, Appl. Phys. Lett. 27, 89–90 (1975).

56. Meakin J, Proc. SPIE Conf. 543: Photovoltaics, 108–118 (1985).

57. Kazmerski L, White F, Morgan G, Appl. Phys. Lett. 29, 268, 269 (1976).

58. Mickelsen R, Chen W, Proc. 15th IEEE Photovoltaic Specialist Conf., 800–804 (1981).

59. Mickelsen R, Chen W, Proc. 16th IEEE Photovoltaic Specialist Conf., 781–785 (1982).

60. Chen W et al., Proc. 19th IEEE Photovoltaic Specialist Conf., 1445–1447 (1987).

61. Potter R, Sol. Cells 16, 521–527 (1986).

62. Hedstr¨om J et al., Proc. 23rd IEEE Photovoltaic Specialist Conf., 364–371 (1993).

63. Gabor A et al., Sol. Energy Mater. Sol. Cells 4, 247–260 (1996).

64. Tarrant D, Ermer J, Proc. 23rd IEEE Photovoltaic Specialist Conf., 372–375 (1993).

65. Kazmerski, L.L., White, F.R., Morgan, G.K., 1976. Appl. Phys. Lett. 29,268.

66. Wolden, C.A., Kurtin, J., Baxter, J.B., Repins, I., Shaheen, S.E., Torvik, J.T., Rockett, A.A., Fthenakis, V.M., Aydil, E.S., 2011. Photovoltaic manufacturing: present status, future prospects, and research needs. J.Vac. Sci. Technol. A 29, 030801.

67. Kurihara, M., Berg, D., Fischer, J., Siebentritt, S., Dale, P.J., 2009. Kesterite absorber layer uniformity from electrodeposited pre-cursors.Phys. Status Solidi C 6, 1241.

68. Hedstro¨m, J., Ohlsen, H., Bodegard, M., Kylner, A., Stolt, L., Hariskos, D., Ruckh, M., Schock, H.W., 1993. ZnO/CdS/Cu(In,Ga)Se$_2$ thin film solar cells with improved performance. In: Proceedings of the 23rd IEEE Photovoltaic Specialists Conference, 1993, p. 364.

69. Granath, K., Bodegard, M., Stolt, L., 2000. The effect of NaF on Cu(In,Ga)Se$_2$ thin film solar cells. Sol. Energy Mater. Sol. Cells 60, 279.

70. Ruckh, M., Schmid, D., Kaiser, M., Scha¨ffler, R., Walter, T., Schock, H.W., 1994. Influence of substrates on the electrical properties of Cu(In,Ga)Se$_2$ thin films. In: Proceedings of the 1994 IEEE First World Conference on Photovoltaic, Energy Conversion, 1994, p.156.

71. Panthani, M.G., Akhavan, V., Goodfellow, B., Schmidtke, J.P., Dunn, L., Dodabalapur, A., Barbara, P.F., Korgel, B.A., 2008. J. Am. Chem. Soc. 130, 16770.

72. Green, M.A., Emery, K., Hishikawa, Y., Warta, W., Dunlop, E.D., 2012. Solar cell efficiency tables (version 39). Prog. Photovolt: Res. Appl. 20,12.

73. Sugimoto, H., Kawaguchi, Y., Yasaki, Y., Aramoto, T., Tanaka, Y., Hakuma, H., Kuriyagawa, S., Kushiya, K. 2011. Challenge to 18% efficiency with 30*30 cm^2-sized.

74. Cu(InGa)(SeS)$_2$ submodules in Solar Frontier. In: 26th European Photovoltaic Solar Energy Conference and Exhibition, Hamburg, 2011.

75. Tiwari, A.N., Lincot, D., Contreras, M., 2010. Prog. Photovolt. 18, 389

76. Gabor, A.M., Tuttle, J.R., Albin, D.S., Contreras, M.A., Noufi, R.,Herman, A.M., 1994. Appl. Phys. Lett. 65, 198.

77. Hibberd, C.J., Chassaing, E., Liu, W., Mitzi, D.B., Lincot, D., Tiwari, A.N., 2010. Non-vacuum methods for formation of Cu(In, Ga)(Se, S)$_2$ thin film photovoltaic absorbers. Prog. Photovolt. 18 (6), 434.

78. Bhattacharya, R.N., Hiltner, J.F., Batchelor, W., Contreras, M.A., Noufi, R.N., Sites, J.R., 2000. 15.4% CuIn$_{1-x}$Ga$_x$Se$_2$-based photovoltaic cells from solution-based precursor films. Thin Solid Films 361, 396.

79. Bhattacharya, R.N., Batchelor, W., Ramanathan, K., Contreras, M.A., Moriarty, T., 2000. Sol. Energy Mater. Sol. Cells 63, 367.

80. Todorov, T.K., Gunawan, O., Gokmen, T., Mitzi, D.B., 2012. Solution processed Cu(In,Ga)(S,Se)$_2$ absorber yielding a 15.2% efficient solar cell. Prog. Photovolt: Res. Appl., 1253.

81. Todorov, T., Mitzi, D.B., 2010. Direct liquid coating of chalcopyrite light absorbing layers for photovoltaic devices. Eur. J. Inorg. Chem. 2010, 17.

82. Todorov, T., Reuter, K.B., Mitzi, D.B., 2010. High-efficiency solar cell with earth-abundant liquid-processed absorber. Adv. Mater. 22, E156.

83. Todorov, T.K., Tang, J., Bag, S., Gunawan, O., Gokmen, T., Zhu, Y.,Mitzi, D.B., 2012. Beyond 11% efficiency: characteristics of state-ofthe-art Cu$_2$ZnSn(S,Se)$_4$ solar cells. Adv. Energy Mater.

84. Habas, S.E., Platt, H.A.S., van Hest, M.F.A.M., Ginley, D.S., 2010. Lowcost inorganic solar cells: from Ink to printed device. Chem. Rev. 110, 6571.

85. Mitzi, D.B., Kosbar, L.L., Murray, C.E., Copel, M., Afzali, A., 2004. High-mobility ultrathin semiconducting films prepared by spin coating. Nature 428, 299.

86. Mitzi, D.B., Yuan, M., Liu, W., Kellock, A.J., Chey, S.J., Deline, V., Schrott, A.G., 2008. A high-efficiency solution-deposited thin-film photovoltaic device. Adv. Mater. 20, 3657.

87. Mitzi, D.B., 2009. Adv. Mater. 21, 3141.

88. Mitzi, D.B. (Ed.), 2009. Solution Processing of Inorganic Materials. John Wiley & Sons, Inc., Hoboken, New Jersey.

89. Mitzi, D.B., Gunawan, O., Todorov, T.K., Wang, K., Guha, S., 2011. The path towards a high-performance solution-processed kesterite solar cell. Sol. Energy Mater. Solar Cells 95, 1421.

90. Wang, H., 2011. Progress in thin film solar cells based on Cu_2ZnSnS_4. Int.J. Photoenergy, 801292.

91. van Hest, M., Ginley, D., 2009. In: Mitzi, D.B. (Ed.), Solution Processing of Inorganic Materials. John Wiley & Sons, Inc., Hoboken, New Jersey.

92. Jorgensen, M., Norrman, K., Krebs, F.C., 2008. Sol. Energy Mater. Sol.Cells 92, 686.

93. Steirer, K.X. et al., 2009. Sol. Energy Mater. Sol. Cells 93, 447.

94. Hoth, C.N., Choulis, S.A., Schilinsky, P., Brabec, C.J., 2007. High photovoltaic performance of inkjet printed polymer:fullerene blends. Adv. Mater. 19, 3973.

95. Wagner, S., Shay, J.L., Migliorato, P., 1974. Appl. Phys. Lett. 25, 434.

96. Haight, R., Barkhouse, A., Gunawan, O., Shin, B., Copel, M., Hopstaken, M., Mitzi, D.B., 2011. Appl. Phys. Lett. 98, 253502.

97. Schorr, S., 2011. Energy Mater. Sol. Cells 95, 1482.

98. Siebentritt, S., Schorr, S., 2012. Prog. Photovolt: Res. Appl. 20, 512.

99. Emsley, J., 1998. The Elements, third ed. Oxford Univ. Press, Oxford, p.289.

100. Katagiri, H., Jimbo, K., Maw, W.S., Oishi, K., Yamazaki, M., Araki, H., Takeuchi, A., 2009. Development of CZTS-based thin film solar cells. Thin Solid Films 517, 2455.

101. Katagiri, H., Jimbo, K., Tahara, M., Araki, H., Oishi, K., 2009. The influence of the composition ratio on CZTS-based thin film solar cells. In: Materials Research Society Symposium Proceedings, 2009, p. 1165.

102. Delbos, S., 2012. Kesterite thin films for photovoltaics: a review. EPJ Photovolt. 3, 35004.

103. Ito, K., Nakazawa, T., 1988. Electrical and optical properties of stannite type quaternary semiconductor thin films. Jpn. J. Appl. Phys. 27, 2094.

104. Chan, C.P., Lam, H., Surya, C., 2010. Preparation of Cu_2ZnSnS_4 films by electrodeposition using ionic liquids. Sol. Energy Mater. Sol. Cells 94, 207.

105. Friedlmeier, T.M., Wieser, N., Walter, T., Dittrich, H., Schock, H.W., 1997. In: 14th European Photovoltaic Solar Energy Conference, Barcelona, 1997.

106. Altosaar, M., Raudoja, J., Timmo, K., Danilson, M., Grossberg, M., Krustok, J., Mellikov, E., 2008. Phys. Status Solidi A 205, 167.

107. Chen, S., Gong, X.G., Walsh, A., Wei, S.H., 2009. Appl. Phys. Lett. 94, 041903.

108. Chen, S., Yang, J.-H., Gong, X.G., Walsh, A., Wei, S.-H., 2010. Intrinsic point defects and complexes in the quaternary kesterite semiconductor Cu_2ZnSnS_4. Phys. Rev. B 81, 245204.

109. Chen, S., Gong, X.G., Walsh, A., Wei, S.H., 2010. Appl. Phys. Lett. 96, 021902.

110. Moynihan, M., Zoppi, G., Miles, R., Forbes, I., 2011. Investigating synthesis of $Cu_2ZnSn(Se_{1-x},S_x)_4$ for values of 0 6 x 6 1 by S for Se substitution and direct sulphurisation of metallic precursors. In: Proceedings of the 26th European Photovoltaic Solar Energy Conference, Hamburg, 2011.

111. Ganchev, M., Iljina, J., Kaupmees, L., Raadik, T., Volobujeva, O., Mere, A., Altosaar, M., Raudoja, J., Mellikov, E., 2011. Thin Solid Films 519, 7394.

112. Kamoun, N., Bouzouita, H., Rezig, B., 2007. Thin Solid Films 515, 5949. Ganchev, M., Kaupmees, L., Iliyna, J., Raudoja, J., Volobujeva, O., Dikov, H., Altosaar, M., Mellikov, E., Varema, T., 2010. Formation of $Cu_2ZnSnSe_4$ thin films by selenization of electrodeposited stacked binary alloy layers. Energy Proced. 2, 65.

113. Tanaka, T., Nagatomo, T., Kawasaki, D., Nishio, M., Guo, Q.X., Wakahara, A., Yoshida, A., Ogawa, H., 2005. J. Phys. Chem. Solids 66, 1978.

114. Tanaka, N., Moritake, H., 2007. Uchiki, preparation of Cu_2ZnSnS_4 thin films by sulfurizing sol–gel deposited precursors. Sol. Energy Mater. Sol. Cells 91, 1199.

115. Moriya, K., Watabe, J., Tanaka, K., Uchiki, H., 2006. Phys. Status Solidi C 3, 2848.

116. Scragg, J.J., Dale, P.J., Peter, L.M., 2008. Electrochem. Commun. 10, 639.

117. Scragg, J.J. et al., 2008. New routes to sustainable photovoltaics: evaluation of Cu_2ZnSnS_4 as an alternative absorber material. Phys. Status Solidi B – Basic Sol. State Phys. 245, 1772.

118. Scragg, J.J., Berg, D.M., Dale, P.J., 2010. A 3.2% efficient Kesterite device from electrodeposited stacked elemental layers. J. Electroan. Chem.646, 52.

119. Scragg, J.J., 2010. Solution processing of inorganic materials. PhD thesis, University of Bath, Department of Chemistry, 2010.

120. Scragg, J.J., Wa¨tjen, J.T., Edoff, M., Ericson, T., Kubart, T., Platzer- Bjo¨rkman, C., 2012. A detrimental reaction at the molybdenum back contact in $Cu_{(2)}ZnSn(S,Se)_{(4)}$ thin-film solar cells. J. Am. Chem. Soc.134, 19330.

121. Shockley, W., Queisser, H.J., 1961. Detailed balance limit of efficiency of p–n junction solar cells. J. Appl. Phys. 32, 510.

122. Timmo, K., Altosaar, M., Raudoja, J., Muska, K., Pilvet, M., Kauk, M., Varema, T., Danilson, M., Volobujeva, O., Mellikov, E., 2010. Sulfur containing $Cu_2ZnSnSe_4$ monograin powders for solar cells. Sol.Energy Mater. Sol. Cells. 94, 1889.

123. Choubrac, L., Lafond, A., Guillot-Deudon, C., Moelo, Y., Jobic, S., 2012. Inorg. Chem. 51, 3346.

124. Katagiri, H., Sasaguchi, N., Hando, S., Hoshino, S., Ohashi, J., Yokota, T., 1997. Preparation and evaluation of Cu_2ZnSnS_4 thin films by sulfurization of E-B evaporated precursors. Sol. Energy Mater. Sol.Cells 49, 407.

125. Katagiri, H., Ishigaki, N., Ishida, T., Saito, K., 2001. Characterization of Cu_2ZnSnS_4 Thin Films Prepared by Vapor Phase Sulfurization. Jpn. J. Appl. Phys. 40, 500

126. Katagiri, H., 2005. Cu_2ZnSnS_4 thin film solar cells. Thin Solid Films 480–481, 426.

127. Katagiri, H., Jimbo, K., Maw, W.S., Oishi, K., Yamazaki, M., Araki, H., Takeuchi, A., 2009. Development of CZTS-based thin film solar cells. Thin Solid Films 517, 2455.

128. Katagiri, H., Jimbo, K., Tahara, M., Araki, H., Oishi, K., 2009. The influence of the composition ratio on CZTS-based thin film solar cells. In: Materials Research Society Symposium Proceedings, 2009, p. 1165.

129. Jimbo, K., Kimura, R., Kamimura, T., Yamada, S., Maw, W., Araki, H., Oishi, K., Katagiri, H., 2007. Cu2ZnSnS4-type thin film solar cells using abundant materials. Thin Solid Films 515, 5997.

130. Repins, I. et al., 2012. Sol. Energy Mater. Sol. Cells 101, 154.

131. Repins, I., et al., 2011. Kesterites and chalcopyrites: a comparison of close cousins. In: MRS Proceedings, 2011, p. 1324.

132. Deligianni, H., Guo, L., Vaidyanathan, R., 2012. Electrodeposition of thin-film cells containing non-toxic elements. US Patent, United States Patent Application 2012004837803, 2012.

133. Ahmed, S., Reuter, K.B., Gunawan, O., Guo, L., Romankiw, L.T., Deligianni, H., 2012. A high efficiency electrodeposited Cu2ZnSnS4 solar cell. Adv. Energy Mater., 253.

134. Guo, Q., Ford, G.M., Yang, W.C., Walker, B.C., Stach, E.A., Hillhouse, H.W., Agrawal, R., 2010. J. Am. Chem. Soc. 132, 2844.

135. Guo, Q., Hillhouse, H.W., Agrawal, R., 2009. Synthesis of Cu_2ZnSnS_4 nanocrystal and its use for solar cells. J. Am. Chem. Soc. 131, 11672.

136. Steinhagen, C., Panthani, M.G., Akhavan, V., Goodfellow, B., Koo, B., Korgel, B.A., 2009. Synthesis of $Cu_{(2)}ZnSnS_{(4)}$ nanocrystals for use in low-cost photovoltaics. J. Am. Chem. Soc. 131 (35), 12554.

137. Kumar, Y.B.K., Babu, G.S., Bhaskar, P.U., Raja, V.S., 2009. Preparation and characterization of spray-deposited Cu_2ZnSnS_4 thin films. Sol. Energy Mater. Sol. Cells 93, 1230.

138. Kumar, Y.B.K., Bhaskar, P.U., Babu, G.S., Raja, V.S., 2010. Effect of copper salt and thiourea concentrations on the formation of Cu_2ZnSnS_4 thin films by spray pyrolysis. Phys. Status Solidi A 207, 149.

139. Fella, C.M., Ilari, G., Uhl, A.R., Romanyuk, Y.E., Seyrling, S., Chirila, A., Tiwari, A.N., 2011. In: Proceedings of the 26th European Photovoltaic Solar Energy Conference, Hamburg, 2011.

140. Barkhouse, D.A.R., Gunawan, O., Gokmen, T., Todorov, T.K., Mitzi, D.B., 2012. Prog. Photovol. Res. Appl. 20, 6.

141. Bag, S., Gunawan, O., Gokmen, T., Zhu, Y., Todorov, T.K., Mitzi, D.B., 2012. Energy Environ. Sci. 5, 7060.

142. Redinger, A., Ho¨nes, K., Fontane´, X., Izquierdo-Roca, V., Saucedo, E., Valle, N., Pe´rez-Rodrı´guez, A., Siebentritt, S., 2011. Detection of a ZnSe secondary phase in coevaporated $Cu_2ZnSnSe_4$ thin films. Appl. Phys. Lett. 98, 101907.

143. Redinger, A., Berg, D.M., Dale, P.J., Siebentritt, S., 2011. J. Am. Chem. Soc. 133, 3320.

144. Redinger, A., Siebentritt, S., 2010. Appl. Phys. Lett. 97, 092111.

145. Riha, S.C., Parkinson, B.A., Prieto, A.L., 2009. Am. Chem. Soc. 131, 12054.

146. Hall, S.R., Szymanski, J.T., Stewart, J.M., 1978. Kesterite, Cu(Zn,Fe)SnS$_4$, and stannite, Cu$_2$(Fe, Zn)SnS structurally similar but distinct minerals. Can. Mineral. 16, 131.

147. Bernardini, G.P., Borrini, D., Caneschi, A., Di Benedetto, F., Gatteschi, D., Ristori, D., Romanelli, M., 2000. EPR and SQUID magnetometry study of Cu$_2$FeSnS (stannite) and Cu$_2$ZnSnS$_4$ (kesterite). Phys. Chem.Min. 27, 453.

148. Raulot, J.M., Domain, C., Guillemoles, J.F., 2005. Ab initio investigation of potential indium and gallium free chalcopyrite compounds for photovoltaic application. J. Phys. Chem. Solids 66, 2019.

149. Paier, J., Asahi, R., Nagoya, A., Kresse, G., 2009. Cu$_2$ZnSnS$_4$ as a potential photovoltaic material: a hybrid Hartree-Fock density functional theory study. Phys. Rev. B 79, 115126.

150. Persson, C., 2010. Electronic and optical properties of Cu$_2$ZnSnS$_4$ and Cu$_2$ZnSnSe$_4$. J. Appl. Phys. 107, 053710.

151. Shay, J.L., Wernick, J.H., 1975. Ternary Chalcopyrite Semiconductors: Growth, Electronic Properties, and Application. Pergamon Press, Oxford.

152. Nagoya, A., Asahi, R., Wahl, R., Kresse, G., 2010. Defect formation and phase stability of Cu$_2$ZnSnS$_4$ photovoltaic material. Phys. Rev. B 81,113202.

153. Biswas, K., Lany, S., Zunger, A., 2010. The electronic consequences of multivalent elements in inorganic solar absorbers: multivalency of Sn in Cu$_2$ZnSnS$_4$. Appl. Phys. Lett. 96, 201902.

154. Siebentritt, S., Igalson, M., Persson, C., Lany, S., 2010. The electronic structure of chalcopyrites-bands, point defects and grain boundaries.Prog. Photovolt.: Res. Appl. 18, 390.

155. Olekseyuk, I.D., Dudchak, I.V., Piskach, L.V., 2004. Phase equilibria in the Cu$_2$S–ZnS–SnS system. J. Alloys Compd. 368, 135.

156. Dudchak, I.V., Piskach, L.V., 2003. Phase equilibria in the Cu$_2$SnSe$_3$–SnSe–ZnSe system. J. Alloys Compd. 351, 145.

157. Go¨decke, T., Haalboom, T., Ernst, F., 2000. Phase equilibria of Cu-InSeI: stable states and non-equilibrium states of the InCuSe subsystem. Zeitschrift fu¨ r Metallkunde 91, 622.

158. Razykov, T.M., Ferekides, C.S., Morel, D., Stefanakos, E., Ullal, H.S.,Upadhyaya, H.M., 2011. Sol. Energy 85, 1580.

159. Washio, T., Nozaki, H., Fukano, T., Motohiro, T., Jimbo, K., Katagiri, H., 2011. J. Appl. Phys. 110, 074511.

160. Washio, T., Shinji, T., Tajima, S., Fukano, T., Motohiro, T., Jimbo, K., Katagiri, H., 2012. 6% Efficiency Cu$_2$ZnSnS$_4$-based thin film solar cells using oxide precursors by open atmosphere type CVD. J. Mater.Chem. 22, 4021.

161. Volobujeva, O., Raudoja, J., Mellikov, E., Grossberg, M., Bereznev, S., Traksmaa, R., 2009. J. Phys. Chem. Solids 70, 567.

162. Schurr, R. et al., 2009. Thin Solid Films 517, 2465.

163. Ge, J., Wu, Y., Zhang, C., Zuo, S., Jiang, J., Ma, J., Yang, P., Chu, J., 2012. Appl. Surf. Sci. 258, 7250.

164. Maeda, K., Tanaka, K., Fukui, Y., Uchiki, H., 2011. Sol. Energy Mater. Sol. Cells 95, 2855.

165. Muska, K., Kauk, M., Altosaar, M., Pilvet, M., Grossberg, M., Volobujeva, O., 2011. Energy Proced. 10, 203.

166. Weber, A., Mainz, R., Schock, H.W., 2010. J. Appl. Phys. 107, 013516.

167. Yoo, H., Kim, J., Zhang, L., 2012. Curr. Appl. Phys. 12, 1052.

168. Salome, P.M.P., Malaquias, J., Fernandes, P.A., Ferreira, M.S., da Cunha, A.F., Leitao, J.P., Gonzalez, J.C., Matinaga, F.M., 2012. Sol.Energy Mater. Sol. Cells 101, 147.

169. Biccari, F., Chierchia, R., Valentini, M., Mangiapane, P., Salza, E., Malerba, C., Ricardo, C.L.A., Mannarino, L., Scardi, P., Mittiga, A., 2011. Energy Proced. 10, 187.

170. Yoo, H., Kim, J.-H., 2011. Comparative study of Cu_2ZnSnS_4 film growth. Sol. Energy Mater. Sol. Cells 95, 239.

171. Araki, H. et al., 2008. Preparation of Cu_2ZnSnS_4 thin films by sulfurization of stacked metallic layers. Thin Solid Films 517, 1457.

172. Araki, H., Kubo, Y., Mikaduki, A., Jimbo, K., Maw, W.S., Katagiri, H.,Yamazaki, M., Oishi, K., Takeuchi, A., 2009. Preparation of Cu_2ZnSnS_4 thin films by sulfurizing electroplated precursors. Sol.Energy Mater. Sol. Cells 93, 996.

173. Bhattacharya, R., 2009. In: Mitzi, D.B. (Ed.), Solution Processing of Inorganic Materials. John Wiley & Sons, Inc., Hoboken, New Jersey.

174. Hodes, G., 1995. In: Rubinstein, I. (Ed.), Physical Electrochemistry. Marcel Dekker, New York, NY, p. 515.

175. Schlesinger, M., Paunovic, M. (Eds.), 2000. Modern Electroplating. John Wiley and Sons, New York, NY, p. 585.

176. Lincot, D. et al., 2004. Sol. Energy 77, 725.

177. Razykov, T.M., Ferekides, C.S., Morel, D., Stefanakos, E., Ullal, H.S.,Upadhyaya, H.M., 2011. Sol. Energy 85, 1580.

178. Bhattacharya, R.N., Batchelor, W., Hiltner, J.F., Sites, J.R., 1999. Appl.Phys. Lett. 75, 1431.

179. Hideaki, A. et al., 2009. Preparation of $Cu_2 ZnSnS_4$ thin films by sulfurization of co-electroplated Cu–Zn–Sn precursors. Phys. Status Solidi (C) 6, 1266.

180. Ennaoui, A., Lux-Steiner, M., Weber, A., Abou-Ras, D., Ko¨tschau, I., Schock, H.-W., Schurr, R., Ho¨lzing, A., Jost, S., Hock, R., Vos, T., Schulze, J., Kirbs, A., 2009. Cu_2ZnSnS_4 thin film solar cells from electroplated precursors: novel low-cost perspective. Thin Solid Films 517, 2511.

181. Patil, P.S., 1999. Mater. Chem. Phys. 59, 185. Pawar, S.M., Pawar, B.S., Moholkar, A.V., Choi, D.S., Yun, J.H., Moon, J.H., Kolekar, S.S., Kim, J.H., 2010a. Single step electrosynthesis of Cu_2ZnSnS_4 (CZTS) thin films for solar cell application. Electrochim. Acta 55, 4057.

182. Pawar, B.S., Pawar, S.M., Shin, S.W., Choi, D.S., Park, C.J., Kolekar, S.S., Kim, J.H., 2010b. Appl. Surf. Sci. 257, 1786.

183. Cui, Y.F., Zuo, S.H., Jiang, J.C., Yuan, S.Z., Chu, J.H., 2011. Synthesis and characterization of co-electroplated Cu_2ZnSnS_4 thin films as potential photovoltaic material. Sol. Energy Mater. Sol. Cells 95, 2136.

184. Septina, W., Ikeda, S., Kyoraiseki, A., Harada, T., Matsumura, M., 2013. Single-step electrodeposition of a microcrystalline $Cu_2ZnSnSe_4$ thin film with a kesterite structure. Electrochim. Acta 88, 4036.

185. Gea, J., Zuob, S., Jiangb, J., Mab, J., Yangb, L., Yanga, P., Chua, J., 2012. Investigation of Se supply for the growth of $Cu_2ZnSn(S_xSe_{1-x})_4$ (x = 0.02–0.05) thin films for photovoltaics. Appl. Surf. Sci. 258, 7844

186. Jeon, M., Tanaka, Y., Shimizu, T., Shingubara, S., 2011a. Formation and characterization of single-step electrodeposited Cu_2ZnSnS_4 thin films: effect of complexing agent volume. Energy Proced. 10, 255. Jeon, M., Shimizu, T., Shingubara, S., 2011b. Mater. Lett. 65, 2364.

187. Li, J., Zhang, Z.W., Ou, Y., Liu, W.F., Jiang, G.S., Zhu, C.F., 2011. Mater. Sci. Forum 685, 105.

188. Li, J., Ma, T., Wei, M., Liu, W.F., Jiang, G.S., Zhu, C.F., 2012. The $Cu_2ZnSnSe_4$ thin films solar cells synthesized by electrodeposition route. Appl. Surf. Sci. 258, 6261.

189. Jusˇkeˇnas, R., Kanapeckaiteˇ, S., Karpavicˇieneˇ, V., Mockus, Z., Paksˇtas, V., Selskieneˇ, A., Giraitis, R., Niaura, G., 2012. A two-step approach for electrochemical deposition of Cu–Zn–Sn and Se precursors for CZTSe solar cells. Sol. Energy Mater. Sol. Cells 101, 277.

190. Sarswat, P.K., Snure, M., Free, M.L., Tiwari, A., 2012. CZTS thin films on transparent conducting electrodes by electrochemical technique. Thin Solid Films 520, 1694.

191. Zhang, X., Shi, X., Ye, W., Ma, C., Wang, C., 2009. Appl. Phys. A 94,381.

192. Kapur, V.K., Basol, B.M., Tseng, E.S., 1987. Sol. Cells 21, 65.

193. Kapur, V.K., Bansal, A., Le, P., Asensio, O.I., 2003. Thin Solid Films 431–432, 53.

194. Nakayama, N., Ito, K., 1996. Sprayed films of stannite Cu_2ZnSnS_4. Appl. Surf. Sci. 92, 171.

195. Madarasz, J., Bombicz, P., Okuya, M., Kaneko, S., 2001. Thermal decomposition of thiourea complexes of Cu(I), Zn(II), and Sn(II) chlorides as precursors for the spray pyrolysis deposition of sulfide thin films. Solid State Ionics 141–142, 439.

196. Rajeshmon, V.G., Kartha, C.S., Vijayakumar, K.P., Sanjeeviraja, C.,Abe, T., Kashiwaba, Y., 2011. Role of precursor solution in controlling the opto-electronic properties of spray pyrolysed Cu_2ZnSnS_4 thin films. Sol. Energy 85, 249.

197. Fischereder, A., Rath, T., Haas, W., Amenitsch, H., Albering, J., Meischler, D., Larissegger, S., Edler, M., Saf, R., Hofer, F., Trimmel, G., 2010. Investigation of Cu_2ZnSnS_4 formation from metal salts and thioacetamide. Chem. Mater. 22, 3399.

198. Edler, M., Rath, T., Schenka, A., Fischereder, A., Haas, W., Edler, M., Chernev, B., Kunert, B., Hofer, F., Reseld, R., Trimmel, G., 2012.Copper zinc tin sulfide layers prepared from solution processable metal dithiocarbamate precursors. Mater. Chem. Phys. 136, 582.

199. Ilari, G.M., Fella, C.M., Ziegler, C., Uhl, A.R., Romanyuk, Y.E., Tiwari, A.N., 2012. $Cu_2ZnSnSe_4$ solar cell absorbers spin-coated from amine-containing ether solutions. Sol. Energy Mater. Sol. Cells 104, 125.

200. Moritake, N., Fukui, Y., Oonuki, M., Tanaka, K., Uchiki, H., 2009. Preparation of Cu_2ZnSnS_4 thin film solar cells under non-vacuum condition. Phys. Status Solidi C 6, 1233.

201. Woo, K., Kim, Y., Moon, J., 2012. Energy Environ. Sci. 5, 5340.

202. Rath, T., Haas, W., Pein, A., Saf, R., Maier, E., Kunert, B., Hofer, F.,Resel, R., Trimmel, G., 2012. Synthesis and characterization of copper zinc tin chalcogenide nanoparticles: influence of reactants on the chemical composition. Sol. Energy Mater. Sol. Cells 101, 87.

203. Shavel, A., Arbiol, J., Cabot, A., 2010. Synthesis of quaternary chalcogenide nanocrystals: stannite $Cu_2Zn_xSnySe_{1+x+2y}$. J. Am. Chem. Soc.132, 4514.

204. Wei, H., Guo, W., Sun, Y., Yang, Z., Zhang, Y., 2010. Hot-injection synthesis and characterization of quaternary $Cu_2ZnSnSe_4$ nanocrystals. Mater. Lett. 64, 1424.

205. Zhou, Z., Wang, Y., Xu, D., Zhang, Y., 2010. Fabrication of Cu_2ZnSnS_4 screen printed layers for solar cells. Sol. Energy Mater. Sol. Cells 94, 2042.

206. Mellikov, E. et al., 2011. Materials challenges in alternative and renewable energy. Ceram. Trans. 224, 137.

207. Mellikov, E., Meissner, D., Varema, T., Altosaar, M., Kauk, M., Volobujeva, O., Raudoja, J., Timmo, K., Danilson, M., 2009. Monograin materials for solar cells. Sol. Energy Mater. Sol. Cells 93, 65.

208. Krustok, J., Josepson, R., Danilson, M., Meissner, D., 2010. Temperature dependence of $Cu_2ZnSn(Se_xS_{1-x})_4$ monograin solar cells. Sol. Energy 84, 379.

209. Kauk, M., Muska, K., Altosaar, M., Raudoja, J., Pilvet, M., Varema, T., Timmo, K., Volobujeva, O., 2011. Energy Proced. 10, 197.

210. Emsley, J., 1998. The Elements, third ed. Oxford Univ. Press, Oxford, p.289.

211. Milliron, D.J., Mitzi, D.B., Copel, M., Murray, C.E., 2006. Solution processed metal chalcogenide films for p-type transistors. Chem.Mater. 18, 587.

212. Su, Z., Yan, C., Sun, K., Han, Z., Liu, F., Liu, J., Lai, Y., Li, J., Liu, Y., 2012. Preparation of Cu_2ZnSnS_4 thin films by sulfurizing stacked precursor thin films via successive ionic layer adsorption and reaction method. Appl. Surf. Sci. 258, 7678.

213. Gao, C., Shen, H., Jiang, F., Guan, H., 2012. Preparation of Cu_2ZnSnS_4 film by sulfurizing solution deposited precursors. Appl. Surf. Sci. 261, 189.

214. Mali, S.S., Shinde, P.S., Betty, C.A., Bhosale, P.N., Woo Oh, Y., Patila, P.S., 2012. Synthesis and characterization of Cu_2ZnSnS_4 thin films by SILAR method. J. Phys. Chem. Sol. 73, 735.

215. Shinde, N.M., Dubal, D.P., Dhawale, D.S., Lokhande, C.D., Kim, J.H.,Moon, J.H., 2012. Room temperature novel chemical synthesis of Cu_2ZnSnS_4 (CZTS) absorbing layer for photovoltaic application Mater. Res. Bull. 47, 302.

Chapter 3. Experimental Techniques, Methodology and Characterization

3.1. Experimental Techniquesand Methodology

3.1.1. Electrochemical Deposition (Electrodeposition)

The electrodeposition technique has significant advantages over other methods for synthesizing nanocrystalline materials: (1) potential of synthesizing large variety of nanograin materials—pure metals, alloys and composite systems with grain sizes as small as 20 nm, (2) low investment, (3) high production rates, (4) few size and shape limitations, and (5) high probability of transferring this technology to existing electroplating and electroforming industries.

Figure 3.1. (a) Auto lab control.

In an electrochemical cell, two conductive electrodes are immersed in an electrolyte containing a certain concentration of a reducible or oxidizable component. Additionally, a large background concentration of inert ions is provided to ensure good electrical conductivity in the solution. The electrodes are connected to an external, controllable voltage (potential difference), and when a sufficient potential difference, E, is applied between them, a current may flow.

The three-electrode cell setup is the most common electrochemical cell setup used in electrochemistry (Figure 3.1). upon the immersion of the electrodes in the electrolyte, the difference of chemical potential between those electrons of the electrode and the others of the solution phase means that there is a certain amount of electron transfer, which occurs until the chemical potential in both phases is equalized. This creates a net charge at the surface of the metal electrode, which is compensated by an accumulation at the interface of ions from the electrolyte, forming what is known as the Helmholtz layer. The potential drop across this layer cannot be measured directly; any physical probe used to do so would also have an unknown

potential drop at its own surface. Because of this fact, we can only ever measure differences in electrode potential, rather than absolute values. Potentials must therefore always be quoted with respect to some reference. Any two dissimilar materials immersed in an electrolyte will develop a potential difference between them, which may change if electrochemical processes cause alterations to their surfaces. Since in the above case of Cu deposition, both electrodes underwent changes as the reaction progressed, the potential difference between them will vary. In order to maintain a steady reference point, we introduce a third electrode, a 'reference' electrode, which is a well-defined system containing a redox couple which adopts a constant potential difference. The potential difference between the two other electrodes is defined and controlled with respect to the potential of the reference (Fig. 3.1). We rename these other two electrodes as the 'working electrode', which is the site of the electrochemical reaction of interest, and to which is applied the desired potential, and the 'counter electrode', which is present only to support the current flow and to which is applied whatever potential is necessary to do this. Current flows only between the working and counter electrodes to ensure that there are no chemical changes in the reference electrode. There are different kinds of reference electrodes, which are suitable for different conditions (e.g. acidic/alkaline solutions, molten salt electrolytes). Their potentials are all defined with respect to the absolute standard, the 'normal hydrogen electrode' (NHE).

In practice, we would like to apply either a constant potential difference between the working and the reference electrode, or a constant current flow between the working and the counter electrodes. The former case—constant potential difference—is more applicable to this work, and the system used to accomplish it is called a potentiostat. The potentiostat maintains a desired potential difference between the working electrode and the reference electrode, even while electrochemical changes are occurring at the working electrode surface. The current flowing between the working electrode and the counter electrode, which may vary as the electrochemistry dictates, is measured as a function of the potential.

3.1.2. Annealing Process:

In order to study the effect of annealing process on the physical and electro-optical properties of the prepared thin films, selected as-grown films were heat treated in different ambient four main annealing regimes were adopted: annealing in vacuum, annealing in the presence of an inert gas such as argon (Ar), (N_2+H_2) and annealing in a selenium or sulfur

atmosphere at various annealing temperature required. Post deposition annealing in vacuum and selenium or sulfur atmospheres was carried out in a closed end quartz tube evacuated by means of vacuum pump figure (3.2).The samples were enclosed in a graphite box with the selenium or sulfur source in the elongated quartz tube. Program adjustment of the required annealing temperature and time set up is provided by means of an automated system.
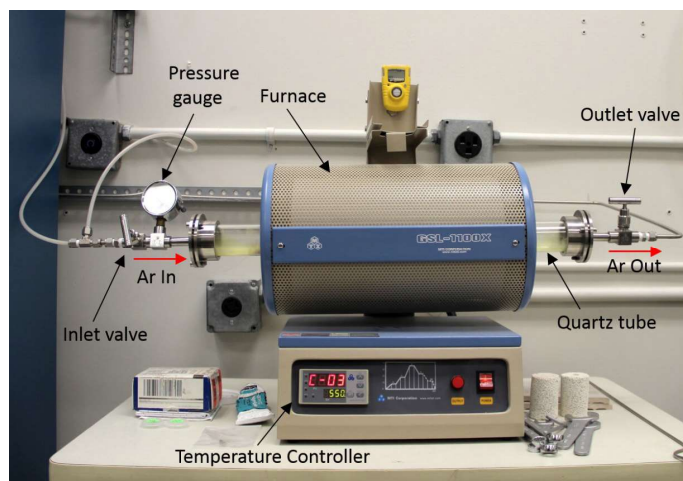
Figure 3.2. The sulfurization/selenization setup.

3.1.3. Hydrothermal technique:

The hydrothermal technique is historically rooted in the geological sciences. In the mid-nineteenth century, the term "hydrothermal" was first used by a British Geologist, Sir Roderick Murchison (1792e1871), to describe the formation of minerals by hot water solutions rising from cooling magma. Since then, extensive study has been performed to study the synthesis of new materials, the development of new hydrothermal methods, and the understanding of reaction mechanism.

Chemists today commonly refer to a hydrothermal or solvothermal synthesis as the synthesis by chemical reactions of substances in a sealed and heated aqueous solution or organic solvent at appropriate temperature (100 – 1000 ^{o}C) and pressure (1-100 MPa). Normally, hydrothermal and solvothermal reactions are conducted in a specially sealed container or high-pressure autoclave under subcritical or supercritical conditions of solvent. The studies on hydrothermal and solvothermal syntheses have mainly focused on the reactivity of the reactants, regularities of synthetic reactions and conditions, and their relationship with the structures and properties of products.

The main difference between hydrothermal and solid-state reactions lies in "reactivity" which is reflected in their different reaction mechanisms. Solid-state reactions depend on the diffusion of the raw materials at interface, whereas in hydrothermal and solvothermal reactions the reactant ions and/or molecules react in solution. Obviously, the difference of reaction mechanisms may lead to different final structures of products, even if the same reactants are used. Hydrothermal and solvothermal syntheses deal with the chemistry in preparation, synthesis, and assembly of special compounds or materials through solution route. More importantly, many compounds or materials with special structures and properties, which cannot be prepared from solid state synthesis, may be obtained by hydrothermal and solvothermal reactions. In some cases, hydrothermal or solvothermal reaction offers an alternative and mild synthetic method for solid-state reactions by lowering reaction temperature. Based on hydrothermal and solvothermal chemistry, we may conduct unique synthetic reactions which cannot take place in solid-state reactions due to evaporation of reactants at high temperatures, prepare new materials with special valence states, metastable structure, condensed and aggregation states, produce metastable phases or materials with low melting point, high vapor pressure, and low thermal stability, grow perfect single crystals with thermodynamically equilibrium defect, controllable morphology and particle size, and make ion-doping directly in synthetic reaction.

The hydrothermal or solvothermal technique has become one of the most important methods for the fabrication of nanostructural materials. In recent years, a large number of nanomaterials have been processed by hydrothermal or solvothermal method and thousands of science papers about the hydrothermal/solvothermal synthesis of nanomaterials have been published. From the perspective of morphology of nanomaterials, the hydrothermal technique has been used to process nanomaterials with a variety of morphological features, such as nanoparticle, nanosphere, nanotube, nanorod, nanowire, nanobelt, nanoplate, and so on.

From the perspective of composition of nanomaterials, the hydrothermal technique can be used to process almost all types of advanced materials like metal, alloy, oxides, semiconductors, silicates, sulphides, hydroxides, tungstates, titanates, carbon, zeolites, ceramics, and a variety of composites. The hydrothermal or solvothermal technique is not only used to process simplest nanomaterials, but also acts as one of the most attractive techniques for processing nanohybrid and nanocomposite materials. In short words, the great advantages of hydrothermal technology for nanomaterials processing are the production of particles that are monodispersed with total

control over their shape and size in addition to their chemical homogeneity with the highest dispersibility.

3.1.4. Reaction Containers:

High-pressure vessel, popularly known as an autoclave, is the basic equipment of hydrothermal and solvothermal synthetic experiment. Advances in hydrothermal and solvothermal synthesis of research depend largely on the equipment available. Crystal growth or materials processing under hydrothermal and solvothermal conditions requires high-pressure vessels to have outstanding capability of containing highly corrosive reagents, resisting high temperature and high pressure. Experimental studies under hydrothermal and solvothermal conditions require facilities that must operate routinely and reliably under extreme conditions. For different objectives and tolerances of hydrothermal synthetic experiment, there is a great variety of high-pressure vessels used for hydrothermal technology. Most of the earlier workers had dealt with this aspect in their own way. An ideal hydrothermal autoclave should have the main characteristics as follows:

- ➢ Should have high mechanical strength in order to bear high pressure and temperature experiments for long duration.

- ➢ Should have excellent acid, alkali, and oxidant resistance.

- ➢ Should have a simple mechanical structure and easy to operate and maintain.

- ➢ Should have good sealing performance in order to obtain the required temperature and pressure.

- ➢ Should have a suitable size and shape in order to obtain a desired temperature gradient.

Up to now, there is no uniform standard for the classification of hydrothermal autoclaves in the world. In accordance with different classification standard, there is more than one name for a hydrothermal autoclave.

Classification of hydrothermal autoclaves is introduced as follows:

- ➢ Classification by sealing methods: self-tightened seal autoclave and external-tightened seal autoclave.
- ➢ Classification by mechanical structure: flange-disc type autoclave; internal-plug-screw type autoclave; big-screw-cap type autoclave; and lever-press type autoclave.

- ➢ Classification by pressure formation methods: internally pressurized type autoclave and externally pressurized type autoclave.

- ➢ Classification by the name of designers: Morey autoclave; Smyth autoclave; Tuttle autoclave; and Barnes rocking reactors.

- ➢ Classification by heating methods: internally heated autoclave and externally heated autoclave.

- ➢ Classification by experimental system: high pressure autoclave and flow reactors and diffusionreactors.

Externally heated and internally pressurized autoclave This type of autoclave is popularly known as a Morey autoclave since Morey first designed this simple, gasketed, sealed steel autoclave of 25-100 mL volume. The cross-section of a typical Morey autoclave is shown in Fig. 3.3 The usual dimensions of a Morey autoclave are 10-20 cm length and 2.5 cm inner diameter. The autoclave generates an auto generous pressure depending on the degree of filling, the fluid, and the temperature.

Figure 3.3. A typical Morey autoclaves.

3.1.5. Spin Coating Process

Spin coating is one of the most common techniques for applying thin films to substrates. It is used in a wide variety of industries and technology sectors. The advantage of spin coating is its ability to quickly and easily produce very uniform films, ranging from a few nanometres to a few microns in thickness.The use of spin coating in organic electronics and nanotechnology is widespread and has built upon many of the techniques used in other semiconductor industries.
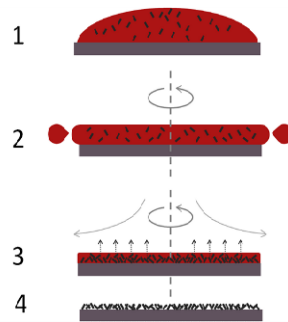
Figure 3.4. Example of spin coating a small molecule in solution using a static dispense.

- Step (1): the substrate is coated in the ink containing the molecules dissolved in a solvent.

- Step (2): Then the substrate is rotated at high speed and the majority of the ink is flung off the side.

- Step (3): Airflow then dries the majority of the solvent, leaving a plasticised film.

- Step (4): the film is completely dried to just leave the molecules on the surface.
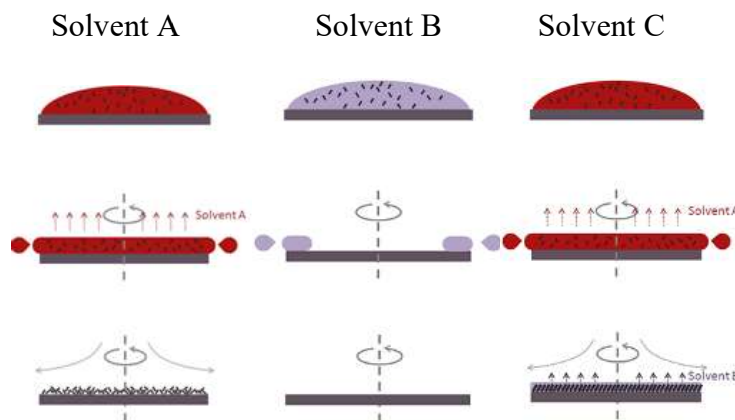
Figure 3.5. Example of solvent blends.

Solvent A: If a low boiling point solvent (high evaporation rate) is used then coating can be achieved more easily but an amorphous (disorganized) film is produced.

- Solvent B: If a high boiling point (slow evaporation rate) solvent is used then coating is harder because the ink has time to dry and dispersed off on all the edge of the substrate leaving no coating.

- Mixture of A & B: If a mixture of solvents is used with a majority of low boiling point (fast evaporation rate) with minority of high boiling point (slow evaporation rate) then coating can

still be achieved because the fast evaporating solvent is removed quickly leaving a plasticised film that is less likely to dry but also gives the molecules time to organize themselves.

3.2. Characterization techniques:

3.2.1. UV- Visible Spectroscopy

This technique of optical spectroscopy has been used to measure the kinetic growth of nanoparticles and to characterize both inorganic and organic nanomaterials. It provides information on the absorption and emission spectra, which determine the electronic structures of ions, atoms, molecules, or crystal during the excitation of electrons from ground to excited states (absorption) and from excited to ground states (emission). The ultraviolet visible (UV-vis) technique measures the absorption of photons in the visible, ultraviolet and near infrared ranges. The characteristic curves observed in the absorption and emission spectra indicate ions and atoms isolated by transitions between the energy levels. As a result, their wavelengths or photon energies can be determined.

In this work, UV-vis spectra were recorded using a high resolution (HR 4000-vis-NIR) spectrophotometer. A lamp produces a beam of light which hits a sample and splits into its component wavelengths. The specific wavelength of light reaches the exit aperture, before interacting with the sample. A detector then measures the transmittance and absorbance of the sample. Transmittance light passes through the sample and hits the detector, while absorbance is a measure of the light absorbed by the sample. The detector senses the light being transmitted through the sample and converts the information to a digital display.

3.2.2. X-ray Diffraction analysis

X-ray diffraction is the most important and widely used method for characterizing of crystalline materials. It is a crystallographic tool used to identify the different crystalline phases present in solid materials and powder samples. As X-rays pass through atomic planes in crystals, can either be transmitted, or it will be scattered by the electrons of the atoms in the material. When two parallel X-rays scatter from two adjacent planes of atoms within the crystal, they can either do so constructively or destructively depending on their phase. Constructive interference occurs when two X-ray waves with phases separated by an integer number of wavelengths add to make a new wave with a larger amplitude, Figure 3.6.
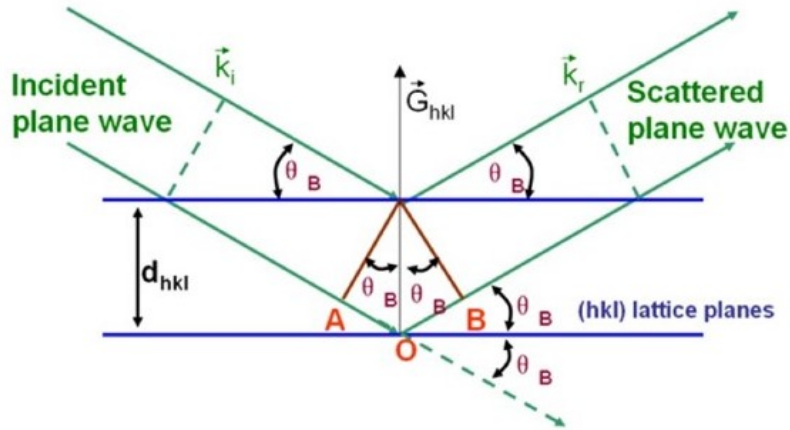
Figure 3.6. Schematic representation of diffraction of X-rays by a crystal (Bragg's Law)

The general relationship between the wavelength of the incident X-rays, angle of incidence and spacing between the crystal lattice planes of atoms is known as Bragg's Law and is expressed as:

$$n\lambda = 2d\sin\theta \dots\dots\dots\dots\dots\dots\dots\dots\dots (3.1)$$

Where n order of reflection, λ is the wavelength of the incident X-rays, d is the inter planar spacing of the crystal and θ is the angle of incidence. Since in a crystal atoms are arranged in a periodic fashion, the diffracted waves will consist of sharp interference maxima (peaks) with the same symmetry as in the distribution of atoms. Measuring the diffraction pattern therefore allows the determination of the distribution of atoms in a crystal.

X-ray diffraction can not only be used to identify the crystal phase of a material by comparison with data from known structures, but also to quantify changes in the cell parameters, crystal orientation, crystallite size and other structural parameters. The average crystallite size can be estimated from the X-ray diffraction pattern by using the Scherrer equation

$$D = K\lambda/B\cos\theta \dots\dots\dots\dots\dots\dots\dots\dots\dots\dots\dots. (3.2)$$

Where B (2θ) is the line broadening at the full width half maximum (FWHM, after taking into account the instrument broadening), K is the Scherrer constant which is around 0.9, λ is the incident X-ray wavelength and D is the crystallite size.

3.2.3. Field emission Scanning Electron Microscopy (FESEM)

FESEM is a technique which is used to obtain topographical and morphological information about a sample (figure 3.7). In SEM measurement, the sample under investigation is

bombarded with a beam of electrons. The electron of an incident beam either excites an electron that leaves the sample if it has sufficient energy (called the secondary electron)or is scattered (called the back-scattered electron). Both secondary and back-scattered electrons are detected by their respective detectors and then used to modulate the brightness of a cathode ray tube (CRT) after amplification. Secondary electrons generally originate near the surface of the sample.

Figure 3.7. image of scanning electron microscopy (FE-SEM), a Zeiss ULTRA 55

If they originate deep inside the sample, they will lose sufficient energy in transit to the surface that they cannot leave the sample. The number of detected electrons changes depending on the orientation of the surface. Due to the change in the number of detected electrons, the brightness on the CRT monitor changes which results in a 3-dimensional image. On the other hand, back scattered electrons possess different energies depending on whether they were scattered from a heavier or a lighter nucleus. Electrons scattered from a heavier nucleus have a higher energy than the ones scattered from a lighter nucleus, and thus, the image of the heavier nucleus element appears brighter. In our study, FE-SEM was performed on thin films deposited on ITO substrate, using Zeiss ULTRA 55 Excel equipped with a 30 kV field emission gun.

3.2.4. Energy-dispersive Spectroscopy (EDS)

Energy-dispersiveSpectroscopy (EDS) allows for a quantitative compositional measurement of a specimen. EDS most commonly uses electrons as probes and measures x-rays emitted from atomic orbitals with specific energies that are characteristic to specific elements.

Specifically, when an incident electron collides with inner core atomic electron, the core electron is ejected, leaving a hole. An outer shell electron fills the core electron and an x-ray photon is emitted.

Typical operating voltages depend on two things: 1) the depth of the site of interest, 2) the inclusion of peaks. Greater operating voltages tend to probe deeper in the specimen. This depth can be estimated using computer simulation software employing Monte Carlo simulations. Greater operating voltages also allow for the inclusion of higher energy peaks, increasing the accuracy of the characterization. Typical operating voltages are twice that of the peak of interest. Characterization accuracy is also increased by longer acquisition times, higher resolution detectors, and lower time spent on processing an x-ray event (dead time).

3.2.5. Transmission electron microscopy (TEM) analysis

TEM is a microscopy technique in which a beam of electrons is transmitted in vacuum through a thin sample, interacting with it to reveal information including its particle size distribution. It is also capable of focusing on a single nanoparticle to identify directly its chemical and electronic structure. The principle behind TEM is similar to a slide projector: as the beam of electrons passes through the sample, only some parts of it are transmitted, forming a contrast image, which passes through a magnifying lens and is then projected onto a fluorescent screen or is detected by a charged couple device (CCD) camera. Figure 3.8 shows a photograph and a schematic diagram of a TEM set-up. The electron gun cathode, which is often made from tungsten filament, is heated by a high current to produce a stream of electrons. These are accelerated by a field of 100-300 keV and as they travel down the column, the increasing voltage increases their kinetic energy and decreases the effective wavelength. The condenser lenses are responsible for primary beam formation and focusing the beam to a small cylinder, while the condenser aperture eliminates any electrons scattered at wide angles. The beam hits the specimen on the sample holder and a large part of it is transmitted, magnified and focused by the objective lens and later the projector lenses. Finally, a fluorescent screen or CCD is used to form an image.

TEM is capable of creating diffraction patterns from a tiny area, which is called Selected Area Diffraction (SAD); by controlling the condenser lens settings, entering a selected area aperture and parallel incident beam illumination, a SAD from an area ranging hundreds to small nanometers in diameter is obtained.

Figure 3.8. image of transmittance electron microscopy (TEM) JEOL JEM 2100F

Energy Dispersive X-ray Microanalysis (EDX) is used to measure the X-rays emitted during electron bombardment in a TEM to define the chemical composition of materials on nano and micro-scales. The elements present in the sample are determined from the X-ray energies emitted from the area being excited by the electron beam. The proportion of detection of characteristic X-rays gives a measure of the amounts of different elements present in the sample. Weight percentages are calculated using specific peak energies relating to individual energy shells of each atom of each element and peak areas are determined using an internal calibrated standard, usually cobalt.

The work reported in this thesis, TEM measurements of thin films were achieved using aJEOL JEM 2100F operating at 200 keV. Samples were prepared by drop casting dispersions of the film in ethanol on holey carbon copper grids.

3.3. Electrical Properties of I–III–VI$_2$ Compounds

The electrical conductivities of CuInSe$_2$, CuGaSe$_2$, CuInS$_2$, and their solid solutions such as Cu(In$_{1-x}$Ga$_x$)Se$_2$ and CuIn(Se$_{1-x}$S$_x$)$_2$ play an immense role in the thin film or single crystal solar cells to control efficiencies of the cells. The electrical transport properties of the compounds at RT and low temperature with effect of intrinsic doping are systematically discussed. The conductivity of the sample can easily be varied at large extent by varying its intrinsic composition ratios without making extrinsic doping. The n- and p-type conductivities can be made in the compounds. However, it is little difficult to make n-type CuGaSe$_2$ rather than p-type because the creation of Ga$_{Cu}$ sites in the CGS is not easy task like In$_{Cu}$ in the CuInSe$_2$, which are responsible for n-type conductivity.

3.3.1. Mott-Schottky Measurement

The measurement of the space charge capacitance can yield both the flat band position and the donor density of a sample. The simplest approach to do this is to use a resistor and a capacitor in series as equivalent circuit and measure the impedance vs applied DC potential at a set frequency. The only contributor to the real impedance is then the resistor and the only contributor to the imaginary impedance is the capacitor and the values for resistance and capacitance can be readily extracted.

Another method is to do impedance sweeps at different applied DC potentials and deconvolute the spectra to get the contribution of the space charge capacitance. This is a much more complicated and time-consuming method one often tries to avoid.

3.3.2. Flat band Potential

In addition to the utilization of the Mott-Schottky equation to determine the flat band potential, there is a method using current-voltage characteristics. The approach is widely used and is based on the onset of the photocurrent. That means the potential where the photocurrent deviates from the measured current in the dark. This is based on the assumptions that when the bands are bent downwards (accumulation), all generated electron-hole pairs recombine and thus no current is generated. When the bands are flat, the electrons are able to escape and current can be measured. However, this method tends to yield more positive flatband potentials since recombination might occur to a large extent even when the bands are bent upwards (depletion).

3.3.3. Electrochemical Impedance Spectroscopy (EIS)

Electrochemical Impedance Spectroscopy (EIS) is an early technique deals with the difference of the electrical elements that the photoelectrochemical cell consists of. It is a very powerful tool for finding the contributions of each element such as resistancesand capacitances.

Impedance

Impedance is a more general expression for resistance. Resistance is mainly used for describing DC-circuits. It can be seen from equations (2.1) and (2.2) the ratio between the voltage and the current will contain a phase angle and is what is called impedance. This is why it is said that impedance is a broadened description of Ohm's law to include AC-circuits.

When AC voltage is applied to a circuit, the voltage and current varies with time. The voltage will be given by the amplitude, U_0, and the angular frequency, ω

$$U = U_0 \sin(\omega t) \qquad \ldots(2.1)$$

This sine wave voltage will give rise to a current in the circuit. If this circuit consists of capacitive

or inductive circuit elements the current will get a phase change, θ, with respect to the voltage:

$$I = I_0 \sin(\omega t + \theta) \qquad \ldots (2.2)$$

As there is a different types of space charges in n- and p-type semiconductors a normal depletion layer contains only ionized donors or acceptors is formed. An inversion layer is formed when the Fermi level crosses the mid gap energy, and the minority carriers outnumber the majority carriers in a thin layer at the surface. When these minority carriers are consumed faster than they are generated, a deep depletion layer forms; under these conditions the surface is not in thermal equilibrium and the Fermi level is not well defined in this region. In an accumulation layer, the adsorbed surface charges are compensated by majority charge carriers that accumulate at the surface
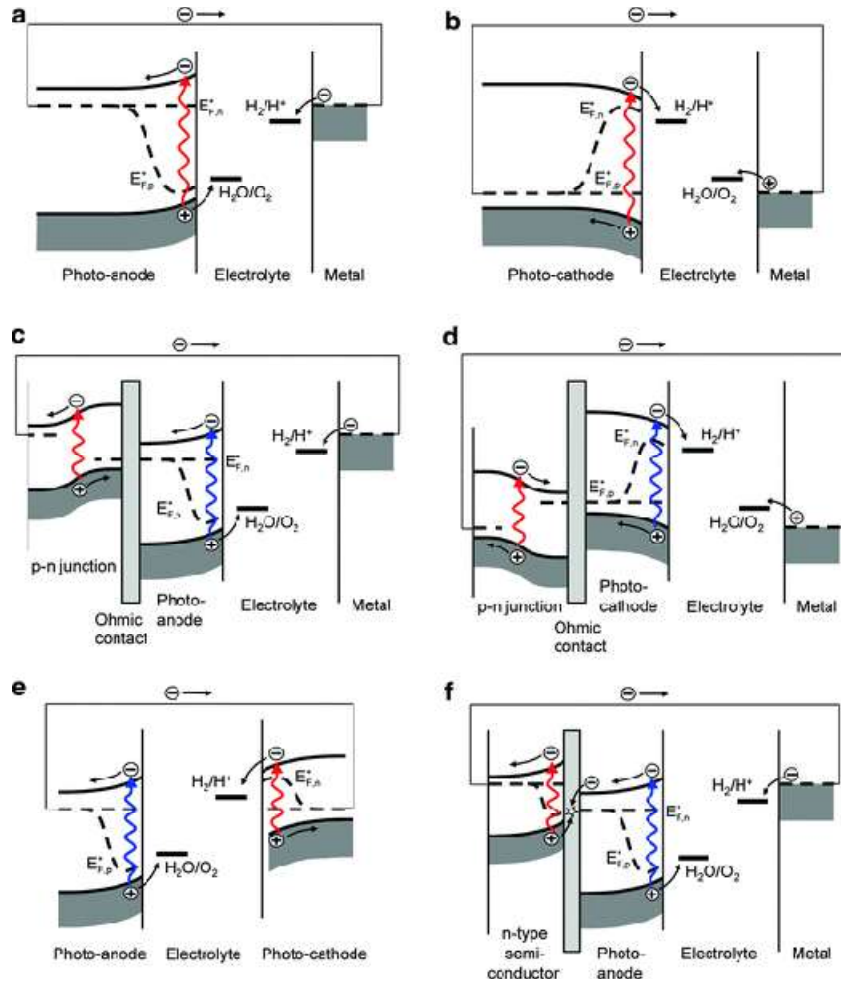
Figure 3.9. Different types of space charges in n- and p-type semiconductors.

When doing impedance measurements, it is beneficial to divide the impedance into two components. One component is the part that is in phase with the voltage and the other is the partthat is 90° out of phase. The component that is in phase is called the resistance, R, and is the real part of the impedance. The part that is out of phase is called the reactance, X, and is theimaginary part of the impedance. Hence, it is beneficial to represent the impedance as a complexnumber, the complex impedance, Z^*:

$$Z^* = R + jX \quad \text{…………………………} \quad (2.3)$$

$$Z^*(\omega) = Z'(\omega) + j.Z''(\omega) \quad \text{…………………}(2.4)$$

117

Figure 3.10. (a) Novocontrol Concept 80 set up device and (b) the Complex impedance Cartesian coordinates diagram.

Figure 3.10. shows the Novocontrol concept set up device used in measuring the EIS for the prepared nanocrystalline powders of $CuIn_xCr_yGa_{1-x-y}Se_2$ where (x = 0.4, and y = 0.0, 0.1, 0.2, 0.3). The impedance is often represented in Cartesian coordinates with R on the horizontal axis and X on the vertical axis. An electrical circuit usually consists of three main elements; a resistor,a capacitor and an inductor. The impedances of these three are quite discrete from each other.An ideal resistor does only have real impedance (resistance). The resistance through a resistor is independent of the frequency and describes transport of charge when the current is in phasewith the voltage. The impedance of an ideal capacitor consists of only the imaginary impedance (reactance). Reactance, since it is imaginary, implies that the charge is not actually transportedbut rather stored, as is the case for a capacitor. In a coil (inductor) an AC-signal will set up amagnetic field that in turn will induce a voltage. The voltage will then be out of phase withrespect to the current and the impedance of the coil will only have reactance. If these threeelements are connected in series the expression for the complex impedance, also called the totalimpedance:

$$Z^* = R - j/\omega C + j\omega L$$

3.3.4. Photo electrochemical analysis

The main component of the PEC cell is the semiconductor, which converts incident photons to electron–hole pairs. These electrons and holes are spatially separated from each other due to the presence of an electric field inside the semiconductor,Figure 3.11. A schematic diagram showing photoelectrochemical current measurement setup. The two electrodes are

interconnected via an external circuit source. An electrolyte is applied to the solar cell, acting as a conducting mediator between the electrodes. A light source Xenon lamp is using for illumination of semiconductor films, various long-wave band pass filters is located between the light source and the sample electrode.The working electrode can be composed of a semiconductor material, polycrystalline or nanocrystal line, which is attached to a conducting substrate.

When n-doped semiconductors are brought into contact with an electrolyte, current willflow until their electrochemical potentials are equalized and equilibrium is attained. The absorption of photons with an energy exceeding the band gap generates electron-hole pairs close to the semiconductor electrolyte interface. In case the Fermi level (EF) lies above the standard redox potential (Vo $_{redox}$), electrons will be withdrawn from the semiconductor to the electrolyte, leaving positive charges behind. A charge separation will occur when the holes reach the surface and react with the electrolyte. The electric field is important regarding the separation process of the photo generated electron/hole pairs. The charge ordering in the electrolyte is often described in the terms of Helmholtz and Gouy-Chapman layers.
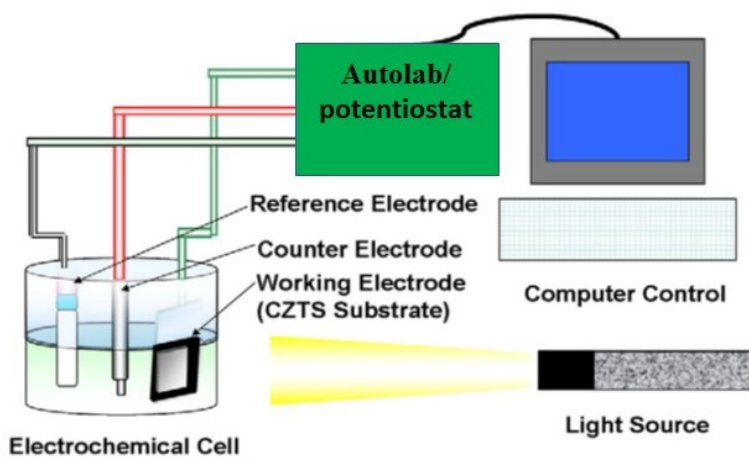

Figure 3.11. A schematic diagram showing photoelectrochemical current measurement setup.

Chapter 4. CIGS thin films

4.1. Objectives

The main objective was to deposit high quality CIS thin films by use of electrodeposition to develop low cost solar cell absorber layer. The main Specific objectives are:

i. To evaluate the electrical and optical properties of CIS thin films deposited by linear sweep cathodic electrodeposition.

ii. To evaluate the effect of annealing temperature on CIS thin films optical and electrical properties.

iii. To determine the quality and type of the deposited CIS thin films using Mott-Schottky measurements.

4.2. Introduction

Many years ago, the gradual and unavoidable consumption of natural energy sources like fossil fuels lead to massive demand of energy alternative sources all over the world [1]. In addition, to solve the problems related to heating and greenhouse effect, it's important to take in consideration those of renewable energy sources, e.g., solar, hydro, wind, tidal, ocean, and geo-thermal energy. One of these renewable energy sources is photovoltacis (PV) technology. This is a widespread alternative source as their low cost and effectiveness choice. It depends on charge carrier generation in some type of light sensitive materials. The first applied solar cell was proposed by Grätzel in 1991 [2]. Among those (PV) technologies thin-film semiconductor absorber materials, where sunlight is converted directly into electricity, Such as CdTe, CdSe, PbS, $CuInSe_2$, $CuInS_2$, $CuIn(Se,S)_2$, $CuInxGa_{1-x}Se_2$ and $Cu(In,Ga)(Se,S)_2$ [3].

$CuInSe_2$ is considered a benign absorber material for thin-film solar cells, due to its high absorption coefficient of about 10^5 cm^{-1} and its band gap nearly 1.5 eV with a well match to the solar spectrum. In addition, $CuInS_2$ is low-cost, environmentally friendly material, and has a long-term stability in photovoltaic applications [4]. Electrodeposition-based technique is one of the foremost promising approaches to reach an enhanced reduction in the production cost this thin film types. Due to its low-temperature processing, large area deposition, and negligible waste of chemicals with higher efficiencies close to 100%. Therefore, several research groups have studied fabrication of $CuInSe_2$, $CuIn(Se,S)_2$, and CIGS-based solar cells by

electrodeposition [5]. So, several techniques have been developed to prepare CISSe thin film solar cells such as, mechanical milling [6], chemical bath deposition [7], evaporation [9], paste coating technologies [11], magnetron sputtering [11], microwave irradiation [12,13] and solvothermal method [14], electrodeposition [15], in order to improve their efficiencies. Some of these methods, in particular the chemical-based ones, have the advantages of simplicity, high throughput and inherent low investment requirements.

Hence, in the present study, we prepared $CuInSe_2$ and $CuInS_2$ thin films from previously electrodeposited $CuInSe_2$ films by selenization or sulfurization of in Se or S-rich atmosphere, respectively, in a graphite box under N_2+H_2 gas in a quartz tube vacuum oven. Then, we further investigated the effect of precursors on the properties of CIS films by X-ray diffraction (XRD), scanning electron microscopy (FESEM) and Mott-Schottky measurements.

The use of Schottky barrier solar cells based on thin-film semiconductors is another way to improve solar cell performance. The Mott-Schottky plot is a usual way for semiconductor material electrochemical characterization [16-18]. A Mott-Schottky plot (inverse square of space charge layer capacitance (C_{sc}^{-2}) versus semiconductor electrode potential (E) gives the doping density by slope of the straight line and flat-band potential by x-axis intercept.

4.3. Theory of CIS electrodeposition:

$CuInSe_2$ thin film electrodeposition conditions were first introduced by Bhattacharya (1983) [19]. This is by far the most investigated such a process, usually referred to as single-step electrodeposition; it involves only one electrochemical process. The drawbacks of this process is that the electrochemical features is arbitrarily difficult control, either the formation of the elements in their elemental form, or as binary compounds additionally to the required ternary CIGS chalcopyrite phase, that refers to the fundamental individual electrochemical reactions concerning the deposition of Cu, In and Se [20]. The single-step electrodeposition of CIS from aqueous solution containing $CuCl_2$, $InCl_3$, and H_2SeO_3 according to the Nernst equation is quite difficult and difference in the reduction potential between these ion species is rather large. The electrochemical reduction reactions among Cu, In and Se ions is illustrated in the following equations [21] (vs. NHE, normal hydrogen electrode):

$$Cu^{2+}_{(aq)} + 2e^- \rightarrow Cu_{(s)} \qquad \text{--- (4.1)}$$
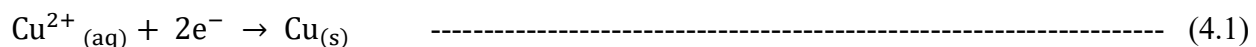
$$E = E^0 - \frac{RT}{2F} \cdot \ln\left(\frac{a_{Cu}}{a_{Cu^{2+}}}\right) = 0.342 + 0.0295 \log a_{cu^{2+}} \text{ -------------------------------------- (4.2)}$$

$$In^{3+}_{(aq)} + 3e^- \rightarrow In_{(s)} \text{ -- (4.3)}$$
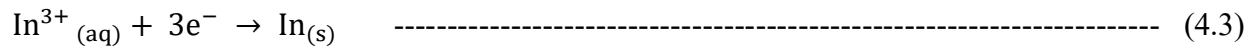
$$E = E^0_{In} - \frac{RT}{3F} \cdot \ln\left(\frac{a_{In}}{a_{In^{3+}}}\right) = -0.338 + 0.0197 \log a_{In^{3+}} \text{ ------------------------------- (4.4)}$$

$$H_2SeO_{3(aq)} = HSeO_2 + (aq) + OH^-_{(aq)} \text{ -- (4.5)}$$

$$HSeO_2 + (aq) + 3H^+_{(aq)} + 4e^- \rightarrow Se_s + 2H_2O_{(l)} \text{ -- (4.6)}$$
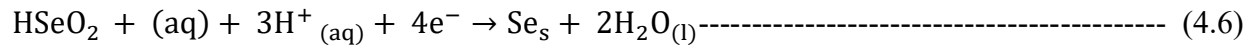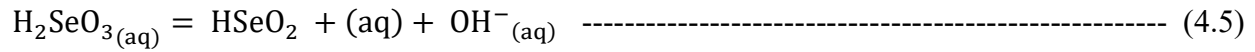
$$E = E^0_{Se} - \frac{RT}{4F} \cdot \ln\left(\frac{a_{Se}}{a_{HSeO}}\right) + 2 a_{3H^+} = 0.74 + 0.0148 \log a_{HSeO^{2+}} - 0.043 \text{ pH-------- (4.7)}$$

where E refers to the deposition potential of Cu, In, and Se, R is the ideal gas constant, F is the Faraday constant, a_X, where $(X=Cu, Cu^{2+}, In, In^{3+}, Se, HSeO^{2+}$ and $H^+)$ refer to activities of Cu, Cu^{2+}, In, In^{3+}, Se, $HSeO_2^+$, and H^+, respectively. To manage a good deposition process, some complexing agents were used in order to bring deposition potentials of the ion species closer by shifting the copper ion potential into the negative direction.

4.4. CIS Structure:
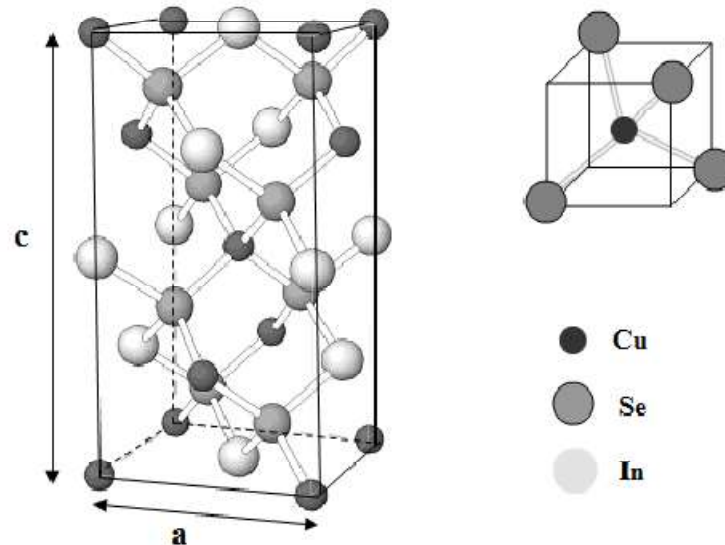
Figure 4.1. Schematic representation of CuInSe$_2$ chalcopyrite crystal structure

4.5. Experimental Procedure

4.5.1. Thin film preparation

$CuInSe_2$ (CIS) films were electrodeposited using Indium-doped tin oxide (ITO) as substrates. Before deposition process, substrates were cleaned successively in an ultrasonic bath with detergent, alcohol solution, and acetone then rinsed with deionized water and subsequently dried. A three-electrode cell was used with a Pt wire as a counter electrode, a (Ag/AgCl) as reference electrode, and the working electrode was ITO coated glass substrate. Electrodeposition was carried out employing an Autolab PGSTAT 302N. The electrolytic bath was consisting of an acidic aqueous solution containing 0.025 mol/L $CuCl_2$, 0.025 mol/L $InCl_3$, and 0.025 mol/L H_2SeO_3 dissolved in high-purity distilled water. The pH of the electrodeposition bath was adjusted at 1.5 using hydrochloric acid (HCl). Also, the addition of KCl as supporting electrolyte provides better stability of the electrodeposition bath solution and improves the quality of the deposited layers. CIS thin films were electrodeposited in potentiostatically, applying a potential of -0.90V vs. Ag/ AgCl for 30 min. Before deposition, the solution was deaerated by argon bubbling and stirred up for 20 min. After completing the electrodeposition, the samples were rinsed with distilled water and dried in air. Then, the as-deposited $CuInSe_2$ films were annealed at 450°C for 20 min under nydron forming gas (10 % H_2 in N_2) atmosphere with a pressure of 10^{-2} bar to improve the crystallinity of the resulted films. A sulfurization process was performed onto the electrodeposited $CuInSe_2$ layers to obtain $CuInS_2$ films. A sufficient amount of molecular sulfur was loaded into a graphite box inside a quartz tube under the forming gas atmosphere. The oven temperature was kept at 400°C for 10 min. The selenized $CuInSe_2$ samples will be referred to as $CuInSe_2$–Se and the sulfurized samples will be referred to as $CuInSe_2$–S in order to differentiate them.

4.5.2. Characterization

The crystal structure of $CuInSe_2$ as grown, $CuInSe_2$–Se selenized and $CuInSe_2$–S sulfurized thin films was investigated using X-ray diffraction (XRD) Rigaku Ultima IV diffractometer with the Bragg-Bentano configuration and CuKα radiation (λ = 1.54060 Å). Chemical composition, surface morphology and topography were characterized using energy dispersive spectroscopy (EDX) and field emission scanning electron microscopy (FESEM).

Mott-Schottky measurements were applied to investigate the manner of the prepared semiconductor layers. Mott-Schottky studies were employed using 0.5 M NaOH as an electrolyte in a three-electrode electrochemical. Reference Ag/AgCl electrode was used and a platinum wire as a counter electrode. Working electrodes were prepared using ITO n-type and $CuInSe_2$-Se $CuInSe_2$-S p-type thin films. The ohmic contacts were made using copper wire and a conductive silver paste. The nature of those ohmic contacts was tested before measurements. The relevant measured area of the photo-electrodes was 0.32 cm^2.

4.6. Results and discussion

4.6.1. XRD analysis

Figure. 1 shows the XRD pattern of the prepared samples containing three diffraction peaks. The first one is for the as-grown $CuInSe_2$ electrodeposited thin films. The second is for the selenized samples and the rest is for the sulfurized samples. The diffraction pattern of the as-grown $CuInSe_2$ polycrystalline thin films evidences poor crystallinity. The as-grown electrodeposited sample shows broad peaks with a low intensity at the positions (112, 220/204 and 116/312) indicating that the grown films have to be annealed for good crystallinity. Also, characteristic peaks with higher intensity for the ITO substrate, marked with *, are obviously shown. The tetragonal structure of the $CuInSe_2$ deposited onto ITO was observed with very small particle size 6 nm. After the annealing processes with selenium (selenization) and sulfur (sulfurization) both in inert atmosphere using Nydron gas (10% of H_2 in N_2), the crystallinity of the prepared samples improved, i.e., the characteristic peak intensity of both $CuInSe_2$ and $CuInS_2$ increased give the improved crystallinity of the prepared samples. The peak position shifts considerably to higher 2θ angles for the sulfurized samples. For the selenized samples the resulted crystallite size was 61 nm. The peaks of $CuInSe_2$ situated at 2θ=26.68, 44.38 and 52.63 degree for 112, (204/220) and (116/312) diffraction planes, respectively, match those of the JCPDS-040-1487 of the $CuInSe_2$ reference card. The diffraction peaks of sulfurized samples were clearly obtained at 27.86, 46.31 and 54.82 degree for 112, (204/220) and (116/312) diffraction planes, respectively, matching those of the JCPDS-027-0159 $CuInSe_2$ reference card with a crystal size of 34 nm calculated at 112 main peaks as shown in Table 4.1.
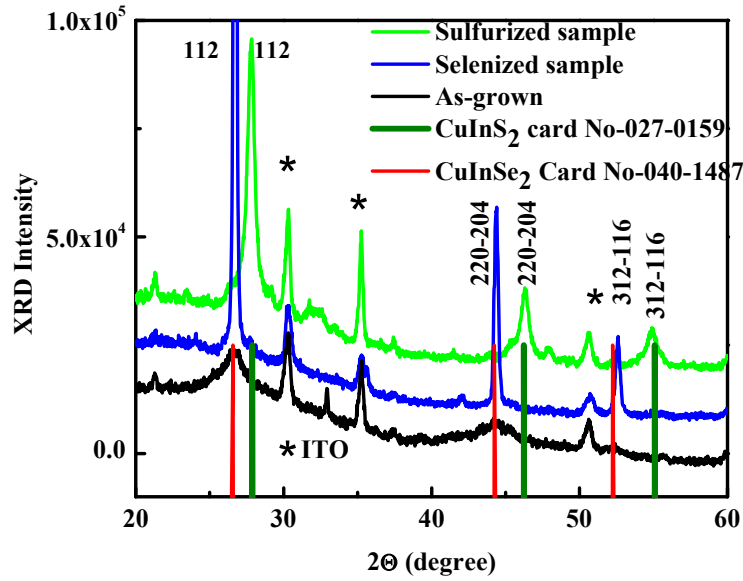
Figure 4.2. XRD spectra of CuInSe₂ as-grown, sulfurized and selenized films.

The crystallite size of the prepared films was calculated according to Scherer's formula:

$$D = \frac{K\lambda}{\beta cos\theta}(4.8)$$

where β is the Full Width at Half Maximum (FWHM), λ wavelength of X-rays with value is 1.5418 Å, K is Scherer's constant depending on the crystallite shape and is close to 1 (K= 0.9 was used) and θ is the Bragg angle at the center of the peak.

Table 4.1. Crystallite size measurement of CuInSe₂ as-grown, sulfurized and selinized films.

Sample	Crystallite size (nm)
CuInSe₂ - as grown	6
CuInSe₂ - sulfurized	34
CuInSe₂ - selenized	61

Table 4.1. displays the crystallite size of different studied samples calculated through the Sherrer equation. The crystallite size of the as grown samples, with molecular formula CuInSe₂, is about 6 nm. Independent of the gas used, the subsequent annealing produces an effective increase of the crystallite size. In sulfur atmosphere, sulfur atoms replaced most of selenium atoms forming CuInS₂ phase. With the smaller atomic size of sulfur than selenium and the growing up of the grains together the calculated

crystal size is about 34 nm, which is more than five times larger than that measured for the as grown films. Annealing in selenium atmosphere still produces larger crystallites and the growing up process of the selenized phase $CuInSe_2$ in selenium rich atmosphere leads to an increase in the crystallite size up to 61 nm. This can be due to the fact that selenium atoms are larger than sulfur atoms, the higher temperature processed for annealing in case of selenium and the time of annealing.

4.6.2. FE-SEM analysis

Figure 4.3 shows FE-SEM images for the $CuInSe_2$-Se and $CuInSe_2$-S films at different magnification scale. It can be clearly seen that all films were uniform, homogenous, well-covered with good adherence. An agglomeration of grains in the films and some $In_2(Se,S)_3$ and $Cu_{2-x}Se$ hexagonal secondary phases in both $CuInSe_2$-Se and $CuInSe_2$-S films can be seen.
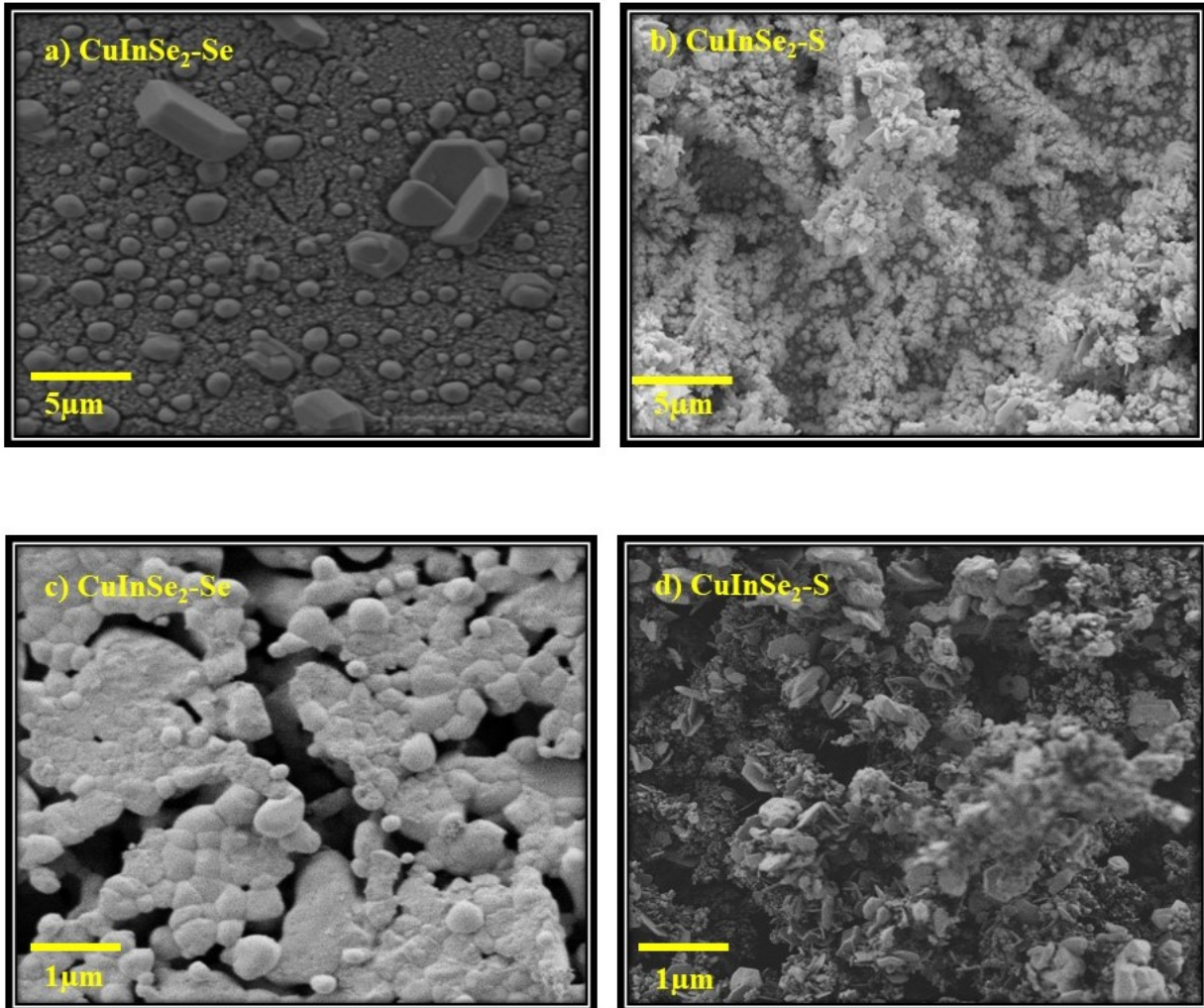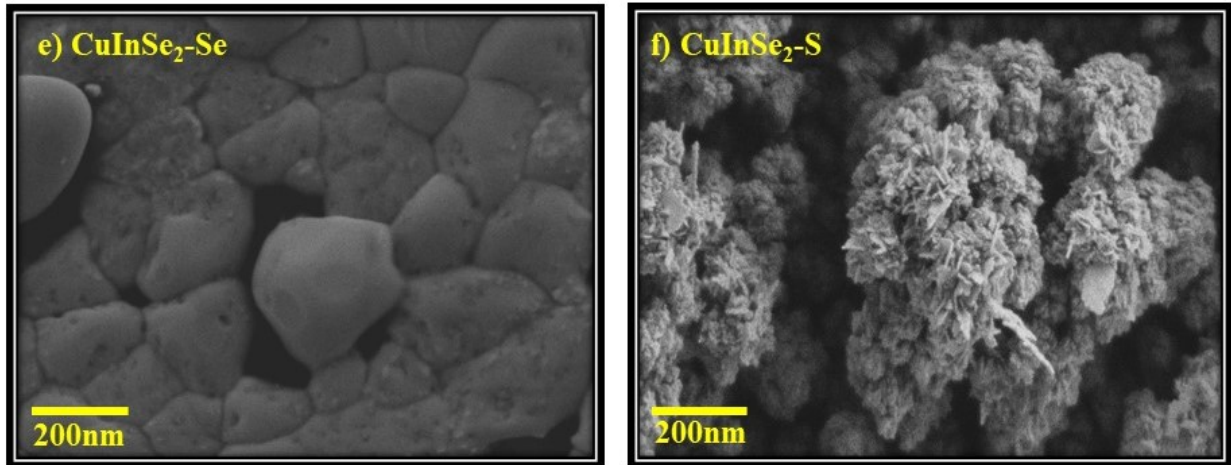
Figure 4.3. FE-SEM images for (CuInSe$_2$-Se) selenized and (CuInSe$_2$-S) sulfurized films at different magnification scales (a) 2µm, (b)1µm, (c)200nm.

FE-SEM images show that the CuInSe$_2$-Se and CuInSe$_2$-S thin films are composed of densely packed small particles with a homogenous uniform distribution and agglomeration of nano-particles. CuInSe$_2$-S thin films are composed of a smaller particle size than the CuInSe-Se films in accordance with the calculated particle size of the XRD results, i.e., 34 nm for sulfurized and 61 nm for selenized samples. Also, hexagonal shapes are clearly visible in both the CuInSe-Se and CuInSe$_2$-S micrographs due to formation of some binary In$_2$(Se, S)$_3$ and Cu$_{2-x}$(Se, S) phases. During the sulfurization process selenium atoms were replaced by sulfur atoms and a small amount of selenium was not completely converted into sulfur resulting in an Se/S ratio= 0.06 (Se/S=2.28/38.at%) as measured by EDX. A clear substitution of the selenium atoms from the as-grown CuInSe$_2$ phase into sulfur atoms and a complete crystallization of CuInS$_2$ thin films is displayed in Figure4.3. The sum of the Cu and In atomic percentage is approximately the same as the selenium percentage.

According to the EDX measurements, the selenized and sulfurized CuInSe$_2$-Se and CuInSe$_2$-S films contained 24.86, 23.92 at.% Cu, 27.49, 33.07 at.% In, 47.65, 2.28 at.% Se and, 38.0 at.% S, respectively, corresponding to copper poor CuInSe$_2$-Se and CuInSe$_2$-S phases with an optimum Cu/In ratio of 0.9 and 0.7 for p-type semiconducting properties [20]. Table 4.2. displays the EDX results for these samples.

Table 4.2. Composition of the CuInSe$_2$-Se and CuInSe$_2$-S films measured by EDS.

Sample	Cu (at%)	In (at%)	Se (at%)	S (at%)	(Cu/In)	(Se&Se+S)/(Cu+In)
CuInSe$_2$-Se	24.86	27.49	47.65	-----	0.9	0.9
CuInSe$_2$-S	23.92	33.07	2.28	38.00	0.7	0.7
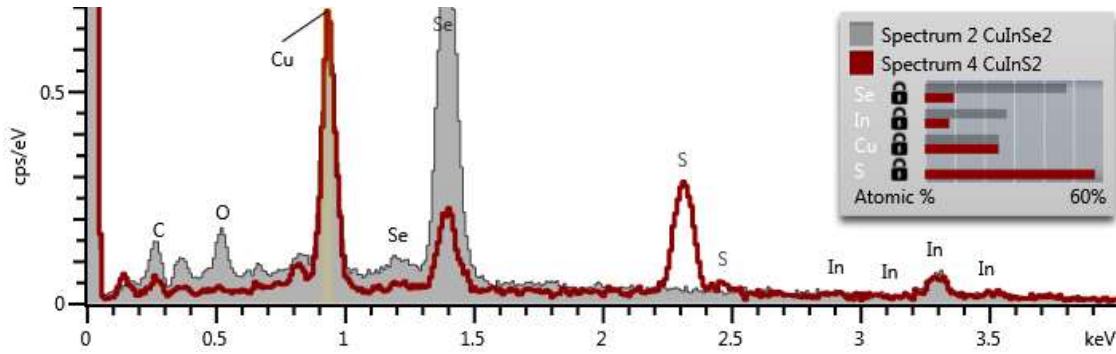
Figure 4.4. EDX spectrum for both CuInSe$_2$ selenized and CuInS$_2$ sulfurized samples.

4.7. Optical measurements

The optical properties of annealed CuInSe$_2$-Se and CuInSe$_2$-S thin films have been studied in order to determine the effect of annealing process in different selenium and sulfur atmosphere. The optical transmittance spectra were measured in the wavelength range 400 - 1000 nm of the visible region.

Figure 4.7. show the transmittance spectra of CuInSe$_2$ samples annealed in Selenium and Sulfur atmosphere, respectively. The optical properties are studied, the transmission spectra of the sample T(λ) are measured:

$$T(\lambda) = \frac{I(\lambda)}{I_0(\lambda)} (4.9)$$

where I$_0$(λ) is the intensity of light illuminating the sample, I(λ) is the intensity of the light transmitted through the sample. Often one uses the term absorbance (or optical density), which is defined according to the formula (10):

$$\text{Abs}(\lambda) = \log\left\{\frac{I_0(\lambda)}{I(\lambda)}\right\} = -\log(T(\lambda)) \qquad (4.10)$$
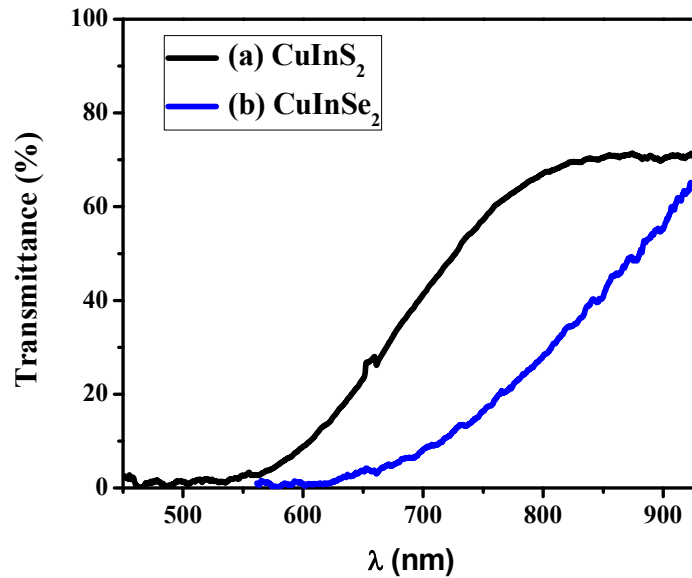
Figure 4.5. Transmittance spectra of CuInSe$_2$ samples annealed in Selenium and Sulfur atmosphere.

The bandgap energy was determined from the Tauc relationship, Eq. (11):

$(\alpha h\upsilon) = A(h\upsilon - Eg)^n$ (4.11)

Where A is constant, hυ is the photon energy of the incident radiation, Eg is the band gap energy, n=½ for allowed direct transition and n=2 for allowed indirect transition.

As CuInSe$_2$-Se and CuInSe$_2$-S is a direct allowed band transitions, so n=1/2.

$(\alpha h\upsilon) = A(h\upsilon - Eg)^{1/2}$ ---(4.12)

By square the values of both sides we will got that:

$(\alpha h\upsilon)^2 = A(h\upsilon - Eg)$ --(4.13)
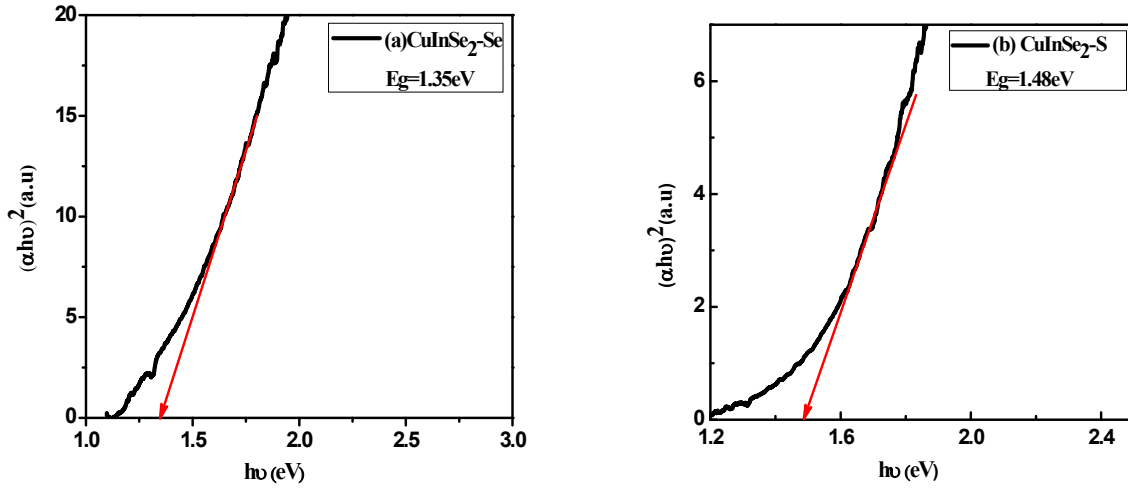
Figure 4.6. Tauc plots for (a) selenized CuInSe$_2$ –Se and (b) sulfurized CuInSe$_2$ –S thin films

Figure 5 (a, b) shows plotting the values of $(\alpha h\upsilon)^2$ as a function of photon energy (hυ) for CuInSe$_2$-Se and CuInSe$_2$-S, respectively. The band gap values can be obtained by extrapolating the slope of curves to the X-axis where $(\alpha h\upsilon)^2 =0$.

The optical band gap is found to be 1.48 and 1.35 eV, for CuInSe$_2$-Se and CuInSe$_2$-S which is agreement with the reported values of the optical band gap of CuInSe$_2$ and CuInS$_2$ [22], As we notice the difference in annealing temperatures and time also affects the resultant band gap energy in addition to the Se/S percentages in both samples.

4.8. Mott-Schottky measurements

To study the charge distribution of the prepared thin films capacity/electrode potential has been studied. The capacity/electrode potential is very sensitive to changes in the charge concentration. Applying Mott-Schottky relationship:

$$\frac{1}{C_{sc}^2} = \frac{2}{qNA^2\varepsilon\varepsilon_0}\left(E - E_{fb} - \frac{kT}{q}\right) \qquad (4.14)$$

where the capacity of space charge is referred as C$_{sc}$, the carrier density N is (the concentration of electron donor for n-type semi-conductor or hole acceptor for the concentration of p-type semi-conductor), the relative electric permittivity is ε, the electric permittivity of vacuum is ε_0, the electronic charge is q, the surface area is A, the Boltzman constant is k, the absolute temperature T, E$_{fb}$ is the flat band potential and E is the applied potential.

By plotting $1/C^2$ vs. V we suspect obtain a straight line with appositive or negative slope. The plot intercept of dC_{sc}^{2-}/dE with the potential axis yields the flat band potential E_{fb}. The flat band potential E_{fb} does not depend on time nor polarization of the layers. The carrier density N can be derived from the gradient dC_{sc}^{2-}/dE, and the intercept with the potential axis yields the flat band potential E_{fb}. Mott-Schottky equation is used for determining the carrier density and the flat band potencial characterizing semiconductor layers [23].

The electrochemical solution used for mott–Schottky measurement was deaerated with argon. The distinguished layer formed by a potentiodynamic cycling in different potential ranges by means of an auto Lab system PGSTAT 302N conducted at 10kHz. The measurements were conducted at room temprature. The calculated negative slope of C_{SC}^{-2} vs. potential is inversely proportional to the acceptor concentration and is an indication of a p-type semiconductor layer. In contrast the positive slope of C_{SC}^{-2} vs. potential refers to an n-type semiconductor.
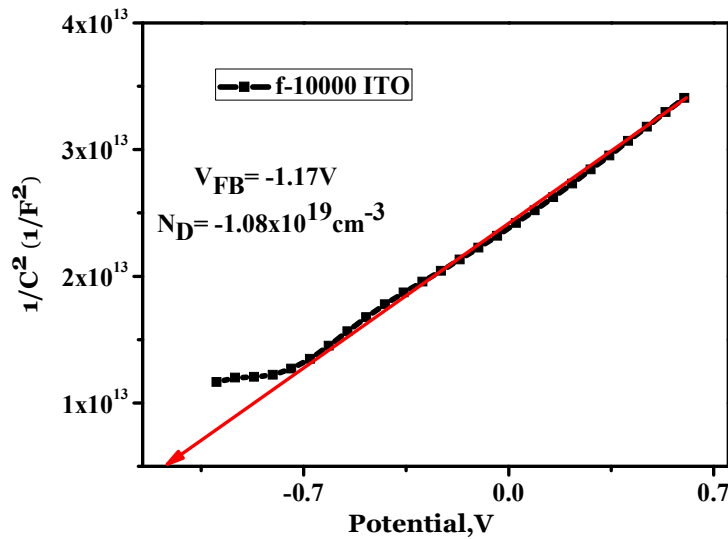
Figure 4.7. Mott-Schottky plots for n-type ITO.
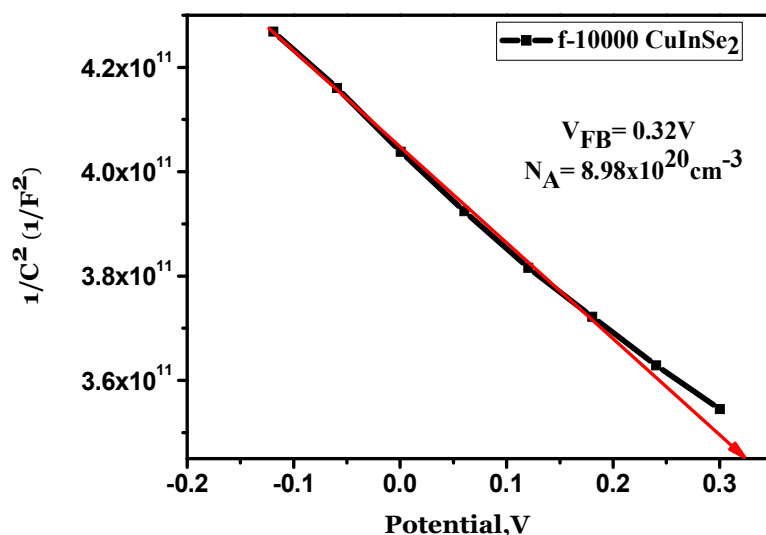
Figure 4.8. Mott-Schottky plots for p-type CuInSe$_2$ selenized thin films.
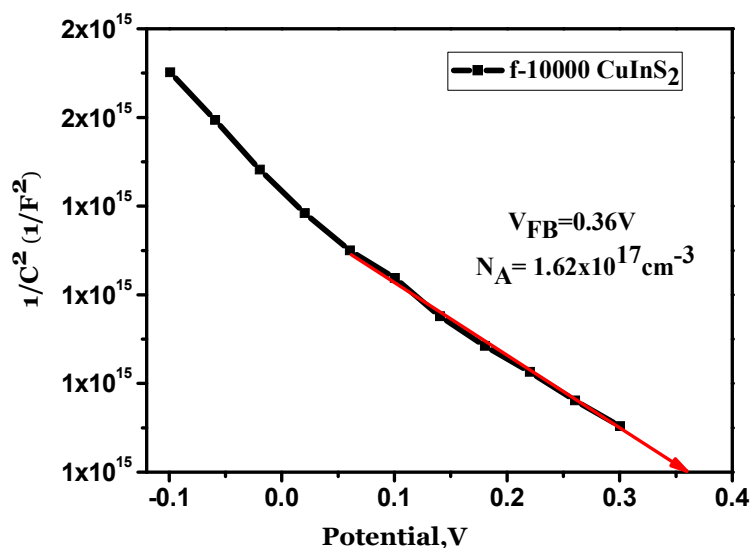
Figure 4.9. Mott-Schottky plots for p-type CuInS$_2$ sulfurized thin films.

Figures (4.7, 4.8, 4.9) show the plots of Mott-Schottky measurements for ITO and CIS thin-films ($1/C^2$ vs. V) in 0.5M NaOH. Figure (4.6) shows the Mott-Schottky (MS) plot for the ITO substrate layer. The resulting slope was positive, indicating that the ITO film is an n-type semiconductor. The flat band potential was found to be -1.17V (vs SCE) by extrapolating the linear section to the x-axis and $N_D \approx 1.18 \cdot 10^{19}$ cm^{-3} was measured using the slope of the curve. Figures (4.8 and 4.9), respectively, show the plots for CuInSe$_2$-Se selenized and CuInSe$_2$-S

sulfurized films. The calculated slopes of the (MS) plots were negative, verifying that the prepared CIS thin film is a p-type semiconductor. The flat band potential was found to be 0.32 and 0.36 V (vs SCE), respectively, extrapolating the linear section to the x-axis. The carrier concentrations, NA $\approx 8.98 \cdot 10^{20}$ and $1.62 \cdot 10^{17}$ cm^{-3}, were calculated using the slope of the curves for both CuInSe$_2$-Se and CuInSe$_2$-S films, respectively. It was noticed that the flat-band potential and acceptor density determined were slightly higher than the p-type semiconductor CIS film values [24, 25].
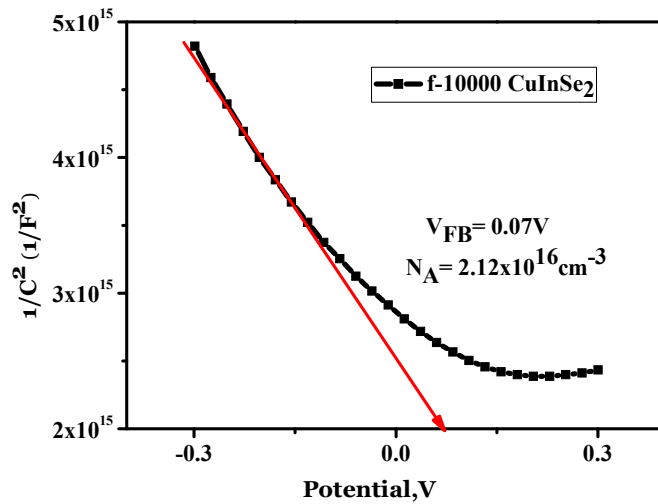

Figure 4.10. Mott-Schottky plots for p-type etched CuInSe$_2$ selenized thin films.
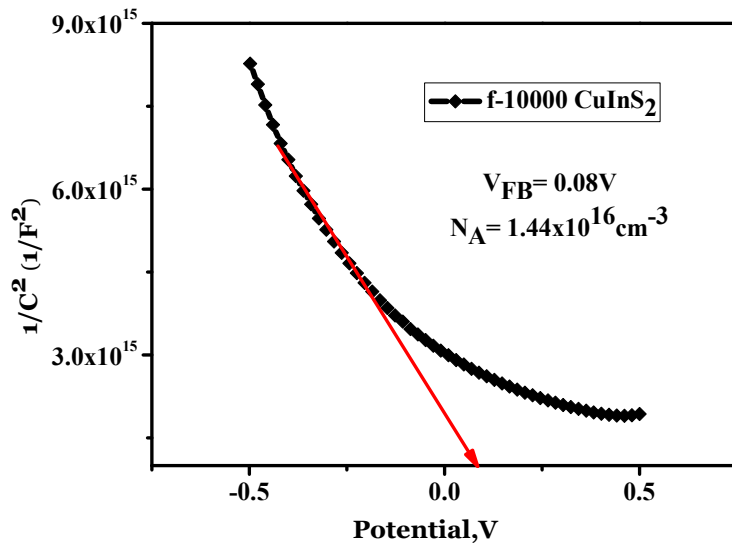

Figure 4.11. Mott-Schottky plots for p-type etched CuInS$_2$ sulfurized thin films.

Before the etching process, the slope of the Mott–Schottky plots were has a higher doping density $N_A \approx 8.98 \cdot 10^{20}$ and $1.62 \cdot 10^{17}$ cm^{-3} and the x-axis intercept associated with the flat band potential was highly positive 0.32 and 0.36 V (vs SCE). Table 4.3. displays the flat band potential and number of acceptors of the CuInSe$_2$-Se and CuInSe$_2$-S films before and after etching.

Table 4.3. Flat band potential V_{fb} (V) and number of acceptors N_A (cm^{-3}) of the CuInSe$_2$-Se and CuInSe$_2$-S films before and after etching.

Sample Name	Measured values	before etching	after etching
CuInSe$_2$-selenized	N_A (cm^{-3})	$8.98 \cdot 10^{20}$	$2.12 \cdot 10^{16}$
	V_{fb} (V)	0.32	0.07
CuInS$_2$-sulfurized	N_A (cm^{-3})	$1.62 \cdot 10^{17}$	$1.44 \cdot 10^{16}$
	V_{fb} (V)	0.36	0.08

In order to explain the resulting number of acceptor values, an etching process was carried out. Etching process using KCN solution influences the Mott-Schottky results.

Figures (4.10 and 4.11) show the Mott-Schottky plots of etched CuInSe$_2$ selenized and etched CuInS$_2$ sulfurized CIS thin-films samples ($1/C^2$ vs. V) in 0.5M NaOH. After the etching process, the slope of the Mott-Schottky (MS) plots showed a decrease in the doping density, and the calculated carrier density $N_A \approx 2.12 \cdot 10^{16}$ and $1.44 \cdot 10^{16}$ cm^{-3} for etched CuInSe$_2$ selenized and etched CuInS$_2$ sulfurized samples, respectively. Also, a drastic decrease in the flat band potential values was observed. It was found that the flat band potential had decreased to 0.07 and 0.08 V (vs SCE) for etched CuInSe$_2$ selenized and etched CuInS$_2$ sulfurized samples, respectively. The carrier charge density for the etched samples was found to have 10^{17}, 10^{20} to 10^{16} cm^{-3}. This decrease in both N_A and the photocurrent potential was attributed to the etching process. Through etching the accumulation of binary Cu$_{2-x}$(Se, S) phases shown in FE-SEM pictures was removed. These binary Cu$_{2-x}$ (Se,S) phases are highly conductive, leading to an increase of the flat band potential values. After the etching process the flat band potential is much closer to the literature values for p-type materials, being approximately +0.1 V [24-26]. The shift in the flat band value is due to the change in the position of the Fermi level, which depends on the density

of acceptors. After etching, the density of acceptors decreases and then the Fermi level shifts towards the middle of the forbidden band resulting in a drop of the flatband potential (V_{fb}).

4.9. Conclusion

In this study, a facile methodology for the preparation of p-type $CuInSe_2$ and $CuInS_2$ thin films has been described. The nano-crystalline $CuInSe_2$ and $CuInS_2$ thin films were successfully prepared by a non-vacuum, low cost electrodeposition technique onto ITO substrates. The resulting thin films showed very good crystallinity and homogeneity of the prepared films in agreement with the XRD, SEM and EDX measurements. In order to detect the prepared thin film carrier density type, Mott-Schottky measurements were carried out confirming that the prepared $CuInSe_2$ and $CuInS_2$ thin films were always p-type. The accumulated binary phases of Cu_{2-x}(Se, S) were successfully eliminated through the etching process which in turn decreased both the flat band potential, V_{fb} (V) and the number of acceptors, N_A (cm^{-3}) for the prepared samples.

4.10. References

[1] J.E. Jaffe, A. Zunger, Phys. Rev. B 29 (1984) 1882.

[2] I. Repins, M.A. Contreras, B. Egaas, C. DeHart, J. Scharf, C.L. Perkins, B. To, R. Noufi, Prog. Photovolt. Res. Appl. 16 (2008) 235.

[3] D. Lincot, Thin Sold Films 487 (2005) 40.

[4] I.M. Dharmadasa, N.B. Chaure, G.J. Tolan, A.P. Samantilleke, J. Electrochem. Soc. 154 (6) (2007) H466.

[5] T. Delsol, M.C. Simmonds, I.M. Dharmadasa, Sol. Energy Mater. Sol. Cells 77(2003) 331.

[6] A. Kampman, J. Rechid, A. Raitzig, S. Wulff, M. Mihhailova, R. Thyen, K. Kalberlah, Mater. Res. Soc. Symp. Proc. 763 (2003) 323

[7] R. Friedfeld, R.P. Raffaelle, J.G. Mantovani, Sol. Energy Mater. Sol. Cells 58(1999) 375.

[8] R.N. Bhattacharya, J.F. Hiltner, W. Batchelor, M.A. Contreras, R.N. Noufi, J.R. Sites, Thin Solid Films 361 (2000) 396.

[9] M.E. Calixto, K.D. Dobson, B.E. McCandless, R.W. Birkmire, J. Electrochem. Soc. 153 (6) (2006) G521.

[10] A.M. Hermann, C. Gonzalez, P.A. Ramakrishnan, D. Balzar, N. Popa, P. Rice, C.H. Marshall, J.N. Hilfiker, T. Tiwald, P.J. Sebastian, M.E. Calixto, R.N. Bhattachary, Sol. Energy Mater. Sol. Cells 70 (2001) 345.

[11] S. Taunier, J. Sicx-Kurdi, P.P. Grand, A. Chomont, O. Ramdani, L. Parissi, P. Panheleux, N. Naghavi, C. Hubert, M. Ben-Farah, J.P. Fauvarque, J. Connolly, O. Roussel, P. Mogensen, E. Mahe, J.F. Guillemoles, D. Lincot, O. Kerrec, Thin Solid Films 480 (2005) 526.

[12] S. Jost, F. Hergert, R. Hock, J. Schulze, A. Kirbs, T. VoX, M. Purwins, Sol. Energy Mater. Sol. Cells 91 (2007) 1669.

[13] S. Jost, F. Hergert, R. Hock, J. Schulze, A. Kirbs, T. VoX, M. Purwins, M. Schmid, Sol. Energy Mater. Sol. Cells 91 (2007) 636.

[14] M. Paire, S. Delbos, J.Vidal, N. Naghavi, J.F. Guillemoles, Chalcogenide thin film Solar Cells, in Solar Cells Materials, Wiley, 2014.

[15] Z. Li kao, N. Naghavi, F. Erfurth, J.F. Guillemoles, I. Gerard, A. Etcheberry, J.L. Pelouard, S. Collin, G.Voorwinden, D. Lincot, Progress in Photovoltaics, 20(2012)582.

[16] M. Paire, L. Lombez, J.F. Guillemoles, D. Lincot, J. Appl. Phys., 108(2010)034907.

[17] R.N. Bhattacharya, J. Electrochem. Soc. 130 (1983) 2040.

[18] O. Savadogo, Solar Energy Materials and Solar Cells 52 (1998) 361-388, Chemically and electrochemically deposited thin films for solar energy materials.

[19] F. Chraibi, M. Fahoume, A. Ennaoui, J.L. Delplancke, Phys. Status Solidi A 186(2001) 373.

[20] Armin E. Zaghi , Marie Buffiere, Guy Brammertz, Maria Batuk, Nick Lenaers, Bas Kniknie, Joke Hadermann, Marc Meuris, Jef Poortmans, Jef Vleugels, aAdvanced Powder Technology 25 (2014) 1254–1261

[21] K. Darowicki , S. Krakowiak, P. Slepski, Electrochimica Acta 51 (2006) 2204–2208, Selection of measurement frequency in Mott–Schottky analysis of passive layer on nickel.

[22] L. Djellal, S. Omeiri, A. Bouguelia, M. Trari, Photoelectrochemical hydrogen-evolution over p-type chalcopyrite $CuInSe_2$, Journal of Alloys and Compounds 476 (2009) 584–589

[23] Sreekanth Mandati, Bulusu V. Sarada, Suhash R. Dey, Shrikant V. Joshi, Journal of Power Sources, 273 (2015) 149-157.

[24] Brandon K. Durant, B.A. Parkinson, Solar Energy Materials&Solar Cells144(2016)586–591.

[25] Zhou Cao, Sui Yang, Mang Wang, Xiaopan Huang, Hongxing Li, Jie Yi, Jianxin Zhong, Solar Energy 139 (2016) 29–35

[26] Sreekanth Mandati, Bulusu V. Sarada, Suhash R. Dey, Shrikant V. Joshi, Journal of Power Sources 273 (2015) 149-157.

[27] M. Sharon, an Introduction to the Physics and Electrochemistry of Semiconductors: Fundamentals and Applications, Published 2016 by John Wiley & Sons, Inc, DOI: 10.1002/9781119274360

Chapter 5. CIGS:Cr thin films

5.1. Objectives

The main objective was to prepare new doped high quality nanocrystalline CIGS and CIGS:Cr powder using low cost hydrothermal process to develop low cost solar cell absorber layer. The specific objectives are:

i. To manage an easy route for the synthesis process of CIGS by incorporation of Cr with different Ga ratios and fixed In ratio.

ii. To evaluate the effect of different Cr% doping on CIGS nanocrystalline powders and thin films.

iii. To Study the EIS for the prepared CIGS:Cr and its relation with the crystal size.

5.2. Introduction:

I-III-VI$_2$ chalcopyrite compounds, particularly copper indium gallium selenide CuIn$_x$Cr$_y$Ga$_{1-x-y}$Se$_2$(CIGS), is intensively applied in the manufacture of thin-film solar cells, due to their high efficiencies and stability [1]. These materials possess advantageous properties for application in solar cells. Their direct band-gap energies as semiconductors lead to a high optical absorption coefficient[2].

CIGS thin films were fabricated using nonvacuum techniques, such as co-evaporation and sputtering techniques [3–5]. However, vacuum based processes resulting low yield, high costs, and difficulties for large areas coatings. These multistage co-evaporation and two-step processes involving sputtering and selenization are considered the main disadvantage facing the development of this type CIGS thin-films solar cell. A lot of alternative methods have been proposed to solve this problem, such as non-vacuum processes such as sol–gel, colloidal methods [6], paste coating [7], inkjet printing [8] and solvothermal processes [9,10]. Obviously, a lot of effort has been directed to the development of two step synthesis processes involving the synthesis of CIGS nanocrystal precursor inks for printing or coating followed by selenization [11–13]. These non-vacuum film deposition-based techniques offer an attractive alternative to vacuum-based processes. Non-vacuum processes are used in industrial applications widely due to their low cost competitive demand in solar cells scale production. One of these non-vacum attractive family processes is the solvothermal method [14–18]. This method of preparation

produces precursor powder that is easily converted into high quality thin films. Our interest in this paper is succeeding in the preparation of well controlled a few hundred nanometer particles of $CuIn_xCr_yGa_{1-x-y}Se_2$ in order to develop well definite thin films with controlled structure. This in role can be modified by some dopants in order to enhance new efficient thin film solar cells. This will be discussed later in some future work.

5.3. EXPERIMENTAL

5.3.1. Synthesis of $CuIn_xCr_yGa_{1-x-y}Se_2$ nano-percursor powders:

$CuIn_xCr_yGa_{1-x-y}Se_2$ was synthesized according the procedure described in [ref.2] using autoclave the solvothermal method. Elemental powders of Cu (99.9%, Sigma–Aldrich), Se (99.99%, Sigma–Aldrich), GaI_3 (99%, Sigma–Aldrich) and $InCl_3$ (99.999%, Sigma–Aldrich) were used as copper, selenium, gallium and indium sources, respectively. $Cr (ClO_4)_3$ was used as Cr^{3+} source and Ethylenediamine (99.5%, Sigma–Aldrich) was used as a solvent. All constituents and solvent were introduced in a nitrogen-filled glove box that no oxygen air disturbs our materials. Awell-defined stoichiometry of the synthesized precursor was achieved by using 2 mmolof the copper elemental powder, 1 mmol of indium, galliummetal sources, and 4 mmol of selenium powder, respectively. Chromium percentage was calculated for every batch process in order to prepare different Cr and Ga series at fixed indium percentage to get this structure $CuIn_xCr_yGa_{1-x-y}Se_2$ with x=0.4 and y= (0.0, 0.1,0.2,0.3).

All weighed materials were stirred together with a suitable amount of solvent and left to stir overnight. Then the stirred solution was loaded into an autoclave Teflon container and annealed in an open air oven for 36h at 190-230°C. The resultant product was washed several times using ethanol and distilled water to remove excess byproduct or impurity materials. Centrifuging and ultra-sonication processeswere repeated every washing time. The centrifuging process were conducted for 10 min at 4000 rpm. Finally, the completely purified precursor powders were dried at 100°C for 2hours. A black nano-crystalline powder of $CuIn_xCr_yGa_{1-x-y}Se_2$ was obtained.

5.3.2. Synthesis of the $CuIn_xCr_yGa_{1-x-y}Se_2$ thin films:

All the collected synthesized precursor powders were washed several times with distilled water and ethanol in order to remove all sub product residue chemicals. These washed powders were then dried in open-air drier at 100°C for 2hrs. After this the powders were loaded into the glove

box redispersion in the same preparation solvent as and left for stirring overnight then filtered using 0.2μ mesh filters. Completely clear dissolved filtered precursors solution of the prepared nanocrystalline powders were obtained available for further processes.

Figure 5.1. Spin-coating process (feeding of dissolved metal solution onto ITO substrate using micropipette).

Indium tin oxide (ITO) glass substrates were cut down into small pieces of the desired surface area.Cleaning process of the glass substrate were applied by washing the substrates using soap, dis.H_2O, ethanol and acetone ultrasonically, dried and then introduced into the glove box. The dissolved nanocrystalline precursor solution was then transformed to thin films by spin coating process. Metal salts nano-crystalline precursor powder to solvent ratio were taken in consideration (1:3). Heat treatment using a pre-heated hot plate was applied for crystal structure growing till the desired film thickness was obtained.

5.4. Charaterization and Measurment

5.4.1. Structure study for both $CuIn_xCr_yGa_{1-x-y}Se_2$nano-crystalline powder and thin films:

The structure and phase of the prepared powder were investigated using X-ray diffraction (XRD) Rigaku Ultima IV diffractometer in the Bragg-Bentano configuration using CuKα radiation (λ = 1.54060 Å). The particle size and morphology of the resultant CIGS precursor powder were characterized by Field Emission Scanning Electron Microscopy (FESEM) of model Zeiss ULTRA 55 equipped with In-Lens and secondary electrons detectors. High-Resolution Transmission Microscopy (HRTEM, 200 KV) JEOL Model: JEM-2100F were used to study the crystalline structure and morphology of nanowirearrays. The chemical composition and the purity of the prepared samples were characterized using energy dispersive spectroscopy (EDX). A Novocontrol broadband dielectric Spectrometer (BDS) (Hundsangen, Germany) integrated by

an SR 830 lock-in amplifier with an Alpha dielectric interface was used for measuring the conductivity of the resultant precursor powders.

5.4.2. Electrochemical impedance spectroscopy (EIS) measurment

The conductivity of the samples in the transversal direction were measured in a range of temperature between 20 and 200°C by impedance spectroscopy in the frequency interval of $10^{-1} <$ f $< 10^7$ Hz applying a 0.1 V signal amplitude. In previous measurements different voltages (0.1, 0.5 and 1V) was considered with the intention to ensure the linear response. From the results observed we have considered that 100 mV is the chosen in order to get a linear regime. The measurements were carried out in dry and wet conditions. A Novocontrol broadband dielectric Spectrometer (BDS) (Hundsangen, Germany) integrated by an SR 830 lock-in amplifier with an Alpha dielectric interface was used. The samples were previously dried and their thicknesses were measured afterwards using a micrometer, taking the average of ten measurements in different parts of the surface. For the study of the conductivity dry conditions the samples were dried in a vacuum cell. Next the samples were sandwiched between two gold circular electrodes coupled to the impedance spectrometer acting as blocking electrodes. The assembly membrane-electrode was annealed in the Novocontrol setup under an inert dry nitrogen atmosphere previously to the start of the actual measurement. For this, firstly a temperature cycle from 20°C to 200°C to 20°C, in steps of 20°C, was carried out. After this, in a new cycle of temperature scan, the dielectric spectra were collected in each step. This was performed to ensure the measurements' reproducibility and to eliminate the potential interference of water retained by the composite membranes, in particular taking into account the hygroscopicity of this kind of samples. For the measurements in wet conditions the samples were previously dissolved in bi-distilled water in the ratio 40:60 wt% (sample:water) to obtain a paste which was subsequently sandwiched between the the two gold circular electrodes. During the measurements the electrodes were kept in a BDS 1308 liquid device, coupled to the spectrometer and incorporating deionized water to ensure a fully hydrated state of the samples below 100°C and in equilibrium with its vapor above 100°C, to simulate 100% RH atmosphere. During the conductivity measurements, the temperature was maintained (isothermal experiments) or changed stepwise from 20 to 200°C controlled by a nitrogen jet (QUATRO from Novocontrol) with a temperature error of 0.1 K during every single sweep in frequency.

From the frequency dependence of complex impedance $Z^*(\omega) = Z'(\omega) + j.Z''(\omega)$, the real part of the conductivity is given as:

$$\sigma'(\omega) = \left[\frac{Z'(\omega) \cdot L}{\left[(Z'(\omega))^2 + (Z''(\omega))^2\right] \cdot S}\right] = \frac{L}{R_0 \cdot S}$$

(1)

where L and S are the thickness and area of the sample in contact with the electrodes, respectively, and R_0 the resistance of the sample.

5.5. Results and discussion

CuIn$_x$Ga$_{1-x}$Se$_2$ (CIGS) Nanocrystal Synthesis.

CIGS nanocrystals were synthesized following the routine shown above:

$$Cu + xInCl_3 + (1 - x - y)GaI_3 + (y\, Cr(ClO)_4)_3)$$
$$+ 2Se \xrightarrow[190 - 230°C]{ethylenediamine} Cu(In_xCr_yGa_{1-x-y})Se_2 \text{ nanocrystals}$$
$$+ by\ products$$
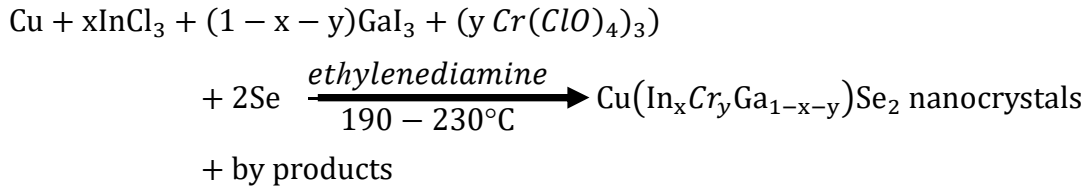
The In and Ga ratio could be changed with different stoichiometric ranges of x from 0 to 1 using this approach.

5.5.1. Structure Study

5.5.1.1. XRD of the CuIn$_x$Cr$_y$Ga$_{1-x-y}$Se$_2$ precursor powder

Figure 5.2. shows the XRD pattern of the prepared sample with a chalcopyrite structure. A sharp diffraction peaks was obtained which confirms that the resulted nanocrystals have a chalcopyrite (tetragonal) phase with a definite structure of CuIn$_{0.4}$Ga$_{0.6}$Se$_2$ and that no other phases are produced in the reaction. Standard CIGS file (PDF card No. 00–035-1101) is used to identify the diffraction peaks. All peaks are identified as a pure phase of the synthesized CuIn$_x$Ga$_{1-x}$Se$_2$ chalcopyrite phase with no secondary phases. It is clearly obvious from the XRD pattern (Figure 5.2) the main characteristic peaks of the tetragonal chalcopyrite structure. The main peaks of CIGS (112) at about 27.36°, CIGS (204)/(220) at $2\theta = 45.35°$, and CIGS (116)/(312) at 2θ =53.62° , respectively.
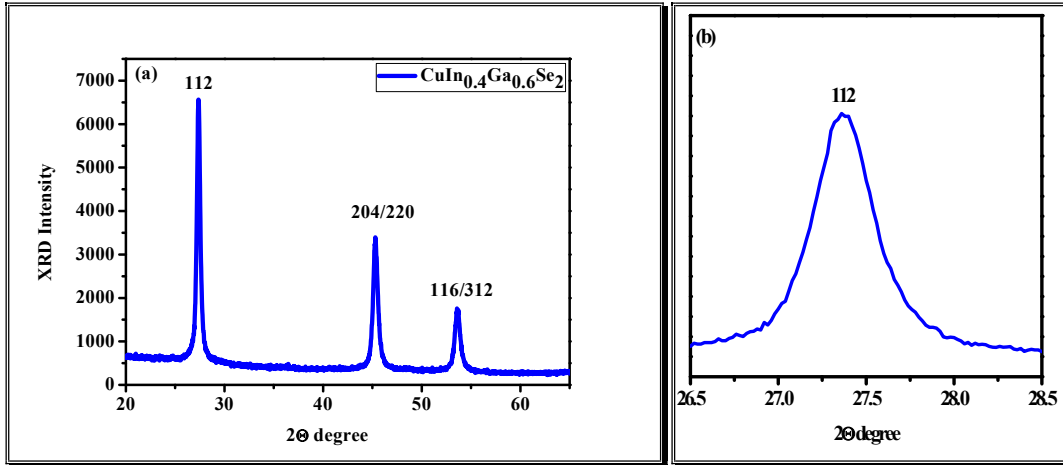
Figure 5.2. (a) XRD patterns of $CuIn_{0.4}Ga_{0.6}Se_2$ precursor nanocrystals prepared by autoclave hydrothermal method and (b) FWHM for 112 peak.
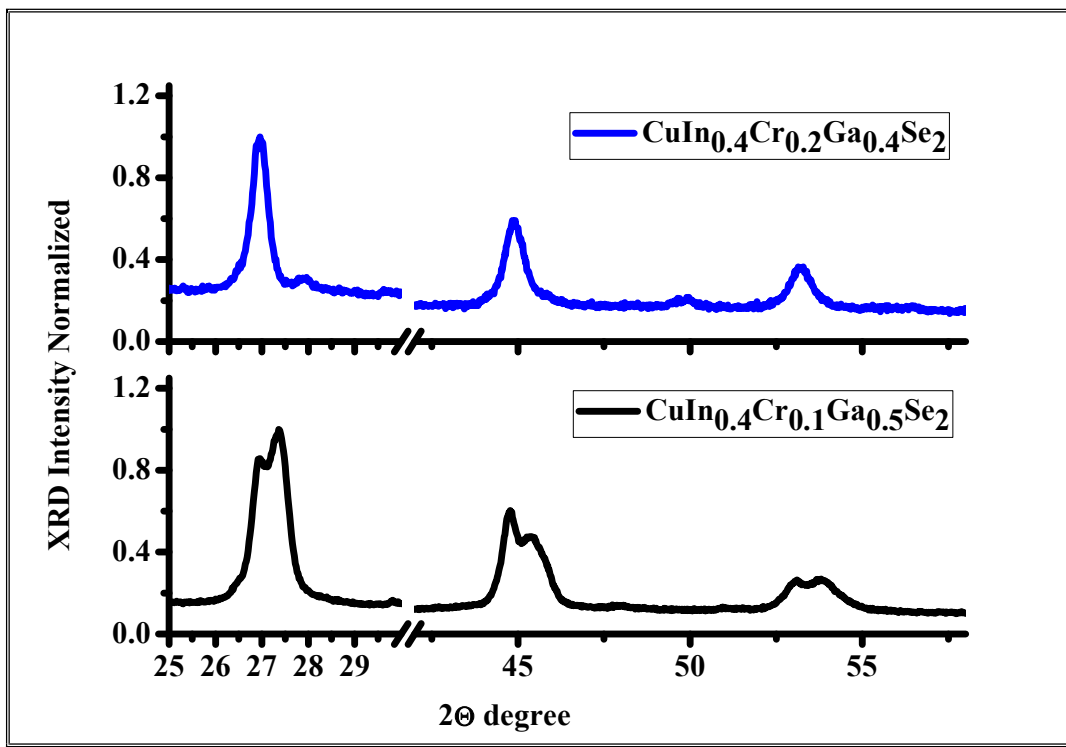

Figure 5.3. XRD patterns of $CuIn_{0.4}Cr_{0.1}Ga_{0.5}Se_2$ and $CuIn_{0.4}Cr_{0.2}Ga_{0.4}Se_2$ precursor nanocrystals prepared by autoclave hydrothermal method.

Figure 5.3. Shows the XRD pattern of $CuIn_{0.4}Cr_{0.1}Ga_{0.5}Se_2$ and $CuIn_{0.4}Cr_{0.2}Ga_{0.4}Se_2$ nanocrystals precursor powders prepared by autoclave hydrothermal method. As it is clearly seen from the graph only those main characteristic peaks of chalcopyrite phase in both $CuIn_{0.4}Cr_{0.2}Ga_{0.4}Se_2$ and

144

$CuIn_{0.4}Cr_{0.1}Ga_{0.5}Se_2$, respectively. In $CuIn_{0.4}Cr_{0.2}Ga_{0.4}Se_2$ we can notice only those main peaks of CIGS (112) at about $26.94°$, CIGS (204)/(220) at $2\theta = 44.88°$, and CIGS (116)/(312) at $2\theta = 53.22°$, respectively. On the other hand, for the sample of $CuIn_{0.4}Cr_{0.1}Ga_{0.5}Se_2$ we can observe the main characteristic peaks of chalcopyrite CIGS in addition to wurtzite $Cu_{2-x}Se$ main peaks. Herein every peak is built up of summation of two divided peaks like camel humps (like it has been doubleted). We refer this peak shape to the presence of Cr^{3+} ions in the crystal lattice by a small percent. The incorporation of ions that has three electrons in the 3d shell with spin up, and the Cu^{1+} ion has a $3d^{10}$ configuration, i.e. there is one hole in the 3d shell, the spin of the Cu^{1+} ion is aligned antiparallel to that of Cr^{3+} ion. These holes are supposed to be delocalized and to occupy the states in a narrow d band. The metallic behavior is associated with the t_{2g} orbital of these delocalized Cu^{1+} holes.

Chromium and copper have $4s^1$ instead of $4s^2$. This is because chromium is 1 d-electron short for having a half-filled d-orbital, therefore it takes one from the s-orbital, so the electron configuration for chromium would just be: $[Ar]\ 4s^13d^5$. Similarly, for copper, it is 1 d-electron short for having a fully-filled d-orbital and takes one from the s-orbital, so the electron configuration for copper would simply be: $[Ar]\ 4s^13d^{10}$. We expect here a strong competition between $Cu_{2-x}Se$ wurtzite phase formation and $CuIn_{0.4}Cr_{0.1}Ga_{0.5}Se_2$ for this we notice clearly both phases formation. The intensity height of the grown phases indicates this confliction as the low content of Cr^{3+} ion then the grown process could show a clear single phase as shown in (Figure 5.3). In contrast to the prepared $CuIn_{0.4}Cr_{0.2}Ga_{0.4}Se_2$ samples where the percentage of Cr^{3+} is equal to 2% which is higher than $CuIn_{0.4}Cr_{0.1}Ga_{0.5}Se_2$ where Cr^{3+} percentage is approximately 10%, the increase in Cr^{3+} content affect clearly the stability of the $CuIn_xCr_yGa_{1-x-y}Se_2$, (x=0.4 and y= 0.0, 0.1, 0.2, 0.3) chalcopyrite phase formation. Then again, a deconvolution in the crystallographic structure due to increase of Cr percent where here 3 times (triple) of the primary incorporation of Cr^{3+} percentage. The $CuIn_{0.4}Cr_{0.3}Ga_{0.3}Se_2$ has 3% of Cr^{3+} ions in addition to Ga^{3+} ions, which in turn this time lead to a competition between Cr^{3+} and Ga^{3+} ions rather than the stated competition between Cr^{3+} and Cu^{1+} ions. But here in this time the Cu^{1+} ions were successive in disturbing the crystal structure forming a mix of copper selenide compounds, i.e; $CuSe_2$ and covellite $Cu_{2-x}Se$ as shown in (figure 5.6) for the $CuIn_{0.4}Cr_{0.3}Ga_{0.3}Se_2$ thin films onto ITO substrates.

Table 5.1. FWHM and particle size calculated for $CuIn_{0.4}Ga_{0.6}Se_2$, $CuIn_{0.4}Cr_{0.2}Ga_{0.4}Se_2$, $CuIn_{0.4}Cr_{0.1}Ga_{0.5}Se_2$, and $CuIn_{0.4}Cr_{0.3}Ga_{0.4}Se_2$ nano-crystalline percuorsor powders at 112 peak.

. Sample Name	hkl	2Θ	Θ	Cos Θ	FWHM	Particle size(nm)
$CuIn_{0.4}Ga_{0.6}Se_2$	112	27.36	13.68	0.9716	0.39	20
$CuIn_{0.4}Cr_{0.1}Ga_{0.6}Se_2$	112	26.92	13.63	0.9718	0.83	10
$CuIn_{0.4}Cr_{0.2}Ga_{0.6}Se_2$	112	26.94	13.45	0.9724	0.48	17

The mean crystallite size of the prepared polycrystalline CIGS was calculated according to Scherer's formula:

$$D = \frac{K\lambda}{\beta cos\theta}$$

where β is the Full Width at Half Maximum (FWHM), λ wavelength of X-rays with value is 1.5418Å, K is the Scherer's constant depending on the crystallite shape and is close to 1 and θ is the Bragg angle at the center of the peak.

In (Figure 5.2) the calculated FWHM was equal to 0.39 for 112 and the particle size was equal to 20 nm. The XRD patterns obtained in this case were assignable to a tetragonal $CuIn_{0.4}Ga_{0.6}Se_2$ crystallographic phase (PDF card No. 00–035-1101) with preferred orientation along the (112) plane. No other stoichiometric composition of CIGS was obtained very clear single chalcopyrite phase. The well defined and sharp diffraction peaks indicated that the material showed good crystallinity and purity and this was an evidence for the absence of any additional diffraction peaks of possible binary phases or impurities. In (Figure 5.3) we can notice the main characteristic peaks for the $CuIn_{0.4}Cr_{0.1}Ga_{0.5}Se_2$ samples were located at 26.93°, 44.77 °, 53.03°, respectively, whereas they were combined with a subsidiary wurtzite $Cu_{2-x}Se$ phase located at 27.35°, 45.48°, 53.79°, respectively,shifted to higher 2Θ degrees.

5.5.1.2. XRD of $CuIn_xCr_yGa_{1-x-y}Se_2$ thin films:

Figure5.4. shows the XRD graph of the thin film $CuIn_{0.4}Ga_{0.6}Se_2$ on ITO substrate. All of the patterns are consistent with chalcopyrite (tetragonal) crystal structure and exhibit the expected amount of peak broadening due to their nanoscale crystal size domain. The diffraction peaks shift to lower 2θ degrees with decreasing Ga content by incorporation of Cr^{3+} ions in Ga^{3+} sites. The increase in the lattice spacing is due to smaller Cr atoms substituting for larger Ga atoms

which in turn lead to a significant change in lattice parameters values. Chalcopyrite type compound semiconductors with $Cu(In,Ga)Se_2$ composition are successfully implemented as absorber layers in thin film solar cells. The stoichiometric compound $Cu(In,Ga)Se_2$ crystallizes in the tetragonal chalcopyrite type crystal structure with space group $I42d$. Within this crystal structure the monovalent cations (Cu^{1+}) occupy the 4a site (0 0 0), the trivalent cations (In^{3+} and Ga^{3+}) are situated on the 4b position (0 0 ½) and the selenium anions are on the 8d site (x ¼ ⅛). The cations are tetrahedrally coordinated by the anions and vice versa, substitution of Ga^{3+} ions with Cr affect lattice values due to the difference in atomic radius of both Cr and Ga atoms. In general $Cu(In,Ga)Se_2$ absorber layers exhibit a copper-poor composition (Cu/(In+Ga) < 1), whereby the chalcopyrite type crystal structure still persists but the occupation of the Wyckoff sites may change and various kinds of intrinsic point defects are present within the material. The kind and concentration of these defects strongly correlate with the electronic and optical properties of the final device and the knowledge about them is crucial to tailor high efficient photovoltaic devices made of such compounds. All the doped samples with Cr show an increase in the lattice value corresponding to the FWHM value for $CuIn_{0.4}Ga_{0.4}Se_2$. We notice the main characteristic peaks of $CuIn_{0.4}Ga_{0.6}Se_2$ and those characteristics of ITO. A well-defined crystallographic chalcopyrite structure with all preferred orientation a long 112, (204)/(220) and (116)/(312) for $CuIn_{0.4}Ga_{0.4}Se_2$ at 2θ =27.49°, 2θ = 45.37°, and 2θ = 53.36° is clearly observed. The mainly peaks of ITO is located at 2θ = 30.58° and 35.48°, respectively.

Figure5.5. shows the XRD graph of the thin film $CuIn_{0.4}Cr_{0.1}Ga_{0.5}Se_2$ and $CuIn_{0.4}Cr_{0.2}Ga_{0.4}Se_2$ on ITO substrate. We notice those main characteristic peaks of $CuIn_{0.4}Cr_{0.2}Ga_{0.4}Se_2$ clearly at 2θ =27.18°, 2θ = 44.68°, and 2θ = 53.33° and those characteristics of ITO. A small percentage of wurtzite $Cu_{2-x}Se$ phase was observed by thin film formation, also duplicity of the main characteristic peaks is observed for $CuIn_{0.4}Cr_{0.1}Ga_{0.5}Se_2$ thin film samples. On the other hand the pure well defined highly oriented 112, (204)/(220) and (116)/(312) peaks for $CuIn_{0.4}Cr_{0.2}Ga_{0.4}Se_2$ were identified.

Figure5.6. shows the XRD graph of the thin film $CuIn_{0.4}Cr_{0.3}Ga_{0.3}e_2$ on ITO substrate. We notice those main characteristic peaks of $CuIn_{0.4}Cr_{0.3}Ga_{0.3}Se_2$ at 2θ =26.96°, 2θ = 44.78°, and 2θ = 53.94° and those characteristics of ITO. Mixture of copper selenide phases are very apparent in the XRD pattern for the $CuIn_{0.4}Cr_{0.3}Ga_{0.3}Se_2$ sample, i.e; covellite $Cu_{2-x}Se$ and $CuSe_2$, which is due to the stated confliction between both Cr^{3+} and Cu^{1+} ions at definite amount of incorporated

Cr^{3+} ions that results in impurity phase formation structure. Using Scherres formula the crystal size of all the prepared thin films of $CuIn_{0.4}Ga_{0.4}Se_2$, $CuIn_{0.4}Cr_{0.1}Ga_{0.5}Se_2$, $CuIn_{0.4}Cr_{0.2}Ga_{0.4}Se_2$, and $CuIn_{0.4}Cr_{0.3}Ga_{0.4}Se_2$ were calculated. It was found that the crystal size is equal to 20, 10, 17, and 18 nm for all the prepared samples of the structure where x = 0.4 and y = 0.0, 0.1, 0.2, 0.3, respectively. It was shown that the FWHM of $CuIn_{0.4}Cr_{0.1}Ga_{0.5}Se_2$ thin film sample show remarkable higher value than those of $CuIn_{0.4}Ga_{0.6}Se_2$, $CuIn_{0.4}Cr_{0.2}Ga_{0.4}Se_2$, and $CuIn_{0.4}Cr_{0.3}Ga_{0.4}Se_2$. This remarkable increase of FWHM value looks like those FWHM values of as grown samples, which confirms the structure defects and the stablished competition between Cr^{3+} and Cu^{1+} ions in the unit cell structure of those with low Cr% = 10, and Cr% = 30.

Table 5.2. FWHM and particle size calculated for $CuIn_{0.4}Ga_{0.6}Se_2$, $CuIn_{0.4}Cr_{0.1}Ga_{0.5}Se_2$, $CuIn_{0.4}Cr_{0.2}Ga_{0.4}Se_2$ and $CuIn_{0.4}Cr_{0.3}Ga_{0.4}Se_2$ nano-crystalline thin films at 112 peak.

| Sample Name	hkl	2Θ	Θ	Cos Θ	Sin Θ	FWHM	Particle size(nm)
$CuIn_{0.4}Ga_{0.6}Se_2$	112	27.49	13.75	0.9778	0.2097	0.4	20
$CuIn_{0.4}Cr_{0.1}Ga_{0.5}Se_2$	112	27.03	13.55	0.9774	0.2112	0.8	10
$CuIn_{0.4}Cr_{0.2}Ga_{0.4}Se_2$	112	27.18	13.40	0.9779	0.2089	0.5	17
$CuIn_{0.4}Cr_{0.3}Ga_{0.3}Se_2$	112	26.96	13.45	0.9777	0.2097	0.44	18
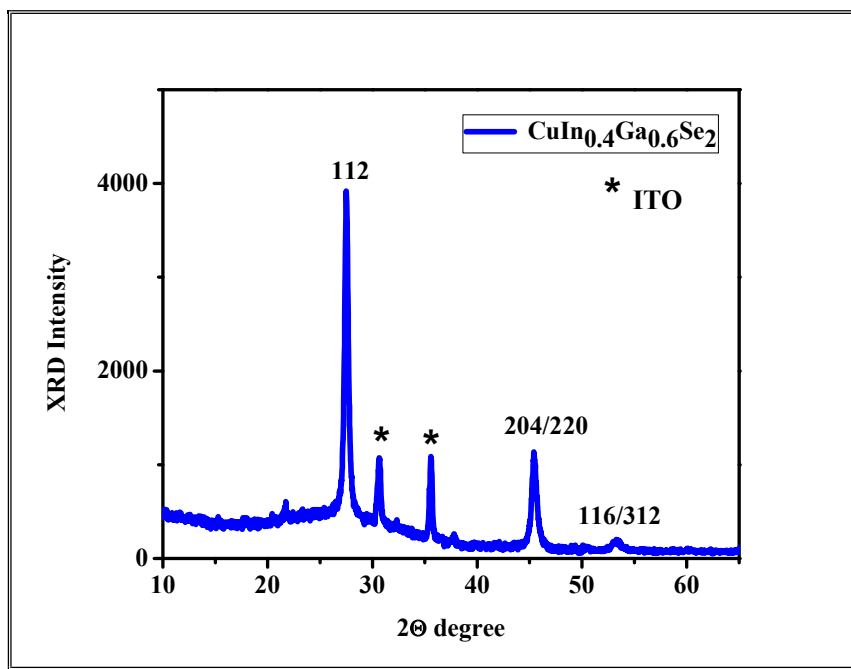
Figure 5.4. XRD patterns of $CuIn_{0.4}Ga_{0.6}Se_2$ thin film deposited on ITO substrate by Spin coating process.
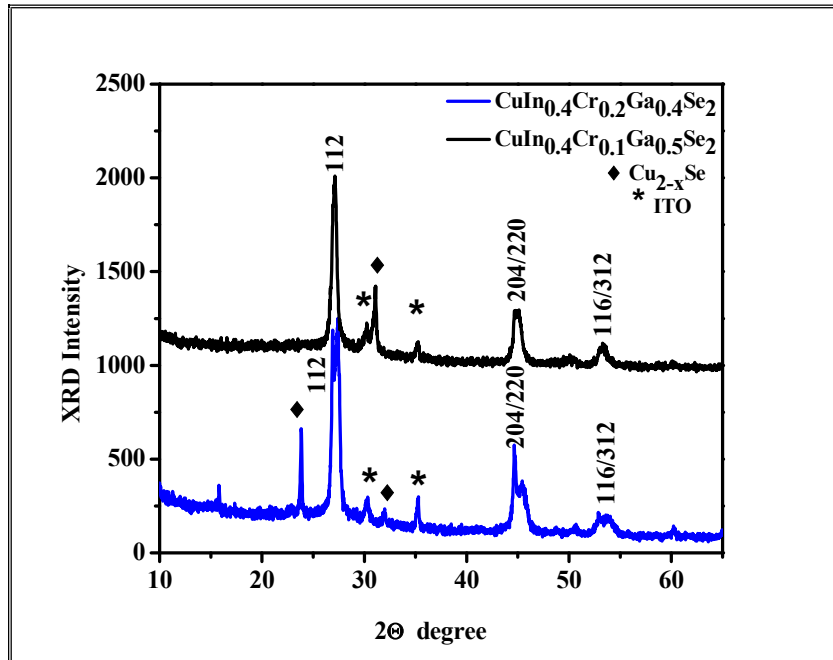
Figure 5.5. XRD patterns of $CuIn_{0.4}Cr_{0.1}Ga_{0.5}Se_2$ and $CuIn_{0.4}Cr_{0.2}Ga_{0.4}Se_2$ thin film deposited on ITO substrate by Spin coating process.
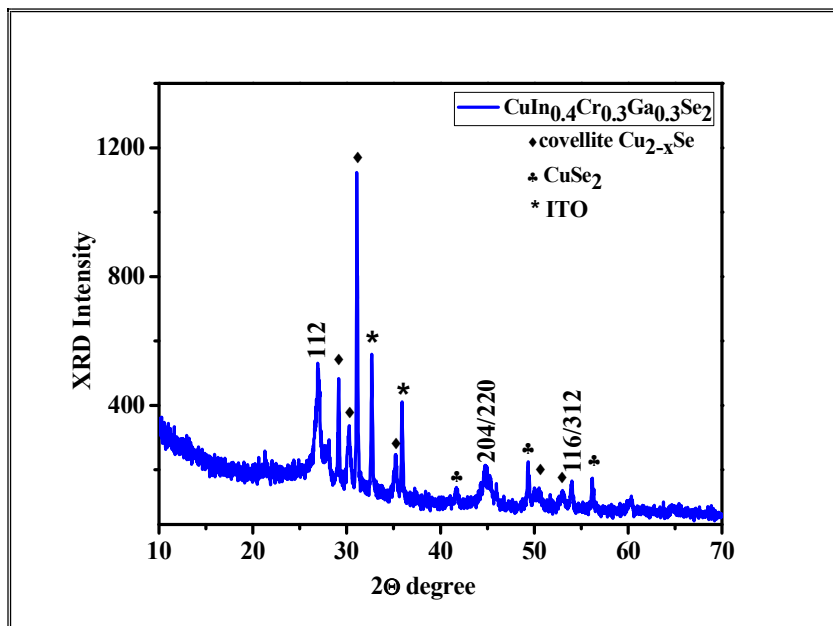
Figure 5.6. XRD patterns of $CuIn_{0.4}Cr_{0.3}Ga_{0.3}Se_2$ precursor thin films prepared by autoclave hydrothermal method

5.5.2. FESEM Analysis

5.5.2.1. FESEM Analysis of $CuIn_xCr_yGa_{1-x-y}Se_2$ nano-crystalline powders:

149

Figure 5.7. (A) and (B). shows FE-SEM images for $CuIn_xCr_yGa_{1-x-y}Se_2$ where x = 0.4 and y = (0.0, 0.1, 0.2, 0.3) nanocrystals. It is clearly observed that SEM images of (a) $CuIn_{0.4}Ga_{0.6}Se_2$, (b) $CuIn_{0.4}Cr_{0.1}Ga_{0.5}Se_2$, (c) $CuIn_{0.4}Cr_{0.2}Ga_{0.4}Se_2$, and (d) $CuIn_{0.4}Cr_{0.3}Ga_{0.3}Se_2$ nano-crystalline precursor powders contain agglomerates of spherical particles and a plate like shapes. As shown in the images we can see a wonderful homogenous collection of spherical particles together with some tetragonals and plate like shapes. Some tetrahedron hexagonal phases were determined in both (b) $CuIn_{0.4}Cr_{0.1}Ga_{0.5}Se_2$, (c) $CuIn_{0.4}Cr_{0.2}Ga_{0.4}Se_2$, and (d) $CuIn_{0.4}Cr_{0.3}Ga_{0.3}Se_2$ which in consistent with the XRD results. Those tetrahedron and hexagonals refers to the presence of $Cu_{2-x}Se$ and $CuSe_2$ phases in a complete matching with XRD peaks refer to CuSe phases presence. For the SEM images of (a) $CuIn_{0.4}Ga_{0.6}Se_2$ nano-crystalline powders only those spherical of the chalcopyrite structure and no other phases indication present. Which in turn confirms the XRD data and of crystal structure and particle size calculations.
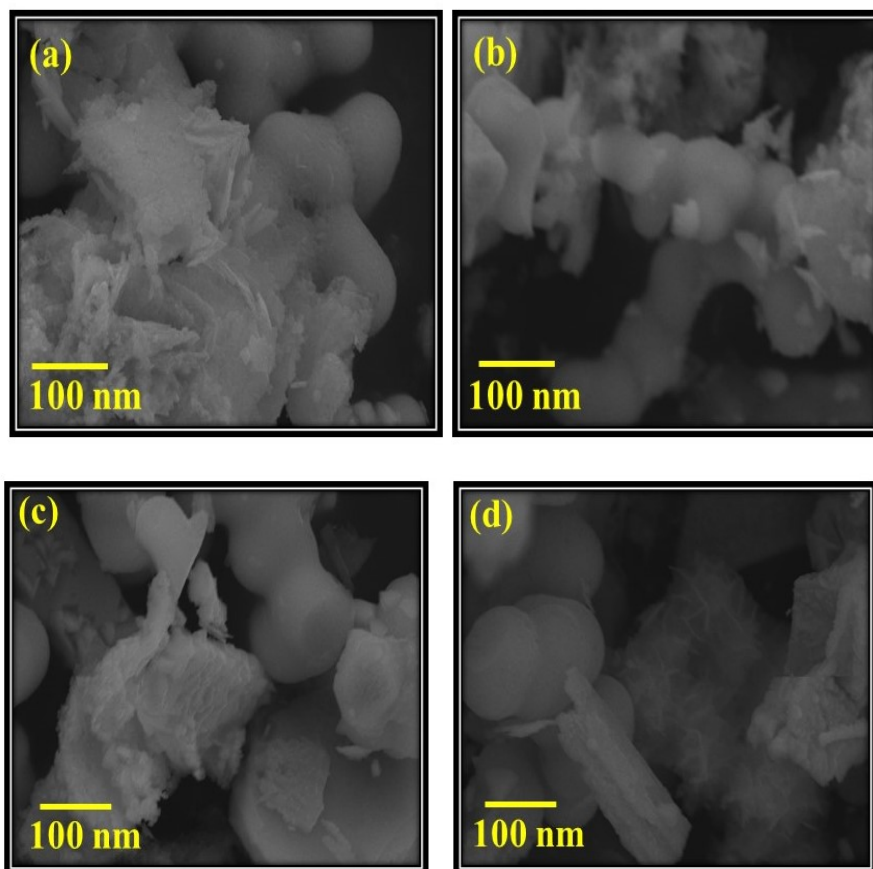

Figure 5.7(A). FE-SEM images for (a) $CuIn_{0.4}Ga_{0.6}Se_2$, (b) $CuIn_{0.4}Cr_{0.1}Ga_{0.5}Se_2$, (c) $CuIn_{0.4}Cr_{0.2}Ga_{0.4}Se_2$, and (d) $CuIn_{0.4}Cr_{0.3}Ga_{0.3}Se_2$ nano-crystalline precursor powders at 100 nm.
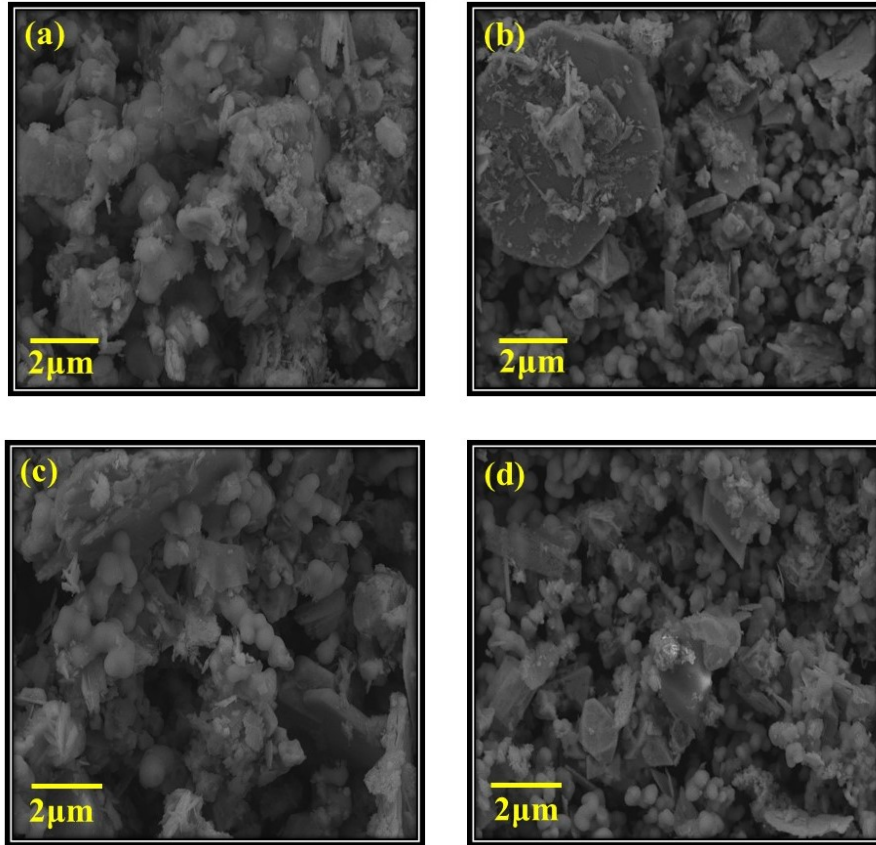
Figure 5.7(B). FE-SEM images for (a) $CuIn_{0.4}Ga_{0.6}Se_2$, (b) $CuIn_{0.4}Cr_{0.1}Ga_{0.5}Se_2$, (c) $CuIn_{0.4}Cr_{0.2}Ga_{0.4}Se_2$, and (d) $CuIn_{0.4}Cr_{0.3}Ga_{0.3}Se_2$ nano-crystalline precursor powders at 2μm.

The structures of the prepared precursor powders provide us with a promising feedback about the expected thin films surface morphology. Which in one way or another will resemble these prepared nano crystalline precursor powders. The average particle size is approximately (10-20nm) in accordance with the HRTEM and XRD crystallite size. Such characteristic properties will play a vital role in the deposition process of the CIGS thin films. Particle size, morphology, uniformity, homogeneity, adhesion and cohesion of the prepared precursor powders; all these properties will affect the nature of the resultant films by any formation process. In general, one aims for particulate precursor powders that with few hundred nanometers and good uniformity in particles shape will lead to a sufficient adhesion to the substrate and sufficient cohesion of one particle to another as shown in (Figure 5.7 (A) and (B)) that still in good intact until the final films formation.

5.5.2.2. FESEM Analysis of $CuIn_xCr_yGa_{1-x-y}Se_2$ thin films:

Figure 5.7(C). shows the FE-SEM images for (a) $CuIn_{0.4}Ga_{0.6}Se_2$, (b) $CuIn_{0.4}Cr_{0.1}Ga_{0.5}Se_2$, (c) $CuIn_{0.4}Cr_{0.2}Ga_{0.4}Se_2$, and (d) $CuIn_{0.4}Cr_{0.3}Ga_{0.3}Se_2$ thin films at 20μm. A very homogenous nano-crystalline thin films have been deposited using spin-coating process.
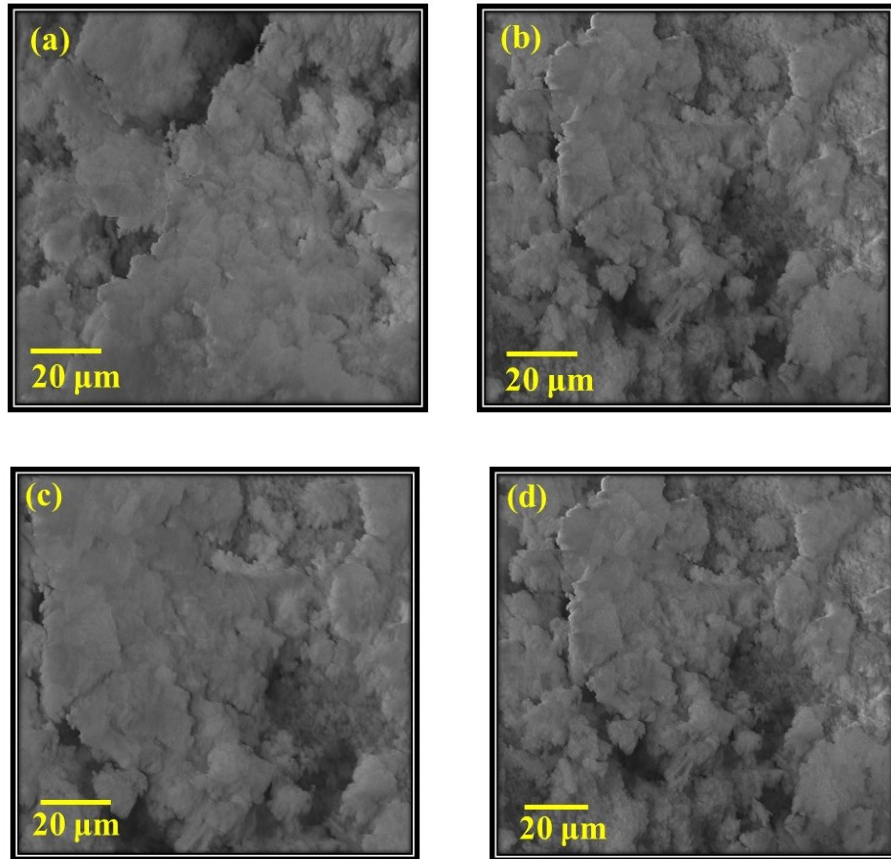

Figure 5.7(C) FE-SEM images for (a) $CuIn_{0.4}Ga_{0.6}Se_2$, (b) $CuIn_{0.4}Cr_{0.1}Ga_{0.5}Se_2$, (c) $CuIn_{0.4}Cr_{0.2}Ga_{0.4}Se_2$, and (d) $CuIn_{0.4}Cr_{0.3}Ga_{0.3}Se_2$ thin films at 20μm.

5.5.3. HRTEM analysis

Figure 5.8. shows the entire HRTEM image at different magnification scales of the prepared sample. The HRTEM images indicating the crystallinity of the synthesized polycrystalline $CuIn_{0.4}Ga_{0.6}Se_2$ powder by the hydrothermal method. We can notice that all HRTEM images contain well-arranged planes with lattice spacing corresponding to tetragonal $CuIn_xGa_{1-x}Se_2$ in accordance with the sharp well defined XRD peaks of the chalcopyrite (tetragonal) $CuIn_xGa_{1-x}Se_2$ and that no other phases are found.
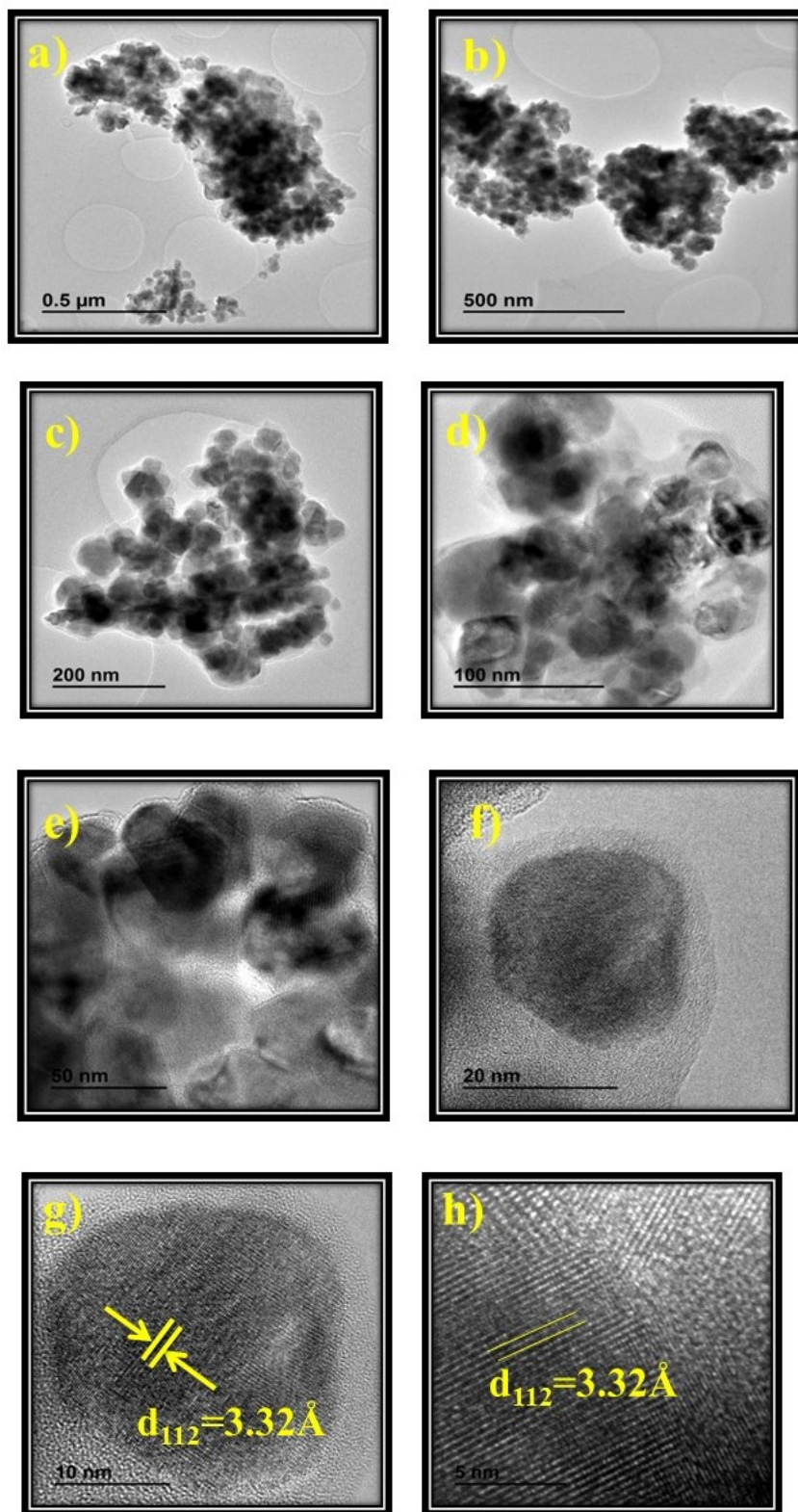
Figure 5.8. (a), (b), (c), (d) HRTEM images for $CuIn_{0.4}Ga_{0.6}Se_2$ nanocrystals. (g), (h) d-spacings of chalcopyrite (tetragonal) $CuIn_{0.4}Ga_{0.6}Se_2$.

The nanocrystals are approximately less than 50 nm in diameter. Both high-resolution TEM (Figure 5.8) and XRD (Figure 5.2) confirmed that the nanocrystals are crystalline with tetragonal chalcopyrite $CuIn_{0.4}Ga_{0.6}Se_2$ structure. The d-spacings observed in HRTEM images are also consistent with tetragonal $CuIn_xGa_{1-x}Se_2$ chalcopyrite phase and no other crystal phases were observed in accordance with the XRD pattern of the prepared powder.

The HRTEM images show well defined small grains of a few tens of nm as also observed by FESEM, shown in (Figure 5.7). Moreover, the measured lattice spacing of 3.32 A° from a high magnification HRTEM image (Figure 5.8 (g, h)) matches well with d (112).

5.5.4. *EDX analysis*

EDX results reveal that the prepared nano crystalline powders contain certain amount of the constituent elements in accordance to the desired structures. EDX analyses showed a stoichiometric ratio closer to the expected 0.87:0.4:0.6:1.98 ratios for copper, Indium, gallium and selenium. However, a slight decrease of Cu and Se was found in the resultant composition in addition to an observed decrease in Cu content. The slightly copper-poor composition is beneficial for the formation of p-type semiconductor. The proposed composition of the prepared nanocrystal precursor powder in the first sample has a molar Cu/In/Ga/Se ratio of 1.0:0.4:0.6:2.0 with a fixed In ratio for all prepared series with incorporation of Cr atoms in Ga sites. the composition of all measured individual particles by EDS was with a slight variation from the prepared ratio as shown in table 5.3.

We observed a copper deficiency from 1.0 to 0.87 indicating that the prepared $CuIn_{0.4}Ga_{0.6}Se_2$ are of p-type material. It is difficult to control the composition ratios in this type of chalcopyrite's, but we have succeeded with this hydrothermal autoclave method in optimizing the resultant product ratios of In and Ga by controlling several factors such as metal source, time of stirring and preparation temperature. A comparison between the proposed precursor composition and the resultant measured EDX composition is indicated in table.5.3.

Table 5.3. composition of nano-crystalline precursor powders.

| Sample	Cu (at%)	In (at%)	Cr (at%)	Ga (at%)	Se (at%)	Cu/ In+Cr+Ga	In/ In+Cr+Ga	Cr/ In+Cr+Ga	Ga/ In+Cr+Ga	Se/ In+Cr+Ga
$CuIn_{0.4}Ga_{0.6}Se_2$	22.62	9.69	----	16.31	51.38	0.87	0.4	----	0.6	1.98
$CuIn_{0.4}Cr_{0.1}Ga_{0.5}Se_2$	29.44	8.8	1.58	11.49	48.69	1.3	0.40	0.07	0.53	2.2
$CuIn_{0.4}Cr_{0.2}Ga_{0.4}Se_2$	26.92	9.87	3.20	9.87	50.14	1.2	0.43	0.14	0.43	2.3
$CuIn_{0.4}Cr_{0.3}Ga_{0.3}Se_2$	33.60	7.22	4.90	6.09	48.19	1.8	0.40	0.27	0.33	2.6
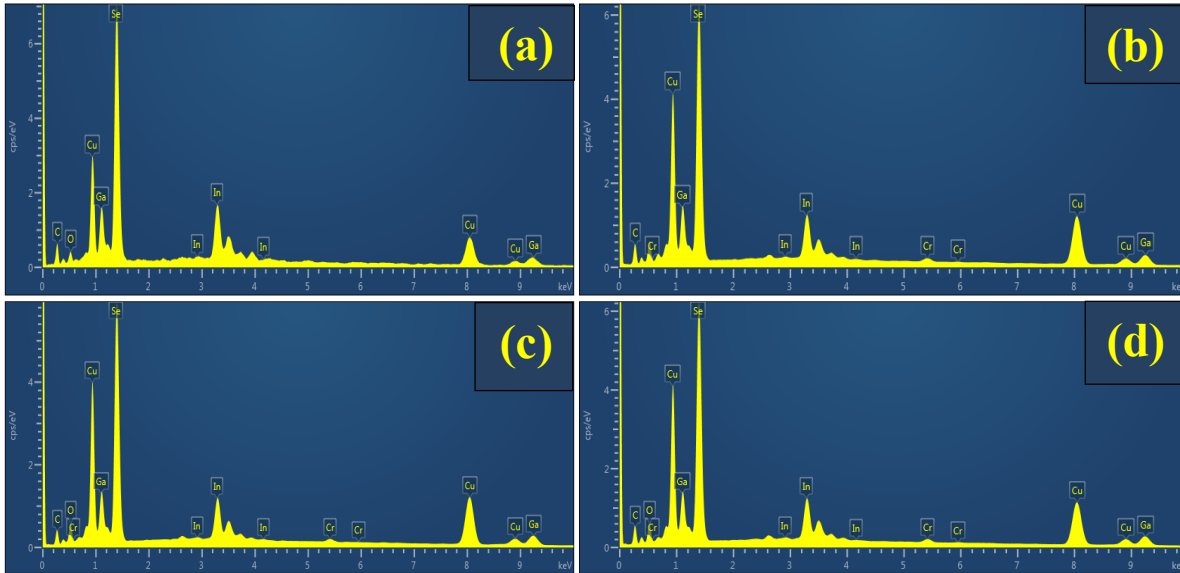
Figure 5.9. EDS charts for (a) $CuIn_{0.4}Ga_{0.6}Se_2$, (b) $CuIn_{0.4}Cr_{0.1}Ga_{0.5}Se_2$, (c) $CuIn_{0.4}Cr_{0.2}Ga_{0.4}Se_2$, and (d) $CuIn_{0.4}Cr_{0.3}Ga_{0.3}Se_2$ precursor powders.

Figure 5.9. show the EDS chart for $CuIn_{0.4}Ga_{0.6}Se_2$, $CuIn_{0.4}Cr_{0.1}Ga_{0.5}Se_2$, $CuIn_{0.4}Cr_{0.2}Ga_{0.4}Se_2$, and $CuIn_{0.4}Cr_{0.3}Ga_{0.3}Se_2$ precursor powders, respectively. For $CuIn_{0.4}Cr_{0.1}Ga_{0.5}Se_2$ sample the proposed composition of the prepared precursor (atomic ratio of Cu/In/Cr/Ga/Se) is equal to 1:0.4:0.1:0.5:2 with an atomic percentage equal 25:10:2.5:12.5:50. The resultant atomic ratio was equal to 1.3:0.4:0.07:0.53:2.3 with an atomic percentage equal 29.44:8.8:1.58:11.49:48.69 for Cu, In, Cr, Ga and Se, respectively. A slight increase in both Cu and Se atomic ratios is observed which in accordance with the XRD results for the presence of wurtzite $Cu_{2-x}Se$ phase in competition with the $CuIn_{0.4}Cr_{0.1}Ga_{0.5}Se_2$ chalcopyrite phase formation. This can be supposed also to the formation of $CuIn_{0.4}Cr_{0.1}Ga_{0.5}Se_2$ wurtzite phase also companion with the chalcopyrite phase. A very slight decrease in Cr and Ga atomic percentage is noticed, but in total Ga+Cr = Ga main atomic ratio before substitution and In ratio is completely fixed which in turn does not

affect the chalcopyrite phase formation even in the formation of the subsidiary phase as we explained in XRD part.

For $CuIn_{0.4}Cr_{0.2}Ga_{0.4}Se_2$ we noticed that the resulted composition atomic ratios for Cu, In, Cr, Ga, and Se were equal to 26.92:9.87:3.20:9.87:50.14 with an atomic percentage equal to (1.2:0.43:0.14:0.43:2.3). The proposed composition for this structure were (1:0.4:0.2:0.4:2) with an atomic ratio equal to (25:10:5:10:50). It is noticed that an equality in both In and Ga atomic ratios, slight decrease in Cr content than proposed it should work as 20% atomic ratio and it was found equal to 14%. This decrease in Cr content never affect the chalcopyrite crystal structure, in contrast it gives stability with preferred orientation to the structure. Not negative effective slight increase with the same ratio in both Cu and Se can be neglectable push this defined composition to be a promising material for CIGS photovoltaic technology.

Mixture of different copper selenide phases appear as secondary phases with the determined chalcopyrite tetragonal structure of $CuIn_{0.4}Cr_{0.3}Ga_{0.3}Se_2$. The proposed composition for this structure were (1:0.4:0.3:0.3:2) with an atomic ratio equal to (25:10:7.5:7.5:50). Herein an equal amount of Ga and Cr atoms was incorporated together in this studied phase with a noticeable remarkable increase and decrease in both Cu and Se atomic ratio compositions, respectively. We found that the resulted composition atomic ratios for Cu, In, Cr, Ga, and Se were equal to 33.60:7.22:4.90:6.09:48.19 with an atomic percentage equal to (1.8:0.4:0.27:0.33:2.6). In abbreviated words we conclude that it is best chosen to prepare doped $CuIn_xCr_yGa_{1-x-y}Se_2$ with an incorporation of Cr atoms by 20% at fixed In content = 40% of total In+Ga = 1.

5.5.5. Optical Properties and electric measurements:

5.5.5.1. Optical Properties:

Near the absorption edge or in the strong absorption zone of the transmittance spectra of materials, the absorption coefficient is related to the optical energy gap, E_g, which can be determined by the Tauc's formula:

$$\alpha = A(h\upsilon - E_g)^n / h\upsilon, \quad\quad\quad (5.1)$$

where A is an energy-independent constant, h is the Planck constant, υ is frequency, and n is an index that characterizes the optical absorption process and is theoretically equal to 2 and ½ for indirect and direct allowed transitions, respectively. The absorbance spectra of the $CuIn_xCr_yGa_{1-}$

$_{x-y}Se_2$ thin films were recorded and are displayed in Figure 5.10. All the $CuIn_xCr_yGa_{1-x-y}Se_2$ thin film samples exhibited broad absorption in the visible region. The absorption coefficients of all the samples prepared using spin-coating process $10^4\,cm^{-1}$ in the visible region, which supports that the deposited $CuIn_xCr_yGa_{1-x-y}Se_2$ material possessed a direct band gap. Extrapolation of the straight line to zero absorption coefficient ($\alpha=0$) allows estimation of E_g. That is, the band gaps were obtained by plotting $(\alpha h\upsilon)^2$ *versus* the energy in eV and extrapolating the linear part of the spectrum ($h\upsilon$). The inset of Figure 5.10. shows the band gaps of the $CuIn_xCr_yGa_{1-x-y}Se_2$ thin films prepared using different Ga and Cr with fixed In atomic ratio times.

The prepared $CuIn_{0.4}Ga_{0.6}Se_2$, $CuIn_{0.4}Cr_{0.1}Ga_{0.5}Se_2$, $CuIn_{0.4}Cr_{0.2}Ga_{0.4}Se_2$, and $CuIn_{0.4}Cr_{0.3}Ga_{0.3}Se_2$ thin films with E_g of 1.12, 1.16, 1.20, and 1.17 eV, respectively, which are close to the optimum value for solar photoelectric conversion of 1.5 eV. The differences of the band gaps and absorption spectra of the thin films was caused by the changing particle size and morphology of the prepared $CuIn_{0.4}Ga_{0.6}Se_2$, $CuIn_{0.4}Cr_{0.1}Ga_{0.5}Se_2$, $CuIn_{0.4}Cr_{0.2}Ga_{0.4}Se_2$, and $CuIn_{0.4}Cr_{0.3}Ga_{0.3}Se_2$ thin films with composition difference. Although composition dependency of E_g has been observed for multinary semiconductor particles like CZTS and $CuInS_2$, there has been little investigation of the influence of the particle composition on light−electricity conversion efficiency, especially for those new prepared $CuIn_{0.4}Ga_{0.6}Se_2$, $CuIn_{0.4}Cr_{0.1}Ga_{0.5}Se_2$, $CuIn_{0.4}Cr_{0.2}Ga_{0.4}Se_2$, and $CuIn_{0.4}Cr_{0.3}Ga_{0.3}Se_2$ thin films.
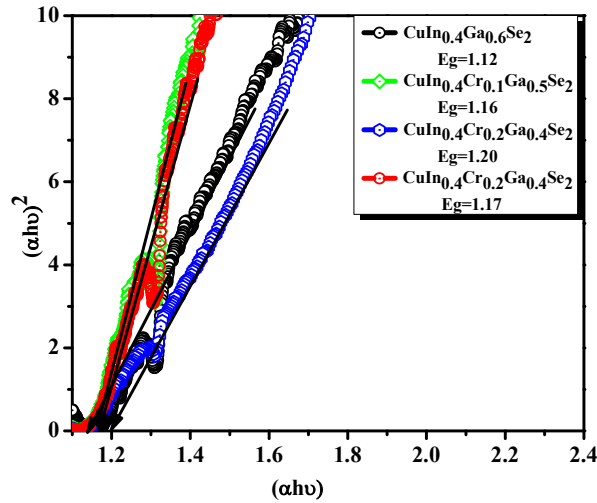
Figure 5.10. Band gap energy chart for $CuIn_{0.4}Ga_{0.6}Se_2$, $CuIn_{0.4}Cr_{0.1}Ga_{0.5}Se_2$, $CuIn_{0.4}Cr_{0.2}Ga_{0.4}Se_2$, and $CuIn_{0.4}Cr_{0.3}Ga_{0.3}Se_2$ precursor powders.

5.5.5.2. Dielectric spectra analysis

In order to get information about the behaviorofthe ionic conductivity, electrochemicalimpedance spectroscopy measurements wereperformedonseveral powdered solid compounds based on Copper (Cu), Indio (In), Gallium (Ga) and Selenium (Se): $CuIn_{0.4}Ga_{0.6}Se_2$(i.e. CIGS salts) doped with Chrome at different proportions. These compounds are labeled as $CuIn_{0.4}Cr_{0.1}Ga_{0.5}Se_2$, $CuIn_{0.4}Cr_{0.2}Ga_{0.4}Se_2$, and $CuIn_{0.4}Cr_{0.3}Ga_{0.3}Se_2$, respectively.

Electrochemical impedance spectroscopy (EIS) measurements were carried out at different temperatures, (20ºC to 200ºC), to obtain information on the samples conductivity. Data for the real part of the conductivity was analyzed in terms of the corresponding Bode diagrams, where variations of the conductivity with the frequency for all the composites in dry and wet conditions are shown in figures 5.11 and 5.12, respectively. In this plot, we can see the double logarithmic plot of the conductivity in S/cm versus frequency in (Hz) for all range of temperatures.
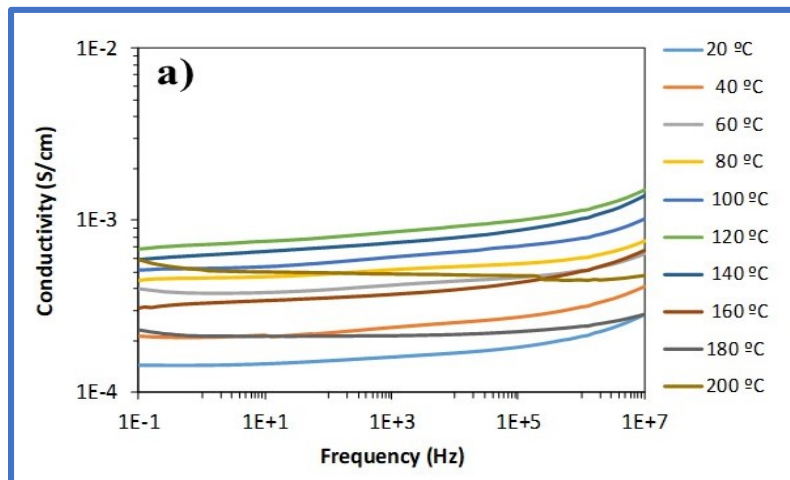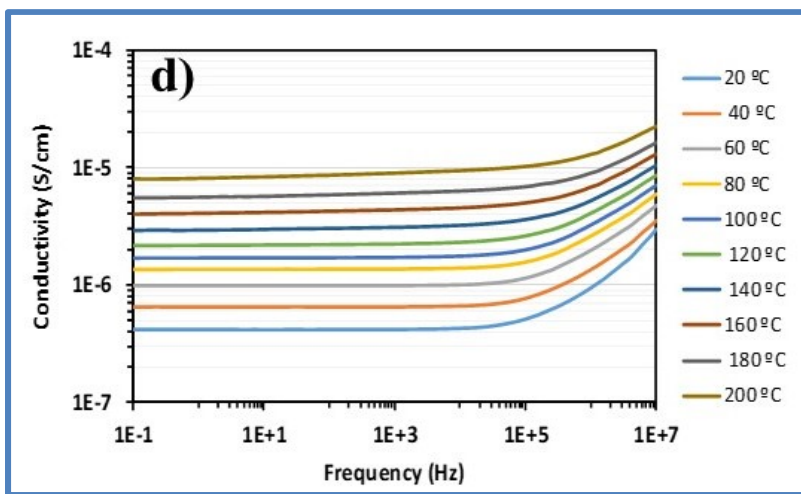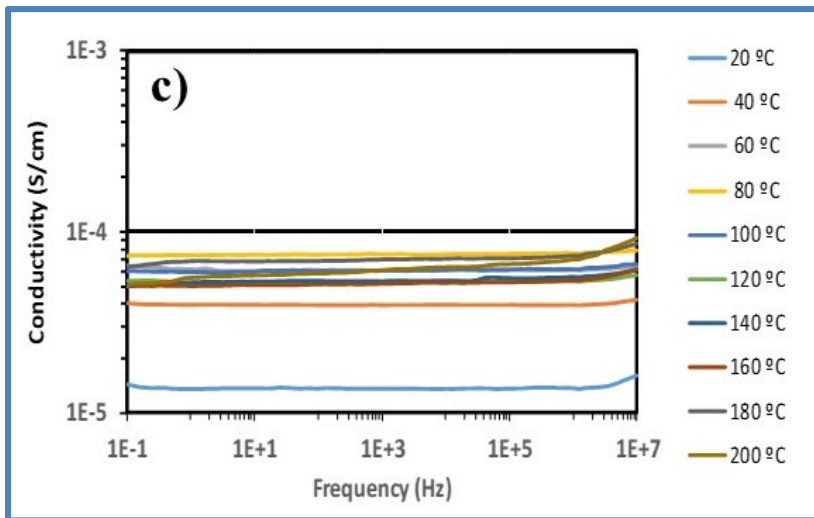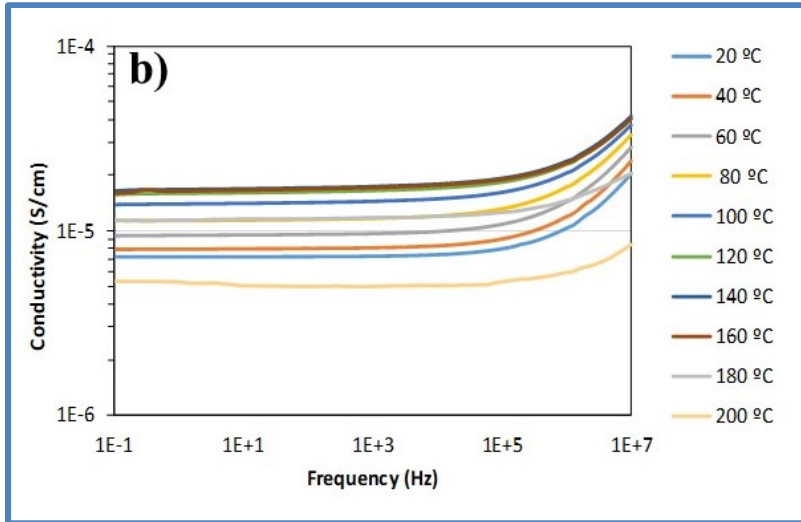
Figure 5.11. Double logarithmic plot of the real part of the conductivity versus frequency for (a) $CuIn_{0.4}Ga_{0.6}Se_2$, (b) $CuIn_{0.4}Cr_{0.1}Ga_{0.5}Se_2$, (c) $CuIn_{0.4}Cr_{0.2}Ga_{0.4}Se_2$, and (d) $CuIn_{0.4}Cr_{0.3}Ga_{0.3}Se_2$ precursor powders obtained in dry conditions.

159
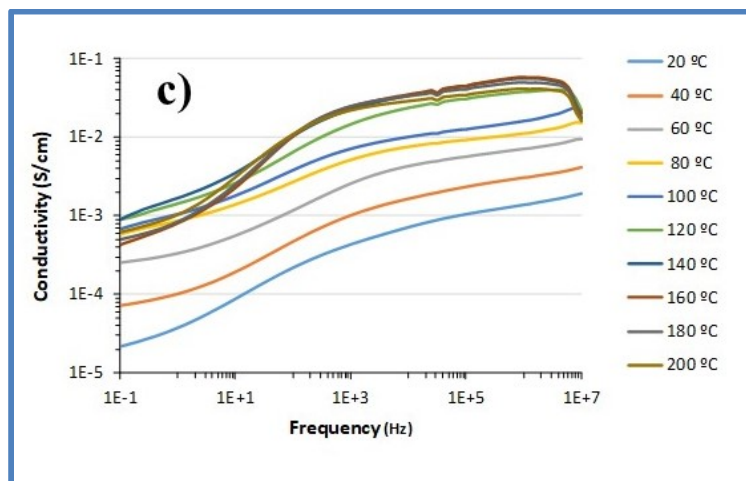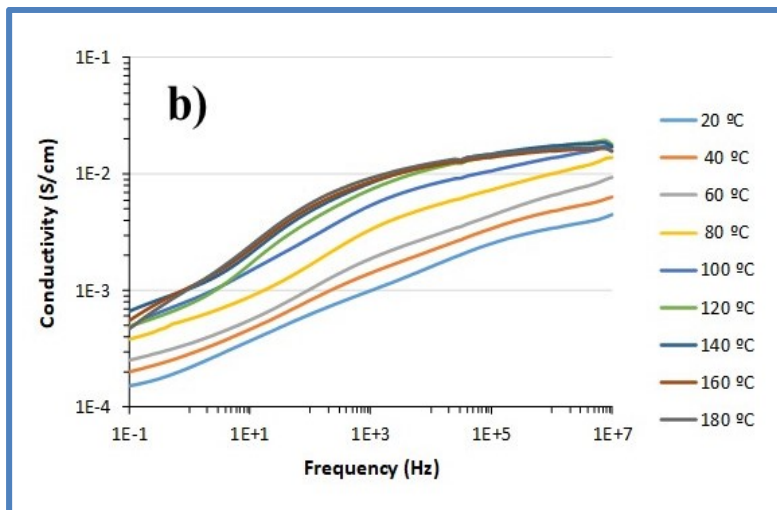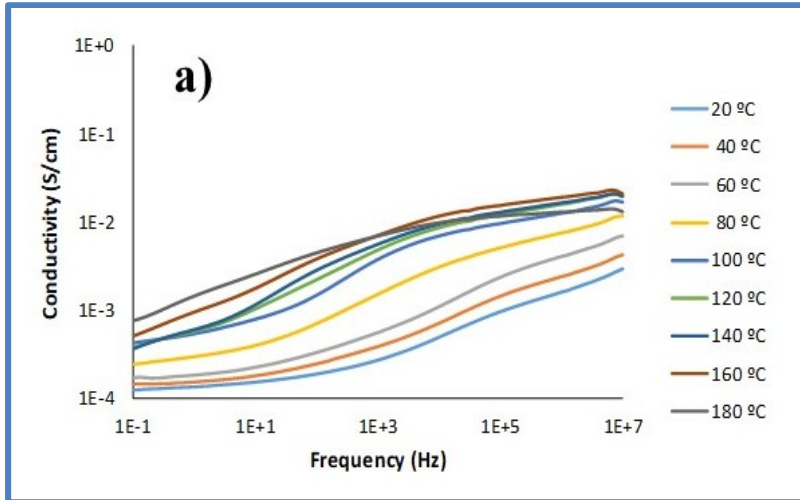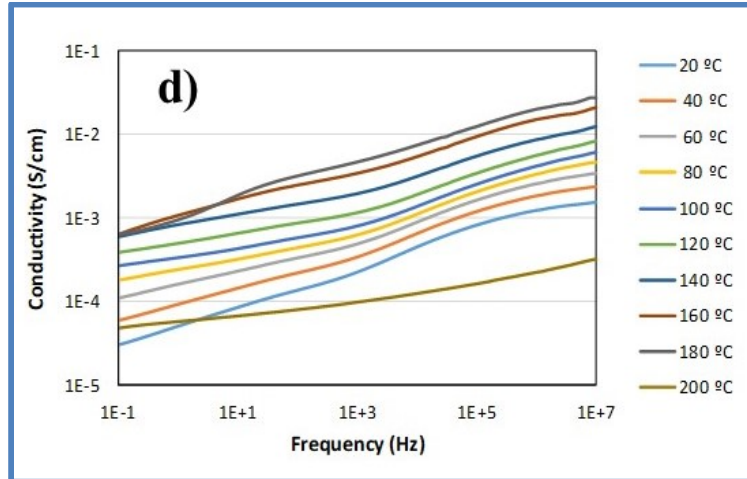
Figure 5.12. Double logarithmic plot of the real part of the conductivity versus frequency for (a) CuIn$_{0.4}$Ga$_{0.6}$Se$_2$, (b) CuIn$_{0.4}$Cr$_{0.1}$Ga$_{0.5}$Se$_2$, (c) CuIn$_{0.4}$Cr$_{0.2}$Ga$_{0.4}$Se$_2$, and (d) CuIn$_{0.4}$Cr$_{0.3}$Ga$_{0.3}$Se$_2$ precursor powders obtained in wet conditions.

A close inspection of this figures shows that the real part of the conductivity for the samples is practically constant for all range of frequencies in the measurement in dry conditions. This behavior is the typical demeanor as a conductor material. However, in case that wet conditions the values of conductivity are higher than that measured in dry conditions, but it is not possible to achieve a reproducibility of the measures. Taking into account this behavior, we will conduct our study focusing on the measures in dry conditions.

In the Figure 5.11. it is show the experimental data of the real part of the conductivity as a function of the frequency at several temperatures. For all temperatures studied the conductivity values increase with the temperature following the order σ' (Cu In$_{0.4}$Ga$_{0.6}$ Se$_2$)>σ' (CuCr$_{0.2}$ In$_{0.4}$Ga$_{0.5}$Se$_2$) >σ' (CuCr$_{0.1}$In$_{0.4}$Ga$_{0.3}$Se$_2$) >σ' (CuCr$_{0.3}$ In$_{0.4}$Ga$_{0.4}$Se$_2$).

The conductivityσ' is characterized by aplateauin thehigh frequency range and its value tends toa constant corresponding to direct-current conductivity (σ_{dc}) of the sample. Deviation from σ_{dc} in the spectrum of the conductivity in the range of low frequencies is due to the EP effect resulting from the blocking electrodes, produced by mobile charge accumulation, however it is only observed in the measurements realized below wet conditions [19,20].

The conductivity also exhibitsa phenomenonofdispersion thatobeysabehavior described byJonscherlaw,3,4$\sigma(\omega) = \sigma_{dc}+\sigma_{ac}$, being σ_{dc} the dc conductivity and the alternate-current

$\sigma_{ac} = A\omega^m$, where A is a factor dependent of the temperature and m for an ideal Debye dielectric and ideal ionic type crystals are 1 and 0, respectively.

Experimental data of the conductivity were fitted to the Jonscher law and the parameters are shown in the Table 5.3. As we can see in Figure 5.8, only two different regions are present. On the one hand, at moderate and low frequencies where the dc-conductivity will be determined (Cond), and the region of subdiffusive conductivity (SD), observed in the interval between 10^5 and 10^7 Hz for the samples $CuIn_{0.4}Ga_{0.6}Se_2$, Cu $Cr_{0.1}In_{0.4}Ga_{0.5}Se_2$ and $CuCr_{0.3}In_{0.4}Ga_{0.3}Se_2$, respectively. Is important highlight that the sample, $CuCr_{0.2}In_{0.4}Ga_{0.4}Se_2$, present a behavior of a pure conductor in all the range of frequencies for all temperatures [21,22].

In our samples the values fitted for the parameter m, takes values between 0.4 and 1 for all the samples except in case of sample $CuCr_{0.2}In_{0.4}Ga_{0.4}Se_2$, where the value was 0, corresponding to an ideal ionic type in all the range of temperatures. For the other samples the values obtained from the fit in the high frequency region can be due to the reorientation motion of dipoles and more likely to the motion of the localized charges, which are dominates over the dc-conductivity [23-24]. From figure 5.11. we can see that the conductivity is a function of the amount of fillers that we have incorporated in the powdered. On the other hand, for $CuCr_{0.2}In_{0.4}Ga_{0.4}Se_2$, nanocomposite we observe that conductivity is practically constant in all the range of frequencies, only at frequencies higher than 10^6 Hz and some temperatures, the behavior of the sample shown a cut-off frequency where it starts increasing with the frequency. For the other samples we can see that the real part of the conductivity is constant at the low frequencies region until a cut-off frequency where it starts increasing with the frequency, as if the sample were a capacitor. The value of ω constant means that the impedance has only a resistive contribution and its value represents the electrical conductivity of the sample. In table 5.4 we gathered the values of the samples conductivity together with the Jonscher parameters.

In the Figure 5.12, measurements made in wet conditions, it can be observed the temperature variations of the conductivity. In this plot, we can see at low temperatures σ_{ac} depends notably on the frequency and this effect tends to disappears when the temperature increases, but in our samples this behavior is not well developed due to the non-reproducibility of the measurements in wet conditions. The emergence of a plateau associated with dc conductivity curves shifts at low temperatures and is little remarkable for the samples. As

expected, the conductivity of all samples is strongly humidity dependent increasing more than two or four orders of magnitude for the samples studied [25]. For example, for the sample $CuCr_{0.2}In_{0.4}Ga_{0.4}Se_2$ the conductivity at 60°C is around 6.2×10^{-5} S/cm, however at the same temperature in wet conditions the conductivity is 5.7×10^{-3} S/cm, such as found in our samples. For all temperatures studied the conductivity values increase with the temperature following the order:

$\sigma_{dc}\, CuIn_{0.4}Ga_{0.4}Se_2 > \sigma_{dc}\, (CuCr_{0.2}In_{0.4}Ga_{0.4}Se_2) > \sigma_{dc}\,(CuCr_{0.1}In_{0.4}Ga_{0.4}Se_2) >$

$\sigma_{dc}\, (CuCr_{0.3}In_{0.4}Ga_{0.4}Se_2).$

Table 5.4. Jonscher parameters obtained by fitting $\sigma(\omega) = \sigma_{dc} + A\omega^m$ to conductivity data, for some indicated temperature in all studied samples.

Cr0	σ_{dc}[S cm]	A	m	Cr0.1	σ_{dc}[S cm]	A	m
T=20°C	1.6×10^{-4}	$10^{-6.96}$	0.39	T=20°C	7.4×10^{-6}	$10^{-10.5}$	0.73
T=60°C	4.2×10^{-4}	$10^{-6.20}$	0.32	T=60°C	9.8×10^{-6}	$10^{-9.98}$	0.68
T=100°C	6.1×10^{-4}	$10^{-5.68}$	0.29	T=100°C	1.5×10^{-5}	$10^{-9.07}$	0.57
T=160°C	3.7×10^{-4}	$10^{-6.17}$	0.34	T=160°C	1.8×10^{-5}	$10^{-9.70}$	0.66
Cr0.2	σ_{dc}[S cm]	A	m	Cr0.3	σ_{dc}[S cm]	A	m
T=20°C	1.4×10^{-5}	0	0	T=20°C	4.3×10^{-7}	$10^{-11.59}$	0.77
T=60°C	6.2×10^{-5}	0	0	T=60°C	1.0×10^{-6}	$10^{-10.97}$	0.72
T=100°C	6.1×10^{-5}	0	0	T=100°C	1.8×10^{-6}	$10^{-10.58}$	0.69
T=160°C	5.3×10^{-5}	0	0	T=160°C	4.5×10^{-6}	$10^{-9.89}$	0.62

Figure 5.11. shows the conductivity values for all samples as a function of temperature. From this plot, we can see that all samples follow a typical Arrhenius behavior with two different behaviors: one in the interval of temperatures between 20 and 120 °C, where the conductivity increases with increasing temperature following the eq (5.2).

$$\ln \sigma_{dc} = \ln \sigma_\infty - \frac{E_{act}}{RT}$$

(5.2)

For temperatures above 120°C, the conductivity strongly begins to fall down may be due to the dehydration of the prepared $CuIn_xCr_yGa_{1-x-y}Se_2$ precursor powders samples.

Following the eq.(5.2), from the slopes of the fits we are calculated the activation energy. The values obtained follow the trend E_{act} (CuCr$_{0.1}$In$_{0.4}$Ga$_{0.4}$Se$_2$) =(7.60±0.15) kJ/mol < E_{act} (CuCr$_{0.2}$In$_{0.4}$Ga$_{0.4}$Se$_2$) =(10.0±0.2) kJ/mol < E_{act} (CuCr$_{0.3}$In$_{0.4}$Ga$_{0.4}$Se$_2$) =(18.8±0.2) kJ/mol.

Figure 5.13.shows the temperature dependence on the conductivity values. The mobile ion concentrations are either assumed constant with the temperature or follow an Arrhenius behavior. However, in most cases the dependence with temperature of mobile ion charges can be more complicated as is happening for PEO-Li+, PEO-Na+ and PEO-Cs+. Here, we can see that all samples can be described following a Arrhenius equation, but in others many cases the behavior is described by a VFT equation.9 Other samples such is the case of H-Cosane, Li-Cosane and Na-Cosane the linear tendency, have been better described with two different slopes, above and below 70-80ºC that differentiate two distinct regions with activation energies, (around 7-8 kJ/mol), a little lowers than in our samples [26-28].
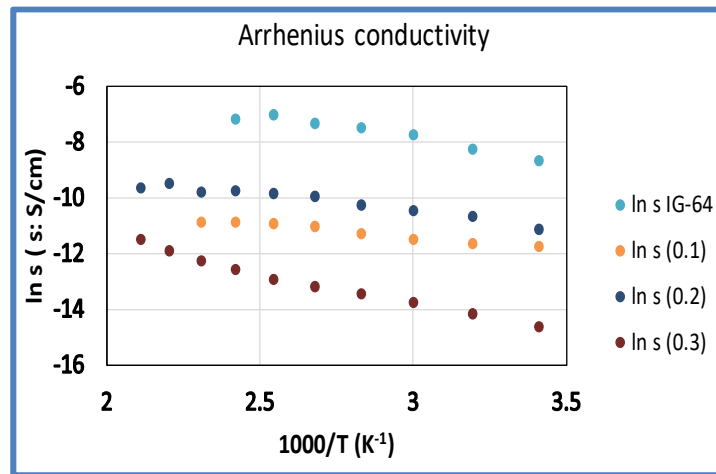
Figure 5.13. Temperature dependence of conductivity obtained from Bode diagram. Figure 5.10. Double logarithmic plot of the real part of the conductivity versus frequency for (**a**) CuIn$_{0.4}$Ga$_{0.6}$Se$_2$, (**b**) CuIn$_{0.4}$Cr$_{0.2}$Ga$_{0.4}$Se$_2$, (**c**) CuIn$_{0.4}$Cr$_{0.3}$Ga$_{0.3}$Se$_2$, and (**d**) CuIn$_{0.4}$Cr$_{0.1}$Ga$_{0.5}$Se$_2$. We can see two different behaviors separate by two temperatures intervals from 20 to 120 ºC and from 120 to 200 ºC.

5.6. Conclusions

The hydrothermal autoclave preparation method of (CIGS) nanocrystal powders from different starting metal source has been developed in this study. Controlling of the stoichiometry with different Indium and Gallium ratios can be achieved with this method. As investigated the adjustment of some preferred parameters like starting materials, time of stirring and reaction

temperature lead to the formation of well-defined $CuIn_{0.4}Ga_{0.6}Se_2$ ternary materials. The XRD showed a preferred orientation along the (112) plane of the tetragonal CIGS. Different molar ratio combinations of the copper, indium and gallium precursors for the preparation of CIGS resulted in a pure $CuIn_{0.4}Ga_{0.6}Se_2$. The resemblance of XRD phase structure, FESEM morphology, HRTEM particle size and EDX composition of the prepared $CuIn_{0.4}Ga_{0.6}Se_2$ with definite structure is a good guidance for successful films preparation. Good acceptable achievement for the preparation of doped $CuIn_xCr_yGa_{1-x-y}Se_2$ with Cr 20% as it shows less conductivity than Cr 0% which results in a promising new absorber material for CIGS solar cells manufacture. Future work will involve the use of these starting materials and preparation-controlled method for developing different doped thin film $CuIn_xCr_yGa_{1-x-y}Se_2$ materials.

References

[1] J. R. Sangoro, C. Iacob, A. L. Agapov, Y. Wanf, S. Berdzinski, H. Rexhausen, V. Strehmet, C. Friedrich, A. P. Sokolov and F. Kremer, Soft Matter, 2014, 10, 3536-3540.

[2] J. Klein, S. Zhang, S. Dou, B. H. Jones, R. Colby and J. Runt, J. Chem Phys., 2006, 124, 144903, 1-8.

[3] (13) P. Barbosa, N. C. Rosero-Navarro, S. Fa-Nian and F. M. L. Figuereido, Electrochim. Acta, 2015, 153, 19-27.

[4] Vega J.; Andrio A; Lemus A.A; del castillo L.F.; Compañ V. Electrochimica Acta 258 (2017) 153-166.

[5] C.Wang, S. Shei, S. Chang, "Novel solution process for synthesis of CIGS nanoparticles using polyetheramine as solvent", Materials Letters, vol.122, pp.52–54, (2014).

[6] S.H. Mousavi, T.S. Müller, P. Oliveira, "Synthesis of colloidal nanoscaled copper–indium–gallium–selenide (CIGS)particles for photovoltaic applications", Journal of Colloid and Interface Science, vol. 382, pp.48–52, (2012).

[7] Sin-Il Gu, Hyo-Soon Shin, Dong-Hun Yeo, Youn-Woo Hong, Sahn Nahm, "Synthesis of the single phase CIGS particle by solvothermal method for solar cell application", Current Applied Physics, vol.11,pp.S99eS102, (2011).

[8] S. Mahboob, S.Malik, N.Haider, C. Nguyen, M. Malik, P. O'Brien, "Deposition of binary,ternary and quaternary metal selenide thin films from di isopropyl diseleno phosphinato-metal precursors", Journal of Crystal Growth, vol.394, pp. 39–48, (2014).

[9] Y. G. Chun, K. H. Kim, K.-H. Yoon, "Synthesis of CuInGaSe2 nanoparticles by solvothermal route", Thin Solid Films 480–481 (2005) 46–49

[10] N.Bhattacharya, Mi-KyungOh, YounghoKim, "CIGS-based solar cells prepared from electro deposited precursor films",Solar Energy Materials & Solar Cells vol.98 (2012) pp.198–202

[11] Ji.Wooa, H.Yoon, Ji.Cha, D. Jung , S.Yoon, "Electrostatic spray-deposited CuInGaSe2 nanoparticles: Effects of precursors'Ohnesorge number substrate temperature, and flow rate on thinfilm characteristics", Journal of Aerosol Science, vol.54, pp1–12, (2012).

[12] M. Kaelin, D. Rudmanna, F. Kurdesaua, H. Zogg, T. Meyer, A.N. Tiwari, "Low-cost CIGS solar cells by paste coating and selenization", Thin Solid Films, vol. 480–481, pp.486–490, (2005).

[13] E.Lee, O.Joo, S.Yoon, B.KounMin, "Synthesis of CIGS absorber layers via a paste coating", Journal of Crystal Growth vol.311,pp.2621-2625, (2009).

[14] V. Kapur, A. Bansal, P. Le, O. Asensio, "Non-vacuum processing of CuIn1-xGaxSe2 solar cells on rigid and flexible substrates using nanoparticle precursor inks", Thin Solid Films, vol. 431 –432, pp. 53–57, (2003)

[15] M. Yeh, H. Hsu, K. Wang, S. Hoa, G. Chen ,H. Chen, "Toward low-cost large-area CIGS thin film: Compositional and structural variations in sequentially electrodeposited CIGS thin films",Solar Energy, vol. 125,pp. 415–425, (2016).

[16] M. Kaelin , D. Rudmanna, F. Kurdesaua, T. Meyerb, H. Zogga, A.N. Tiwaria, "CIS and CIGS layers from selenized nanoparticle precursors", Thin Solid Films, vol. 431 –432, pp.58–62, (2003).

[17] D. Lincot, J.F. Guillemoles, S. Taunier, D. Guimard, J. Sicx-Kurdi, A. Chaumont , O. Roussel , O. Ramdani , C. Hubert , J.P. Fauvarque, N. Bodereau, L. Parissi, P. Panheleux, P. Fanouillere, N. Naghavi, P.P. Grand, M. Benfarah, P. Mogensen, O. Kerrec, "Chalcopyrite thin film solar cells by electrodeposition",Solar Energy, vol. 77,pp. 725–737, (2004).

[18] F. Roux, S. Amtablian, M. Anton, G. Besnard, L. Bilhaut, P. Bommersbach, J. Braillon, C. Cayron, A. Disdier, H. Fournier, J. Garnier, A. Jannaud, J. Jouhannaud, A. Kaminski, N. Karst, S. Noël, S. Perraud, O. Poncelet, O. Raccurt, D. Rapisarda, A. Ricaud, D. Rouchon, M. Roumanie, E. Rouviere, O. Sicardy, F. Sonier, K. Tarasov, F. Tardif, M. Tomassini, J. Villanova, "Chalcopyrite thin-film solar cells by industry-compatible ink-based process", Solar Energy Materials & Solar Cells, vol. 115, pp. 86–92, (2013).

[19] Sangoro, J.R.; Serghei, A.; Naumov, S.; Galvosas, P.; Kärger, J.; Wespe, C.; Bordusa, F.; Kremer, F. Charge Transport and Mass Transport in Imidazolium-Based Ionic Liquids. Phys. Rev. E 2008, 77, 051202.

[20] Serguei, A.; Tress, M.; Sangoro, J.R.; Kremer. F. Electrode Polarization and Charge Transport at Solid Interfaces. Phys. Rev. B 2009, 80, 184301.

[21] Jonscher, A.K. The 'Universal' Dielectric Response. Nature 1977, 267, 673-679.

[22] Jonscher, A.K. Dielectric Relaxation in Solids; Chelsea Dielectric Press Limited, London, 1983.

[23] Leys, J.; Wübbenhorst, M.; Preethy Menon, C.; Rajesh, R.; Thoen, J.; Glorieux, C.; Nockemann, P.; Thijs, B; Binnemans, K; Longuemart, S. Temperature dependence of the electrical conductivity of imidazolium ionic liquids. J. Chem Phys. 2008, 128, 064509.

[24] Greenhoe, Brian M.; Hassan, Mohammad K.; Wiggins, Jeffrey S.; Mauritz, Kenneth A. Universal power law behavior of the AC conductivity versus frequency of agglomerate morphologies in conductive carbon nanotube-reinforced epoxy networks. J. Polym. Sci. B 2016, 54, 1918-1923.

[25] Haile, S.M.; Lentz, G.; Kreuer, K-D.; Maier, J. Superprotonic conductivity in Cs3(HSO4)2(H2PO4). Solid State Ionics 1995, 77, 128-134.

[26] sadakiyo M, Yamada Teppei, Kitagawa H. Ratinal Designs for highly Proton-Conductive metal-Organic Frameworks. JACS Communications. 131, 2009, 9906-9907.

[27] Fuentes, I.; Andrio A; Teixidor F.; Viñas C.; Compañ V. Enhanced conductivity of sodium versus lithium salts measured by impedance spectroscopy. Sodium cobaltacarboranes as electrolytes of choice. PCCP 19, 2017, 15171-15186.

[28] Fuentes, I.; Andrio A; García-bernabé A.; Escporihuela J.; Teixidor F.; Viñas C.; Compañ V. Structural and dielectric properties of cobalt carborane composite polybenzimidazole membranes as solid Polymer electrolytes at high temperature. PCCP 20, 2018, 10173-10184.

Chapter 6. CTZS thin films

6.1. Objectives

The main objective was to deposit high quality CZTS thin films by use of electrodeposition and chemical bath technique to develop low cost solar cell absorber layer. The main objectives are:

i. To develop an electrodeposition-route to fabricate CZTS precursors, using linear sweep electrodeposition. The success of this objective is judged by the ability to produce a film of controlled, uniform composition which can be varied rationally as required.

ii. To optimise the sulfurisation process used to convert the precursor into a CZTS film; to achieve complete conversion and demonstrate the correct phase and suitable properties for a thin film device.

iii. To investigate the morphological, optical and electrical properties of the resulted CZTS films in order to confirm the quality of the prepared films.

6.2. Introduction

At present, photovoltaic solar cell investigations have rapidly increased due to the higher demand of cleaner energy consumption. In this sense, chalcogenides semiconductors exhibit unique optical, electrical and chemical properties [1-5]. Consequently, in the last years, these compounds have attracted the attention of the scientific community. In particular, the thin film technology has been heavily promoted by the interest in CdTe and CIGS-based solar cells [6-8]. However, these materials contain scarce elements in the earth's crust, such as In, Te and Ga and toxic ones as Cd and Se [9, 10]. Cu_2ZnSnS_4 system (CZTS) that crystallizes kesterite structure is one of the most promising absorber materials for solar cells, because of its low band gap around 1.5 eV and its high absorption coefficient (10^4 cm^{-1}) [11]. In addition, the absence of toxic elements and incorporation of low cost, abundant and environmentally friendly elements as Zn and Sn, instead of In and Ga [12]. Currently, 12.6% of efficiency record has been achieved using hydrazine-based solution. Shockley–Queisser photon balance calculations display 32.2% of theoretical conversion limit for CZTS solar cells [13]. Thus, it is important to highlight that the CZTS efficiency could improve noticeably and becomes closer to CIGS efficiency (20.1%). In

the past, several chemical routes for CZTS synthesis have been studied as well as their thin film deposition [14].

There are various preparation methods of CZTS divided into two main parts; (1) physically vacuum deposition techniques like sputtering [15, 16], evaporation [17, 18, 19] and pulsed laser deposition (PLD) [20]; (2) chemically based non-vacuum deposition techniques such as electrodeposition [21, 22], hydrazine-based solution [23] and sol gel-based methods [24]. Electrodeposition technique is with favorable unique advantages that are low-cost, large area plating, convenient industrial process, so electrodeposition is highly competitive degree than other manufacturing techniques for CZTS synthesis. Three electrode cell processes are characterized by four main deposition techniques depending upon the starting precursor species of ions. (1) stacked elemental layer approach (SEL), (2) metal alloy electrodeposition (MAE), (3) electrophoretic deposition (EPD), and (4) quaternary electrodeposition (QED).

In each case, a post-deposition annealing step in the presence of a molecular conductor source (chalcogenide) to enhance the growth process. Each process possesses their own merits and drawbacks, and all of them have drawn significant attention as comfortable methods for large area CZTS thin film deposition.

Here, we propose a single-step electrochemical deposition method (SED) to deposit quaternary elements of copper, zinc, tin and sulfur onto ITO substrates. The as deposited CZTS films were further thermally treated in different atmospheres argon and sulfur, respectively; at different temperatures in order to enhance the crystallinity of the prepared films. The physical properties, microstructure and morphology of the as deposited and treated ones were studied by X-ray diffraction. The best structure with the smallest crystal size was further studied by scanning electron microscopy and EDS. Optical properties were measured in order to calculate the band gap energy and the absorption coefficient. Photoelectrochemical properties were studied also for the sulfurized samples.

6.3. Experimental

6.3.1. Methods

CZTS thin-film precursor is grown by single-step electrodeposition using -1.05 V versus saturated calomel electrode (SCE) at RT for 45 min. The CZTS thin films were electrodeposited

potentiostatically on ITO substrates. Substrate cleaning process is performed in an ultrasonic using some organic solvents (soap, ethanol, acetone, 15 min each step) in order to obtain uniform and good adherent deposition. Electrochemical baths were formed of an aqueous solution containing $CuSO_4$ (20 mM), $ZnSO_4$ (10 mM), $SnSO_4$ (20 mM) and $Na_2S_2O_3$ (0.2 M).

Tartaric acid is used to adjust pH of the solution at 5.0 and tri-sodium citrate ($Na_3C_6H_5O_7$) was as complexing agent. The precursor films formed were annealed in Ar atmosphere and in sulfur atmosphere.

Table 6.1. Preparation parameters for Cu_2ZnSnS_4 as-grown, annealed in Ar atmosphere and sulfurized.

annealing atmospheres	Temperature (°C)	Annealing Time (min)	Potential (V)	pH	Deposition Time (s)
Cu_2ZnSnS_4 - sulfurized	400	45	-1.05	5.0	2700
Cu_2ZnSnS_4 - Annealed in Ar	450	45	-1.05	5.0	2700
Cu_2ZnSnS_4 -as-grown	----	----	-1.05	5.0	2700

6.3.2. Materials characterization

The crystal structure of CZTS is investigated by XRD (Rigaku Ultima IV diffractometer in the Bragg-Bentano configuration) using the CuKα radiation (λ = 1.54060 Å). The microstructural and elemental analyses were characterized using a Zeiss ULTRA 55 model scanning electron microscope (SEM) equipped with an energy dispersive spectroscopy (EDS) system. To determine the band gap energy was estimated from the optical absorption, which was measured by recording the transmission spectra using a UV-Visible spectrophotometer (Ocean Optics HR4000) coupled to an integrating sphere (in order to collect both specular and diffuse transmittance).

6.3.2.1. Photoelectrochemical and electrochemical analyses

The PEC measurements were performed in a quartz cell to facilitate the light reaching the photoelectrodes surface. The light exposed surface of the working electrode is 0.25 cm^2. The electrolyte used in all PEC measurements is 0.1 M Na_2SO_4. A potentiostat/galvanostat Autolab PGSTAT302N (Metrohm, Netherlands) with a Pt rod counter-electrode and an Ag/AgCl

saturated in 3 M KCl reference electrode was used. The chronoamperometry curves of the films were also obtained in dark and under illumination with an intensity of about 1 SUN (100 mW cm^{-2}) at the film surface.

6.4. Results and discussion

6.4.1. Structural properties

The X-ray diffraction (XRD) patterns of Cu_2ZnSnS_4 quaternary alloy nanostructures as deposited, annealed in Ar and in sulfur atmosphere are shown in Figure 1. There are five peaks attributed to the diffractions of the (112), (101), (11 0), (105), and (312) planes, at $2\theta = 28.35°$, 44.05°, 46.68°, 47.31°, 55.54° and 28.27º, 44.05º, 47.32º, 47.42º, 55.96º, respectively for Cu_2ZnSnS_4 annealed in sulfur and in Ar atmospheres. The Cu_2ZnSnS_4 (CZTS) nanostructures were found to consist of the tetragonal structure kesterite phase, with the (112), (105), (220) and (312) diffraction peaks corresponding to those of JSPDS card 26-0575.

XRD patterns shown in Figure 1with diffraction angle 2θ varied from 10 to 60 degrees. The observed peaks are attributed to both CZTS and ITO. However, the XRD pattern of the as deposited CZTS film shows the ITO characteristic peaks only. After annealing in Ar atmosphere (without sulfur) the XRD pattern corresponds to the kesterite CZTS phase in addition to ITO peaks. Those annealed in sulfur atmosphere indicates a good crystallized kesterite phase and disappear of ITO peaks referring to successful growth of CZTS kesterite phase.

There are no peaks for secondary phases in contrast to some reports states that copper sulfide, tin sulfide, and copper tin sulfide compounds exist as intermediates during sulfurization. Those secondary phase sulfides always form mixtures with CZTS at low sulfurization temperatures whereas they did not appear in the prepared CZTS films. This result is due to the selective process of precursor starting materials, sensitivity control of solution pHs and complexing agent concentration dependence. Careful equilibrium between temperature and annealing atmosphere thus in absence of sulfur we have increased the temperature of annealing to 450°C. In the same time, we have decreased annealing temperature in presence of sulfur to 400°C. Both annealing process were done for 45 min which is also in decrease with comparison to other stated work where the annealing temperature is set for 1h or more.
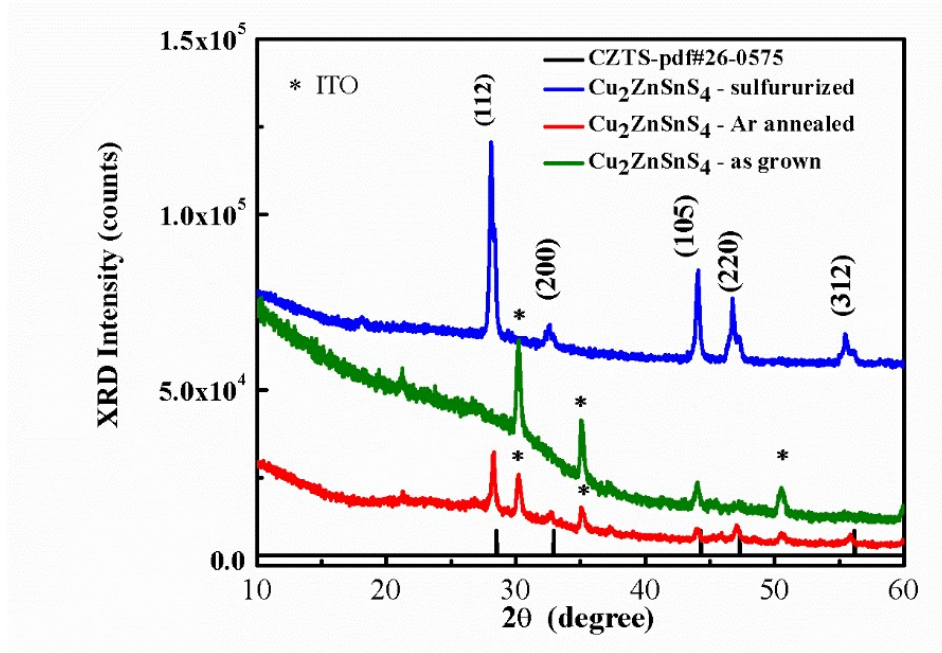
Figure 6.1. XRD patterns of the CZTS films as deposited, annealed at 450°C, 400°C in Ar and sulfur atmosphere, respectively for 45min.

As the annealing process were done in different atmospheres as a function of time stability, lead to an optimized resultant CZTS kesterite phase. Crystallite size was calculated according to Scherer's formula:

$$D = \frac{K\lambda}{\beta\cos\theta}$$

where β is the Full Width at Half Maximum (FWHM), λ wavelength of X-rays with value is 1.5418 Å, K is Scherer's constant depending on the crystallite shape and is close to 1 (K= 0.9 was used) and θ is the Bragg angle at the center of the peak. Table 2 displays the crystallite sizes for CZTS films annealed in Ar and in sulfur atmospheres, respectively.

Table 6.2. Crystallite size measurement of Cu_2ZnSnS_4 annealed in Ar atmosphere and sulfurized films.

Sample	Crystallite size (nm)
Cu_2ZnSnS_4 - Annealed in Ar	27.8
Cu_2ZnSnS_4 - sulfurized	17.3

It is worth to notice that the crystallite size of kesterite phase Cu_2ZnSnS_4 sulfurized ones has larger crystallite size than those annealed in Argon atmosphere. The annealing process in Argon atmosphere were held at 450 °C which lead to complete kesterite phase formation with all kesterite indexed peaks in addition to those of ITO used substrate. In the mean while those grown in sulfur atmosphere shown sharp indexed peaks for kesterite phase only and no substrate ITO representative peaks.

6.4.2. Optical Properties

Figure 6.2. shows the transmittance and absorbance spectra for the CZTS thin films as-grown and sulfurized, respectively. As can be seen the transmittance for the sulfurized sample is higher in all the studied wavelength range, meaning that the reflectance of the surface has decreased after the sulfurization process.
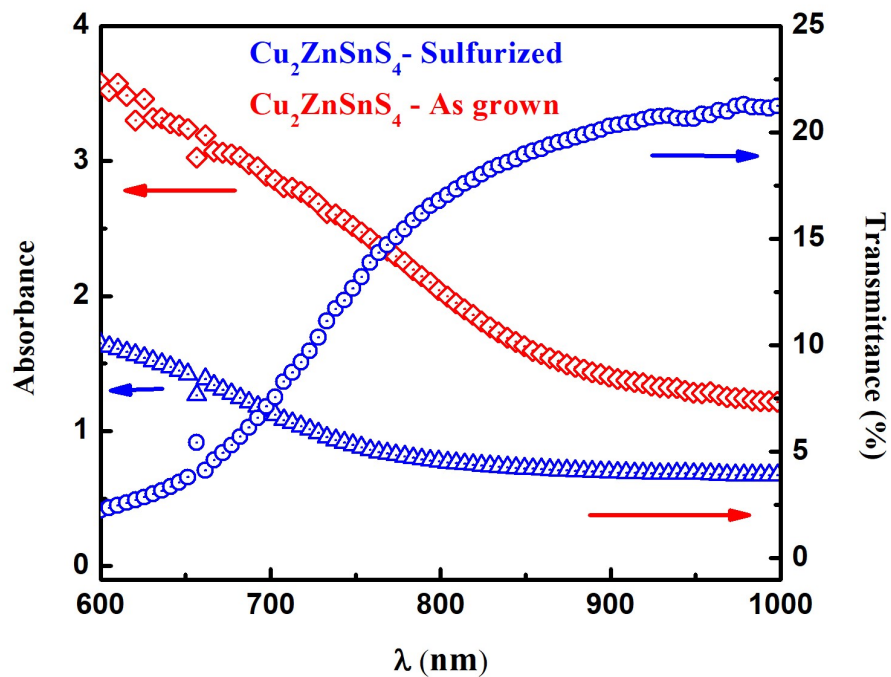
Figure 6.2. Absorbance and transmittance spectra for kesterite Cu_2ZnSnS_4, As-grown (red) and Sulfurized (blue) thin films.

For a direct-band-gap semiconductor, the optical band gap energy can be evaluated by the expression $(\alpha h\nu)^2 = A(h\nu - Eg)$, where Eg is the optical band gap energy, A is an energy independent constant, h is the Planck constant, ν is frequency, and n is an index that

characterizes the optical absorption process and is theoretically equal to 1/2 for the direct allowed transitions.

All the CZTS thin film samples exhibited broad absorption in the visible region. The band gaps were obtained by plotting $(\alpha h\upsilon)^2$ versus the photon energy in eV. Extrapolation of the straight line to zero absorption coefficient ($\alpha = 0$) allows estimation of Eg.

Figure 6.3. shows the Tauc plot of Cu_2ZnSnS_4 kesterite thin films before annealing the (as grown) and sulfurized samples in sulfur atmosphere. The band gaps of the as grown films were 1.83 eV and 1.52 eV for the sulfurized ones which is close to the reviewed CTZS band gap values.
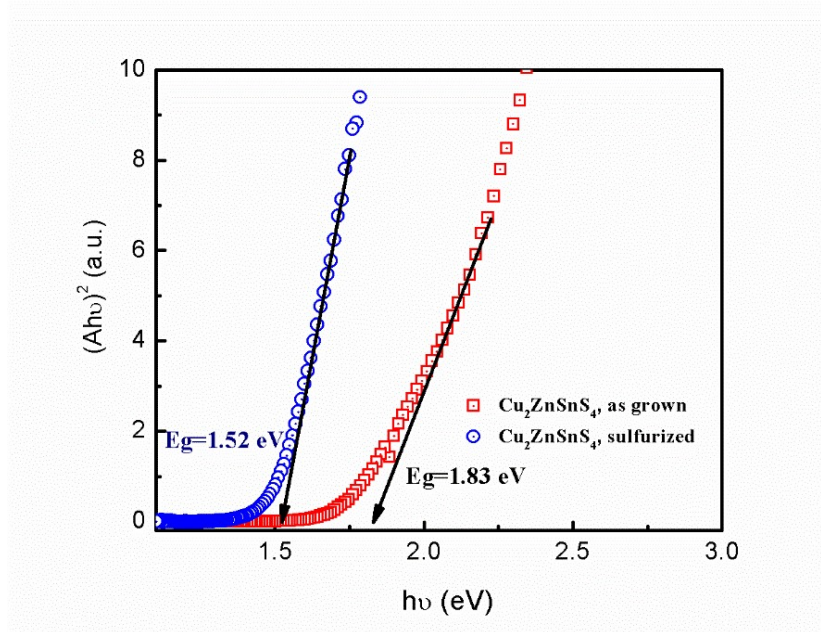

Figure 6.3. Tauc plot of $(Ah\upsilon)^2$ versus (hv) for kesterite Cu_2ZnSnS_4 ,As-grown and Sulfurized thin films.

6.4.3. Scanning Electron Microscopy

Figure 6.4. shows Scanning Electron Microscopy (SEM) images of the sulfurized CZTS films at different magnifications. Scanning Electron Microscopy is one of the predominant techniques to survey the surface of the samples. The SEM analysis reveals that the grown films revealing good crystallinity in agreement with XRD data. Uniform, homogenous, well-covered and good adherence agglomeration of grains with the films. No secondary phases have been detected in contrast to annealing in sulfur atmosphere at low temperatures like, ZnS, SnS, CuSnS and CuS.
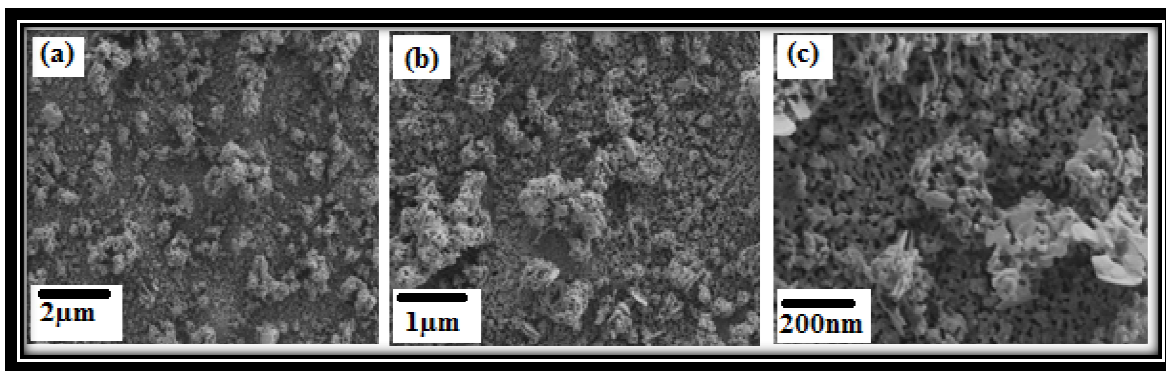
Figure 6.4. SEM images for kesterite thin films Cu$_2$ZnSnS$_4$-sulfurized at different magnifications.

The growth temperature determines growth of CZTS films presence of sulfur enhance the crystallinity of the films. The films deposited at 400 °C in sulfur atmosphere show homogeneity with smooth islands or small grains owing to combination of CZTS formed in Ar atmosphere and sulfur. The smooth region is related to the stoichiometry of the pure kesterite CZTS formed phase with (Cu:Zn:Sn:S=2:1:1:4) ratio of constituent films which is highly required to develop efficient thin film solar cells. The SEM images of the sulfurized CZTS films grown with optimum growth conditions show very uniform grain sizes.

6.4.4. EDS Analysis

The composition of the as-deposited sample was evaluated by a quantitative EDS analysis. Figure 6.5 shows a typical EDS spectrum revealing peaks of Cu, Zn, Sn and S, due to the deposited CZTS thin film. It is also obviously noticed that no presence of any additionally peaks arising from substrate ITO.

The fundamental properties of CZTS have proven to be suitable to serve as an active layer in solar cell devices. In the Cu-based chalcogenides the Cu content is of key importance, that it is strongly affects morphological, structural and electrical properties of the films. Therefore, as a first optimization for experimental conditions to synthesize CZTS, we studied structural and morphological properties of CZTS thin films as well as corresponding solar cell parameters by varying the content of Cu. Controlling the amount of copper lead to varying all other constituent elements, which in turn lead to varying all other elemental ratios: i.e, Zn/Sn, (Cu/(Zn+In) and (S/metal) ratios.

Figure 6.5 shows a typical EDS spectrum of sulfurized films. Peaks corresponding to the four components Cu, Zn, Sn, and S of CZTS films are evident in ECS spectrum.
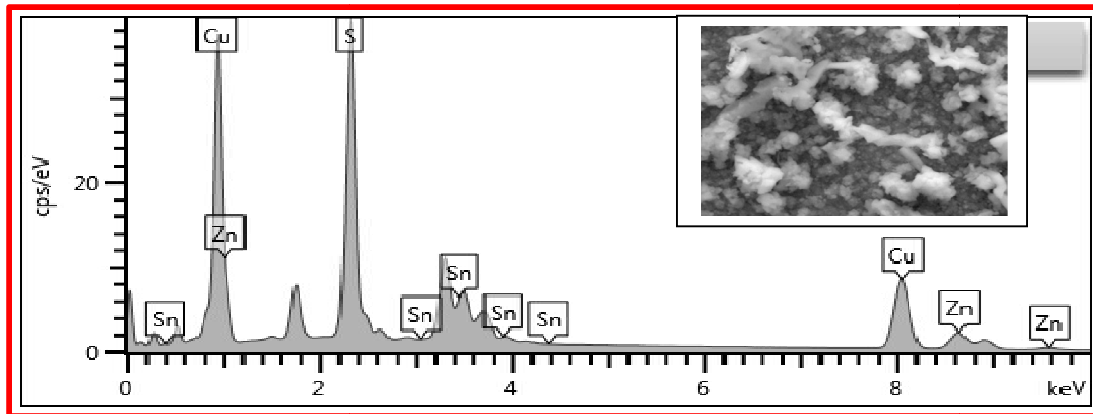
Figure 6.5. EDS elemental composition analysis for sulfurized Cu_2ZnSnS_4 kesterite thin films.

The composition of the studied samples is presented in the Table 3 and their relative positions are indicated in the phase diagram (Figure6.5). The calculated ratios [Cu]/([Zn]+[Sn])=0.5 and [Zn]/[Sn]=1.4, where the [s]/([metal]) ratio is equal to 1.65; which is clearly the most effected one due to the high ratio of sulfur more than 50%. The apparent composition of the elements is 12.59 at%, 14.79 at%, 10.27 at% and 62.32 at % for Cu, Zn, Sn, and S elements, respectively. In general, it has been observed that sulfurized films are moderately poor in Cu and rich in S. The calculated [Cu]/([Zn] + [Sn])=0.5 and [Zn]/[Sn]=1.4, where the [s]/([metal]) ratio is equal to 1.65; which is clearly the most effected one due to the high ratio of sulfur more than 50%.

Table 6.3.Compositional analysis of sulfurized Cu_2ZnSnS_4 kesterite thin films.

Elements composition atomic (%)					Elemental composition ratio		
	Cu (%)	Zn (%)	Sn (%)	S (%)	Cu/Zn+Sn	Zn/Sn	S/metal
Cu_2ZnSnS_4	12.59	14.79	10.27	62.35	0.5	1.4	1.65

6.4.5. Photoelectrochemical measurements of CZTS

Photoelectrochemistry has been employed to explore the semiconducting properties of sulfurized Cu_2ZnSnS_4. When semiconductor electrodes are exposed to periodic illumination, the current driven is affected by the creation of electron–hole pairs, which alters the concentration of minority carriers and thereby promotes processes governed by these carriers. During photoexcitation both photopotential and photocurrent can be observed, even at open circuit

potential. The photo excited electrons and holes are separated in the space charge layer and are driven by the electric field in opposite directions. This migration induces an inverse potential in the electrode (photopotential), reducing the potential difference across the space charge layer and retarding the migration of the carriers. In the case of p-type semiconductors, the Fermi level of the semiconductor decreases (the electrode potential increases) when the band edge level bends downward in the space charge layer. Moreover, a negative photocurrent is registered when photogenerated electrons move across the space charge region towards the electrode/electrolyte interface and increase the cathodic current [21].

Figure 6.6. shows the photocurrent registered at open circuit potential and the photopotential developed across the sulfurized CZTS at 400°C. The cathodic nature of the photocurrent and the positive value of the photopotential confirm the p-type character of the sulfurized CZTS film.
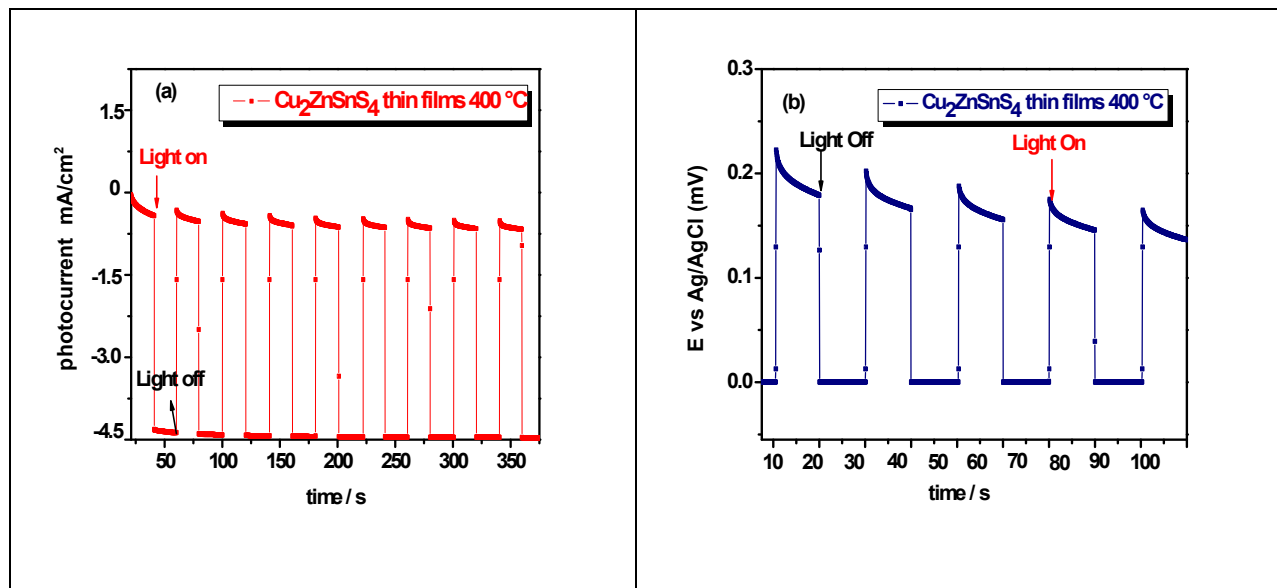
Figure 6.6. (a) Photocurrent and (b) Photopotential response of sulfurized Cu_2ZnSnS_4 thin films (T = 400 °C), using chopped light (10 s on/10 s off) in 0.1 M Na_2SO_4 solution.

6.4.6. Conclusion

Cu_2ZnSnS_4 thin films with kesterite structure were successfully synthesized using single step electrodeposition process. Annealing process in Argon and sulfur atmosphere were studied as function of time, as the time was fixed where in Argon atmosphere the temperature was held higher than those in sulfur atmosphere.

178

Characterization techniques have revealed the formation of pure kesterite phase for the prepared Cu_2ZnSnS_4 films in both argon and sulfur atmosphere. XRD structure study showed indexed peaks for Cu_2ZnSnS_4 thin films with kesterite structure with average crystal size about 17 nm.The morphological study for the sulfurized samples indicates that both films are polycrystalline with a uniform homogenous surface morphology suitable for solar cell applications. The elemental EDS analysis promotes that the prepared sulfurized films with Cu poor, Zn and S rich Cu_2ZnSnS_4 sulfurized kesterite films. For the photoelectrochemical performance of the $Cu_2ZnSnS_4$the photocurrent registered at open circuit potential and the photopotential developed across the sulfurized CZTS at 400°C improve the cathodic nature of the photocurrent and the positive value of the photopotential confirms the p-type character of the film.

6.4.7. References

[1] I. Repins, C. Beall, N. Vora, C. DeHart, D. Kuciauskas, P. Dippo, B. To, J. Mann, W. C. Hsu, A. Goodrich, and R. Noufi, Sol. Energy Mater. Sol. Cells (101), 154–159 (2012).

[2] I. Dudchak and L. Piskach, J. Alloys Compd. 351(1), 145–150 (2003).

[3] S. Chen, X. G. Gong, A. Walsh, and S.-H. Wei, Phys. Rev. B 79 (16), 165211 (2009).

[4] C. Persson, J. Appl. Phys. 107(5), 053710 (2010).

[5] B. Shin, O. Gunawan, Y. Zhu, N. A. Bojarczuk, S. J. Chey, and S. Guha, Prog. Photovoltaics 21(1), 72–76 (2013).

[6] S. Siebentritt, Thin Solid Films (535), 1–4 (2013).

[7] J. T. Watjen, J. Engman, M. Edoff, and C. Platzer-Bjorkman, Appl. Phys. Lett. 100(17), 173510 (2012).

[8] J. J. Scragg, J. T. Watjen, M. Edoff, T. Ericson, T. Kubart, and C., J. Am. Chem. Society 134(47), 19330–19333 (2012).

[9] S. Ahn, S. Jung, J. Gwak, A. Cho, K. Shin, K. Yoon, D. Park, H. Cheong, and J. H. Yun, Appl. Phys. Lett. 97(2), 021905 (2010).

[10] K. Redinger, X. Hoenes, V. Fontane, V. Izquierdo-Roca, E. Saucedo, N. Valle, A. Perez Rodrıguez, and S. Siebentritt, Appl. Phys. Lett. 98(10), 101907 (2011).

[11] J.J. Scragg, D. Berg, P.J. Dale, J. Electroanal. Chem, (646)1–2, 52-59 (2010).

[12] S.G. Lee, J. Kim, H.S. Woo, Y. Jo, A.I. Inamdar, S.M. Pawar, H.S. Kim, W. Jung, H. S. Im, Curr. Appl. Phys. (14), 254–258 (2014).

[13] P.P. Gunaicha, S. Gangam, J.L. Roehl, S.V. Khare, , Sol. Energy (102), 276-281(2014).

[14] J.-S. Seol, S.-Y. Lee, J.-C. Lee, H.-D. Nam, and K.-H. Kim, Sol. Energy Mater. Sol. Cells (75), 155 (2003).

[15] H. Katagiri, K. Jimbo, W. S. Maw, K. Oishi, M. Yamazaki, H. Araki, and A. Takeuchi, Thin Solid Films (517), 2455 (2009).

[16] P. A. Fernandes, P. M. P. Salome, A. F. da Cunha, and B.-A. Schubert, Thin Solid Films (519), 7382 (2011).

[17] N. Vora, J. Blackburn, I. Repins, C. Beall, B. To, J. Pankow, G. Teeter, M. Young, and R. Noufi, J. Vac. Sci. Technol., A (30), 051201 (2012).

[18] B. Shin, O. Gunawan, Y. Zhu, N. A. Bojarczuk, S. J. Chey, and S. Guha, Prog. Photovoltaics: Res. Appl. (21), 72 (2013).

[19] I. Repins et al., Sol. Energy Mater. Sol. Cells (101), 154 (2012).

[20] T. R. Knutson, P. J. Hanson, E. S. Aydil, and R. L. Penn, Chem. Commun. (50), 5902 (2014).

[21] J. J. Scragg, D. M. Berg, and P. J. Dale, J. Electroanal. Chem. (52) 646, (2010).

[22] R. Schurr et al., Thin Solid Films (517), 2465 (2009).

[23] T. K. Todorov, K. B. Reuter, and D. B. Mitzi, Adv. Mater. (22), E156 (2010).

[24] Y. Fahrettin, Solar Energy (85) 2518–2523 (2011).

Chapter 7. Conclusion and Future work

7.1. Conclusion and Future work

The fastest growing sector of the PV market is based on 'thin film' PV technologies. The 'thin film' materials in this context are semiconductors that overcome one limitation of crystalline silicon—the benchmark PV material—in that they have direct band gaps. This means that their light absorption coefficients are very high, and much thinner films of material can be used to be used to collect the same amount of light, making them less materials-intensive. In the most part, the thin film materials are compound p-type semiconductors, the major systems being $Cu(In,Ga)(S,Se)_2$ (CIGS), $CuInS_2$ (CIS) and CdTe. The power conversion efficiency record for laboratory scale CIGS devices has recently exceeded 20% for the first time. Another key advantage of these materials as compared to Si is their tolerance to defects and grain boundaries, which allows for less stringent quality requirements. At the same time, their compound nature means that the range of processing methods available to produce them is immense. The success of CIGS, CIS and CdTe is only diminished by the fact that they contain expensive and rare materials. The cost and availability of In is a particular issue that will become pressing in the context of the anticipated deployment of PVs on terawatt scales.

This thesis is concerned with a relatively new compound semiconductor material that has a great deal of potential for use in photovoltaic (PV) energy systems. Cu_2ZnSnS_4, abbreviated to 'CZTS', is closely related to a family of materials that have been in development for PV applications since the 1970s, and have reached mass production in recent years. PV systems generate power by direct transfer of the energy in sunlight into electrical current, and they have the potential to provide vast amounts of renewable energy. This fact has been long recognized, but historically the costs of PV have been high and the manufacturing capacity too low to have a significant impact on the energy generation sector. This is now changing; there are increasing concerns about the effects and causes of climate change, and the fact that current energy sources are finite, polluting and insecure.

The main purpose of this thesis is to study the superstrate absorber layer of the CIGS by two different preparation techniques i.e; electrodeposition and spin coating. Understanding the thin film material system with the factors controlling the yielded properties of the thin films is the main goal in order to yield high-efficiency solar cells. In this work, I have conducted a detailed

characterization of the structural and optoelectronic properties of p-type $CuInSe_2$ and $CuInS_2$ thin films, $CuIn_xCr_yGa_{1-x-y}Se_2$ where x=0.4, y= (0.0, 0.1, 0.2, 0.3) nano-crystalline powders and thin films and Cu_2ZnSnS_4 kesterite thin films. The $CuInSe_2$ and $CuInS_2$ thin films were successfully prepared by a non-vacuum, low cost electrodeposition technique onto ITO substrates. The resulting thin films showed very good crystallinity and homogeneity of the prepared films in agreement with the XRD, SEM and EDX measurements. In order to detect the prepared thin film carrier density type, Mott-Schottky measurements were carried out confirming that the prepared $CuInSe_2$ and $CuInS_2$ thin films were always p-type. The accumulated binary phases of $Cu_{2-x}(Se,S)$ were successfully eliminated through the etching process which in turn decreased both the flat band potential, V_{fb} (V) and the number of acceptors, N_A (cm^{-3}) for the prepared samples. The annealing temperature and time of annealing was the main effecting actor in the production of p-type material nano-crystalline thin films.

Polycrystalline powders of $CuIn_xCr_yGa_{1-x-y}Se_2$ at composition intervals of x=0.4, y= (0.0, 0.1, 0.2, 0.3) powders were prepared using hydrothermal auto-clave method. The synthesized nano-crystalline precursor powders were carefully controlled by washing and drying process in order to remove any impurity phases present. Those polycrystalline powders were then dissolved in ethylene diamine in order to develop suitable solution for spin coating process.

The Polycrystalline thin films of $CuIn_xCr_yGa_{1-x-y}Se_2$ were deposited onto various substrates then those on ITO substrates were studied. I showed that films with compositions of $x = 0.3$ tend to show an ordered defect compound (ODC) towards the surface of the films and formation of different crystalline phases. This order defect and phase deformation was clearly observed on XRD peaks and clearly deviation from preferred orientation of the peaks.

All the diffraction peaks were obtained which confirmed that the resulted nanocrystals have a chalcopyrite (tetragonal) phase with a definite structure of $CuIn_{0.4}Ga_{0.6}Se_2$, where x = 0.4 and y = 0.0 and that no other phases are produced in the reaction. Standard CIGS file (PDF card No. 00–035-1101) is used to identify the diffraction peaks. All peaks are identified as a pure phase of the synthesized $CuIn_yGa_{1-x-y}Se_2$ chalcopyrite phase with no secondary phases for y = 0.4 and x = 0.1, 0.2. It is clearly obvious from the XRD pattern the main characteristic peaks of the tetragonal chalcopyrite structure. The main peaks of CIGS (112) at about 27.1°, CIGS (204)/(220) at 2θ = 45.8°, and CIGS (116)/(312) at 2θ =52.5°, respectively.

One of the important and new approaches of this thesis was the identification and behavior of Cr doped $CuIn_{0.4}Ga_{0.6}Se_2$ at constant Indium content and different Chromium concentration.

I have identified that the doping of chromium until 2% showed a phase stability and higher conductivity than those of free chromium content and where chromium equal 1%.

Finally, Cu_2ZnSnS_4 thin films with kesterite structure were successfully synthesized using single step electrodeposition process. Annealing process in Argon and sulfur atmosphere were studied as function of time, as the time was fixed where in Argon atmosphere the temperature was held higher than those in sulfur atmosphere. Characterization techniques have revealed the formation of pure kesterite phase for the prepared Cu_2ZnSnS_4 films in both argon and sulfur atmosphere. XRD structure study showed indexed peaks for Cu_2ZnSnS_4 thin films with kesterite structure with average crystal size about 17 nm.

The morphological study for the sulfurized samples indicates that both films are polycrystalline with a uniform homogenous surface morphology suitable for solar cell applications. The elemental EDS analysis promotes that the prepared sulfurized films with Cu poor, Zn and S rich Cu_2ZnSnS_4 sulfurized kesterite films. For the photoelectrochemical performance of the $Cu_2ZnSnS_4$the photocurrent registered at open circuit potential and the photopotential developed across the sulfurized CZTS at 400 °C improve the cathodic nature of the photocurrent and the positive value of the photopotential confirms the p-type character of the film.

In summary, I have shown the effects of controlling starting material, annealing temperature and time resulting in a p-type nano-crystalline $CuInSe_2$ thin films and this was confirmed by Mott-Schottky measurements. I showed that hydrothermal synthesis of $CuIn_xCr_yGa_{1-x-y}Se_2$resulted in nanocrystalline powders with a chalcopyrite structure and no other phases were formed which depends on the choosing of the starting metal salts and suitable solvent. Doping with Cr appears to improve the structural quality of the films till y = 0.2 then phase changes and deformation occurs. This was seen by a XRD and EIS measurement that the conductivity values increase with the temperature following the order $\square$'(Cu $In_{0.4}$ $Ga_{0.6}$ Se_2)>$\square$' (Cu $Cr_{0.2}$ $In_{0.4}$ $Ga_{0.5}$ Se_2) >$\square$' (Cu $Cr_{0.1}$ $In_{0.4}$ $Ga_{0.3}$ Se_2) >$\square$' (Cu $Cr_{0.3}$ $In_{0.4}$ $Ga_{0.4}$ Se_2). These results suggest that the $CuCr_{0.2}In_{0.4}Ga_{0.5}Se_2$ alloy is a suitable candidate for higher bandgap solar cells. However, various issues must still be resolved in order to make the entire compositional alloy to be usable in solar cells.

7.2 Future Work

Therefore, based on these unresolved issues, I recommend the following topics as subjects for future study of this alloy:

1. Detailed surface studies of the $CuCr_{0.2}In_{0.4}Ga_{0.5}Se_2$ alloy in order to study the effects of the observed ordered defect compound.

2. Systematic study and characterization of a $CuCr_{0.2}In_{0.4}Ga_{0.5}Se_2$ /CdS heterojunction in order to understand better the interaction between the two layers.

4. Growth of polycrystalline $CuCr_{0.2}In_{0.4}Ga_{0.5}Se_2$ thin films on Mo-coated borosilicate glass in order to study the effects of Na vs. no Na on Mo-coated substrates.

5. Fabrication of devices consisting of $CuCr_{0.2}In_{0.4}Ga_{0.5}Se_2$ layers in order to relate optoelectronic defects to device performance.

6. Detailed electrical characterization that includes identification of deep defects in the films via capacitance methods.